

**A. Computational Chemistry Applied to the
Analysis of Air Pollution Reaction Mechanisms**

**B. Fundamental Studies of Droplet Evaporation and
Discharge Dynamics in Electrospray Ionization**

Thesis by
James N. Smith

In Partial Fulfillment of the Requirements
for the Degree of
Doctor of Philosophy

California Institute of Technology
Pasadena, California

2000
(Submitted May 11, 2000)

© 2000

James N. Smith

All Rights Reserved

Acknowledgements

It's the night before the deadline for handing in this thesis, and time to contemplate all those who have contributed to my life and work at Caltech. It's an daunting task, and I'm a bit reluctant to enter into it for fear that I will forget somebody important (it's going to be a late night!).

I have benefited greatly in having two advisors who complemented each other in ways both academic and personal. Rick Flagan is a man whose depth of knowledge in aerosol science still amazes me. What I will miss most about Rick, however, will be the brainstorming sessions that inevitably ended up with about a dozen crazy ideas and one true gem. I will always value his perspective on problems in science and academia, and hope we will never stop brainstorming wherever I end up in the next few years. I owe a great deal to Jack Beauchamp for his persistence in asking me to try his idea: "droplet ping-pong." After about a year of reminders, I did try it out. As I sit in lab writing this note I occasionally glance over to the ping-pong experiment, operating tonight on an electrospray of methanol. It will generate about 2000 droplet size and charge time sequences tonight, data of a quality and quantity never achieved until now. A pretty good idea. In the years I have known Jack I have truly enjoyed the great breadth of his curiosity. I have always felt a sense of being in his care, and hope that I can somehow reciprocate this in the years to come.

Caltech is made up of a lot of great staff. Priscilla Boon was always there to lend a hand with my complicated problems. I'm also grateful to Mike, Guy, and Ray in the Chemistry instrument shop for helping me to gain a useful vocation in case this research thing doesn't pan out. Linda and Fran in Environmental Engineering Sciences were always there to help out, or just there for a pleasant chat. Carol Mann helped me quite a lot in my dealings with Rick's organizational side.

I have made so many friends here at Caltech. I'm not sure I could possibly make a list of these people (nor do I see the usefulness of such a list), so I will forgo such

a task (it's getting REALLY late!). I do, however, want to acknowledge the help of some of these people in making this thesis possible. Pat Chuang will always be a great friend and confidant, and I look forward to being with him again as I start work at NCAR in Boulder, CO. Pat Lemieux is another one of those great friends who has helped me in figuring out so many things, not all of which related to research. The Beauchamp group (Ron, Heather, Ryan, Daniel, and Rob), have provided me with the much-needed daily encouragement during the past six months. It has also been fun to be sharing the last stages of graduate life with Rob Griffin, exchanging stories of our miseries and triumphs.

I think I must have had the best push-start in life for having been raised by my parents, in the presence of such great brothers and a great sister. My mom and dad have provided me with so much support and love during these last several years as a student. I hope that I can spend more time with all of them as I shift into a new life and career. My mother- and father-in-law have also been so supportive to myself and my family, and I feel fortunate for this.

Finally, I have shared this whole graduate student experience with my wife, Cathy. I don't think either of us knew what we were getting into when we decided to leave our professions in the Bay Area and move down to Pasadena so that I may be a student again ... certainly not two kids, a year in Sweden, and the past six months of sleeping on the floor of a nearly-empty apartment. Through it all she has been both patient and understanding and, when I most needed it, stubborn and insistent. I am especially glad for her insistence that I be present as a father to Anna and Mikael. In a world where the balance between family and career is often tipped towards the latter, Cathy asserted those things that were most important and, in so doing, has given me gifts that I will cherish for all time.

Abstract

The first part of the thesis investigates the use of theoretical quantum chemical calculations for the study of the reaction pathways of the atmospheric aromatic-OH reaction. The computational model is comprised of a semi-empirical PM3 geometry optimization followed by a single point calculation performed using the Becke3LYP hybrid density functional and a 6-31G(d,p) basis. Zero-point energies were calculated using PM3, and transition states barrier heights estimated by a constrained optimization procedure developed for this study. Full mechanisms for the OH-initiated photooxidation of toluene, *m*-xylene, *p*-xylene, 1,2,4-trimethylbenzene and *m*-ethyltoluene are developed. The lowest energy intermediates have been determined and predicted products from these structures are compared to available experimental product data. These studies serve to refine proposed mechanisms currently available for toluene, *m*-xylene and *p*-xylene, while providing new information on the 1,2,4-trimethylbenzene and *m*-ethyltoluene reaction pathways.

In the second part of the thesis, an experimental technique is described for probing the mechanism and dynamics of charged droplet breakup in electrospray ionization. At its core is an instrument that can perform simultaneous, *in situ* measurements of size and charge on individual droplets. Charged droplets are sampled directly from the spray source into a drift cell with a uniform electric field. A simultaneous diameter and charge measurement is made on individual droplets at the center of the cell using phase Doppler anemometry. By reversing the field in the drift chamber once the initial size and charge measurement is made, the droplet can be made to pass again through the measurement region of the phase Doppler anemometer. In this way, repeated measurements of the size and charge can be made on a single droplet. This technique has been applied to a variety of solutions used commonly in electrospray ionization and lead to the following generalizations. (1) The discharge dynamics of droplets with the same initial diameter and charge are highly reproducible for all

solvents and analyte/solvent combinations studied to date. (2) Published over a hundred years ago, Lord Rayleigh's analysis of charged droplet instabilities resulting from solvent evaporation is remarkably accurate in predicting observed discharge events for all three solvents. (3) Droplet discharge events are characterized by loss of 15-20% of the charge from methanol and acetonitrile droplets, and 20-40% from water droplets, with little accompanying loss of solvent. (4) Discharge events occur in a reproducible temporal pattern, with decreasing time intervals between successive events, dictated by solvent evaporation and the approach to the Rayleigh limit. The droplet size decrease agrees well with a model of solvent evaporation. (5) The addition of biomolecules or salt (up to 10^{-3} M) to the solution does not significantly alter discharge dynamics. The size-charge correlation and discharge dynamics of negatively charged droplets formed in electrospray ionization of 10^{-4} M NaCl in methanol are similar to those observed for positively charged droplets. (6) The life history of a single electrosprayed droplet can be followed through numerous discharge events (sequences with up to 50 measurements and 6 discharges have been observed) in the absence of radial confinement. This implies that no significant displacement of the droplet arises from discharge events and is inconsistent with any notion of high energy chaotic fission processes. (7) Droplet size-charge correlations show that, in certain instances, droplets from an electrospray fall into discrete groupings that can be attributed to fission events.

Contents

Acknowledgements	iii
Abstract	v
Part A: Computational Chemistry Applied to the Analysis of Air Pollution Reaction Mechanisms	1
1 Introduction	2
1.1 Background	2
1.2 Overview of Computational Chemistry	3
Bibliography	7
2 Mechanism of Atmospheric Photo-oxidation of Aromatics: A Theoretical Study	8
2.1 Introduction	9
2.2 Calculation Method	11
2.3 Results of Calculations	18
2.3.1 Reactions which Lead to the Formation of the Bicyclic Radical	18
2.3.2 Reactions of Aromatic-OH Adduct with NO ₂	31
2.4 Summary and Analysis	36
2.5 Conclusion	47
Bibliography	49
Part B: Fundamental Studies of Droplet Evaporation and Discharge Dynamics in Electrospray Ionization	53

3	Introduction	54
3.1	Overview of Part B	57
	Bibliography	60
4	A Survey of Past Research in Electrospray Ionization	61
4.1	Introduction	61
4.2	Droplet Formation and Charging	61
4.3	Charged Droplet Evaporation and Breakup	65
4.4	Gas-phase Ion Production from Charged Droplets	70
4.4.1	Modeling Studies	76
4.4.2	Experimental Studies	79
4.5	Review of Unresolved Issues in Electrostatic Spraying and Electrospray Ionization	83
	Bibliography	86
5	Mobility Measurements of Charged Droplets and Ions	90
5.1	Introduction	90
5.2	A Mobility-Based Technique for Investigating Dynamic Processes In- volving Ions and Droplets	92
5.2.1	The Mobility of a Charged Droplet	94
5.2.2	The Mobility of a Gas Phase Ion	96
5.3	Modeling the Dynamics of Charged Droplet Breakup and Ion Forma- tion in a Drift Cell	101
5.4	Conclusion	110
	Bibliography	114
6	Fundamental Studies of Droplet Evaporation and Discharge Dynam- ics in Electrospray Ionization	116

Bibliography	122
7 A Study of the Evolution of Droplet Size and Charge in Electrospray	124
Ionization: The Droplet Ping-Pong Experiment	124
7.1 Introduction	125
7.2 Background	126
7.3 Instrumentation	130
7.3.1 Theory	130
7.3.2 Electrospray Source	133
7.3.3 Drift Cell	134
7.3.4 Phase Doppler Anemometer	138
7.3.5 Data Acquisition and Instrument Control System	140
7.4 Experiment	141
7.4.1 Size-Charge Correlation of Electrosprayed Droplets	143
7.4.2 Time Evolution of Droplet Size and Charge	143
7.5 Analysis	150
7.6 Conclusion	152
Bibliography	154
8 The Design and Calibration of a Phase Doppler Anemometer	157
8.1 Introduction	157
8.2 Background	158
8.3 System Description	161
8.3.1 Optical Components	161
8.3.2 Signal Digitization	168
8.3.3 Signal Processing	168
8.3.4 Software Interface	170
8.4 Particle Size Calibration	170
8.5 Conclusion	178
Bibliography	182

9	The Mechanism of Droplet Discharge in Electrospray Ionization:	
	Solvent and Buffer Gas Composition Effects	183
9.1	Introduction	183
9.2	Experimental Arrangement	184
9.3	Solvent Effects: Electrosprays of Methanol, Acetonitrile, and Water	185
9.4	Droplet Charge Polarity Effects	195
9.5	Electrolyte Concentration Effects	198
9.6	Buffer Gas Composition Effects	201
10	Recommendations for Future Work	205
	Bibliography	213
	Appendices	214
A	Phase Doppler Anemometer Operations Manual	215
A.1	Introduction	215
	A.1.1 Phase Doppler Theory	215
	A.1.2 Adjustments to Instrument that Affect Measurement Range	222
A.2	Calibration	228
	A.2.1 When to Calibrate	228
	A.2.2 Calibration Fundamentals	229
	A.2.3 Methods for Producing Calibrated Particles	230
	A.2.4 Laser Safety	232
A.3	Optical System Description	234
	A.3.1 Transmitter	234
	A.3.2 Alignment of Transmitter Optics	236
	A.3.3 Receiver	239
	A.3.4 Positioning of Receiver	244
A.4	Data Acquisition and Signal Processing	246
	A.4.1 Signal Processing	248
	A.4.2 Data Acquisition using a Digital Oscilloscope	250

A.4.3	System Software	251
A.5	Machine Drawings and Parts Lists	256
A.5.1	Transmitter	256
A.5.2	Receiver	259
Bibliography		266
B	The Design and Operation of a Simple, Low-Cost Drop-on-Demand	
	Generator	268
B.1	Introduction	268
B.2	Operation Principle	269
B.3	Instrument Description	270
B.3.1	Generator Head	271
B.3.2	Fluid Delivery System	272
B.3.3	Electronics: PZT Driver Circuitry	274
B.4	Performance	276
B.5	Operation and Troubleshooting	279
B.6	Parts List and Drawings	282
Bibliography		286
C	An Optical Receiver for Laser Induced Fluorescence Studies	287
C.1	Introduction	287
C.2	Instrument Description	287
C.2.1	Receiver Head and Optical Light Guide	287
C.2.2	Detector Assembly	290
C.3	Parts List and Drawings	291
D	Quantification of the Energetics of Droplet Fissioning with Droplet	
	Ping-Pong Measurements	297
D.1	Theory	297
D.2	Conclusion	300

List of Figures

- 2.1 Possible reactions in a generalized mechanism of aromatic-OH photo-oxidation. R represents either an H atom or an alkyl group, depending on the aromatic considered. 19
- 2.2 Reaction coordinate diagram for toluene. Indicated are the three favored pathways. Shown below the plots are the corresponding aromatic-OH adduct, peroxy radical, and bicyclic radical corresponding to the pathways. The structures are labeled P1, P2, and P3 corresponding to paths 1, 2, and 3, respectively. 37
- 2.3 Reaction coordinate diagram for *m*-xylene. Indicated are the energies of the two favored pathways. Shown below the plots are the corresponding aromatic-OH adduct, peroxy radical, and bicyclic radical corresponding to the pathways. The structures are labeled P1 and P2 corresponding to paths 1 and 2, respectively. 38
- 2.4 Reaction coordinate diagram for *p*-xylene. Shown below the path are the corresponding aromatic-OH adduct, peroxy radical, and bicyclic radical corresponding to the favored pathway. 39
- 2.5 Reaction coordinate diagram for 1,2,4-trimethylbenzene. Indicated are the energies of the three favored pathways. Shown below the diagram are the corresponding aromatic-OH adduct, peroxy radical, and bicyclic radical corresponding to the pathways. The structures are labeled P1, P2, and P3 corresponding to paths 1, 2, and 3, respectively. 40
- 2.6 Reaction coordinate diagram for *m*-ethyltoluene. Indicated are the energies of the three favored pathways. Shown below the diagram are the corresponding aromatic-OH adduct, peroxy radical, and bicyclic radical corresponding to the pathways. The structures are labeled P1, P2, and P3 corresponding to paths 1, 2, and 3, respectively. 41

2.7	ΔH_{rxn} values for Reactions 4 and 5 for different aromatic systems. . .	43
2.8	Subsequent reaction of oxy radicals formed from Reaction 5 of the generalized mechanism.	44
2.9	β -scission of a bicyclic oxy radical of toluene to give ring fragmentation products. Decomposition path A is the favored path for fragmentation of the acyclic radical.	45
2.10	Fragmentation products formed from the bicyclic oxy radical.	46
3.1	Schematic of the electrospray process.	55
4.1	Lord Kelvin's droplet high-voltage generator.	63
4.2	Schematic of Charged Residue Model (left) and Ion Desorption Model (right) for ion formation from highly charged droplets. Circles indicate presence of solvent molecules and "M" represents analyte.	71
4.3	A plot of the size and charge of an evaporating offspring droplet in the IDM.	72
5.1	Principle of operation for mobility measurements using a drift cell. Ions (or charged droplets) drift through a buffer gas under the influence of an electric field and gravity, quickly achieving steady state and separating into packets based on their size and charge.	93
5.2	Range of charging on droplets of water and methanol for $E=200$ V/cm and a static buffer gas of N_2 at 1 atm. Maximum allowed charge corresponds to Rayleigh limit, minimum allowed charge is for electrostatic forces to just exceed gravitation.	95
5.3	Mobility of an evaporating methanol droplet in a drift cell, under the following conditions: $E=200$ V/cm, $q=10^5$ elementary charges, static N_2 buffer gas at 1 atm. Diameter at which Rayleigh instability occurs for methanol and 10^5 charges is indicated.	96

5.4	Maximum mobility for charged water droplets before onset of Rayleigh instability. Numbers of charges that correspond to the stability limit are shown for selected droplet diameters. Superimposed on graph are drift velocities for bare ions under the same cell conditions. Also shown are mobilities for various electric fields within the drift cell. Other drift cell conditions: static N ₂ buffer gas at 1 atm and 293 K.	98
5.5	Maximum mobility for charged methanol droplets before onset of Rayleigh instability. Numbers of charges that correspond to the stability limit are shown for selected droplet diameters. Superimposed on the graph are drift velocities for bare ions under the same cell conditions. Other drift cell conditions: static N ₂ buffer gas at 1 atm and 293 K.	100
5.6	Droplet diameter as a function of time for uncharged droplets of methanol and water in vapor-free N ₂ gas, from Equation 5.8 with correction for temperature depression. Temperatures of bath gas are indicated.	105
5.7	Water droplet lifetimes as a function of relative humidity for an initial droplet diameter of 40 μm at 20° C.	106
5.8	Droplet diameter and mobility as a function of time for a water droplet with an initial diameter of 40 μm and with initially one-half of the Rayleigh limit of charge (5.6×10^6 elementary charges). Drift cell conditions: 200 V/cm electric field; static N ₂ buffer gas at 1 atm and 293 K.	108
5.9	Droplet diameter and mobility as a function of time for a methanol droplet with an initial diameter of 40 μm and with initially one-half of the Rayleigh limit of charge (3.1×10^6 elementary charges). Drift cell conditions: 200 V/cm electric field; static N ₂ buffer gas at 1 atm and 293 K.	109

5.10	Axial position of the 40 μm water droplet depicted in Figure 5.8 as a function of time in a drift cell. Also shown is the position as a function of time of bare gas-phase bradykinin ions that are formed instantly at each discharge event. These ions propagate through the cell with a mobility taken from Table 5.2.2.	111
5.11	Axial position of the 40 μm methanol droplet depicted in Figure 5.9 as a function of time in a drift cell. Also shown is the position as a function of time of bare gas-phase bradykinin ions that are formed instantly at each discharge event. These ions propagate through the cell with a mobility taken from Table 5.2.2.	112
6.1	Experimental apparatus for studying droplet evaporation and discharge dynamics.	117
6.2	Electrospray ionization size-charge correlations for positively charged droplets of (a) water, (b) acetonitrile, (c) methanol, and for (d) negatively charged droplets of methanol with 10^{-4} M NaCl. Also plotted are curves representing the Rayleigh instability limit.	118
6.3	Evaporation and discharge of a positively charged methanol droplet in 51 V/cm electric field. (a) Variation of droplet diameter with time. (b) Variation of droplet charge with time, represented as number of elementary charges and as percent of the Rayleigh limit of charge for measured droplet diameter.	119
7.1	PDA system optical arrangement.	128
7.2	Typical signals from a phase Doppler receiver.	129
7.3	Experimental apparatus for studying droplet evaporation and discharge dynamics.	131
7.4	IMS electrostatic field calculated with SIMION. Charging electrode is located in the upper left of the figure, and outlet is on the lower right.	135
7.5	IMS fluid flow field calculated with FIDAP. Gas inlet is located to the left of the figure, which shows a small region of the drift cell.	136

7.6	Electrical circuit for reversing field in the drift cell.	137
7.7	Phase Doppler anemometer transmitter (above), and receiver (below). Transmitter baseplate is 45 mm in length and the receiver is 3.3 cm in diameter by 24 cm in length.	138
7.8	Programmable gain amplifier circuit for phase Doppler receiver. . . .	140
7.9	Data acquisition and experiment control flowchart.	142
7.10	Plots of size and charge measurements of individual droplets in a me- thanol electrospray. A: Droplet diameter histogram; B: Droplet charge histogram; C: Diameter versus charge, plotted alongside the Rayleigh stability limit curve; D: Diameter versus charge, with charge repre- sented as the percentage of the Rayleigh limit.	144
7.11	Time series plots for a methanol droplet in a 51 V/cm field. A: Time se- ries of droplet diameter; B: Time series of droplet axial speed; C: Time series of droplet charge, presented in number of elementary charges and in percent of the Rayleigh limit of charge. Arrows indicate dis- crete discharge events; D: Channel 1 raw signal.	145
7.12	Time series plots of (A) diameter and (B) charge from an electro- spray of spectroscopic grade methanol, showing a non-volatile particle charged at the Rayleigh limit.	147
7.13	Summary of time series plots for methanol droplets with initial diam- eter of $25.2 \pm 0.5 \mu\text{m}$ in a 51 V/cm field. A: Superposition of diameter time sequences. Also plotted is the predicted evaporation dynamics of a neutral droplet in a vapor-free gas. B: Superposition of droplet charge time sequences, presented as percent of the Rayleigh limit of charge. Shown also are charge histograms for selected groups of measurements.	149
7.14	Superposition of eight measurements of positively charged methanol droplets with an initial charge of $3.49 \pm 0.08 \times 10^6 e$ and an initial diam- eter of $27.2 \pm 0.05 \mu\text{m}$	150
8.1	PDA system optical arrangement.	160

8.2	Theory of PDA measurements. (a) Radial intensity profile at the measurement volume. (b) The measurement volume, defined by the intersection of two phase-matched laser beams. (c) Schematic diagram of path of each beam through a refracting particle and to an external detector.	160
8.3	Typical signals from a phase Doppler receiver.	161
8.4	PDA system schematic.	162
8.5	PDA transmitter assembly diagram. See Table 8.2 for parts identification.	165
8.6	PDA receiver assembly diagram. See Table 8.3 for parts identification.	166
8.7	PDA pre-amplifier and programmable gain amplifier circuit.	166
8.8	Flowchart for PDA calibration and data acquisition modules.	171
8.9	Data acquisition panel for PDA control software.	172
8.10	Theoretical calibration curves obtained with geometrical optics theory (Equations 8.3–8.12) and with Mie theory (SCATAP results), using design parameters for optical configuration. Also plotted is a 6th order polynomial least squares fit to the Mie theory data.	175
8.11	Experimental arrangement for testing and calibration of PDA. Distances of transmitter and receiver to measurement volume are not to scale.	177
8.12	Velocity-phase shift correlation for water droplets falling at terminal velocity.	179
8.13	Calibration curve for PDA. Droplet diameter is determined from the measured terminal velocity. Also plotted is the theoretical calibration curve obtained with SCATAP using “design” parameters for optical configuration.	180
9.1	The droplet ping-pong experiment: measurement concept.	185
9.2	Experimental apparatus for studying droplet evaporation and discharge dynamics.	186

- 9.3 Plots of size and charge measurements of individual droplets in a positive-ion electrospray of 10^{-4} M NaCl in water. A: Droplet diameter histogram; B: Droplet charge histogram; C: Diameter versus charge, plotted with a curve representing the Rayleigh stability limit. 188
- 9.4 Plots of size and charge measurements of individual droplets in a positive-ion electrospray of pure acetonitrile. A: Droplet diameter histogram; B: Droplet charge histogram; C: Diameter versus charge, plotted with a curve representing the Rayleigh stability limit. 189
- 9.5 Plots of size and charge measurements of individual droplets in a positive-ion electrospray of pure methanol. A: Droplet diameter histogram; B: Droplet charge histogram; C: Diameter versus charge, plotted with a curve representing the Rayleigh stability limit; D: Diameter versus charge, with charge represented as the percentage of the Rayleigh limit. 190
- 9.6 Evaporation and discharge of a positively charged water droplet in a 317 K N_2 buffer gas and a 51 V/cm electric field. A: Variation of droplet diameter with time. Also plotted is the predicted evaporation dynamics of a water droplet in a vapor-free N_2 gas at 317 K. B: Variation of droplet axial speed with time. C: Variation of droplet charge with time, represented as number of elementary charges and as percent of the Rayleigh limit of charge for measured droplet. 192
- 9.7 Evaporation and discharge of a positively charged acetonitrile droplet in a 51 V/cm electric field. Also plotted is the predicted evaporation dynamics of a acetonitrile droplet in a vapor-free N_2 gas. A: Variation of droplet diameter with time; B: Variation of droplet axial speed with time; C: Variation of droplet charge with time, represented as number of elementary charges and as percent of the Rayleigh limit of charge for measured droplet. 193

- 9.8 Evaporation and discharge of a positively charged methanol droplet (10^{-6} M NaCl added) in a 51 V/cm electric field. Also plotted is the predicted evaporation dynamics of a neutral methanol droplet in a vapor-free N_2 gas. A: Variation of droplet diameter with time; B: Variation of droplet axial speed with time; C: Variation of droplet charge with time, represented as number of elementary charges and as percent of the Rayleigh limit of charge for measured droplet. 194
- 9.9 Diameter versus charge for a negative-ion electrospray of 10^{-4} M NaCl in methanol. A: Droplet charge histogram; B: Droplet diameter histogram; C: Diameter versus charge, plotted with a curve representing the Rayleigh stability limit; D: Diameter versus charge, with charge represented as the percentage of the Rayleigh limit. 196
- 9.10 Evaporation and discharge of a negatively charged droplet of comprised of equal volumes of methanol and water in a 51 V/cm electric field. Also plotted is the predicted evaporation dynamics of a water droplet in a vapor-free N_2 gas. A: Variation of droplet diameter with time; B: Variation of droplet axial speed with time; C: Variation of droplet charge with time, represented as number of elementary charges and as percent of the Rayleigh limit of charge for measured droplet. 197
- 9.11 Diameter versus charge, with charge represented as the percentage of the Rayleigh limit, for a positive-ion electrospray of methanol with the following concentrations of NaCl: A. 10^{-6} M; B. 10^{-5} M; C. 10^{-4} M. 199
- 9.12 Evaporation and discharge of positively charged droplets of 10^{-6} – 10^{-4} M NaCl in methanol in a 51 V/cm electric field. A: Variation of droplet diameter with time; B: Variation of droplet axial speed with time; C: Variation of droplet charge with time, represented as percent of the Rayleigh limit of charge for measured droplet size. 200

9.13	Evaporation and discharge of a positively charged methanol droplet in a quiescent buffer gas and a 51 V/cm electric field. Also plotted (dashed line) is the predicted evaporation dynamics of a neutral methanol droplet in a vapor-free N ₂ gas. A: Variation of droplet diameter with time; B: Variation of droplet axial speed with time; C: Variation of droplet charge with time, represented as number of elementary charges and as percent of the Rayleigh limit of charge for measured droplet.	202
9.14	Evaporation and discharge of a positively charged methanol droplet in a nearly saturated buffer gas and a 51 V/cm electric field. A: Variation of droplet diameter with time; B: Variation of droplet axial speed with time; C: Variation of droplet charge with time, represented as number of elementary charges and as percent of the Rayleigh limit of charge for measured droplet.	203
9.15	Evaporation and discharge of a positively charged methanol droplet in an O ₂ buffer gas and a 51 V/cm electric field. A: Variation of droplet diameter with time; B: Variation of droplet axial speed with time; C: Variation of droplet charge with time, represented as number of elementary charges and as percent of the Rayleigh limit of charge for measured droplet.	204
10.1	Modeled time series of droplet charge for an evaporating methanol droplet with initially 80% of the Rayleigh limit of charge.	206
10.2	Time between fission events for the 40 μm methanol droplet portrayed in Figure 10.1. Also plotted is the theoretical minimum sampling time for the same droplet, based on its aerodynamic response time.	207
10.3	Modeled position of the charged droplet from Figure 10.1 during the ping-pong experiment, in a 50 V/cm electric field. Also plotted is the position of a bare gas phase Bradykinin ion in a +2 charge state.	208

10.4	Proposed modification of the drift cell to allow for the injection of desorbed ions from the oscillating trapped droplet into a mass spectrometer.	211
10.5	Overview of LIF receiver system showing primary components.	212
A.1	PDA system optical arrangement.	216
A.2	Theory of PDA measurements. (a) Radial intensity profile at the measurement volume. (b) The measurement volume, defined by the intersection of two phase-matched laser beams.	217
A.3	Calibration for PDA, showing phase shift versus particle size relationship using SCATAP and the experimentally obtained relationship resulting from calibration with a VOAG. For optical configuration see Table A.1.	220
A.4	Calibration curves for various collection angles, showing the effect that an uncertainty in the angle might have in the particle size measurement. For optical configuration see Table A.1.	221
A.5	PDA calibration curves for pure water as a function of collection angle. For optical configuration see Table A.1.	224
A.6	Visibility of PDA signals. As a scattering particle becomes large in relation to the fringe separation the visibility will decrease.	226
A.7	Particle size versus PDA signal visibility for water droplets ($n = 1.33$), using the optical configuration in Table A.1.	227
A.8	PDA calibration with a VOAG: Measured diameter vs. VOAG calibration diameter.	232
A.9	PDA transmitter.	234
A.10	Photograph of the PDA transmitter showing the main parts. 1: Polarized HeNe laser, 2: Beamsplitter assembly, 3: Front lens.	235
A.11	Close-up of the beamsplitter assembly, showing the beamsplitter and turning mirror. 1: Locking knob for turning mirror carriage. 2: Vertical rail. 3: Adjustment knob for tilting beamsplitter mount.	237

A.12 PDA receiver.	240
A.13 Photograph of PDA receiver showing key elements. 1: Rear tube, 2: Spatial filter, 3: Adjustment knob for tilt adjustment, 4: Collection lens and retainer ring.	241
A.14 Image of slit projected across laser beams (diagram not to scale). . .	243
A.15 Close-up of receiver spatial filter slit.	246
A.16 Actual signals from the PDA receiver (signals are inverted due to the use of an inverter amplifier as the preamp). Top: A badly misaligned receiver, particle is scattering outside the crossover region, as evident by the presence of two Gaussian bursts. Middle: Receiver is close to being aligned, since the top envelope of the sinusoid is Gaussian. However, lower part of envelope is not Gaussian, which indicates particle is not passing through exact intersection point. Bottom: A well-aligned system, showing a Gaussian profile for both upper and lower envelopes.	247
A.17 Panels from the PDA system software. Top: PDA parameters and data on the front panel. Bottom: Signal monitor panel.	252
A.18 Flowchart for monitor module.	253
A.19 Flowchart for PDA calibration and data acquisition modules.	255
A.20 Assembly diagram for PDA transmitter.	256
A.21 Assembly diagram for PDA receiver.	259
B.1 Overview of DoD generator head showing primary components. . . .	269
B.2 Photograph of DoD generator head and external reservoir.	270
B.3 Detailed view of the spring that electrically connects both outer surfaces of the piezoelectric disk to the generator head.	271
B.4 Schematic of fluid delivery system.	273
B.5 Schematic of the PZT driver electronics.	275
B.6 Typical size (horizontal axis, in μm) and velocity (vertical axis, in cm/s) distribution for charged droplets injected into an ion mobility spectrometer, as measured with a phase Doppler anemometer.	277

B.7	Droplet diameter and velocity as a function of pulse properties, as measured with a phase Doppler anemometer.	278
B.8	Assembly diagram for drop-on-demand generator head.	283
C.1	Overview of LIF receiver system showing primary components.	288
C.2	Optical response in one-half of the measurement volume, showing uniform collection efficiency.	289
C.3	Assembly diagram for LIF receiver. For parts description see Table C.1.	292
D.1	Model for impulse imparted to parent droplet during Rayleigh instability.	298
D.2	Maximum impulse imparted to a water droplet as a function of droplet diameter, assuming that displacement lies within the 100 μm PDA measurement volume.	301

List of Tables

2.1	Toluene photooxidation products: molar yields.	10
2.2	<i>M</i> -xylene photooxidation products: molar yields.	11
2.3	<i>P</i> -xylene photooxidation products: molar yields.	12
2.4	Relative energies (in kcal/mol) for isomers of the methylhydroxycyclohexadienyl radical using various computational methods. ^a	14
2.5	Comparison of relative energies of different structural isomers based on experimental data and theoretical calculations.	15
2.6	A comparison of experimentally and theoretically derived ΔH_{rxn} values for the toluene + OH reaction.	16
2.7	Calculated energies (in hartrees) of molecules involved in reactions with aromatics in this study. ^a	20
2.8	PM3 Equilibrium structures for a representative selection of the most stable reaction products of aromatics with OH (Reaction 1b). ^a	21
2.9	PM3 equilibrium structures for a representative selection of the most stable reaction products of aromatic-OH adducts with O ₂ (Reaction 2b). ^a	22
2.10	PM3 equilibrium structures for a representative selection of the most stable reaction products in the formation of bicyclic endoperoxy radicals from peroxy radical intermediates (Reaction 4). ^a	23
2.11	Calculated energies (in hartrees) of the most stable reaction intermediates for the reaction pathways leading to the formation of the bicyclic endoperoxy radicals.	25
2.12	Calculated energies (in hartrees) for the products of the reaction of NO with a representative selection of the most stable peroxy intermediates and for the products of the reaction of O ₂ with a representative selection of the most stable bicyclic intermediates.	26

2.13	Approximate transition state energies for the reactions of aromatic-OH adducts with O ₂	29
2.14	Approximate transition states for the addition reactions of bicyclic endoperoxy radical with O ₂	30
2.15	Approximate transition states for the formation of the bicyclic endoperoxy radical.	32
2.16	PM3 geometries for equilibrium and approximate transition state structures for reactions of aromatic-OH adducts with NO ₂	34
2.17	Calculated energies (in hartrees) of the products formed by the reactions of NO ₂ with the toluene-OH adduct.	35
4.1	Modern experimental observations of charged droplet breakup.	69
5.1	Mobilities of Ions	97
7.1	Calculated charge and diameter for methanol droplets at the Rayleigh instability limit. Also shown are droplet velocities in a 50 V/cm electric field and droplet relaxation times.	132
7.2	Phase Doppler Anemometer optical configuration for the current investigation.	139
8.1	Estimated PDA system maximum particle size and velocity.	163
8.2	PDA transmitter parts list.	164
8.3	PDA receiver parts list.	167
8.4	Optical configuration for Instrument Calibration.	174
A.1	Typical optical configuration for PDA.	219
A.2	Estimated PDA system maximum particle size and velocity.	223
A.3	PDA transmitter parts list.	258
A.4	PDA receiver parts list.	260
B.1	Drop-on-demand parts list.	282

C.1 LIF receiver parts list. 291

Part A: Computational Chemistry
Applied to the Analysis of Air Pollution
Reaction Mechanisms

Chapter 1 Introduction

1.1 Background

In a recent review by Atkinson on the current status of knowledge of the gas-phase reactions of non-methane hydrocarbons,[1] the mechanisms and products of the OH radical-initiated reactions of aromatic hydrocarbons were highlighted as one of the most important unresolved issues. The fact that similar statements have appeared in similar reviews dating back to the earliest works by Shepson in 1984[2] is testament to the difficulties associated with studying the reactions of these large hydrocarbons. In the investigation presented here, a method for studying the reaction mechanisms of aromatics is presented based on theoretical chemical techniques. These techniques are then applied to the initial oxidation steps of five aromatic compounds. This chapter is derived from an article that appeared in the *Journal of Physical Chemistry* in 1996.[3] It has been modified from the published form to provide a more detailed explanation of the computational method and a better separation of the experimental results from their interpretation. The study was instigated as part of an independent studies course in computational chemistry at Caltech, Chemistry 120b, taught by W. A. Goddard III. It was the result of a collaboration with J. M. Andino, then a graduate student in J. H. Seinfeld's research group at Caltech. J. M. Andino was primarily responsible for supplying the mechanisms and interpreting the results of the calculations. My primary responsibilities were in the development and implementation of the theoretical chemical techniques, which will be briefly introduced in the following paragraphs.

1.2 Overview of Computational Chemistry

An excellent overview of the many implementations of theoretical chemistry can be found in the available literature.[4, 5] The major objective of a theoretical calculation is to determine molecular properties; examples include geometry, total energy, and vibrational modes, through the application of a model-independent set of mathematical relations. Many approaches exist for doing this. The most popular is an *ab initio* calculation, which defines the fundamental building blocks of a molecule as consisting of electrons, nuclei, and the electrostatic forces by which they interact (thus the source of the term *ab initio* which means “from first principles”). In *ab initio* chemistry, the mathematical relation that is used to describe the interactions is the Schrödinger equation, for which a wavefunction is found that forms the basis for calculating all properties of a molecule.

Most *ab initio* calculations start by invoking the Born–Oppenheimer approximation, which states that the motion of the electrons and the nuclei can be completely de-coupled. This approximation has been shown to be quite accurate under practically all conditions.[5] As a result of this, the calculation is simplified to one of calculating the optimum wave function for electrons in the presence of seemingly static, but oppositely charged, nuclei. For systems of more than one electron, this wave function cannot be calculated exactly, and numerous approximation methods have been developed. The most difficult challenge in developing these methods is to account for the instantaneous interactions between electrons, so-called “electron correlation.” Models that do not include electron correlation cannot be relied upon for consistently accurate results, but are generally less computationally intensive compared to models that include it. An exception is the semiempirical method, which attempts to improve upon the non-correlated wave function by adding parameters that are optimized using experimentally obtained values for molecular structure, enthalpy, and other physical properties. Since it is based upon this parameterization, the semiempirical method can be considered only as good as the database of experimental observations that are used in this parameterization; semiempirical methods

cannot be reliably extended to molecular structures that are fundamentally different than those in the database. However, one area where it has enjoyed considerable popularity is in the calculation of molecular structure, especially for large compounds of biological interest where more rigorous methods are not practical due to computational requirements.

In addition to *ab initio* and semiempirical methods, a third approach is gaining prominence, and plays a central role in the proceeding study. In density functional theory, the role of the wave function is replaced with the electron density, ρ . The total energy of the molecular system is then expressed as a sum of functionals (a mathematical term meaning functions in which the independent variable is itself a function) of ρ and sometimes $\nabla\rho$. Like the *ab initio* approach, the most challenging aspect of density functional theory is the determination of the exchange–correlation functional that is used to describe electron correlation and exchange (the latter referring to the electrons as Fermi particles – thus an exchange between any two electrons must result in a sign change in the wavefunction). The density functional approach is inherently more computationally efficient, however, and has been shown to produce results that are comparable to high–level wave function–based *ab initio* methods, but requiring fewer computational resources. In addition, the seemingly insignificant change from wave function to electron density produces an unexpected result. The Kohn–Sham Theory, developed in 1964 and for which Walter Kohn was awarded the Nobel Prize in 1998, mathematically proves the existence of an exchange–correlation functional for which the calculated total energy is the *exact* ground state energy. If the Kohn–Sham theory also provided us with the form of that functional, then most problems in the physical sciences could be solved at the computer keyboard! Unfortunately, there is no known means for developing such functionals. In the past 36 years, however, many forms of the exchange–correlation functional have been developed and have proved to be both accurate and computationally efficient. One example is the functional used in this study, Becke3LYP, which has had considerable success in the calculation of the structure and energies of compounds similar to those in the current study.

In implementing a theoretical technique for determining the total energy of a

molecule, the size of the molecule and its atomic structure are the main factors to consider. As in most numerical methods, the accuracy of the calculation must be weighed against available computing power. One of the goals of the current study was to present a method that can be performed with modest computational resources. In light of this, a brief discussion of the selection and implementation of the theoretical method will be given.

Traditionally, electronic structure calculations proceed via a two step process. First an optimized structure is found that minimizes the total energy of the compound. This procedure is computationally intensive, requiring first- and second-order derivatives. This calculation is usually accompanied by a determination of the zero point energy of the molecule, obtained by calculating the normal mode vibrations of the constituent atoms. Once the optimized structure is found, the second step in the process is to determine its total energy, called a "single-point energy calculation." Since this step is intrinsically less computationally demanding than the optimization step, it can be done at a higher level of theory. A common practice in most calculations of both optimized structure and energy makes use of a universally-recognized observation: the geometry obtained by the optimization step seems in most cases to be less dependent on the level of theory than the calculation of the final energy in the single-point calculation step. In light of this, most methods involving large structures such as those in the proceeding study call for optimizations at a relatively low level of theory, followed by a single-point energy calculation at the highest level that is allowed by the available resources. In this investigation, we proposed the use of a semiempirical method called PM3 for all geometry optimizations and zero point energy determinations. This is followed by a density functional calculation using the Becke3LYP functional and a 6-31G(*d,p*) basis set to describe the electron density. Theoretical studies that have been published since ours on the same aromatic compounds, most of which had narrower scope and used higher levels of theory for the geometry optimization step, obtained values for the relative energies of structural isomers that were quite consistent with ours.[6, 7]

The most challenging aspect of the study was to develop a quantitative means

for describing the barrier for each reaction step. This was done with a constrained optimization procedure, which is explained in greater detail in Section 2.2. The main problem with this technique for locating the transition state is that it does not constrain the spin state of the electronic system. In going from reactants to products, the technique published here allows the spin state of the system to change over factors of two or more. Since, in a unimolecular step, the spin state must be conserved in moving from the precursor compound to the transition state, the conditions under which the calculations are made are clearly not reflective of reality. This point has been raised in a subsequent study of benzene oxidation,[8] where the authors claim that we greatly overestimated the barrier height of O₂ addition to the OH-aromatic adduct by our constrained optimization method. In spite of questions of the accuracy of the barrier heights presented in the original paper, the main conclusions of the study regarding the most important pathways and reaction intermediates remain unchanged.

Bibliography

- [1] R. Atkinson. Gas-phase degradation of organic compounds in the troposphere. *Pure Appl. Chem.*, 70(7):1327–1334, 1998.
- [2] P. B. Shepson, E. O. Edney, and E. W. Corse. Ring fragmentation reactions on the photooxidations of toluene and ortho-xylene. *J. Phys. Chem.*, 88(18):4122–4126, 1984.
- [3] J. M. Andino, J. N. Smith, R. C. Flagan, W. A. Goddard, and J. H. Seinfeld. Mechanism of atmospheric photooxidation of aromatics: a theoretical study. *J. Phys. Chem.*, 100(26):10967–10980, 1996.
- [4] J. B. Foresman and Æ. Frisch. *Exploring Chemistry with Electronic Structure Methods*. Gaussian, Inc., Pittsburgh, PA, 1996.
- [5] W. J. Hehre, L. Radon, J. A. Pople, and P. V. R. Schleyer. *Ab Initio Molecular Orbital Theory*. John Wiley and Sons, New York, 1986.
- [6] L. J. Bartolotti and E. O. Edney. Density-functional theory derived intermediates from the OH initiated atmospheric oxidation of toluene. *Chem. Phys. Lett.*, 245(1):119–122, 1995.
- [7] R. Freschen, F. M. Tao, and S. Hewitt. Ab initio calculations of the ground state geometry, energy, and vibrational frequencies of methylhydroxycyclohexadienyl. In *Informal Symposium on Kinetic and Photochemical Processes in the Atmosphere*, Riverside, CA, 1998.
- [8] G. Ghigo and G. Tonachini. Benzene oxidation in the troposphere. Theoretical investigation on the possible competition of three postulated reaction channels. *J. Am. Chem. Soc.*, 120(27):6753–6757, 1998.

Chapter 2 Mechanism of Atmospheric Photo-oxidation of Aromatics: A Theoretical Study

Abstract

The mechanisms of atmospheric photooxidation of aromatic compounds are of seminal importance in the chemistry of the urban and regional atmosphere. It has been difficult to experimentally account for the full spectrum of oxidation products in laboratory studies. In an effort to fully elucidate the atmospheric reaction pathways for the aromatic-OH reaction, we have conducted theoretical calculations on aromatic intermediates. Energies have been determined for these intermediates using semi-empirical UHF/PM3 geometry optimizations combined with single point energy calculations using density functional theory (DFT). A hybrid DFT model, the Becke 3 parameter functional with the non-local correlation functional of Lee, Yang and Parr, was used in conjunction with the 6-31G(*d,p*) basis set to study the intermediate structures. Full mechanisms for the OH-initiated photooxidation of toluene, *m*-xylene, *p*-xylene, 1,2,4-trimethylbenzene and *m*-ethyltoluene are developed. The lowest energy intermediates have been determined and predicted products from these structures are compared to available experimental product data. These studies serve to refine proposed mechanisms currently available for toluene, *m*-xylene and *p*-xylene, while providing new information on the 1,2,4 trimethylbenzene and *m*-ethyltoluene reaction pathways.

2.1 Introduction

Aromatic compounds are of great interest in atmospheric chemistry because of their abundance in motor vehicle emissions and because of their reactivity with respect to ozone and organic aerosol formation. Understanding the atmospheric oxidation mechanisms of aromatics has long been cited as the most critical need in further development of reaction mechanisms for the urban and regional atmosphere.[1] The major atmospheric sink for aromatics is reaction with the hydroxyl radical. Whereas rate constants for the OH reaction with aromatics have been well characterized,[2] mechanisms of aromatic oxidation following the initial OH attack have been highly uncertain. In experimental photooxidation studies of toluene, *m*-xylene, and *p*-xylene, summaries of which are available in the excellent review by Atkinson[2] and subsequent studies by Atkinson and associates,[3, 4] typically less than 50% of the reacted carbon has been identified as products. A difficulty in accounting for the remaining fraction of reacted carbon lies in the fact that the intermediates involved in aromatic-OH oxidation have not been unambiguously identified. Consequently, theoretical studies can be useful in evaluating the possible mechanisms of oxidation. We present theoretical calculations on possible structural intermediates formed in the OH-initiated reactions of toluene, *m*-xylene, *p*-xylene, 1,2,4-trimethylbenzene, and *m*-ethyltoluene. The aromatics chosen correspond to ones that our group has studied in the laboratory. From these energy determinations, the most likely intermediate species have been identified, and overall mechanisms for the photooxidation of these aromatics are proposed.

The aromatic-OH reaction proceeds by both abstraction and addition pathways (see Atkinson,[2] Atkinson and Aschmann,[3] and references therein). The addition pathway, occurring roughly 90% of the time, is the more relevant route. Products identified in the OH addition reactions of toluene, *m*-xylene, and *p*-xylene in previous laboratory studies appear in Tables 2.1–2.3. The yields presented in the tables are defined as the ratio of the molar concentration of the product to that of reacted aromatic. As noted above, generally less than 50% of the carbon in these systems

Table 2.1: Toluene photooxidation products: molar yields.

compound	yield	ref
glyoxal	0.105 ± 0.019	[6]
	0.058	[7]
	0.150 ± 0.040	[8]
	0.08	[9]
methyl glyoxal	0.146 ± 0.006	[6]
	0.077	[7]
	0.140 ± 0.04	[8]
	0.075	[9]
methylbutenedial	0.058	[7]
hydroxymethylbutenedial	0.034	[7]
oxoheptadienal	0.027	[7]
methylhydroperoxide	0.018	[7]
formaldehyde	0.01	[7]
hexadienyl	0.01	[7]
hydroxyoxoheptadienal	0.01	[7]
maleic anhydride	0.040 ± 0.004	[8]
<i>o</i> -cresol	0.204 ± 0.027	[10]
<i>m</i> - and <i>p</i> -cresol	0.048 ± 0.009	[10]
<i>m</i> -nitrotoluene	$(0.0135 \pm 0.0029) + (1.90 \pm 0.25) \times 10^{-16}[\text{NO}_2]$	[10]
<i>o</i> -nitrotoluene	0.07[<i>m</i> -nitrotoluene]	[10]
<i>p</i> -nitrotoluene	0.35[<i>m</i> -nitrotoluene]	[10]

has been accounted for experimentally. In the current study, we compare available experimental product data for the toluene, *p*-xylene, and *m*-xylene systems to our proposed mechanisms to evaluate the extent of agreement between the theoretical mechanisms and observed product data. The theory is then used to predict additional products that might be found in these three systems. Since only two studies on products resulting from 1,2,4-trimethylbenzene photooxidation are available,[5, 6] neither considering the full mechanism for photooxidation, and none for the reactions of *m*-ethyltoluene, we develop plausible atmospheric reaction mechanisms for both of these species based on theory alone.

Table 2.2: *M*-xylene photooxidation products: molar yields.

compound	yield	ref
glyoxal	0.13 ± 0.03	[8]
	0.086	[11]
	0.086 ± 0.011	[6]
methylglyoxal	0.42 ± 0.05	[8]
	0.375	[11]
	0.319 ± 0.009	[6]
formaldehyde	0.17 ± 0.02	[8]
	0.099	[12]
2,4-dimethylphenol	0.111	[12]
	0.0018	[12]
4-nitro- <i>m</i> -xylene	0.0032 +	[12]
	$1.6 \times 10^{-17}[\text{NO}_2]$	

2.2 Calculation Method

The theoretical approach of this study employs semi-empirical and density functional computational techniques to determine the most energetically favored intermediates in the reaction mechanisms, taking into account transition state complexes. These methods are used to determine the lowest energy structures in the most computationally efficient manner, balancing the desire for reasonable computational times with the highest level of theory. Semi-empirical optimizations require less computational time, and, given that all of the structures studied are similar (aromatic structures with C, N, O, and H atoms), semi-empirical optimizations are adequate for screening and optimizing the structures. The higher level density functional calculations provide accurate energy determination rivaling that of an MP2 *ab initio* calculation, while being more computationally efficient.[13]

To examine the accuracy of semi-empirical optimizations followed by density functional calculations, calibration studies were conducted on a variety of compounds,

Table 2.3: *P*-xylene photooxidation products: molar yields.

compound	yield	ref
glyoxal	0.24 ± 0.02	[8]
	0.225 ± 0.039	[6]
methylglyoxal	0.12 ± 0.02	[8]
	0.105 ± 0.034	[6]
3-hexene-2,5-dione	detected	[8]
formaldehyde	0.17 ± 0.02	[8]
2,5-dimethylphenol	0.188	[12]
2-nitro- <i>p</i> -xylene	$0.0120 + 2.8 \times 10^{-17}[\text{NO}_2]$	[12]

including methylhydroxycyclohexadienyl (MHCHD) radicals resulting from toluene photooxidation, alkyl radicals, alkoxy radicals and nitroalkenes, using different geometry optimization and single point energy calculation schemes. In the first study, high- and low-level computational techniques were applied to MHCHD radicals. Since experimental data for the energies of these radicals are not available, comparisons of theoretical and experimental results are not possible. Assuming that the most rigorous computational method most accurately reflects the true energy of the species, these calculations can be used to find a balance between the highest level of theory necessary and the required computational time. A second study compared the results of the technique chosen for the current study to experimental values to establish its accuracy.

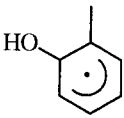

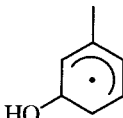
For the first study, techniques used for geometry optimization include: density functional theory (DFT)[14] using the hybrid density functional, Becke3LYP, of Becke[15, 16] and Lee et al.[17, 18] and a 6-31G(*d,p*) basis set; restricted open-shell Hartree Fock (ROHF) optimization using a 6-31G(*d,p*) basis set; a semi-empirical unrestricted Hartree-Fock PM3 (UHF/PM3) optimization;[19] and a molecular mechanics optimization using the MM+ functional form.[20] Of the semi-empirical techniques, the PM3 parameterization was used.[19] PM3 belongs to a class of calculations

using the Modified Neglect of Diatomic Overlap (MNDO) method, and is most often cited as producing the best optimizations for hydrocarbon systems and complexes containing nitrogen and oxygen.[21] In addition to providing reliable geometry, PM3 has also been shown to provide accurate vibrational frequencies that can be compared directly to experiment without *post hoc* correction.[22] These vibrational frequencies allow for the calculation of zero-point energies. The MM+ functional form of the potential was used in the molecular mechanics optimizations since it is most appropriate for small organic molecules.[20]

The DFT and ROHF optimizations were performed on HP 9000/735 workstations using Gaussian 92[17] and PSGVB, version 2.13,[23] respectively, while the UHF/PM3 and molecular mechanics optimizations were performed on a personal computer using Hyperchem, release 4.0.[24] Single point calculations were performed following the geometry optimizations utilizing either the ROHF method or density functional theory[14] using the Becke3LYP hybrid density functional. Both calculations used a 6-31G(*d,p*) basis set and were performed on HP 9000/735 workstations using Gaussian 92. The results for the MHCHD radicals are given in Table 2.4, with relative energy defined as the difference in energy between any given structural isomer and the lowest energy structural isomer. Table 2.4 indicates that the MM+ optimization, followed by the DFT calculation, does not reproduce the results of the high-level DFT optimization followed by the DFT calculation. The UHF/PM3 geometry optimization method, however, gives relative energies that are quite close to the DFT values. Of the techniques studied, a semiempirical UHF/PM3 geometry optimization followed by a single point calculation using the Becke3LYP density functional and a 6-31G(*d,p*) basis set exhibits the best combination of computational efficiency and accuracy. This method was therefore chosen for all of the calculations that are presented in this study.

A second set of calculations were performed to calibrate the chosen computational scheme. Geometry optimizations using the UHF/PM3 method followed by a single point calculation using the Becke3LYP density functional and a 6-31G(*d,p*) basis set were performed on radicals and stable species for which experimental energy data

Table 2.4: Relative energies (in kcal/mol) for isomers of the methylhydroxycyclohexadienyl radical using various computational methods.^a

geometry opt/single-point calculation methods			
Becke3LYP / Becke3LYP	0 ^b	1.1	1.8
ROHF / Becke3LYP	0 ^c	0.9	1.7
ROHF / ROHF	0 ^d	0.8	0.7
UHF-PM3 / Becke3LYP	0 ^e	1.2	1.6
MM+ / Becke3LYP	0.1	0 ^f	0.4

^aThe 6-31G(*d,p*) basis set was used for all *ab initio* calculations.


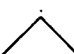
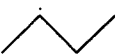




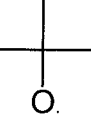
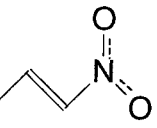
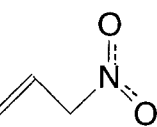
Footnotes *b-f* are absolute energies. ^b -347.3406 au. ^c -347.3364 au.

^d -345.1331 au. ^e -347.3374 au. ^f -347.3318 au.

exist. The relative energies of isomers of the structures were compared and tabulated in Table 2.5. For the compounds in this table, the PM3/Becke3LYP technique reproduces the relative energies between structural isomers to within 1.6 kcal/mol. As a test of the ability of the chosen method to predict heats of reaction, ΔH_{rxn} values derived from literature data[25] and PM3/DFT calculations for the toluene + OH reaction resulting in the formation of cresol isomers are compared. These data appear in Table 2.6, and indicate an agreement between experiment and theory to within 2 kcal/mol.

The computational studies described above were designed to provide some insight into the accuracy that can be expected with chosen method. It is often quite difficult to quantify the accuracy of a computational method without putting numerous conditions on the cases that can be studied. However, for the determination of relative stabilities of nearly identical structural isomers, systematic biases which are inherent in any computational scheme will often cancel. In light of this, the accuracy reported above of ± 2 kcal/mol seems to be a reasonable criterion for the ordering of the stabil-

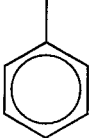
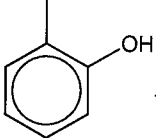
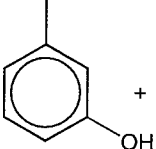
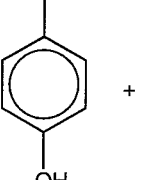
Table 2.5: Comparison of relative energies of different structural isomers based on experimental data and theoretical calculations.

structure	relative energy, experiment ^a (kcal/mol)	relative energy, calculated ^b (kcal/mol)
	3.8	4.3
	0	0
	4.9	3.3
	0	0
	6.6	6.1
	0	0
	2.6	3.3
	0	0
	5	5.1
	0	0

^a Experimental data from NIST Standard Reference Database.[25]

^b Relative energies determined using UHF/PM3 geometry optimization followed by Becke3LYP single-point energy calculation.

Table 2.6: A comparison of experimentally and theoretically derived ΔH_{rxn} values for the toluene + OH reaction.

reactants	products	ΔH_{rxn} , theoretical (kcal/mol)	ΔH_{rxn} , experimental (kcal/mol)
 + OH	 + H	+1.38	+0.8 ± 0.4
	 + H	+1.25	-0.8 ± 0.7
	 + H	+1.94	+0.9 ± 0.4

ity of the aromatic intermediates encountered in this study. The determination of the accuracy of heats of reaction, however, is a much more difficult problem to address, especially for reactions involving free radical species. In interpreting the results of reaction energy calculations for this study, we have been careful not to apply the same ± 2 kcal/mol criterion to the selection of preferred reaction pathways. In most cases, we will only make a statement as to a preferred pathway based on heats of reaction that are overwhelmingly large positive or negative values.

Because molecular mechanics provides a fast, first approximation to the optimized structure, this technique was used before employing the UHF/PM3 method in the present study of aromatic mechanisms. To examine whether the individual structures investigated were at global rather than local minima, several starting geometries of each structure were subjected to PM3 geometry optimization calculations. The heats of formation (obtained using PM3) of the different geometries were compared, and the lowest energy structure was chosen for subsequent single point density functional calculations. In cases where the semi-empirically derived heats of formation were similar,

several conformations were subjected to single point density functional calculations to locate the lowest energy conformation. All structures were characterized as being genuine minima (i.e., the frequency calculation revealing no imaginary components) at the PM3 level.

Transition state geometries were estimated with a constrained optimization procedure at the UHF/PM3 level using Gaussian 92. Conventional direct optimization schemes available through Gaussian 92 were attempted. However, because of the complexity of the structures studied, it was not possible to locate the structure with an initial geometry corresponding to a single negative eigenvalue of the second derivative matrix, a condition that is necessary before a conventional transition state optimization can proceed. The constrained optimization method relies on the assumption that the transition states are governed by the formation of a single bond in each step (for example, the C-O bond in the formation of the MHCHD radicals). Starting with the equilibrium geometry of the complex, the distance of the bond formed in the reaction step is adjusted by small increments (0.1 Å steps, in this case), and frozen while the geometry of the molecule is optimized. At the end of each optimization the PM3-derived energy of the structure is noted. This procedure is repeated until a point of maximum energy is obtained. The constrained optimization procedure at the UHF/PM3 level was used to obtain a first estimate of the transition state structure. Once this was found, DFT single point calculations were performed on this structure and small geometrical perturbations of the structure to ensure that the UHF/PM3 calculation was successful in locating a peak in the energy of the complex. Because of the large number of structures considered in this study, transition states were located for representative cases and subsequently applied to homologous transition state complexes. The procedure described above, while not intended to display the level of accuracy obtained by the more rigorous transition state algorithm, is intended only to provide an estimate for the barrier height. This estimate is presumed to be an upper limit due to the lack of an adequate means to account for electron correlation during the determination of the structure of the transition state.

2.3 Results of Calculations

A generalized summary of the steps considered in the OH-aromatic mechanism appears in Figure 2.1, and henceforth all references to reactions will relate to this figure. The mechanism shown in Figure 2.1 was subjected to two sets of calculations. The first set focused on those reactions that lead to the formation of a bicyclic, endoperoxy radical. In this study, the term “bicyclic radical” shall be used to describe this intermediate, which is shown as the product of Reaction 4. In this first set of calculations, all structural isomers of each intermediate were studied in order to determine the most stable form. Barrier heights were estimated and used with the calculations of the most stable intermediates to predict the compounds most likely to be formed. Knowledge of these intermediates will be used to predict final reaction photooxidation products for the five aromatics previously mentioned. The second set of calculations were applied to Reactions 3a-e, where reactions of the aromatic-OH adduct with NO_2 are considered. The goal of these calculations is to gain a more qualitative understanding of the most important pathways for these reactions. The results of these calculations are used to either confirm or contradict the plausibility of each proposed pathway.

2.3.1 Reactions which Lead to the Formation of the Bicyclic Radical

The first step in the study of the reaction pathways of the photooxidation of aromatics was the determination of the structure and energy of each of the species that participate in reactions with the aromatic intermediates. The results are shown in Table 2.7. So that we were consistent with our treatment of all reactants, geometries for the molecules shown in Table 2.7 were obtained using the same techniques, a PM3 optimization followed by Becke3LYP energy determination, that were later applied to each aromatic intermediate. For all energy data presented in this study the results of the Becke3LYP energy calculation were corrected to 298 K by using the normal mode vibrational frequencies and thermal corrections obtained at the PM3

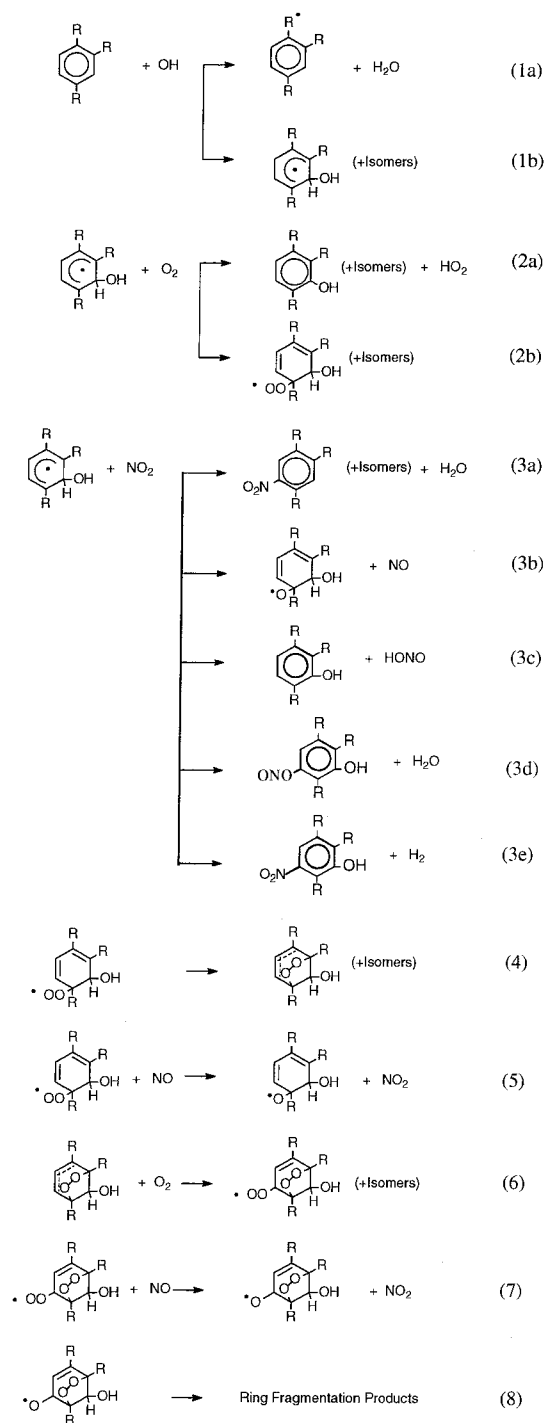


Figure 2.1: Possible reactions in a generalized mechanism of aromatic-OH photooxidation. R represents either an H atom or an alkyl group, depending on the aromatic considered.

Table 2.7: Calculated energies (in hartrees) of molecules involved in reactions with aromatics in this study.^a

molecule	$E_e^{0\ b}$	$E^{298\ c}$
OH	-75.7268	-75.7153
O ₂	-150.3165	-150.3093
H ₂ O	-76.4190	-76.3943
HONO	-205.6981	-205.6736
NO ₂	-205.0700	-205.0573
NO	-129.8879	-129.8803

^a Structures optimized by using PM3 and energies determined by using Becke3LYP/6-31g**. ^b Electronic energy at 0 K. ^c Corrected energies at 298 K, which includes zero-point energies and thermal corrections determined by using PM3 normal mode vibrations.

level. The following sections will summarize the results of the first set of calculations that describe the formation of the bicyclic radical.

The Geometry of Reaction Intermediates

The formation of the bicyclic radical from the aromatic precursor is believed to occur through the formation of two reaction intermediates. The first task in this study was to determine the most stable geometry for each of these intermediates. Tables 2.8–2.10 show the structures for a representative selection of the most stable reaction intermediates for each of the five aromatics considered. As the next section will indicate, in most cases there was not a unique low-energy structural isomer for each intermediate. The uncertainty in our ability to predict the relative energy of these structural isomers, nominally ± 2 kcal/mol, will result in the prediction of a number of intermediates, and thus multiple reaction pathways, for each aromatic. Although all of these structures could not be presented in Tables 2.8–2.10, the most important geometrical features were preserved in all cases. Every effort was made to be consistent in the conformations of each structural isomer in order to obtain reliable relative

Table 2.8: PM3 Equilibrium structures for a representative selection of the most stable reaction products of aromatics with OH (Reaction 1b).^a

parameter	Structure 1				parameter	1,2,4-tmb
	toluene	<i>m</i> -xylene	<i>p</i> -xylene	<i>m</i> -ethyltoluene		
$r(C_1, C_2)$	1.505	1.507	1.505	1.507	$r(C_1, C_2)$	1.388
$r(C_2, O_1)$	1.414	1.416	1.415	1.416	$r(C_3, O_1)$	1.417
$r(C_2, C_3)$	1.498	1.507	1.497	1.507	$r(C_2, C_3)$	1.507
$r(C_3, C_4)$	1.370	1.379	1.377	1.379	$r(C_3, C_4)$	1.506
$r(C_4, C_5)$	1.411	1.407	1.416	1.408	$r(C_4, C_5)$	1.378
$r(C_5, C_6)$	1.406	1.407	1.405	1.407	$r(C_5, C_6)$	1.406
$r(C_6, C_1)$	1.381	1.379	1.381	1.379	$r(C_6, C_1)$	1.413
$r(C_1, C_7)$	1.479	1.479	1.478	1.479	$r(C_1, C_7)$	1.486
$r(C_3, C_8)$		1.479		1.490	$r(C_2, C_8)$	1.480
$r(C_4, C_9)$			1.486		$r(C_4, C_9)$	1.479
$\angle(C_1, C_2, C_3, O_1)$	128	127	127	128	$\angle(C_2, C_3, C_4, O_1)$	127

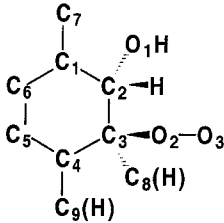
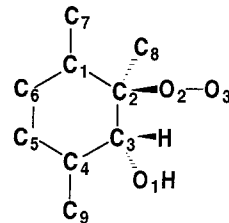
^a All bond distances are in angstroms and angles are in degrees.

energies.

The Energy of Reaction Intermediates

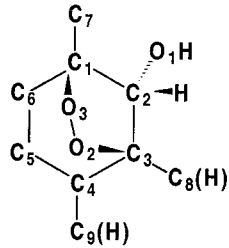
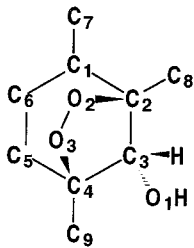
Once the structure of each intermediate was determined, the electronic energy (at 0 K) and the total energy corrected for zero point vibrations and thermal energies were calculated. The results of these calculations are summarized in Tables 2.11 and 2.12. In Table 2.11, the structures and energies are displayed for the most stable intermediates whose relative energies were determined to be within uncertainty. In Table 2.12, the intermediates that result from the reactions of the peroxy radical with NO and the bicyclic radical with O₂ are presented for some representative cases. A

Table 2.9: PM3 equilibrium structures for a representative selection of the most stable reaction products of aromatic-OH adducts with O₂ (Reaction 2b).^a

						
parameter	toluene	<i>m</i> -xylene	<i>p</i> -xylene	<i>m</i> -ethyltoluene	parameter	1,2,4-tmb
r(C ₁ ,C ₂)	1.510	1.514	1.510	1.513	r(C ₁ ,C ₂)	1.512
r(C ₂ ,O ₁)	1.411	1.409	1.410	1.420	r(C ₃ ,O ₁)	1.409
r(C ₂ ,C ₃)	1.555	1.563	1.556	1.562	r(C ₂ ,C ₃)	1.566
r(C ₃ ,O ₂)	1.478	1.494	1.478	1.496	r(C ₂ ,O ₂)	1.497
r(O ₂ ,O ₃)	1.253	1.253	1.255	1.252	r(O ₂ ,O ₃)	1.252
r(C ₃ ,C ₄)	1.494	1.504	1.501	1.503	r(C ₃ ,C ₄)	1.512
r(C ₄ ,C ₅)	1.345	1.343	1.356	1.345	r(C ₄ ,C ₅)	1.354
r(C ₅ ,C ₆)	1.443	1.448	1.440	1.445	r(C ₅ ,C ₆)	1.440
r(C ₆ ,C ₁)	1.351	1.349	1.354	1.350	r(C ₆ ,C ₁)	1.358
r(C ₁ ,C ₇)	1.482	1.481	1.481	1.482	r(C ₁ ,C ₇)	1.483
r(C ₃ ,C ₈)		1.525		1.543	r(C ₂ ,C ₈)	1.526
r(C ₄ ,C ₉)			1.482		r(C ₄ ,C ₉)	1.480
∠(C ₃ ,O ₂ ,O ₃)	114	116	114	117	∠(C ₂ ,O ₂ ,O ₃)	116
∠(C ₁ ,C ₂ ,C ₃ ,O ₁)	125	124	125	121	∠(C ₂ ,C ₃ ,C ₄ ,O ₁)	125
∠(C ₂ ,C ₃ ,C ₄ ,O ₂)	118	117	117	122	∠(C ₁ ,C ₂ ,C ₃ ,O ₂)	118

^a All bond distances are in angstroms and angles are in degrees.

Table 2.10: PM3 equilibrium structures for a representative selection of the most stable reaction products in the formation of bicyclic endoperoxy radicals from peroxy radical intermediates (Reaction 4).^a

						
parameter	toluene	<i>m</i> -xylene	<i>p</i> -xylene	<i>m</i> -ethyltoluene	parameter	1,2,4-tmb
r(C ₁ ,C ₂)	1.577	1.572	1.577	1.570	r(C ₁ ,C ₂)	1.518
r(C ₂ ,O ₁)	1.388	1.389	1.388	1.389	r(C ₃ ,O ₁)	1.389
r(C ₂ ,C ₃)	1.565	1.572	1.565	1.572	r(C ₂ ,C ₃)	1.574
r(C ₃ ,O ₂)	1.403	1.424	1.402	1.423	r(C ₂ ,O ₂)	1.424
r(O ₂ ,O ₃)	1.595	1.580	1.595	1.580	r(O ₂ ,O ₃)	1.580
r(C ₁ ,O ₃)	1.422	1.424	1.422	1.423	r(C ₄ ,O ₃)	1.423
r(C ₃ ,C ₄)	1.505	1.510	1.511	1.511	r(C ₃ ,C ₄)	1.570
r(C ₄ ,C ₅)	1.393	1.393	1.402	1.393	r(C ₄ ,C ₅)	1.509
r(C ₅ ,C ₆)	1.393	1.393	1.389	1.393	r(C ₅ ,C ₆)	1.387
r(C ₆ ,C ₁)	1.511	1.510	1.510	1.511	r(C ₆ ,C ₁)	1.404
r(C ₁ ,C ₇)	1.519	1.519	1.519	1.519	r(C ₁ ,C ₇)	1.473
r(C ₃ ,C ₈)		1.519		1.532	r(C ₂ ,C ₈)	1.521
r(C ₄ ,C ₉)			1.471		r(C ₄ ,C ₉)	1.520
∠(C ₁ ,C ₂ ,C ₃ ,O ₁)	125	125	114	114	∠(C ₂ ,C ₃ ,C ₄ ,O ₁)	114
∠(C ₂ ,C ₃ ,C ₄ ,O ₂)	114	112	114	112	∠(C ₁ ,C ₂ ,C ₃ ,O ₂)	115
∠(C ₆ ,C ₁ ,C ₂ ,O ₃)	116	115	115	116	∠(C ₃ ,C ₄ ,C ₅ ,O ₃)	112

^a All bond distances are in angstroms and angles are in degrees.

complete set of tabulated energy data for all reaction intermediates is available from the authors upon request.

A review of the results of the energy calculations can point out many important trends in the stability of the structural isomers. Looking first at the initial hydroxyl radical attack, it is generally observed that addition to all sites *ortho* to substituted alkyl groups are preferred. Each of the aromatic-OH adducts had two or more important low-energy conformations with the exception of *p*-xylene, for which only one structural isomer of the aromatic-OH adduct exists. For toluene, OH additions to the *meta* and *para* positions yield structures that are only 1.6 and 1.2 kcal/mol, respectively, higher in energy than addition to the *ortho* site. All three structures should thus be considered in the reaction mechanism. The lowest energy aromatic-OH structure for *m*-xylene also corresponds to addition to position 2, whereas addition to positions 4 (or 6, due to symmetry) and 5 are higher in energy by 0.9 and 3.5 kcal/mol, respectively. Thus two important aromatic-OH adducts can be considered in the case of *m*-xylene, both of which form by addition to a position that is *ortho* to one of the substituted methyl groups. The lowest energy aromatic-OH adducts for 1,2,4-trimethylbenzene correspond to OH additions to positions 3 and 5. The energies of these adducts are identical. Addition to position 6 is 2.1 kcal/mol higher in energy, and shall also be included in reaction mechanism considerations. Closely following the trends observed with *m*-xylene, the most stable aromatic-OH adduct for *m*-ethyltoluene corresponds to addition to position 2, with addition to sites 4 and 6 yielding structures that are 0.7 and 0.6 kcal/mol, respectively. Addition to position 5 is higher in energy by 3.0 kcal/mol.

Under atmospheric conditions, molecular oxygen is expected to rapidly add to the aromatic-OH adduct, forming a peroxy radical (Reaction 2b) with three structural isomers.[26] Calculations performed on the equilibrium geometries for each structural isomer reveal that at least two of the structural isomers are very similar in energy. Although Table 2.11 lists a single structural isomer for each peroxy intermediate, the addition sites of the other important isomers are indicated in parentheses where appropriate, and can be expected to have energies within 2 kcal/mol of the value

Table 2.11: Calculated energies (in hartrees) of the most stable reaction intermediates for the reaction pathways leading to the formation of the bicyclic endoperoxy radicals.

aromatic		OH addition (Reaction 1b)			O ₂ addition (Reaction 2b)			O ₂ bridge formation (Reaction 4)			
molecule	E_e^0	E^{298}	site	E_e^0	E^{298}	site ^a	E_e^0	E^{298}	sites	E_e^0	E^{298}
toluene	-271.5774	-271.4454	3	-347.3348	-347.1876	2 (4,6)	-497.6616	-497.5035	2,4	-497.6750	-497.5168
			4	-347.3355	-347.1883	3 (1)	-497.6606	-497.5025	3,5	-497.6721	-497.5139
			2	-347.3374	-347.1902	3 (1,5)	-497.6621	-497.5040	3,1	-497.6751	-497.5169
<i>m</i> -xylene	-310.8971	-310.7363	4	-386.6589	-386.4826	5 (3,1)	-536.9828	-536.7963	5,3	-536.9962	-536.8086
			2	-386.6603	-386.4840	3	-536.9851	-536.7986	3,1	-537.0008	-536.8132
<i>p</i> -xylene	-310.8969	-310.7359	2	-386.6253	-386.4492	3 (1,5)	-536.9848	-536.7968	3,1	-536.9988	-536.8108
1,2,4-tmb	-350.2154	-350.0250	6	-425.9739	-425.7671	1	-576.3036	-576.0861	1,5	-576.3194	-576.1019
			3	-425.9773	-425.7705	2	-576.3049	-576.0874	2,4	-576.3210	-576.1035
			5	-425.9774	-425.7706	4 (2)	-576.3031	-576.0856	4,6	-576.3177	-576.1002
<i>m</i> -ethyltoluene	-350.2116	-350.0216	4	-425.9740	-425.7675	5 (3,1)	-576.2976	-576.0801	5,3	-576.3077	-576.0902
			6	-425.9742	-425.7677	5 (1,3)	-576.2996	-576.0821	5,1	-576.3114	-576.0939
			2	-425.9751	-425.7686	3 (1,5)	-576.2967	-576.0792	3,1	-576.3121	-576.0946

^a Addition sites in parentheses indicate comparable low-energy structures.

Table 2.12: Calculated energies (in hartrees) for the products of the reaction of NO with a representative selection of the most stable peroxy intermediates and for the products of the reaction of O₂ with a representative selection of the most stable bicyclic intermediates.

molecule	OH site	O site	E_c^0	E^{298}	OH site	O ₂ bridge sites	O ₂ addition site	E_c^0	E^{298}
toluene	2	3	-422.4566	-422.3062	2	3,1	4	-648.0151	-647.8483
<i>m</i> -xylene	2	3	-461.8238	-461.6413	2	3,1	4	-687.3402	-687.1399
<i>p</i> -xylene	2	3	-461.7941	-461.6131	2	3,1	6	-687.3344	-687.1354
1,2,4-trimethylbenzene	5	4	-501.1425	-500.9301	5	4,6	3	-726.6533	-726.4208
<i>m</i> -ethyltoluene	6	5	-501.1191	-500.9067	6	5,1	2	-726.6518	-726.4236

listed in the table. These results imply that many isomers of the peroxy radical need to be considered in the reaction with NO (Reaction 5) as well as the rearrangement step that leads to the bicyclic radical.

The formation of the bicyclic radical from a peroxy radical is postulated to occur in order to rationalize the observed formation of α -dicarbonyls from aromatic photooxidation reactions.[27] Calculations were performed on all possible bicyclic radicals, with the exception of those radicals containing a four-membered carbon-oxygen ring for which ring strain energies were assumed to be much higher than the corresponding five- and six-membered rings. In all cases, the allylically stabilized bicyclic radical with a five-membered ring was found to be the most stable structure. In fact, the other non-allylically stabilized bicyclic radicals were at least 20 kcal/mol higher in energy, making their formation from the peroxy radicals about 10 kcal/mol endothermic. For otherwise identical bicyclic structures, the intermediates with five-membered carbon-oxygen ring were observed to be more stable than those with six-membered rings, suggesting that ring strain for the five-membered rings may be smaller. Reactions 5 and 6 were considered in order to identify final products from the photooxidation of aromatics, as well as to indicate important reactions which should be considered in an overall mechanism. The continuation of the reactions which led to the formation of the bicyclic radical involve the addition of molecular oxygen, Reaction 6. For each allylically-stabilized bicyclic radical, there are two possible addition sites for O₂. Calculations performed on these two possible conformations of the bicyclic peroxy radical indicate that both structures have relative energies within 2 kcal/mol, consistent with the results of the calculations on the peroxy radicals formed by Reaction 2b. The results of the energy calculations are shown in Table 2.12, where the energies for a representative selection of the most stable bicyclic peroxy radicals are displayed. The results of energy calculations for formation of the alkoxy radical by the reaction of the peroxy radical with NO, Reaction 5, was treated in a similar manner due to the abundance of low-energy structural isomers of the peroxy radical. The results of these calculations will be used to estimate a heat of reaction in order to determine the relative importance of this reaction compared to the formation of the bicyclic radical.

Transition State Analysis

An estimate was made of the transition state structure and associated barrier height for each step in the reaction pathway, based on the constrained optimization method introduced in Section 2.2. The emphasis in these procedures was to develop a means for estimating the reaction barrier heights that is based on the local structure or substituents near the site of the reaction, so that the results of calculations on one system can be employed for the description of another homologous system. As discussed in Section 2.2, the results of these analyses should be considered an approximation to the actual first-order saddle point, and the barrier heights obtained are most likely an upper limit to the actual values. The characterization of the reaction barriers for OH addition to the aromatic (Reaction 1b), O₂ addition to the aromatic-OH adduct (Reaction 2b), the formation of the bicyclic radical (Reaction 4) and reaction of the bicyclic radical with O₂ to form the bicyclic peroxy radical (Reaction 6) were studied. An investigation of the OH addition to aromatic ring found no discernible barrier for all additions to a secondary carbon in the aromatic ring. Addition to a tertiary carbon, such as that in position 1 for toluene, results in a barrier of 15 kcal/mol above the sum of the aromatic and OH energies, presumably due to steric hindrance caused by the substituted alkyl group. On this basis, we have excluded the consideration of the addition of OH to a tertiary carbon.

The barrier heights associated with the addition of molecular oxygen to the aromatic-OH adduct are summarized in Table 2.13. In this table, the results of constrained optimization calculations for a variety of structures are presented in terms of the nature of the carbon at the addition site (tertiary or secondary) and the substituent groups at the two positions *ortho* to the addition site. The nature of the carbon atom at the addition site has been seen to affect the equilibrium C-O bond distance for the peroxy radical (see $r(\text{C}_3\text{-O}_2)$ in Table 2.9) and the substituent alkyl group at the addition site may also contribute to steric effects. The *ortho* substituents may also play an important role in the sterics of ring addition. The results of Table 2.13 indicate the lowest barriers, approximately 3 kcal/mol, for the addition of O₂

Table 2.13: Approximate transition state energies for the reactions of aromatic-OH adducts with O₂.

aromatic	addition site ^a	ortho groups ^b	$E_e^0(\text{TS})$ (au)	$E^{298}(\text{TS})$ (au)	$r(\text{C-O})^c$ (Å)	$E^{298}(\text{reactants})$ (au)	barrier height (kcal/mol)
<i>p</i> -xylene	C _s	Me,OH	-536.9635	-536.7780	1.90	-536.7904	7.8
	C _t	H,OH	-536.9673	-536.7818	1.85	-536.7904	5.4
	C _s	H,Me	-536.9669	-536.7814	1.85	-536.7904	5.6
toluene	C _s	H,OH	-497.6406	-497.4857	1.90	-497.4995	8.7
	C _t	H,OH	-497.6454	-497.4905	1.85	-497.4995	5.6
	C _s	H,H	-497.6491	-497.4942	1.80	-497.4995	3.3
<i>m</i> -xylene	C _t	H,OH	-536.9686	-536.7833	1.90	-536.8023	11.9
<i>m</i> -ethyltoluene	C _t (Et)	H,OH	-576.2861	-576.0711	1.80	-576.0779	4.3
	C _t	H,OH	-576.2803	-576.0631	1.85	-576.0779	9.3
	C _s	H,H	-576.2892	-576.0742	1.80	-576.0779	2.3

^a Represented in terms of the local structure of the aromatic-OH adduct at the addition site, where all tertiary carbons (C_t) are bound to methyl (Me) groups unless indicated. ^b In the two positions *ortho* to the addition site. ^c Transition state bond distance for C-O bond which is formed in the addition of O₂. Structures obtained using the constrained optimization procedure described in Section 2.2.

Table 2.14: Approximate transition states for the addition reactions of bicyclic endoperoxy radical with O₂.

aromatic	addition site ^a	ortho groups ^b	E _c ^o (TS) (au.)	E ²⁹⁸ (TS) (au.)	r(C-O) ^c (Å)	E ²⁹⁸ (reactants) (au.)	barrier height (kcal/mol)
toluene	C _s	Me, H	-647.9641	-647.7973	1.9	-647.8262	18.2
	C _s	CO, H	-647.9643	-647.7975	1.9	-647.8262	18.0
p-xylene	C _t	CO, H	-687.3104	-687.1114	1.9	-687.1201	5.5

^a Represented in terms of the local structure of the bicyclic endoperoxy radical at the addition site. ^b In the two positions ortho to the addition site. Me represents a methyl group bound to a tertiary carbon, whereas CO represents an attachment site for the O₂ bridge. ^c Transition state bond distance for C-O bond which is formed in the addition of O₂.

to a secondary carbon with no substituted groups in the *ortho* positions. Addition to a secondary carbon with adjacent OH or alkyl groups corresponds to barriers of 5-10 kcal/mol, as does addition to a tertiary carbon adjacent to the OH addition site. These barrier heights are consistent with the low rate constants that have been observed for Reaction 2b on the order of 10⁻¹⁶ cm³ molecule⁻¹ sec⁻¹. [26] The bond distance that is used for determining the transition state structure is also listed in the table, and varies from 1.8–1.9 Å.

In a similar analysis, the barrier heights are estimated for the addition of molecular oxygen to the bicyclic radical to form a bicyclic peroxy radical. These were the largest systems ever attempted in this analysis, and the relaxation of the molecular geometry around a constrained bond distance became increasingly difficult. The results are however shown in Table 2.14, and vary from 5.5 to 18 kcal/mol for *p*-xylene and toluene, respectively. This large range of barrier heights display the degree of uncertainty in particular analysis due to size of the system. Based on the calculated barriers for the formation of the peroxy radical, a barrier of 15–20 kcal/mol for the formation of the bicyclic peroxy radical would be expected due to the more constrained, inflexible nature of the bicyclic radical.

The barriers involved in the formation of the bicyclic radical were investigated next. The results are presented in Table 2.15. As in the case of peroxy formation, the

data are presented in terms of the general characteristics of the aromatic intermediate at the site of the reaction. In the table, the original addition site of molecular oxygen to form the peroxy radical is termed the "Peroxy Site," and is characterized by the carbon type, tertiary or secondary. The "Endoperoxy Attachment Site" is the carbon atom that participates in the formation of the new bond. The results show the largest barrier associated with the secondary carbon at the peroxy site, with a value of 17 kcal/mol. The smallest barriers are associated with the participation of tertiary carbons in the carbon-oxygen ring, with values of around 10 kcal/mol.

2.3.2 Reactions of Aromatic-OH Adduct with NO₂

It has been suggested that aromatic-OH adducts react with NO₂ to yield nitroaromatics according to Reaction 3a of the generalized mechanism.[27] To explain the observed variation of aromatic photooxidation product yields with varying NO₂ concentration, alternative paths for aromatic-OH adduct reaction with NO₂ that result in the formation of oxy type radicals (Reaction 3e),[3] or the formation of a phenolic type compound and HONO (Reaction 3d) have been proposed.[3] Two additional pathways can be suggested for Reaction 3: Pathway 3c forming the hydroxy aromatic nitrite, and 3b forming the hydroxy nitroaromatic (nitrophenol, nitro-dimethylphenol, etc.).

As mentioned previously, the goal of this second set of calculations is to gain a more qualitative understanding of the most important reaction pathways of aromatic-OH intermediates with NO₂. Unlike the first set, only the reactions of the toluene-OH adduct with NO₂ were studied. In addition, only a single structural isomer of each intermediate was considered. For this study, we have adopted the conventional view that NO₂ will add to an alkyl-substituted hydroxycyclohexadienyl radical in a position *ortho* to the hydroxyl substituent.[27] For all reactions that occurred in a single step, barrier heights were determined using the constrained optimization methods described previously. For other reaction steps, and in particular those in Reactions 3a, b, and c which involve a rearrangement and subsequent loss of water or molecular hydrogen,

Table 2.15: Approximate transition states for the formation of the bicyclic endoperoxy radical.

aromatic	peroxy site ^a	endoperoxy attachment site ^b	$E_e^0(\text{TS})$ (au)	$E^{298}(\text{TS})$ (au)	$r(\text{C-O})^c$ (au)	$E^{298}(\text{peroxy})$ (au)	barrier height (kcal/mol)
<i>m</i> -xylene	C _t	C _t	-536.9672	-536.7800	2.20	-536.7986	11.7
toluene	C _s	C _t	-497.6318	-497.4764	2.10	-497.5040	17.3
	C _t	C _s	-497.6396	-497.4842	2.05	-497.5040	12.4
<i>p</i> -xylene	C _t	C _s	-536.9625	-536.7775	2.05	-536.7968	12.1

^a Represented in terms of the type of carbon that is bound to an oxygen at the original site of O₂ addition for the peroxy radical, and ^b at the bond which is created when the O₂ bridge is formed. ^c Transition state bond distance for bond which is created when O₂ bridge is formed.

a transition state analysis was not attempted. Although only a partial picture of the total reaction can be provided in the absence transition state information for these rearrangement steps, valuable information on the stability of intermediates as well as heats of reaction for each proposed pathway will be presented.

The most important intermediates involved in these reactions are the complexes formed when NO_2 adds to the ring to form either a C-N bond or a C-O bond. The results of the PM3 geometry optimizations for these intermediates are shown in Table 2.16. Also indicated in the table is some important geometry information used to estimate the barrier heights for these reaction steps. Energies for all reactants and products were calculated using the Becke3LYP hybrid density functional with a 6-31G(*d,p*) basis set, and were corrected to 298 K using PM3-derived frequencies. All reaction steps were assumed to follow the singlet spin state potential energy surface. The calculated energies are presented in Table 2.17.

The barriers predicted for the formation of the first intermediates for reactions 3a and 3c are 5 and 1 kcal/mol, respectively. Heats of reaction for the formation of these intermediates are -26.3 and -24.5 kcal/mol, respectively. Based on these results, both intermediates are predicted to be formed during the photooxidation reactions of toluene. The heat of reaction for 3e was calculated to be +38.3 kcal/mol, and thus the formation of an alkoxy radical from reaction with NO_2 can be excluded from consideration. The single step H-abstraction process by NO_2 to form HONO and an alkyl substituted phenol, Reaction 3d, was found to have a barrier of 2 kcal/mol and a heat of reaction of -52.8 kcal/mol. Thus this step can be considered a likely source for these phenolic compounds.

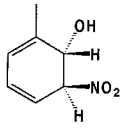
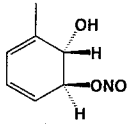
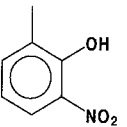
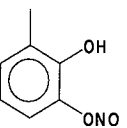
Reaction heats for the total processes of 3a, b, and c, whereby reaction of NO_2 with the aromatic-OH adduct leads to the formation of nitroaromatics, hydroxy nitroaromatics, and hydroxy aromatic nitrites, were calculated to be -51.7, -24.5, and -26.3, respectively. Formation of the stable aromatics seems likely, but the rearrangement steps involved may tend to favor certain structural isomers over others. More work needs to be done in this area to fully characterize these important reactions.

Table 2.16: PM3 geometries for equilibrium and approximate transition state structures for reactions of aromatic-OH adducts with NO_2 .

parameter	opt value ^b	TS value ^c	parameter	opt value	TS value	parameter	TS value
$r(\text{C}_1, \text{C}_2)$	1.512		$r(\text{C}_1, \text{C}_2)$	1.509		$r(\text{C}_2, \text{H}_2)$	1.0
$r(\text{C}_2, \text{O}_1)$	1.408		$r(\text{C}_2, \text{O}_1)$	1.407		$r(\text{H}_2, \text{O}_2)$	1.7
$r(\text{C}_2, \text{C}_3)$	1.560		$r(\text{C}_2, \text{C}_3)$	1.556		$\angle(\text{C}_1, \text{C}_2, \text{C}_3, \text{H}_2)$	37
$r(\text{C}_3, \text{O}_2)$	1.436	2.2	$r(\text{C}_3, \text{N})$	1.549	2.6	$\angle(\text{H}_2, \text{O}_2, \text{N})$	104
$r(\text{C}_3, \text{C}_4)$	1.500		$r(\text{C}_3, \text{C}_4)$	1.492			
$r(\text{O}_2, \text{N})$	1.411		$r(\text{N}, \text{O}_2)$	1.211			
$r(\text{N}, \text{O}_3)$	1.164		$r(\text{N}, \text{O}_3)$	1.213			
$\angle(\text{C}_3, \text{O}_2, \text{N})$	113		$\angle(\text{C}_3, \text{N}, \text{O}_2)$	120			
$\angle(\text{O}_2, \text{N}, \text{O}_3)$	108		$\angle(\text{O}_2, \text{N}, \text{O}_3)$	123			
$\angle(\text{C}_1, \text{C}_2, \text{C}_3, \text{O}_1)$	127		$\angle(\text{C}_1, \text{C}_2, \text{C}_3, \text{O}_1)$	127			
$\angle(\text{C}_2, \text{C}_3, \text{C}_4, \text{O}_2)$	119	100	$\angle(\text{C}_2, \text{C}_3, \text{C}_4, \text{N})$	124	101		

^a All bond distances in angstroms, all angles in degrees. ^b Equilibrium structure. ^c Approximate transition state structure.

Table 2.17: Calculated energies (in hartrees) of the products formed by the reactions of NO₂ with the toluene-OH adduct.

molecule	E_e^0	E^{298}
3-nitrotoluene	-476.0749	-475.9356
2-cresol	-346.7967	-346.6581
	-552.4537	-552.2865
	-552.4548	-552.2894
	-551.2802	-551.1439
	-551.2802	-551.1342

2.4 Summary and Analysis

A summary of the results of both the energy calculations and the transition state analyses is provided for the OH-initiated reactions that lead to the formation of the bicyclic radical in the form of the reaction coordinate diagrams shown in Figures 2.2–2.6. With the exception of *p*-xylene, each diagram displays several reaction pathways corresponding to a different aromatic-OH adduct formed in the first step of the reaction. At each stationary point the most stable intermediate is displayed for each pathway. In the case of the peroxy radical, where multiple low-energy structural isomers were predicted, only the conformation that leads to the formation of the bicyclic radical is shown.

A comparison of the available experimental product data to results predicted from Figures 2.2–2.6 can provide a valuable confirmation of the predictions of these calculations. Where there is no experimental data, the results of these calculations can be used to predict the products and intermediates that are most likely to be found. Based on the presence of three stable structural isomers of the toluene-OH adduct, one can predict via Reaction 2a the formation of *o*-, *m*-, and *p*-cresol, with the *o*-cresol dominating cresol formation. This is consistent with experimental evidence, shown in Table 2.1. Comparing the theoretical predictions for the presence of stable structural isomers of the *m*-xylene-OH adduct to experimentally determined products in Table 2.2, we note experimental evidence for 2,6- and 2,4-dimethylphenol (with the 2,6-dimethylphenol yield dominating), consistent with the OH addition to the 2 and 4 positions. There is no experimental evidence for 3,5-dimethylphenol, consistent with our finding that OH addition to the 5 position can be excluded. Because of the symmetry of *p*-xylene, only one structure of the *p*-xylene-OH adduct is predicted, consistent with experimental evidence of the formation of only 2,5-dimethylphenol (see Table 2.3). Given that there are no experimental data available on the ring-retaining products of 1,2,4-trimethylbenzene, the calculations can be used to predict the phenolic compounds formed. We predict the formation of 2,3,6-trimethylphenol, 2,4,5-trimethylphenol and 2,3,5-trimethylphenol from the O₂ reaction with the adducts

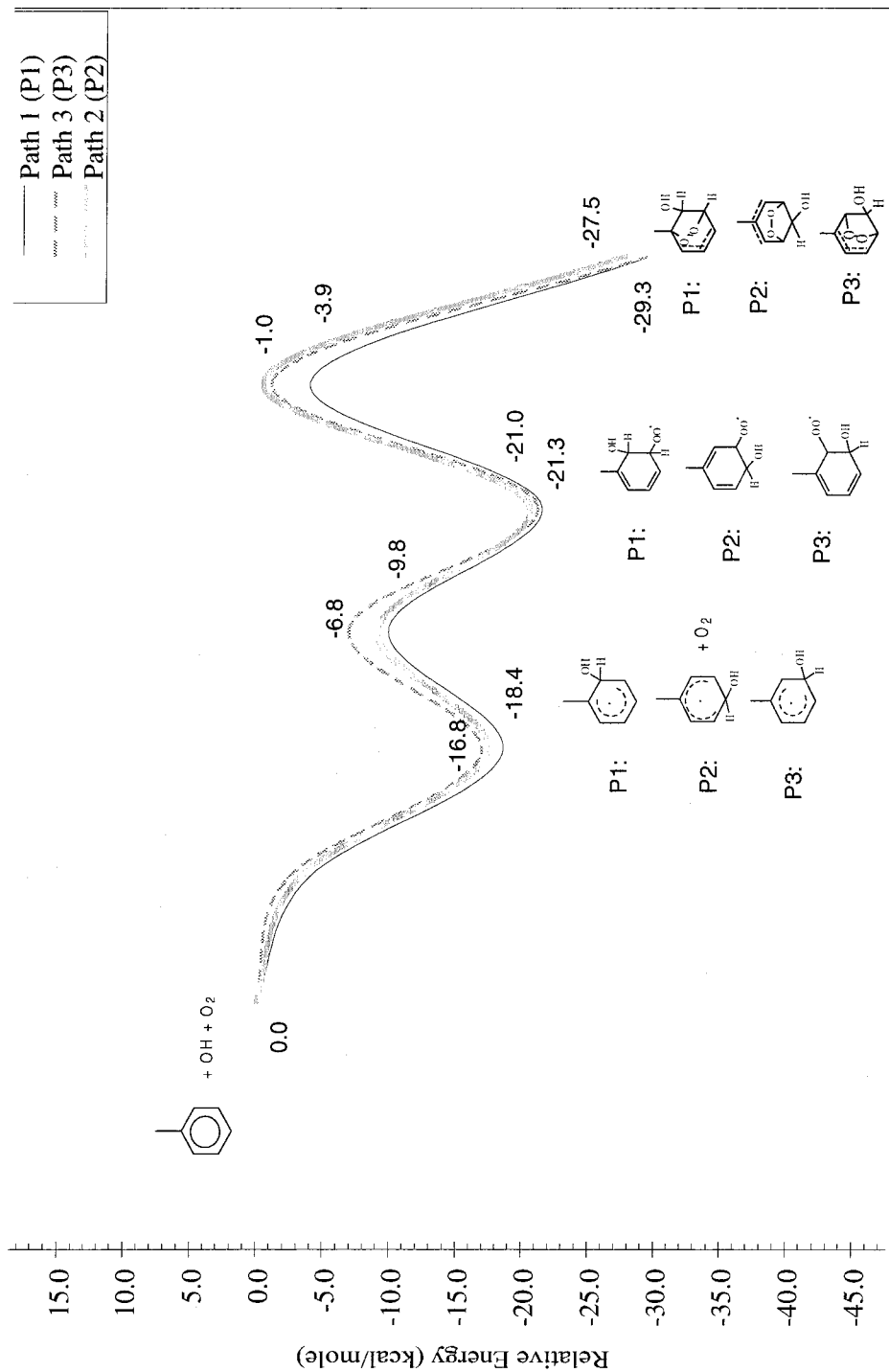


Figure 2.2: Reaction coordinate diagram for toluene. Indicated are the three favored pathways. Shown below the plots are the corresponding aromatic-OH adduct, peroxy radical, and bicyclic radical corresponding to the pathways. The structures are labeled P1, P2, and P3 corresponding to paths 1, 2, and 3, respectively.

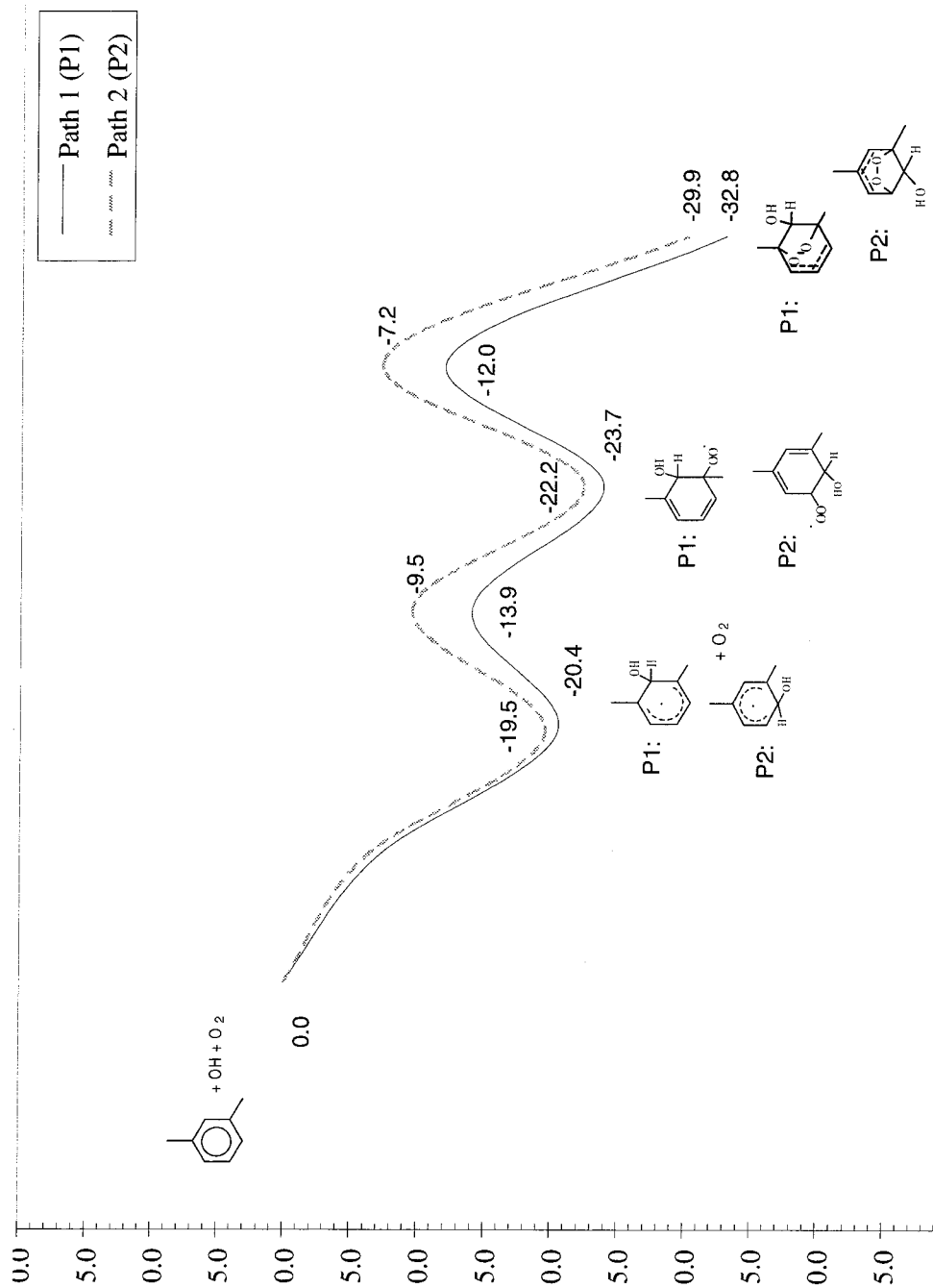


Figure 2.3: Reaction coordinate diagram for *m*-xylene. Indicated are the energies of the two favored pathways. Shown below the plots are the corresponding aromatic-OH adduct, peroxy radical, and bicyclic radical corresponding to the pathways. The structures are labeled P1 and P2 corresponding to paths 1 and 2, respectively.

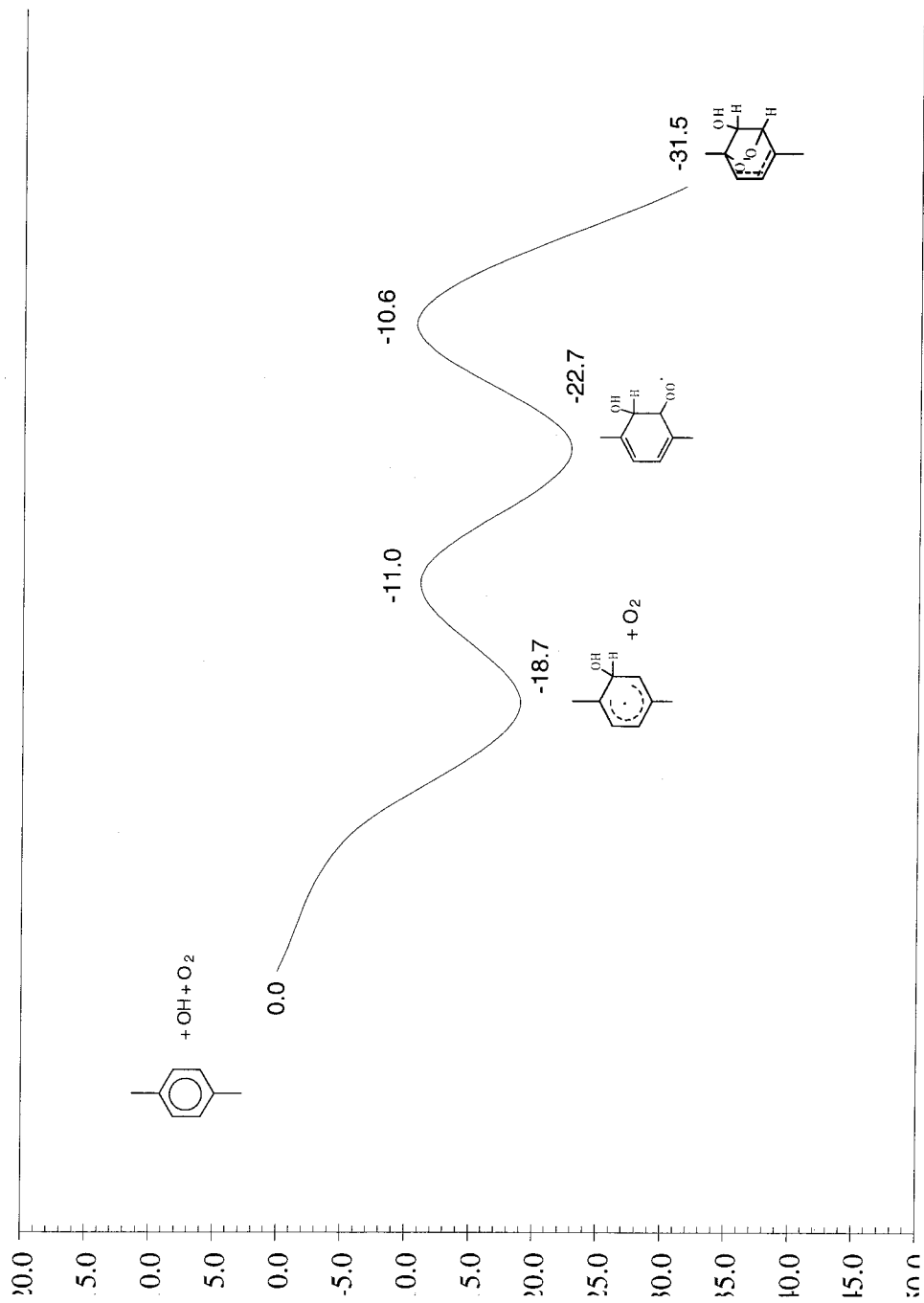


Figure 2.4: Reaction coordinate diagram for *p*-xylene. Shown below the path are the corresponding aromatic-OH adduct, peroxy radical, and bicyclic radical corresponding to the favored pathway.

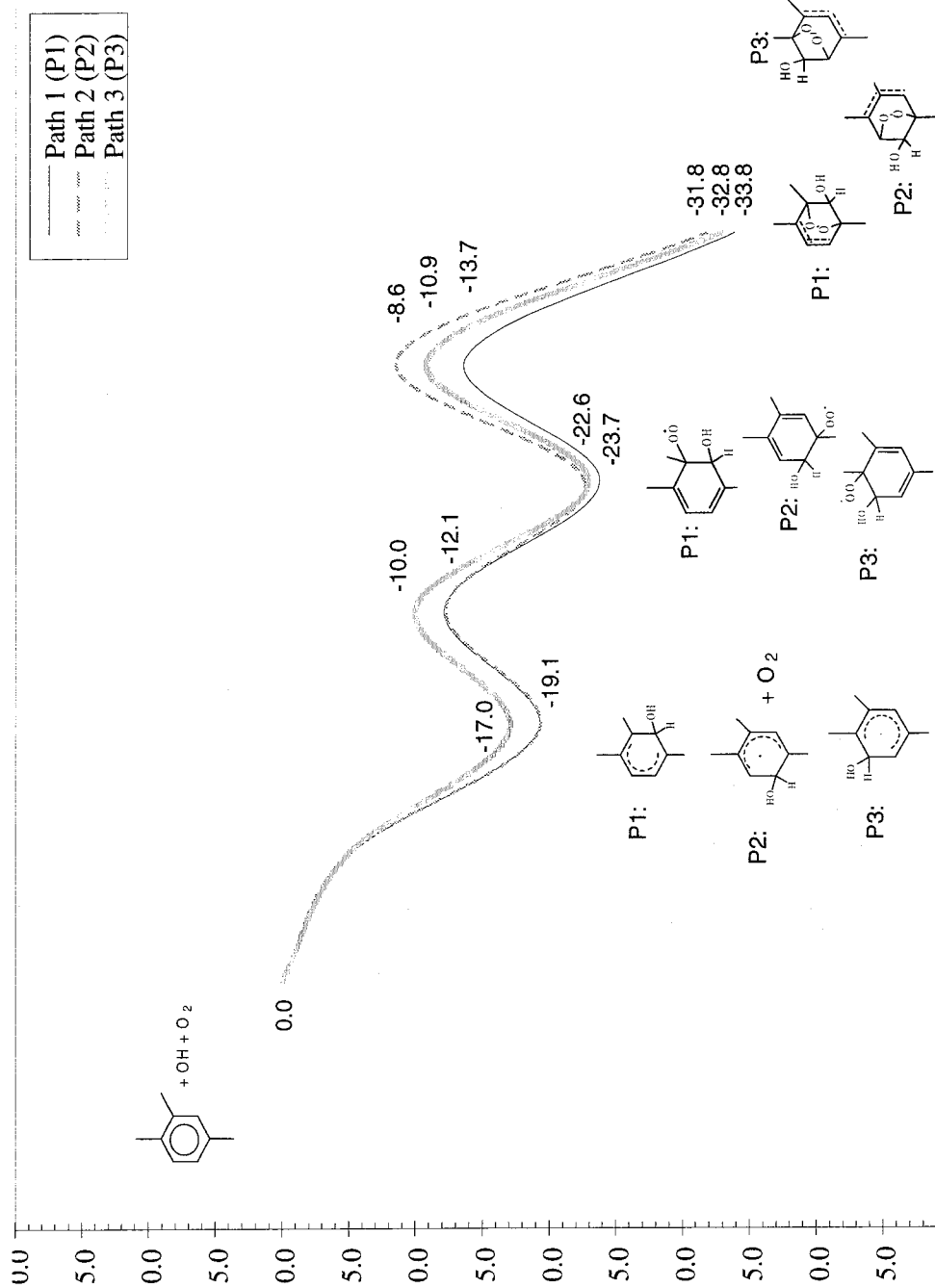


Figure 2.5: Reaction coordinate diagram for 1,2,4-trimethylbenzene. Indicated are the energies of the three favored pathways. Shown below the diagram are the corresponding aromatic-OH adduct, peroxy radical, and bicyclic radical corresponding to the pathways. The structures are labeled P1, P2, and P3 corresponding to paths 1, 2, and 3, respectively.

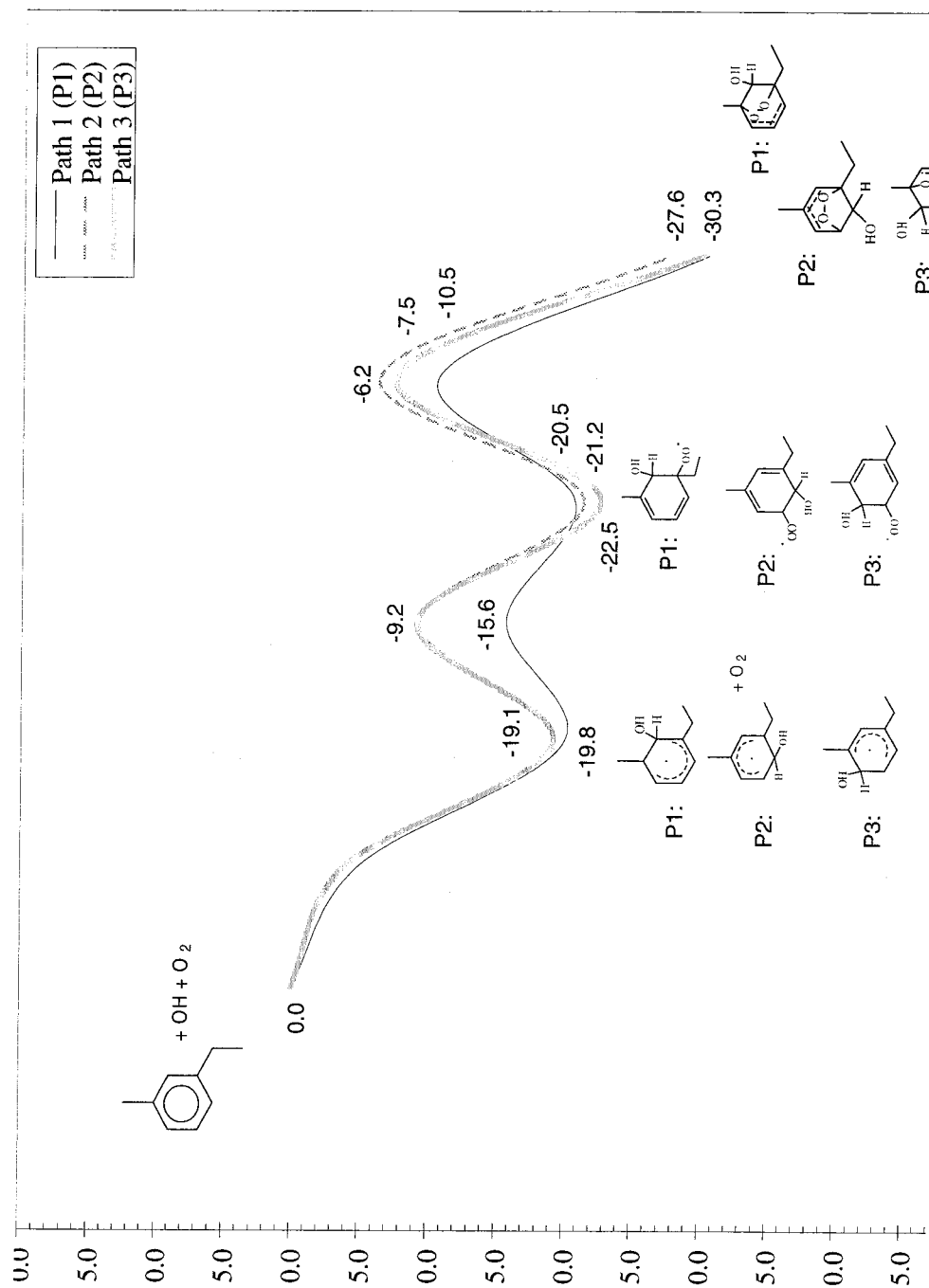


Figure 2.6: Reaction coordinate diagram for *m*-ethyltoluene. Indicated are the energies of the three favored pathways. Shown below the diagram are the corresponding aromatic-OH adduct, peroxy radical, and bicyclic radical corresponding to the pathways. The structures are labeled P1, P2, and P3 corresponding to paths 1, 2, and 3, respectively.

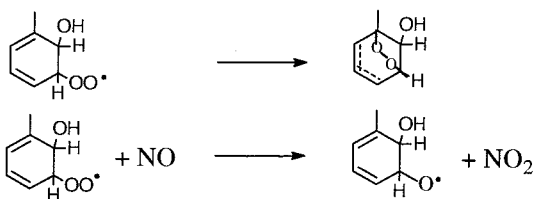
formed from OH addition to the 3, 5 and 6 positions, respectively. As with the case of 1,2,4-trimethylbenzene, there are no experimental data available for ring-retaining products formed from the *m*-ethyltoluene-OH reaction. Based on our energy determinations, we predict the formation of 2-ethyl-6-methylphenol, 2-ethyl-4-methylphenol, and 4-ethyl-6-methylphenol from the O₂ reaction with the adducts formed from OH addition to the 2, 4, and 6 positions.

Alkyl peroxy radicals present in polluted atmospheres generally react with NO to form alkoxy radicals.[2, 28] Aromatic peroxy radicals, in contrast, are believed to cyclize forming bicyclic radicals.[27] To test this hypothesis, we examined the ΔH_{rxn} for Reactions 4 and 5 in the generalized mechanism for aromatic-OH reaction. Representative aromatic peroxy radicals, bicyclic radicals, and aromatic oxy radicals, along with the ΔH_{rxn} values for Reactions 4 and 5 are presented in Figure 2.7. Not all of the lowest energy aromatic peroxy radicals (which appear in the reaction coordinate diagrams) appear in Figure 2.7. The peroxy radicals chosen for Figure 2.7 are representative cases chosen to demonstrate that the two pathways for peroxy radical reaction are possible, and that Reaction 5 cannot be unambiguously excluded from a generalized reaction mechanism. The addition of Reaction 5 results in the formation of oxy radicals. These radicals can go on to react according the scheme in Figure 2.8 to yield ring-retained hydroxy carbonyl compounds or decompose by C-C bond scission to ultimately form a di-unsaturated dicarbonyl. These carbonyl compounds can serve to account for part of the carbon unaccounted for in laboratory studies of aromatic-OH systems.

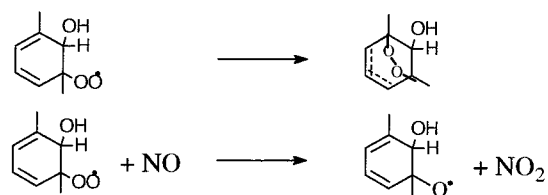
Given the steric hindrance problems associated with another cyclization, the bicyclic peroxy radical reacts with NO to form a bicyclic oxy radical and NO₂. The energies determined for the bicyclic peroxy radicals are all similar in magnitude. Thus, all bicyclic peroxy structures resulting from the lowest energy bicyclic radicals must be considered in an overall mechanism.

The only path for the resulting bicyclic oxy radicals is fragmentation via favorable β -scission reactions. These fragmentation reactions yield an acyclic radical and, eventually, dicarbonyl products (see Tables 2.1–2.3). Shown in Figure 2.9 is an exam-

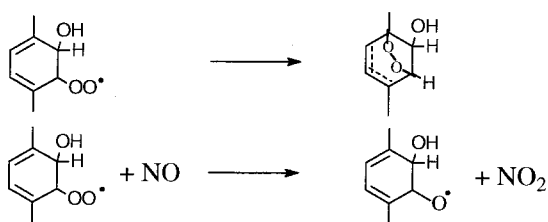
Toluene:



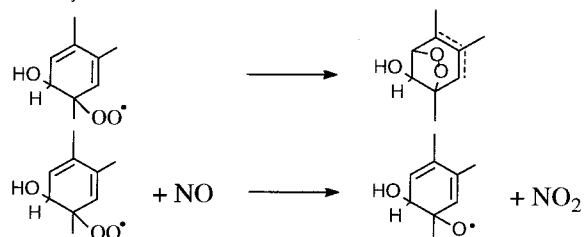
m-Xylene:



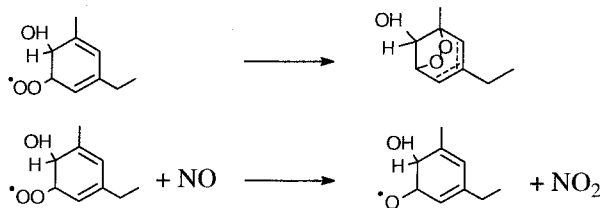
p-Xylene:



1,2,4 Trimethylbenzene:



m-Ethyltoluene:

Figure 2.7: ΔH_{rxn} values for Reactions 4 and 5 for different aromatic systems.

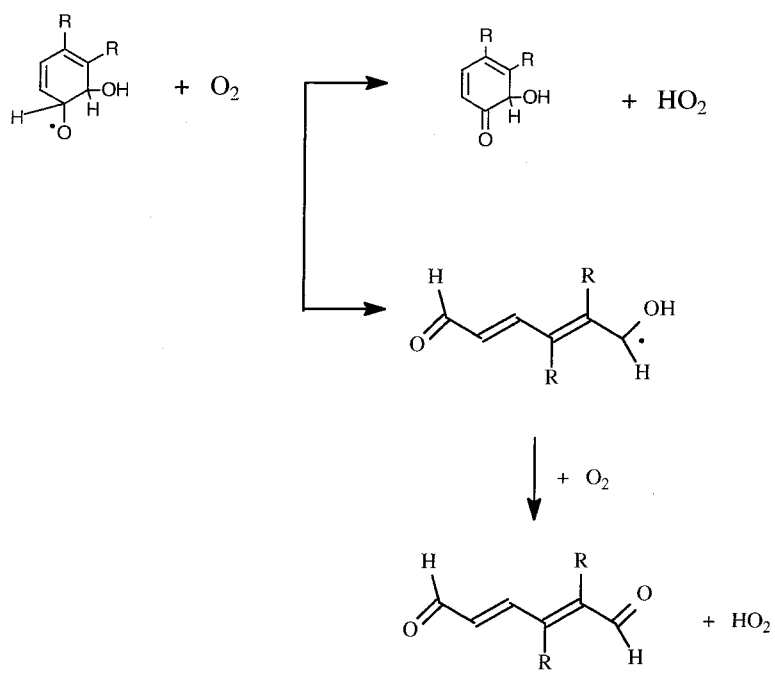


Figure 2.8: Subsequent reaction of oxy radicals formed from Reaction 5 of the generalized mechanism.

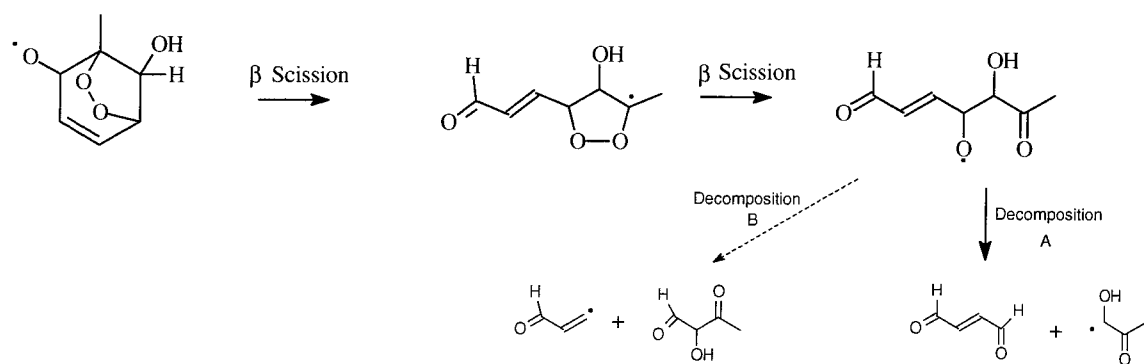


Figure 2.9: β -scission of a bicyclic oxy radical of toluene to give ring fragmentation products. Decomposition path A is the favored path for fragmentation of the acyclic radical.

ple of the β -scission process for a bicyclic oxy radical formed in the photooxidation of toluene. The key issue is the method of fragmentation of the resulting acyclic radical. Calculations of the ΔH_{rxn} , for the decomposition of the acyclic radical were conducted using the NIST Structures and Properties estimation program.[25] This program is based on the group additivity theory of Benson.[29] These calculations result in the prediction that each acyclic radical undergoes fragmentation at the bond between the carbon attached to the oxygen atom and the saturated carbon center rather than the unsaturated carbon center. This point is clearly shown in Figure 2.9. Decomposition path A, illustrating fragmentation between the carbon with the oxygen atom attached to it and the unsaturated carbon center, is the favored path based on group additivity calculations. Decomposition path B is the unlikely method of fragmentation based on group additivity considerations. Shown in Figure 2.10 are the bicyclic oxy radicals and the products that are predicted to form following the β -scission process analogous to that depicted in Figure 2.9. It is well known that α -hydroxy carbonyls subsequently react with O_2 to form HO_2 and the corresponding dicarbonyl product.[27] Note from Tables 2.1–2.3 that a number of the ring fragmentation products theoretically predicted for toluene, *m*-xylene, and *p*-xylene have been identified experimentally.

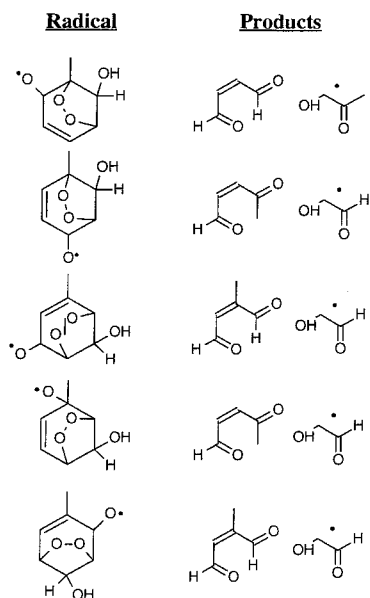
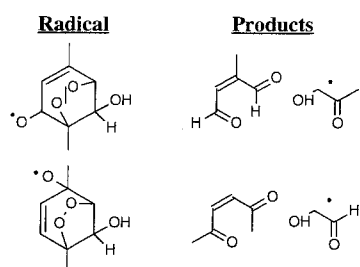
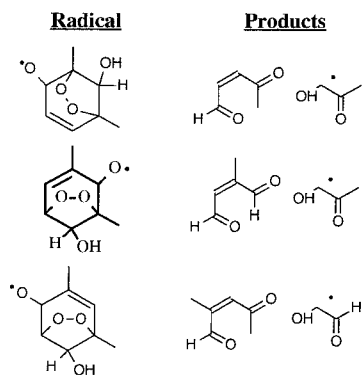
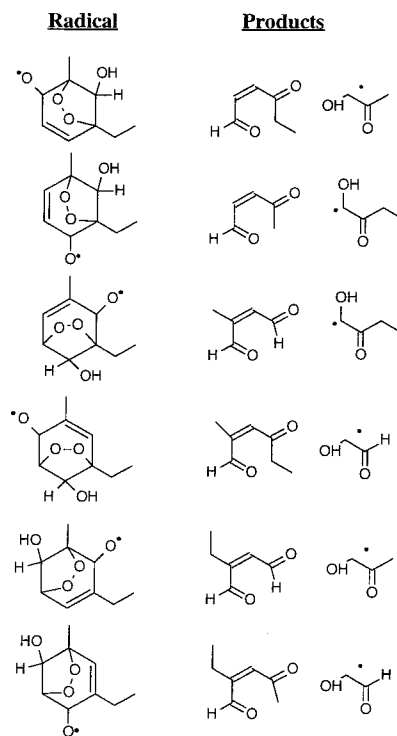
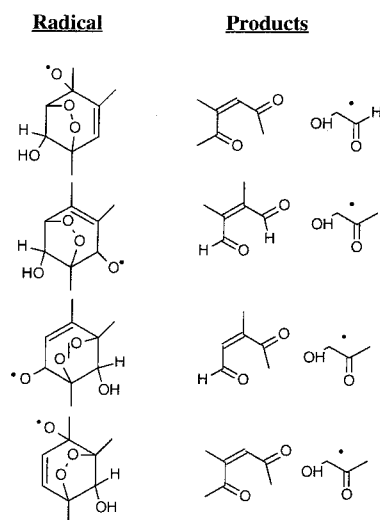
Toluene**p-Xylene****m-Xylene****m-Ethyltoluene****1,2,4-Trimethylbenzene**

Figure 2.10: Fragmentation products formed from the bicyclic oxy radical.

Experimental evidence has been found for the presence of nitroaromatic compounds in the photooxidation of toluene, *m*-xylene, and *p*-xylene (see Tables 2.1–2.3). Consistent with the theoretical prediction that all three possible toluene-OH adducts form, experimental evidence exists for three different nitrotoluene products. Similarly, consistent with the prediction that only two of the possible *m*-xylene-OH adducts form, experimental evidence exists for only two nitro-*m*-xylene products. Hydroxyl radical addition to the 2 position of *m*-xylene, with subsequent reaction with NO₂ yields 4-nitro-*m*-xylene, whereas addition to the 4 position yields 5-nitro-*m*-xylene. Observations of the nitroaromatics from the *p*-xylene photooxidation systems are also consistent with theory. Only one nitroaromatic, 2-nitro-*p*-xylene, is detected in laboratory studies. Since experimental data are not available for the nitroaromatics resulting from the 1,2,4-trimethylbenzene and *m*-ethyltoluene systems, the results of the previous section, indicating the favored aromatic-OH adducts, can predict the nitroaromatic species expected to form in photooxidation studies of 1,2,4-trimethylbenzene and *m*-ethyltoluene. From OH addition to the 3 position and 5 positions, 4-nitro-1,2,4-trimethylbenzene and 6-nitro-1,2,4-trimethylbenzene are predicted to form, and 5-nitro-1,2,4-trimethylbenzene should not form. For *m*-ethyltoluene, the formation of 4-nitro-*m*-ethyltoluene from OH addition to the 2 position, 5-nitro-*m*-ethyltoluene from OH addition to the 4 position, and 2-nitro-*m*-ethyltoluene from addition to the 6 position are predicted.

2.5 Conclusion

We have elucidated the intermediates in five atmospheric aromatic-OH photooxidation systems, using quantum chemical calculations. In general, the predicted site of initial OH attack is *ortho* to a substituent alkyl group. In addition, the NO₂ reaction with the aromatic-OH adduct was investigated. The results indicate that this reaction most likely proceeds via four pathways, forming the nitroaromatic (Reaction 3a), hydroxy nitroaromatic compounds (Reaction 3b), hydroxy aromatic nitrites (Reaction 3c), and phenolic compounds (Reaction 3d). Whereas it is difficult to predict,

a priori, the site of O₂ addition to the aromatic-OH adduct, we have identified the most likely structural isomers of the peroxy radical, including those which lead to the formation of an allylically stabilized bicyclic radical. The allylically stabilized five-membered ring bicyclic radicals are, in all cases, at least 20 kcal/mol more stable than any other bicyclic radical. The aromatic peroxy radical reaction with NO (Reaction 5) is determined to be a plausible reaction to include in aromatic-OH reaction mechanisms. Subsequent reaction of the oxy radicals formed in Reaction 5 can lead to ring-retaining hydroxy carbonyl compounds or can fragment to form di-unsaturated dicarbonyls. These additional compounds can account for part of the remaining carbon unaccounted for in laboratory studies of aromatics. When compared to available product data, the theoretical results for toluene, *m*-xylene, and *p*-xylene indicating the intermediates formed and their subsequent reactions are found to be consistent with experimental results. The technique has been applied to two important, yet relatively unstudied, 1,2,4-trimethylbenzene and *m*-ethyltoluene, to predict their reaction intermediates and stable products.

Acknowledgements

This work was supported by U.S. Environmental Protection Agency Center for Airborne Organics (R-819714-01-0), National Science Foundation grant ATM-9307603, the Coordinating Research Council (A-5-1), and the Chevron Corporation. The authors thank J. K. Perry and T. P. W. Jungkamp for helpful discussions.

Bibliography

- [1] John H. Seinfeld. *Rethinking the Ozone Problem in Urban and Regional Air Pollution*. National Academy Press, Washington, DC, 1991.
- [2] R. Atkinson, D. L. Baulch, R. A. Cox, R. F. Hampson, J. A. Kerr, and J. Troe. Evaluated kinetic and photochemical data for atmospheric chemistry. 3. IUPAC subcommittee on gas kinetic data evaluation for atmospheric chemistry. *J. Phys. Chem. Ref. Data*, 18(2):881–1097, 1989.
- [3] R. Atkinson and S. M. Aschmann. Products of the gas-phase reactions of aromatic-hydrocarbons - effect of NO₂ concentration. *Int. J. Chem. Kinet.*, 26(9):929–944, 1994.
- [4] R. Atkinson, S. M. Aschmann, and J. Arey. Rate constants for the gas-phase reactions of OH and NO₃ radicals and O₃ with sabinene and camphene at 296±2 K. *Atmos. Environ. A*, 24(10):2647–2654, 1990.
- [5] H. Bandow and N. Washida. Ring-cleavage reactions of aromatic-hydrocarbons studied by FT-IR spectroscopy. 2. Phototoxidation of ortho-xylenes, meta-xylenes, and para-xylenes in the NO_x-air system. *Bull. Chem. Soc. Jpn.*, 58(9):2541–2548, 1985.
- [6] E. C. Tuazon, H. Macleod, R. Atkinson, and W. P. L. Carter. Alpha-dicarbonyl yields from the NO_x-air photooxidations of a series of aromatic-hydrocarbons in air. *Environ. Sci. Technol.*, 20(4):383–387, 1986.
- [7] B. E. Dumdei, D. V. Kenny, P. B. Shepson, T. E. Kleindienst, C. M. Nero, L. T. Cupitt, and L. D. Claxton. MS MS analysis of the products of toluene photooxidation and measurement of their mutagenic activity. *Environ. Sci. Technol.*, 22(12):1493–1498, 1988.

- [8] H. Bandow and N. Washida. Ring-cleavage reactions of aromatic-hydrocarbons studied by FT-IR spectroscopy. 3. Photooxidation of 1,2,3-trimethylbenzenes, 1,2,4-trimethylbenzenes, and 1,3,5-trimethylbenzenes in the nox-air system. *Bull. Chem. Soc. Jpn.*, 58(9):2549–2555, 1985.
- [9] P. B. Shepson, E. O. Edney, and E. W. Corse. Ring fragmentation reactions on the photooxidations of toluene and ortho-xylene. *J. Phys. Chem.*, 88(18):4122–4126, 1984.
- [10] R. Atkinson, S. M. Aschmann, J. Arey, and W. P. L. Carter. Formation of ring-retaining products from the OH radical-initiated reactions of benzene and toluene. *Int. J. Chem. Kinet.*, 21(9):801–827, 1989.
- [11] M. W. Gery, D. L. Fox, R. M. Kamens, and L. Stockburger. Investigation of hydroxyl radical reactions with ortho-xylene and meta-xylene in a continuous stirred tank reactor. *Environ. Sci. Technol.*, 21(4):339–348, 1987.
- [12] R. Atkinson, S. M. Aschmann, and J. Arey. Formation of ring-retaining products from the OH radical-initiated reactions of ortho-xylene, meta-xylene, and para-xylene. *Int. J. Chem. Kinet.*, 23(1):77–97, 1991.
- [13] J. B. Foresman and Æ. Frisch. *Exploring Chemistry with Electronic Structure Methods*. Gaussian, Inc., Pittsburgh, PA, 1996.
- [14] R. G. Parr and W. Yang. *Density Functional Theory of Atoms and Molecules*. Oxford University Press, New York, NY, 1989.
- [15] A. D. Becke. Density-functional exchange-energy approximation with correct asymptotic-behavior. *Phys. Rev. A: At. Mol. Opt. Phys.*, 38(6):3098–3100, 1988.
- [16] A. D. Becke. Density functional theories in quantum-chemistry - beyond the local density approximation. *ACS Symp. Series*, 394:165–179, 1989.
- [17] M. J. Frisch, G. W. Trucks, H. B. Schlegel, P. M. W. Gill, B. G. Johnson, M. W. Wong, J. B. Foresman, M. A. Robb, M. Head-Gordon, E. S. Replogle,

- R. Gompert, I. L. Andres, K. Raghavachari, J. S. Binkley, C. Gonzalez, R. L. Martin, D. J. Fox, D. J. Defrees, J. Baker, J. J. P. Stewart, and J. A. Pople. Gaussian 92/DFT, 1993.
- [18] H. Lee, C. T. Lee, and R. G. Parr. Conjoint gradient correction to the Hartree-Fock kinetic-energy and exchange-energy density functionals. *Phys. Rev. A: At. Mol. Opt. Phys.*, 44(1):768–771, 1991.
- [19] J. J. P. Stewart. Optimization of parameters for semiempirical methods. 1. Method. *J. Comput. Chem.*, 10(2):209–220, 1989.
- [20] U. Burkert and N. L. Allinger. *Molecular Mechanics*. ACS Monograph 177. American Chemical Society, Washington, DC, 1982.
- [21] B. F. Plummer, L. K. Steffen, and W. C. Herndon. Polycyclic aromatic-hydrocarbons with 5-membered rings - modeling of experimental x-ray and neutron-diffraction structures. *Struct. Chem.*, 4(4):279–285, 1993.
- [22] M. B. Coolidge, J. E. Marlin, and J. J. P. Stewart. Calculations of molecular vibrational frequencies using semiempirical methods. *J. Comput. Chem.*, 12(8):948–952, 1991.
- [23] M. N. Ringnalda, J. M. Langlois, B. H. Greeley, R. B. Murphy, T. V. Russo, C. Cortis, Muller R. P., B. Martin, R. E. Donnelly, Jr., D. T. Mainz, J. R. Wright, W. T. Pollard, Y. Cao, Y. Won, G. H. Miller, W. A. Goddard, III, and R. A. Friesner. PSGVB, 1995.
- [24] Autodesk. Hyperchem, 1994.
- [25] S. E. Stein, J. M. Rukkers, and R. L. Brown. NIST standard reference database 25: NIST structures and properties database and estimation program, 1991.
- [26] R. Knispel, R. Koch, M. Siese, and C. Zetzsch. Adduct formation of OH radicals with benzene, toluene, and phenol and consecutive reactions of the adducts with NO_x and O₂. *Ber. Bunsen-Ges. Phys. Chem.*, 94(11):1375–1379, 1990.

- [27] R. Atkinson and A. C. Lloyd. Evaluation of kinetic and mechanistic data for modeling of photochemical smog. *J. Phys. Chem. Ref. Data*, 13:315–444, 1984.
- [28] T. J. Wallington, P. Dagaut, and M. J. Kurylo. Ultraviolet-absorption cross-sections and reaction-kinetics and mechanisms for peroxy-radicals in the gas-phase. *Chem. Rev.*, 92(4):667–710, 1992.
- [29] S. W. Benson. *Thermochemical Kinetics*. John Wiley and Sons, New York, NY, 2 edition, 1976.

**Part B: Fundamental Studies of Droplet
Evaporation and Discharge Dynamics in
Electrospray Ionization**

Chapter 3 Introduction

The use of evaporating charged droplets to create gas-phase ions from analyte species in solution has grown from a method first proposed 30 years ago to become one of the most important means for studying a liquid phase compounds with mass spectrometry. Today the technique, called electrospray ionization, is widely recognized as one of the gentlest means of creating ions for mass spectrometry, imparting little or no internal energy to the gas-phase ions. Large and weakly bound complexes can be studied with relative ease facilitating increased use in fields such as biological and environmental chemistry. For large molecules, electrospray generally produces ions with a broad distribution of charge states having relatively low mass-to-charge ratios. This has allowed for the use of conventional mass spectrometers with limited mass range for measuring very high molecular weight compounds. It has also brought about a revolution in the high-resolution determination of molecular weight for biological molecules. Electrospray has also become one of the most important techniques for coupling liquid separation methods with mass spectrometry.[1] It is also a simple and elegant technique that can be built from items that are common in most research laboratories, and runs at atmospheric pressure and at moderate temperatures.

A schematic of the electrospray process is shown in Figure 3.1. A dilute solution of analyte in a volatile solvent is introduced through a small needle into a chamber in which dry nitrogen gas is passed at atmospheric pressure. An intense electrostatic field is formed at the tip of the needle by applying a few kilovolts potential difference between the needle and the chamber walls. The polarity of the applied field determines the polarity of the ions produced: the configuration for positive ions is depicted in the figure, and will be the example used throughout the discussion and analysis that follows. At the tip of the needle, the high electric field pulls liquid phase ions towards the liquid-gas interface. As a result of combined hydrodynamic and electrostatic forces, the liquid surface at the tip of the needle forms a cusp, called a Taylor cone,

which emits a fine spray of charged droplets. These charged droplets evaporate until they reach a critical size for which electrostatic repulsion of surface charges is balanced by surface tension. At this size and charge level, collectively known as the Rayleigh limit, any small perturbation to the surface of the droplet will cause it to become unstable and break apart. The droplets that result from this instability will repeat the sequence. Ultimately a point is reached when all the solvent has evaporated. What remains is a collection of gas-phase ions, possibly still weakly bound to solvent molecules, in a high-pressure cloud of solvent molecules. The ions are then transferred to the high vacuum region of a mass spectrometer for mass analysis.

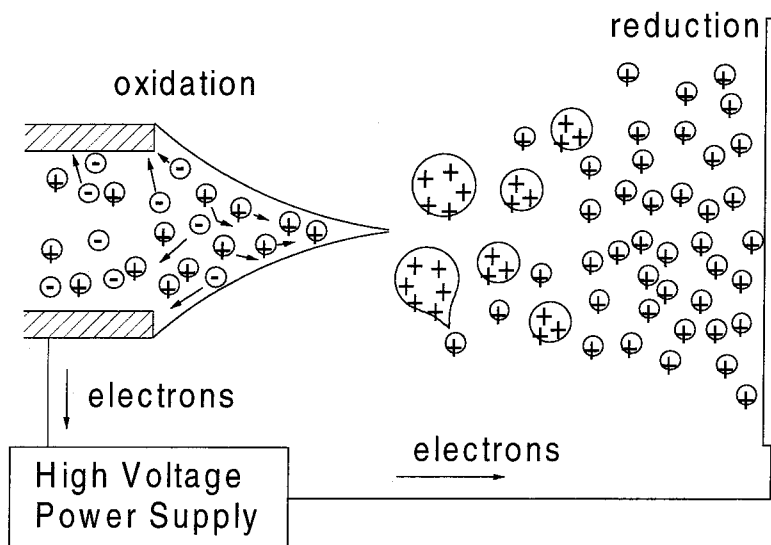


Figure 3.1: Schematic of the electrospray process.

In spite of its simplicity in implementation, many questions remain about the process by which ions are formed from these charged droplets. Unresolved issues include the relationship between analyte concentration in solution to that in the gas phase and whether desorption of one species is preferred over another in multi-component mixtures. This lack of quantitative understanding of the mechanism of ion formation in electrospray, at the very least, limits the quantitative information

that can be derived from a mass spectrum of electrosprayed ions. At worst, it may lead to a misrepresentation of the chemistry of the bulk phase. Moreover, little is known regarding the dynamics of droplet breakup, and less still is known about the mechanism and dynamics of ion formation.

Practical reasons exist for understanding the ion formation process in electrospray ionization. The efficiency of sample introduction into the mass spectrometer limits its sensitivity. The spray originates at atmospheric pressure: only a small fraction of the ions formed at the source, roughly one in 10^5 , successfully enters the high vacuum region of a mass spectrometer. An understanding of the process should make it possible to devise methods to efficiently collect and analyze ions produced by electrosprays.

The chapters that follow comprise the initial steps toward the goal of understanding the mechanism and dynamics of ion production in electrosprays. This work focuses primarily on the processes of droplet evaporation and discharge, and lays the groundwork for subsequent planned investigations of ion formation. An experimental technique has been developed for trapping and studying charged droplets produced in actual electrosprays. This “ping-pong experiment” is described in detail in Chapter 7. It enables measurement of the time evolution of size and charge evolution for individual charged droplets. This same trapping technique forms an integral part of a proposed apparatus for studying ion formation from electrosprayed droplets.

As Chapter 4 will show, understanding evaporation and discharge of highly charged droplets is essential for characterizing many different processes. The production of gas-phase ions during the evaporation of charged droplets enables the use of electrospray ionization sources for mass spectrometry. The instability that develops when a volatile, highly-charged droplet evaporates causes it to break apart to form smaller droplets in electrostatic atomization. The spray of fine, highly charged droplets thus produced finds applications in electrostatic painting, fuel atomization for combustion, and crop spraying. While the main emphasis of the present study is the process of ion formation in electrospray, the results will also aid in understanding charged droplet breakup in electrostatic atomization.

3.1 Overview of Part B

In Chapter 4, a history of research in charged droplet breakup and ion formation, some dating back to the 18th century, will be presented. In this chapter, the current status of knowledge on the processes of charged droplet formation, evaporation, breakup, and ion formation will also be described. Since numerous review articles and books have been published on electrostatic atomization[2, 3]and electrospray,[1, 4, 5] no attempt will be made to present a complete history or a thorough review of experiments performed in these fields. Instead the most significant studies will be presented, highlighting the results that relate the chemical and physical properties of the solution and analyte compounds the formation of free gas-phase ions.

In Chapter 5, fundamental theories and modeling results are presented that relate to the experimental method used in this study. These concepts are applied to the process of ion formation from highly charged droplets, and demonstrate the capabilities of the current technique for providing essential information on these processes. A separation technique based on a property of charged droplets called “mobility” is an essential element of the current study, thus modeling results of the mobility of ions and charged droplets will be presented. Since solvent evaporation is principally responsible for reduction in droplet size in these sprays, the behavior of a evaporating, highly charged droplet within a drift cell (an instrument with which mobility measurements are made) is modeled.

With the background and theoretical basis of the proposed technique established, subsequent chapters are devoted to the presentation of the experimental technique and the results of experiments performed with an electrospray ionization source. Chapter 6 provides an concise overview of the method and some results of measurements made, using a technique called the “ping-pong technique,” on electrosprays of methanol, acetonitrile, and water. It has been written in the form of a communication for the *Journal of the American Chemical Society*. Additional data in support of the claims made in this chapter can be found in Appendix 9.

Following the summary of the ping-pong experiment provided in Chapter 6, Chap-

ter 7 presents more specific information on its design and a more thorough analysis of the data. In this chapter, the key elements of the experiment are discussed in detail: the electrospray source, drift cell, associated electronics, and software. The instrument used to measure size and charge on the electrosprayed droplets is also presented: a phase Doppler anemometer that was built in-house for these investigations. In this chapter, electrosprays of methanol are investigated in greater detail than that which was provided in Chapter 6.

Chapter 9 is a detailed summary of experiments performed using the ping-pong technique. This chapter presents data from these investigations that support the statements made in Chapter 6 regarding the effects of solvent and electrolyte concentration on droplet discharge dynamics. In addition, we present some results that suggest that the droplet environment may play an important role in determining the extent of charge loss resulting from the discharge process.

The phase Doppler anemometer is described in Chapter 8. This chapter has been written for submission to *Review of Scientific Instruments*, and emphasizes the design and calibration of the instrument. The design has many possible uses in a variety of research and educational environments, and is distinguished by its low cost, ease in assembly (using mostly off-the-shelf components) and high degree of adaptability. A novel calibration method permits instrument characterization over the size range expected for investigations of electrosprayed droplets, i.e., 10–50 μm , while minimally disturbing the position of the instrument. Although a phase Doppler system is insensitive to slight misalignment of its optics, the ability to verify calibration without otherwise touching the optical setup increases confidence in the measurements. This calibration procedure is thus an essential part of the investigations presented in Chapters 6 and 7.

A discussion of future research goals for the project is presented in Chapter 10. Here, the possibility of ion detection from these charged droplets is explored. The model developed in Chapter 5 is applied to the ping-pong experiment, and a new experimental configuration is proposed based on the results of the model.

Four appendices are also included. In Appendix A, an operations manual and

complete parts list are presented for the PDA system. It is hoped that preparing an operations manual for the instrument and publishing it as part of this document will make the instrument useful for other investigators. Another operations manual can be found in Appendix B for a “drop-on-demand” generator. As the name suggests, this device allows for the creation of a single 50–100 μm droplet with the press of a button. The manual, along with a complete set of machine drawings and parts lists, have been developed in response to numerous requests for information on this instrument. Appendix C describes another optical assembly that has been developed and would possibly find use in future research activities related to electrospray. This instrument is an optical receiver for aerosol laser induced fluorescence measurements. A discussion of possible uses for this device will be given in Chapter 10 in relation to the study of progeny droplets from the discharge events recorded in the ping-pong experiment. Finally, Appendix D presents calculations that lead to a numerical estimate of the impulse applied to the droplet as a result of the disruption process. This calculation was born from the observation that the ping-pong technique is remarkably successful in tracking the evolution of droplet size and charge through several fission events in spite of having no radial trapping force. The estimate provided in the appendix was made using a simple model of the droplet breakup process, and there are surely many interesting avenues to explore in the general area of droplet disruption energetics, made possible by the ability of the experiment to measure the displacement of a droplet that has undergone a disruption event.

Bibliography

- [1] A. P. Bruins. Mechanistic aspects of electrospray ionization. *J. Chromatogr. A*, 794:345–357, 1998.
- [2] D. Michelson. *Electrostatic Atomization*. Adam Hilger, Bristol, 1990.
- [3] Adrian G. Bailey. *Electrostatic Spraying of Liquids*. Electrostatics and electrostatic applications. John Wiley and Sons, Ltd., Somerset, 1988.
- [4] R. B. Cole, editor. *Electrospray Ionization Mass Spectrometry: Fundamentals, Instrumentation, and Applications*. John Wiley and Sons, New York, 1997.
- [5] P. Kebarle and L. Tang. From ions in solution to ions in the gas phase: The mechanism of electrospray mass spectrometry. *Anal. Chem.*, 65:972A, 1993.

Chapter 4 A Survey of Past Research in Electropray Ionization

4.1 Introduction

Contemplation of the fundamental processes in electrostatic atomization and electropray ionization prompts one to divide the process into individual steps. First, a collection of charged droplets is formed by a combination of mechanical and electrostatic processes at the source exit. Secondly, each droplet evaporates until it reaches a critical size at which increased charge density causes the droplet to break apart in some manner. Finally, at some point during the process of droplet evaporation or breakup, gas-phase ions are formed. This chapter presents a discussion of the current status of knowledge in each of these areas. It concludes with a list of issues that might lend themselves to the proposed experimental technique. Where appropriate, anecdotes from the history of the development in each area will be given. Since the electrostatic atomization and electropray ionization are operationally identical up to the formation of ions, I will refrain from applying either term to the processes of charged droplet formation, evaporation, and breakup by referring to this as creating an electrostatic spray.

4.2 Droplet Formation and Charging

Most mechanically generated sprays and all those produced naturally carry some kind of charge distribution. The quantity and polarity of the charge depends on the presence of free charge carriers in solution. For natural sprays, the polar nature of water and the abundance of dissolved salts assure the presence of both positive and negative ions in solution. The inevitable differences in the mobilities of the dissolved

ions leads to different migration times to interfacial regions. Electrical double layers develop at all surfaces, populating surfaces with ions of high mobility. Negative ions accumulate on natural water surfaces, producing surface charge densities on the order of 10^{-10} C/m². Application of an electric field greatly enhances this charge level in a process is called induction charging. Disruption of the liquid shears the surface double layers, creating droplets containing a surplus of positive or negative ions.

Many of the early studies of droplet electrification focused on charging processes. Lord Kelvin provided an interesting illustration of induction charging and its effect on droplet formation with his water dropper apparatus, developed in 1867 and shown schematically in Figure 4.1. The reservoir is grounded. Any slight imbalance in the dripping rate of the two nozzles causes an imbalance in the electric charge that accumulates in the metal cups. The cups are electrically connected to two ring electrodes as shown in the figure. These rings alter the charging of the droplets and creates a feedback mechanism that leads to even greater charge accumulation in the cups. In this way, the voltage of rings increases to 10–20 kV within minutes. Kelvin observed that, during the time that the voltage was increasing on the electrodes, the droplet production rate from the nozzles increased noticeably. This suggests that the electric field surrounding the nozzle strongly influences the spray. One might consider this the first demonstration of electrostatically-assisted spraying, but this dispersive effect had been investigated even earlier. In the 18th century, Abbé Nollet experimented with electrified liquids. Nollet observed that, if a person were highly electrified by connection to a high-voltage generator, he would not bleed normally when he cut himself. Instead blood would spray from the wound!

In 1912, Smoluchowski proposed a model that has led to our present understanding of spray electrification. The basic tenet of the model is that the charge of any droplet produced by mechanical shear depends upon the number of ions that happened to be contained in the droplet at the instant that it was formed. The model suggests that the charge of the droplet is independent of the mechanism by which it is created, an assumption that has been shown to be valid for low-conductivity, non-aqueous solutions. For aqueous solutions, however, charge redistribution at the moment the

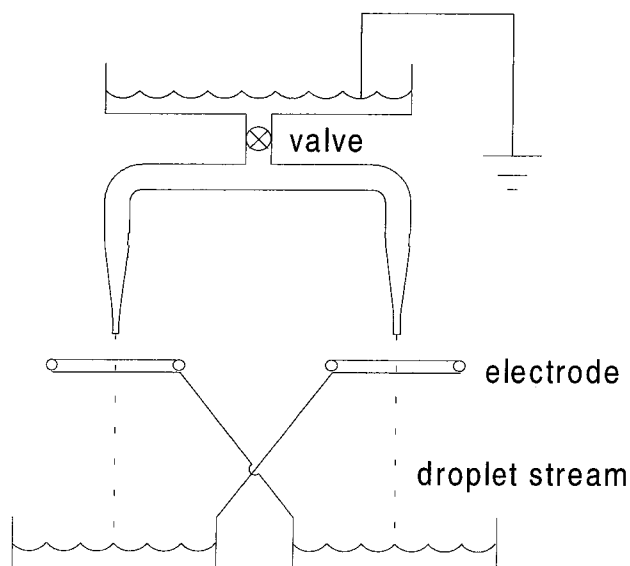


Figure 4.1: Lord Kelvin's droplet high-voltage generator.

droplet is formed limits the charge transfer to the droplet. Most of the interest in the use of electrospray and electrostatic atomization makes use of aqueous solutions, so a few significant studies on the complex formation processes of charged aqueous droplets will be mentioned.

In 1958 Blanchard conducted a series of experiments on the charging of sea spray.[1] In the case of sea spray electrification, droplet charging was believed to be enhanced by the earth's own electric field of about 130 V/m in fair weather. Sea spray electrification is an important source of gas-phase ions in the lower atmosphere.[2] In 1967, Iribarne made what was to be one of two important contributions in two different disciplines involving electrostatic sprays. In a study with Mason, he investigated the process of droplet formation from bubble bursting in solutions with varied conductivity.[3] They applied the Gouy theory of the electrical double layer to the description of the liquid surface. In Gouy theory, the charge distribution near the water surface is characterized by a surface layer containing ions of one polarity and a diffuse layer of opposite polarity ions extending into the bulk liquid. The depth

and relaxation time of this double layer are both a function of the electrolyte concentration, and this in addition to the mechanism of droplet formation determine how much charge is deposited on the droplet during formation. By applying Gouy theory, Iribarne and Mason were able to predict the charge density as a function of depth for their aqueous liquids. In their model for charged drop formation from a bursting bubble, they assumed a double layer of a given thickness was skimmed from the liquid surface during the formation process. With this, Iribarne and Mason were able to accurately predict the amount of charge that was conveyed to a droplet as a function of the size of the bursting bubble. Although the process under study is in some ways quite different from the formation of charged droplets in electrostatic sprays, Iribarne and Mason's approach to charge distribution in the bulk liquid and the dynamics of ion distribution at the moment of droplet formation is quite useful for the understanding of the formation and charging processes of any mechanically dispersed liquid. One additional point from their study is worth mentioning, since it relates the dynamics of charge distribution in the forming droplet. In their study, the droplet formation time was assumed to be about $10 \mu\text{s}$. For electrolyte concentrations above 10^{-5} M , they point out that the double layer relaxation time is much less than the droplet formation times, and so equilibrium can be achieved in the surface layer during the formation process. If the electrolyte were lower than 10^{-5} M , the charge on the droplet would be less than what would otherwise be the case due to the dynamics of double layer relaxation.

Studies into the means by which charged droplets are produced in an electrostatic spray have endorsed an induction charging mechanism in which counter-ions in solution are replenished through electrochemical reactions in the needle of the electrostatic spray apparatus.[4, 5] In this electrophoretic model of the charging mechanism, the electrospray process can be viewed as a special type of electrolytic cell where part of the charge transport takes place in the form of dispersed charged droplets, and later as desolvated, gas-phase ions. A schematic of this process can be seen in Figure 3.1 in the previous chapter. For the example in the figure for positively charged droplets, negative ions that are in abundance in the bulk solution after the

formation of positively charged droplets are neutralized by electrochemical oxidation at the liquid-metal interface. Alternatively, the excess positive ions can be supplied to the bulk solution by the conversion of metal ions in the needle to positive ions and electrons. Proof of these electrochemical processes was provided by Blades and co-workers.[5] When the needle of the electrostatic spray apparatus is made of a metal such as zinc, trace levels of Zn^{2+} were found in the mass spectrum of the sprayed solution. In addition, the levels of metal ions that were detected were found to be consistent with the currents needed to maintain the electrostatic spray.

One final study will be mentioned in this section on the formation and charging of droplets, as it applies to the method used to create charged droplets in this study. In a study by Takumatsu and co-workers, the formation of a single charged droplet in a uniform electric field is modeled and studied experimentally.[6] Using the method of images to model the equilibrium charge on a droplet forming in a constant electric field, they estimated the resulting charge to be

$$Q = 4\pi\epsilon_0 (1.63) r^2 E_0. \quad (4.1)$$

Here, ϵ_0 is the permittivity of free space, r is the radius of the pendant droplet, and E_0 is the field strength. The predicted charge closely agreed with their experimental observations. Moreover, they found that if the nozzle from which the droplet is formed is projected into the space between the parallel plates that form the constant electric field in the direction of the spray, the charge on the droplet is increased dramatically. This latter geometry is more representative of typical electrostatic sprays such as that depicted in Figure 3.1.

4.3 Charged Droplet Evaporation and Breakup

An excellent review of the major developments in charged droplet evaporation and breakup can be found in a recent article by Davis.[7] A review of the relevant research in this field starts with the analysis by Lord Rayleigh in 1882 of the charge-retaining

ability of droplets.[8] Rayleigh showed that a droplet of a given radius, R_R , can sustain a maximum level of charge that corresponds to the point at which electrostatic repulsion of surface charges is exactly balanced by surface tension. That charge level,

$$Q_R = 8\pi\sqrt{\epsilon_o\gamma R_R^3}, \quad (4.2)$$

is now called the Rayleigh limit of charge, and the process of breakup is often referred to as Rayleigh instability. In the expression above, ϵ_o is the permittivity of free space and γ is the liquid surface tension. The maximum field, E_R , for stability was also calculated:

$$E_R = \sqrt{\frac{4\gamma}{\epsilon_o R_R}}. \quad (4.3)$$

Although, as will be seen later, Rayleigh's work accurately predicts the instabilities observed for a highly charged droplet, it provides no insights into the nature of the fission event. Since Rayleigh's time, however, numerous experiments have been performed on charged droplets, and theoretical studies have attempted to elucidate this process. Some of these will be described in this section. Macky performed one of the first experiments of the breakup of charged droplets in 1931.[9] Macky sought to understand the behavior of free drops in a thundercloud. He took photographs of droplet instability and made measurements of the electric fields required to bring on these instabilities. One of the most interesting features of charged droplet instability that was portrayed in the photographs was the way in which the droplets broke apart. The droplets formed a thin ligament from which small droplets were ejected, mirroring the way droplets form from an electrostatic spray tip. The two analogous processes are shown in the schematic of the process in Figure 3.1. In 1964, Sir Geoffrey Taylor published results of modeling and experiments of the processes referred to by Macky.[10] Taylor was able to predict the formation of this thin ligament of fluid, which in its ideal form is a conical surface with a half-angle of 49.3° . Today this conical protrusion is referred to as a Taylor cone. As in Macky's study, no quantitative results were provided on the characteristics of the droplets emanating from the tip of the cone.

Following the work of Macky, Taylor, and others, experimentalists have been able to determine more about the process of charged droplet breakup using an apparatus similar to the one used by Millikan in his famous experiment to measure the fundamental unit of charge.[11] In this device, two parallel plates are positioned in the form of a capacitor to create a vertical electric field. A charged droplet is introduced in this region between the plates, where by carefully adjusting the applied potential the drop can be suspended and studied. Various optical techniques were used to probe the size of the droplet, and the magnitude of the applied field was used to deduce the charge level. One of the earliest studies to make use of this device to quantify charge droplet breakup was conducted by Abbas and Latham in 1967.[12] In their study of water, aniline, and toluene they found that the droplet undergoes a series of disintegration events that share the following characteristics: (i) the disintegrations always occurred at the top of the droplet, where theoretical predictions show that electrical pressure is greatest (although the fields that were used to suspend the droplets were not reported, the device itself was able to provide a maximum of 600 V/cm); (ii) within experimental uncertainty, each disintegration occurred at the Rayleigh limit; and (iii) each disintegration was accompanied by a loss of about 25% of the charge residing on the droplet and about 25% of its mass.

Since Abbas and Latham's study, numerous others have been performed using a more sophisticated version of Millikan's oil-drop apparatus, the electrodynamic balance,[13] and employing modern laser-based optical particle sizing techniques. From these studies, the following picture of the droplet breakup process is emerging. With few exceptions, the mass loss for each fission event is quite low, in the range of 1 to 5%. There is also good agreement in the loss of charge from the fission event: 10 to 25%. Thus, charged droplets undergo an "uneven" fission process. Figure 4.2 illustrates the distinction between an uneven and an even fission event. In an uneven fission event, the precursor drop disrupts to form a large "parent" drop that retains most of the mass and about 75–85% of the original charge. The remainder of the mass and charge are distributed among one or more minute "offspring" droplets. In an even fission event, the drop breaks into two equally sized droplets each with

half the mass and charge. The distinction between the two events is important when considering the chemical properties of the progeny droplets: in an even fission event the ratio of the number of analyte ions to charge-paired electrolyte ions in the bulk solution of the droplet is not changed, whereas in an uneven fission event the small offspring droplets that form as a result of fission are enriched in analyte ions by a factor of about 7. This effect will be discussed in greater detail in Section 4.4.

Minor discrepancies remain in observations of the charge-to-mass ratio at which Rayleigh fissioning occurs. Table 4.1 presents results from selected experiments. The studies agree that the limit of charge as set forth by Lord Rayleigh represents an upper limit for droplet stability. The subject of some debate is whether the techniques used to study the phenomena of droplet breakup are somehow perturbing the droplet in such a way as to initiate a premature fission event. Two specific concerns have been mentioned. The first is that the fields applied in the electrodynamic balance, commonly 60 Hz and 2–6 kV, might create local regions of high electric field on the droplet surface that would lead to premature fission. The second concern applied to studies such as that by Gomez and Tang in which actual electrostatic sprays are studied with optical techniques.[14] Gomez and Tang report a relatively low instability limit of 70–80%, and show photographs of the droplets in the process of breakup that further support Macky's findings that Taylor cones form on the droplets themselves. The photographs also showed significant distortion in the droplets due to high relative velocities of the droplets in the surrounding gas. This is t to induce early onset of instability. Gomez and Tang observed that the site of the Taylor cone on the droplet was randomly positioned on the upper or lower side of the droplet, but that the offspring droplets themselves were always ejected sideways due to the space-charge field induced by the other drops in the spray.

Several investigators have presented mathematical models on the process of charged droplet breakup; two are particularly relevant. One of the gaps in the knowledge of the fission mechanism is in the description of the offspring droplets that are formed. Although investigators such as Gomez and Tang have been able to see these droplets in photographs of the fission process, their small size and short lifetime inhibits the

Table 4.1: Modern experimental observations of charged droplet breakup.

Investigators	Droplet Diameter Range Studied (μm)	Q for Fission (% Q_R)	Mass Loss Each Fission (%)	Charge Loss for Each Fission (%)
Davis and Bridges[7]	4–20	90	1–2	15–25
Gomez and Tang[14]	20–100	70–80	not measured	not measured
Richardson et al.[15]	not reported	96–108	1.5–2.5	10–20
Schweitzer and Hanson[16]	15–40	96–104	5	23

use of standard optical particle sizing techniques that are used for studying the precursor droplet. This leads to the following question: how many offspring droplets can be produced by the fission event, and what are their size and charge? More than one droplet must be formed since a single droplet would carry about 4–5 times the Rayleigh limit of charge. Roth and Kelly use an energy conservation model[17] to predict that 2–7 droplets would be formed from Rayleigh instability. The predicted progeny droplet diameters range from 14 to 20% of the parent droplet diameter. Although these predictions agree with the few available experimental observations, assumptions in the model are at odds with observations of the fission mechanism. The most significant discrepancy arises from the assumption that the progeny droplets are formed isotropically rather than from a greatly distorted droplet as Gomez and Macky have observed. The second example of a model for the process of droplet breakup is a study into the process of electrostatic spraying by Gáñan-Calvo and associates.[18] Scaling law arguments based on a charge transport model predicted the current and droplet size in an electrostatic spray. The results of the study showed a high dependence of both parameters on solution viscosity and conductivity.

To conclude this section on studies of charged droplet breakup and evaporation, some discussion on the latter issue is warranted. Two crucial issues have been ad-

dressed with regard to the process of droplet evaporation in electrostatic sprays: (i) whether electric charge on the surface of an evaporating liquid particle might alter the evaporation rate; and (ii) whether charge is conserved during evaporation. Numerous investigations have addressed these issues. Law's study is cited here, insofar as it answers both questions in a single experiment.[19] Law's conclusions are: (i) charge on an evaporating liquid droplet does not influence the evaporation rate; and (ii) charge is not dissipated by the process of evaporation.

4.4 Gas-phase Ion Production from Charged Droplets

Although Dole and associates are generally credited for first proposing the idea that evaporating charged droplets can be used as ion sources[20], observations of gas-phase ion production from charged droplets dates back to the 19th century.[2] In 1890, Elster and Geitel detected electric charge in the vicinity of waterfalls, and in 1892, Lenard found that when aqueous liquids were dispersed into sprays not only were there charged droplets but also a considerable amount of positive and negative gas-phase ions.

The history of electrospray ionization, with its emphasis on gas phase ions, departs from that of electrostatic atomization in 1968. At that time, Malcolm Dole and his colleagues first demonstrated the use of electrostatic sprays as a source of ions for mass spectrometry. Their interest in this electrospray was as a source of ions of synthetic polymers. Making use of the techniques developed by the aerosol scientists in the field of electrostatic spraying, Dole demonstrated the first practical device for generating gas-phase ions from solution that was quite similar in design to the modern electrospray system described in Chapter 3. They proposed a scheme for ion formation has now come to be called the charged residue model (CRM), also known as the single ion in droplet theory, which is depicted schematically in Figure 4.2. A highly charged droplet emitted from an electrospray source will evaporate until the

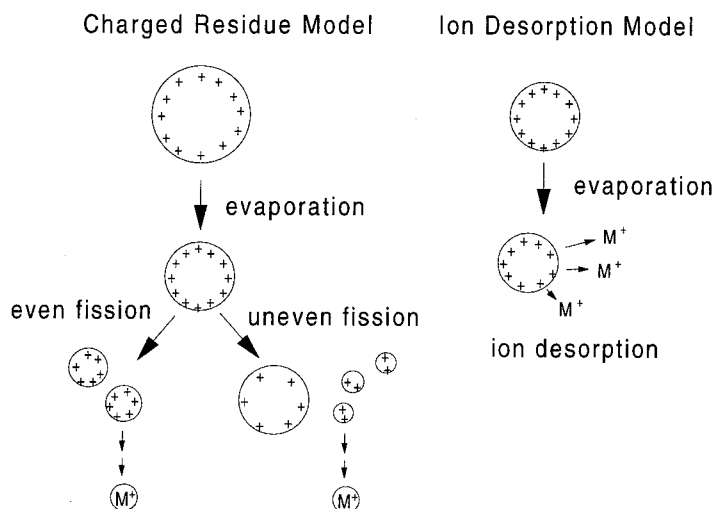


Figure 4.2: Schematic of Charged Residue Model (left) and Ion Desorption Model (right) for ion formation from highly charged droplets. Circles indicate presence of solvent molecules and “M” represents analyte.

Rayleigh limit is reached, at which point it will undergo a fission event. In CRM, the process of evaporation and Rayleigh fissioning repeats itself until all that remains is a collection of extremely small charged droplets that contain only one analyte molecule. When the solvent evaporates from that single residual molecule, it will retain some of the droplet’s charge and become a free gas-phase ion. Although Dole’s contribution to the development of electrospray is without question, the CRM has been found to apply only in solutions of certain large “macromolecules.”[21] A more universal model of the process of ion formation is thought to be the ion evaporation model of Iribarne and Thomson.

In spite of the pioneering work by Dole in 1968, the use of charged droplets to produce ions received little attention until 11 years later. At that time, Iribarne and Thomson were investigating the contention that cloud droplets may be an important source of gas-phase ions in the atmosphere. They proposed a model for ion formation that has come to be called the ion desorption model, or IDM. In IDM, which is shown schematically in Figure 4.2, the evaporation of a highly charged droplet could make

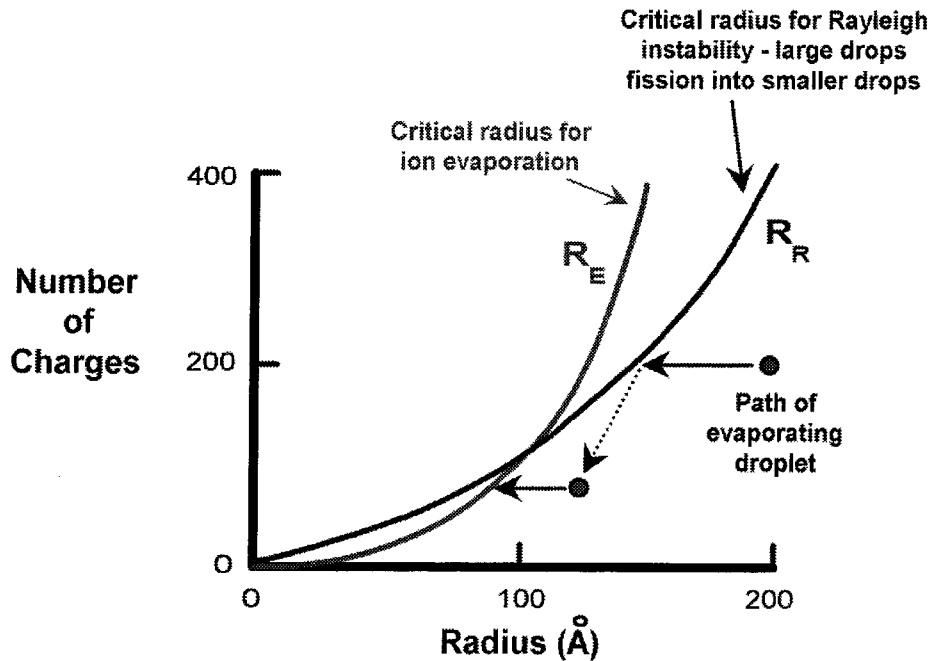


Figure 4.3: A plot of the size and charge of an evaporating offspring droplet in the IDM.

the electric field at the surface of the droplet sufficiently intense as to lift solute ions from the droplet and into the ambient gas. They suggest that this process probably occurs on offspring droplets of about 50–60 nm in diameter, each of which carry about 100 elementary charges. The path of one of these offspring droplets as it evaporates can be plotted as a function of its size and charge, as shown qualitatively in Figure 4.3. As the droplet evaporates, it will do so without loss of charge as discussed previously. During the process of evaporation the droplet reaches a diameter which corresponds to the Rayleigh limit for its charge, and will undergo a fission event which will result in a droplet with a reduced size and charge. The IDM states that there is will be a range of droplet size and charge where the curve that represents the critical radius for ion evaporation will cross that for the Rayleigh limit, as seen in Figure 4.3. The result is that the droplet will undergo no further fissioning, but will shed charge by the direct desorption of ions.

Iribarne and Thomson presented a model for this process based on transition state theory. In their model, evaporation of ions from a droplet is an activated process described by a rate equation:

$$\dot{N}_{iz} = AN_i S \exp\left(\frac{-\Delta G_{iz}}{RT}\right), \quad (4.4)$$

where \dot{N}_{iz} is the flux from the droplet surface of ions of analyte species i with z charges attached, N_i is concentration of species i in the bulk liquid of the droplet, S is the surface area, A is a proportionality constant that relates the bulk concentration N_i to its number density in the surface layer, and ΔG_{iz} is the difference in Gibbs free energy of an ion of species i with z charges when it is on the surface of the droplet to when it is in the gas and far enough away that solvation forces are negligible. This latter term is the most parameter in determining the tendency for a solution-phase ion to be directly desorbed into the gas. Iribarne and Thomson expressed this change in Gibbs free energy as:

$$\Delta G_{iz} = \Delta G_{iz}^{\circ} + zf\Delta r^*. \quad (4.5)$$

In the above expression the first term, ΔG_{iz}° , is the work required to remove an ion from the surface of the droplet. A good part of this term is the work in getting past the influence of solvent and for increasing the surface area of the droplet as the ion leaves. The second term is work done on the ion by electrostatic repulsion from the surface charge on the droplet. In this expression, f is the electrostatic force given by $f = Q/4\pi\epsilon_0 r^2$, z is the charge on the ion, and Δr^* is the location of the barrier that the ion must surmount in order to leave the droplet.

From Equations 4.4 and 4.5, one can make the following statements regarding the relationship between the abundance of gas phase ions, determined by \dot{N}_{iz} , and the various variables that are used to describe the electrospray system. For singly charged ions, $\dot{N}_{iz} \propto n_i$. This has been found to be the case for analyte concentrations ranging from 10^{-7} M up to about 10^{-4} M. Further increases in n_i do not further enrich the surface of the droplet with analyte ions. The effect of ΔG_{iz}° on ion formation is significant, as Equation 4.4 predicts that an increase in solvophobicity leads to more

efficient ion formation. This has been observed with increases in alkyl chain length in tetraalkyl ammonium halides.[22] One feature from Equation 4.4 is the relationship between the desorption rate and the ion charge state of the ion at the time just prior to its desorption, z . The equation indicates that the ion desorption rate depends exponentially on z . It is important to note the equation gives no information that would allow one to calculate the charge state, nor does it suggest that this charge state corresponds with that of the bulk solution. As it will be shown, there is, in fact, very little correspondence between the charge state of the desorbed ions and for that in the bulk solution. The process of charge attachment to the analyte is a competitive process whereby the electrostatic repulsion from the other charges on the ion, as well as gas-phase reactions that directly follow ion desorption.

The significance of Iribarne and Thomson's IDM cannot be understated, although its practical applications have been limited because many of the parameters in Equations 4.4 and 4.5 are extremely difficult to quantify. Some criticisms of the method with regard to the study of biomolecules were reviewed by Mann.[23] The first is that the model assumes the immediate development of an image charge on the surface of the droplet for calculating the electrostatic contribution to the free enthalpy of solvation for the ion. The transition state put forth by Iribarne and Thomson is a late transition state, resembling more the final products by mathematical necessity. However, the transition occurs earlier when the ion emerges from the droplet surface. It has also been argued that for cases of the desorption of large compounds the fields needed to cause the ions to leave the droplets cannot be attained. The hydrodynamic instabilities caused by a single ion leaving the droplet would prompt Rayleigh fissioning before suitable field intensity could be achieved. Also, the droplet size required to obtain the desired field strength is often calculated to be smaller than that of the ion itself.

In spite of such criticisms, and because of the interest in extending the main theme of Iribarne and Thomson's formulation to a more accurate model of the process of ion desorption, most subsequent studies into the mechanism of ion formation have assumed some form of the IDM. For example, the assertion that gas phase ion in-

tensities detected by a mass spectrometer are highly dependent upon the chemical properties of the analyte ions should be immediately apparent to anyone who has reviewed the study of Hiraoka.[24] In this study, a solution containing a diverse selection of analyte ions was electrosprayed into an apparatus in which the capillary inlet to a mass spectrometer could be traversed in order to obtain the axial and radial distribution of ions in the electrostatic spray plume. Ions that are easily desorbed from solution were observed close to the electrospray needle, and under the influence of the space-charge field these ions quickly diffused to the outside of the spray cone. Conversely, ions with lower desorption efficiencies were more likely to be found in the central region of the spray plume. In practical terms, Hiraoka's study shows that for a complex solution of analyte ions the relative intensities of the ion peaks in a mass spectrum will be dependent upon the position of the capillary inlet with respect to the electrospray needle – a situation that emphasizes the need for a quantitative understanding of the process of ion formation.

Many studies have been performed to attempt to obtain a quantitative understanding of the process of ion formation in electrospray. The remainder of this section will be devoted to a review of some of those studies. The total number of investigations into the mechanism of ion formation is far greater than those described below; the attempt here is to present some representative studies in the most important aspects of ion formation. These include two models for gas-phase ion abundance based on solvent and analyte properties: one qualitative model developed by Tang and Kebarle and another by Fenn that addresses the observation of multiply charged ions from electrospray sources. A number of experiments will then be described in which the electric field required for ion desorption is measured. The section will end with some studies of the dependence of charge state on ion intensity, a representation of a large number of investigations devoted to the application of electrospray to the study of biological compounds.

4.4.1 Modeling Studies

Tang and Kebarle[25] have examined the dependence of analyte ion intensity may depend on the concentration of the analyte ion in solution. They point out that solvents usually contain one or more electrolytes as impurities in addition to the analyte ion under study. For example, reagent grade methanol contains impurities of mostly ammonium and sodium salts at a total level of approximately 10^{-5} M. At such concentrations, these electrolyte ions compete with analyte ions in the formation of surface charges on the droplet. These surface charges are the precursors for ion formation in the IDM. Tang and Kebarle predict the gas-phase ion current, $I(A^+, g)$, for a certain analyte ion A^+ to be

$$I(A^+, g) = \frac{k_A[A^+]}{k_E[E^+] + k_A[A^+]} fI, \quad (4.6)$$

where I is the total ion current produced by the electrospray, f is a proportionality constant that represents the fraction of droplet charge that is converted into gas phase ions and is related to the electric field strength on the droplet surface, and k_A and k_E are rate constants that express the rate of transfer of ions from the droplet to the gas phase. This model has been quite successful in predicting some aspects of the behavior of electrosprayed solutions. For example, at low analyte concentrations such that $[E^+] \gg [A^+]$, the relation predicts a linear relationship between the gas phase ion current and the analyte concentration in solution. As mentioned earlier, experimental observations have confirmed this linear relationship for analyte concentrations up to about 10^{-5} M. Considering that reagent grade solvents contain about the same concentration of electrolyte impurities, Equation 4.6 might agree with this observation. This linear relation is required for quantitative analysis of a solution by mass spectrometry. Thus, one general conclusion that can be drawn from this is that low concentrations of analyte, below about 10^{-5} M, are preferable.

In addition, a predictive relationship between the total ion current, I , and the conductivity of the solution is presented, based on Tang and Kebarle's observations

and those of others:

$$I = H\lambda_m^{\circ n} C^n, \quad n \approx 0.2 - -0.4, \quad (4.7)$$

where λ_m° is the molar conductivity of the solution at infinite dilution of the electrolyte, whose concentration is given by C , and H is a proportionality factor. Equation 4.7 is valid for strong electrolytes (thus fully dissociated in solution) at low concentrations such that ion pairing is minimized. It demonstrates that the gas-phase ion current is only weakly dependent upon electrolyte concentration. Combining the results of Equations 4.6 and 4.7,

$$I(A^+, g) = \frac{k_A[A^+]}{k_E[E^+] + k_A[A^+]} f H \lambda_m^{\circ n} ([E^+] + [A^+])^n. \quad (4.8)$$

For high concentrations of $A^+[A^+] \gg [E^+]$, Equation 4.8 reduces to

$$I(A^+, g) = f H \lambda_m^{\circ n} [A^+], \quad n \approx 0.2 - 0.4. \quad (4.9)$$

Tang and Kebarle's derivation predicts a slower, nonlinear increase in gas-phase analyte ion current with solution analyte ion concentration at concentrations higher than about 10^{-4} M (again assuming electrolyte present in solution at about 10^{-5} M). The source of this saturation effect is the slow increase of I with electrolyte concentration that is shown in Equation 4.7. In actual experiments this analyte ion intensity is observed to actually decrease at concentrations above 10^{-3} M. This observation is not predicted by Equation 4.7. It is expected that the downward experimental trend of $I(A^+, g)$ with increasing analyte concentrations is caused by the decrease of the fraction of surface ions that become gas phase ions, f . Recall that f increases due to surface fields; decreases in this parameter could be induced by incomplete droplet evaporation. Adding credence to this is the observation that an increase in electrolyte concentration at constant flow rate leads to a decrease in the radius of the nascent droplets at low concentrations, followed at higher concentrations by an increase in radius.[26]

Application of Tang and Kebarle's relations requires values for several parameters,

the most important of which are the coefficients, k . An important observation from Equation 4.6 is that the gas-phase intensity does not depend upon the individual values of k_A and k_E , but rather the ratio k_A/k_E . This ratio can be determined under conditions where $[A^+]=[E^+]$, again using Equation 4.6. The authors tabulated some of these ratios.[25] The practical implications of their result are that solvents that contain electrolytes with a low evaporation rate coefficient, k_E , should be used whenever possible. Many other implications of their model, as well as comparisons with experimental observations, are available in various papers by Kebarle and co-workers.[27, 25]

A model developed by Enke[28] uses an equilibrium approach based on competition among ions in the solution for a limited number of charge sites on the surface of the droplets. The main factor that affects the relationship between solution- and gas-phase ion concentration in Enke's model is the partitioning of ions between two "phases": the interior, solvated, ion-paired phase and the surface excess charge phase. As a result of this proposition, an equation identical to Equation 4.6 was derived for a two-electrolyte system. For a three-electrolyte system Enke was able to reproduce the experimentally-observed decrease in gas-phase ion abundance at high solution concentrations, a result not achieved with Kebarle's model. From the success of this equilibrium model, Enke concludes that the diffusive processes required to establish equilibrium between the two phases are fast enough to do so. This leads to the practical recommendation that analyte concentration in solution should be well below the total concentration of all excess charge (that is, the sum of all analyte ion concentrations compared to that of the electrolyte).

Fenn has presented a more qualitative model of ion formation.[22] Fenn's model addresses the issue of multiply charged ion formation in electrospray ionization. As mentioned previously, one of the features that makes electrospray ionization unique among ion sources is its ability to create multiply-charged gas phase ions. For most compounds of biological interest, such as proteins, charge is provided in the form of protons bound to basic sites. Fenn argues that the source of protons is excess charge on the surface of the evaporating droplet. Thus, the density of charges of

a protein cannot exceed that on the droplet surface. Therefore, the charge state of the protein is determined by the number of surface charges that it can span on the surface of the droplet. The protein near the droplet surface can be seen as “casting a shadow” (what Fenn calls the molecule’s “sphere of influence”) on the surface of the droplet. All surface charge lying within that shadow are available for attachment to the analyte molecule.

Fenn’s picture of ion desorption leads to the following conclusions. First, the ions that leave the droplet at an early stage of droplet evaporation depart at a slower rate and with fewer charges than those that leave at later stages. A slowly evaporating solvent will thus lead to a greater proportion of low charge states. In addition, the geometry of the analyte plays an important role in determining its likelihood of desorption. A linear molecule lying on the surface of a droplet will have most of its surface covered by excess charges from the droplet, whereas a spherical molecule will have a lower proportion and will thus desorb relatively later in the process of droplet evaporation when surface fields are sufficient to pull the ion from the droplet. Fenn estimated the strength of the electric field required to cause the ion to leave the charged droplet by assuming that the distance between charges on an evaporated ion cannot be less than the distance between charges on the droplet surface when the ion is formed. With this assumption, and by calculating the linear charge density of an emitted chain polymer ion, he determined this field to be 2.7, 1.6, and 1.5 V/nm for oligomer ions having respectively 2, 3, and 6 charges.

4.4.2 Experimental Studies

In addition to Fenn’s theoretical determination of the droplet surface field during ion desorption, several experimental investigations have been undertaken to determine this. Two are mentioned here, both based on the measurement of the mobility of highly charged droplets at reduced pressures. At pressures of around 2 torr, a charged droplet of the size that is normally considered to lead to ion desorption (below 40 nm) has a diameter that is less than the mean free path of the surrounding gas. In this free

molecular regime, the mobility of the droplet is directly proportional to the electric field on the surface of the droplet. Katta and co-workers[29] used a technique similar to electrospray, called “thermospray,” along with an ion mobility spectrometer to determine this surface field. To make this measurement, they assumed that the ions are directly desorbed from the droplets via the IDM. Therefore the maximum surface fields that they encountered for the offspring droplets was assumed to be the field at which ion desorption occurs. Their result is a desorption field that ranges from 1.5 to 2.7 V/nm. In their experiment, they were unable to observe ions emanating from these droplets and thus could not prove that these fields were indeed sufficient for ion formation.

The second study by Loscertales and Fernández de la Mora[30] extended the work of Katta without the need for the assumptions mentioned above. They used a more sensitive form of the ion mobility spectrometer, the differential mobility analyzer (DMA), to measure the mobility of charged particles and ions. Since the DMA is not generally suited for analyzing volatile droplets, they performed their mobility analysis on solid particle residues that resulted from the complete evaporation of the electrosprayed solution. The validity of their measurement rests on the assumption that ion desorption abruptly stops when the last of the solvent evaporates. Thus, the field at the surface of the residual particle remains the same as it was when it was a solution drop shedding ions (with a small correction to account for a change in the electrical conductivity as the droplet becomes a solid particle). They argue, similar to Katta, that in the IDM the rate of ion desorption from the small offspring droplets will adjust itself to maintain the surface potential at a constant value. They support this argument with the observation that, for a variety of conditions involving small, monovalent ions and solutions with varied conductivity, the electric field on the surface of the residue particles was found to be independent of particle diameter. With the ability to observe ion and droplet current (albeit without the ability to irrefutably discriminate between the two: the mobility spectra for ions are identified as such based upon the judgement that they are Gaussian shaped with an appropriate width), they were able to show that ions directly desorb from the droplets. This

provides experimental evidence in support of the IDM. As a result of their analysis, a correction was made to the expression for ΔG_{iz} given in Equation 4.5, which borrows from the image potential model originally developed to describe field ejection of ions from a solid metal lattice. The correction is

$$\Delta G_{iz}^{IPM} = \Delta G_{iz}^{IDM} - eEd_o, \quad (4.10)$$

where d_o represents the diameter of the evaporating ion. Their estimation of the required field strength for ion desorption ranged from 0.9 V/nm for the more solvophobic compounds to a high value of 1.9 V/nm for Li^+ in ethylene glycol. The field strength mostly depends upon the ion-solvent pair, and thus was independent of the liquid conductivity and the nature of the counter-ion in solution.

As mentioned numerous times previously, the distribution of charges on the resulting analyte ions a very distinctive feature of electrospray. One area where this is closely studied is in the field of biochemistry, where it is proposed that the charge state can lead to information as to the conformation of proteins in solution.[31] Generally, an unfolded protein shows higher charge states in its electrospray mass spectrum than the same protein in its native state. Since this may provide important insights as to the structural aspects of proteins in solutions, it is not surprising to find numerous studies devoted to understanding the extent to which the gas phase charge distribution reflects that of the solution phase. As the model by Fenn suggests, this correspondence is not straightforward and may be influenced by the solvophobicity of the analyte ion and its geometry.

Thomson has pointed to the dangers in associating the charge state as recorded in a mass spectrometer with that in solution.[32] In a recent investigation of electrosprayed protein ions, he presents evidence that shows the dependence of the recorded charge state distribution on the potential difference between neighboring electrostatic lens elements in the high-pressure region of the electrospray ion source. It is believed that collisions between partially desolvated gas phase analyte ions and neutral solvent molecules might cause the loss of a proton or an electron in the analyte. Thomson's

study however provides evidence to the contrary. The effect of high collision energies in this region, he argues, is to shift the analyte towards lower charge state due to better declustering of lower charge state ions and due to higher fragmentation of higher charge state ions. Charge loss due to collisional loss of a proton or electron does not occur.

Thomson also found that this region of the electrospray ion source where the ions are emerging from the droplet can consist of a mixture of monomers clustered with solvent, plus dimers and possibly higher multimers. Such findings are supported by the recent results by Lee and co-workers using an electrospray source that has been designed to impart exceptionally low internal energy to the analyte ions.[33] These weak collision energies make it possible to create clusters of multi-protonated proteins with hundreds of solvent molecules attached. It is unclear however if these clusters are originating from the droplet during desorption or whether the bare ion is formed and then later achieves thermodynamic equilibrium with the vapor concentration in the source. In the original presentation of the IDM, Iribarne and Thomson assume that the ions that desorb from the droplet are significantly solvated. As Kebarle and Tang point out,[27] the transfer of $\text{Na}^+(\text{H}_2\text{O})_7$ from solution to gas phase requires about 56 kcal/mol, and is energetically preferred over the bare ion Na^+ , which has a Gibbs free energy of solvation of about 98 kcal/mol. Studies such as these suggest that there are important processes that take place after the ion is released from the droplet. These processes can be as important in dictating the final gas phase ion distribution as the chemical processes in the droplet. One cannot rule out the possibility that highly solvated ions could be emerging directly from the droplet.

Other studies collaborate Thomson's results showing poor correspondence between gas and solution phase ion intensities. Meunier and associates found for the protein apomyoglobin a correspondence between the phases only at a pH of 4.2.[34] They propose that the discrepancies can mainly be explained by the preferential fragmentation of highly charged ions in the source and by the variation of pH in the droplet as it evaporates and undergoes Rayleigh fissioning.

One interesting observation made by numerous investigators and reviewed by Man-

soori and associates[35] is that, under certain conditions, intense $[M+H]^+$ ions are observed electrosprayed from strongly basic solutions and $[M-H]^-$ ions from strongly acidic solutions. Their study confirmed the results of others in that the yields of $[M+H]^+$ and $[M-H]^-$ ions of amino acids vary only slightly in the pH range 3–11, despite orders of magnitude changes in the calculated bulk phase concentrations. The question of the mechanism for “wrong-way-round” ionization is still unclear however. Based upon the theories and observations presented above, it seems likely that the process is controlled by reactions of ions in three different environments: in the bulk solution of the charged droplet, on the surface of the droplet, and in the gas phase.

4.5 Review of Unresolved Issues in Electrostatic Spraying and Electrospray Ionization

To conclude this chapter, a summary of some of the unresolved issues previously mentioned is presented below.

- Although numerous studies have been presented in support of the Rayleigh limit of charge, an experimental technique that can study this process under low external field conditions would further bolster our current understanding of this process.
- In electrostatic sprays, information regarding the nature of offspring droplets is needed. Specifically, the number of droplets produced by a single fission event as well as the size and charge level of these droplets is needed.
- The kinetic energy imparted in the offspring droplets, if measured, can supply valuable information as to the mechanism and energetics of the droplet fission process.
- In Tang and Kebarle’s expression for the relationship between gas phase and solution phase ion concentrations (Equation 4.6), and similarly with Enke’s derivation of a similar expression, a number of parameters were identified as

crucial for achieving a quantitative understanding of the process. These are the so-called “ k coefficient” for each analyte compound, and the factor f , which describes the physical process of field desorption. An especially important area of application is in the characterization of multiple analyte solutions, where a competitive process for surface sites is thought to occur. Characterization of these parameters for multicomponent (two or more analytes with an electrolyte) is needed.

- The evolution of droplet pH during the process of evaporation and fission, if measured, can provide important insights into the poorly understood role of chemical transformations within the evaporating droplet.
- In Fenn’s model and also in observations of protein charge state by Meunier, a slowly evaporating solvent is thought to lead to ions of low charge state. It is thought that these ions depart from the droplet at an earlier time, thus as Hiraoka points out there could be a very different spatial distribution of low charge state ions in the electrospray plume. A more complete characterization of this process is needed.
- It is unclear whether the formation of clusters consisting of one or two analyte and several solvent molecules occurs directly as a result of the desorption process or whether a bare ion emerges from the droplet and picks up solvent molecules through gas phase interactions. Further study is needed to provide a clearer picture of the process of ion desorption.
- The study by Loscertales and Fernández de la Mora makes many assumptions regarding the appropriateness of using solid residue particles in describing the properties of the offspring droplets. This was necessitated by their use of the DMA for characterizing particle mobility. If one can achieve similar sensitivity while still allowing for the study of the liquid phase offspring droplets, one can test many of the conclusions of their study while making more accurate measurements of such parameters as the surface field and the effective Gibbs

free energy of ion evaporation for various compounds.

Bibliography

- [1] D.C. Blanchard. Electrically charged drops from bubbles in sea water and their meteorological significance. *J. Meteorology*, 15:383–396, 1958.
- [2] Adrian G. Bailey. *Electrostatic Spraying of Liquids*. Electrostatics and electrostatic applications. John Wiley and Sons, Ltd., Somerset, 1988.
- [3] J.V. Iribarne and B.J. Mason. Electrification accompanying bursting of bubbles in water and aqueous solutions. *Trans. Faraday Soc.*, 63:2234–2245, 1967.
- [4] R.J. Pfeifer and C.D. Hendricks. *AIAA J.*, 6:496, 1968.
- [5] A.T. Blades, M.G. Ikonomou, and P. Kebarle. Mechanism of electrospray mass-spectrometry - electrospray as an electrolysis cell. *Anal. Chem.*, 63(19):2109–2114, 1991.
- [6] T. Takamatsu, Y. Hashimoto, M. Yamaguchi, and T. Katayama. Theoretical and experimental studies of charged droplet formation in a uniform electric field. *J. Chem. Eng. Japan*, 14:178–182, 1981.
- [7] E.J. Davis and M.A. Bridges. The Rayleigh limit of charge revisited: light scattering from exploding droplets. *J. Aerosol Sci.*, 25:1179–1199, 1994.
- [8] Lord Rayleigh. On the equilibrium of liquid conducting masses charged with electricity. *Proc. Roy. Soc.*, 14:184–86, 1882.
- [9] W.A. Macky. Some investigations on the deformation and breaking of water drops in strong electric fields. *Proc. Roy. Soc. A*, 133:565–586, 1931.
- [10] G.I. Taylor. Disintegration of water drops in an electric field. *Proc. Roy. Soc. A*, 280:383–397, 1964.

- [11] R.A. Millikan. *Electrons (+ and -), Protons, Photons, Neutrons and Cosmic Rays*. Cambridge Univ. Press, 1935.
- [12] M.A. Abbas and J. Latham. The instability of evaporating charged drops. *J. Fluid Mech.*, 30:663–670, 1967.
- [13] E. James Davis. Microchemical engineering: the physics and chemistry of the microparticle. In Thomas B. Drew, editor, *Advances in Chemical Engineering*, volume 18. Academic Press, Inc., New York, 1992.
- [14] A. Gomez and K. Tang. Charge and fission of droplets in electrostatic sprays. *Phys. Fluids*, 6:404–414, 1993.
- [15] C.B. Richardson, A.L. Pigg, and R.L. Hightower. On the stability limit of charged droplets. *Proc. Roy. Soc. A*, 422(1863):319–328, 1989.
- [16] J.W. Schweitzer and D.N. Hanson. Stability limit of charged drops. *J. Colloid Interface Sci.*, 35:417–423, 1970.
- [17] D.G. Roth and A.J. Kelly. Analysis of the disruption of evaporating charged droplets. *IEEE Trans. Ind. Appl.*, IA-19:771–775, 1983.
- [18] A.M. Gañán Calvo, J. Dávila, and A. Barrero. Current and droplet size in the electrospraying of liquids. Scaling laws. *J. Aerosol Sci.*, 28:249–275, 1997.
- [19] S.E. Law. Charge and mass flux in the radial electric field of an evaporating charged water droplet: an experimental analysis. *IEEE Trans. Ind. Appl.*, 25:1081–1087, 1989.
- [20] M. Dole, L.L. Mach, R.L. Hines, R.C. Mobley, L.P. Ferguson, and M.B. Alice. Molecular beams of macroions. *J. Chem. Phys.*, 49:2240, 1968.
- [21] T. Nohmi and J.B. Fenn. Electrospray mass-spectrometry of poly(ethylene glycols) with molecular-weights up to 5 million. *J. Am. Chem. Soc.*, 114:3245, 1992.

- [22] J.B. Fenn. Ion formation from charged droplets: roles of geometry, energy, and time. *J. Am. Soc. Mass Spectrom.*, 4:524–535, 1993.
- [23] M. Mann. Electrospray: its potential and limitations as an ionization method for biomolecules. *Org. Mass Spectrom.*, 25:575–587, 1990.
- [24] K. Hiraoka. How are ions formed from electrosprayed charged liquid droplets? *Rapid Commun. Mass Sp.*, 6:463–468, 1992.
- [25] L. Tang and P. Kebarle. Effect of the conductivity of the electrosprayed solution on the electrospray current. factors determining analyte sensitivity in electrospray mass spectrometry. *Anal. Chem.*, 63:2709–2715, 1991.
- [26] I. Hayati, A.I. Bailey, and T.F. Tadros. Investigations into the mechanisms of electrohydrodynamic spraying of liquids. 1. Effect of electric-field and the environment on pendant drops and factors affecting the formation of stable jets and atomization. *J. Colloid Interface Science*, 117:222, 1987.
- [27] P. Kebarle and L. Tang. From ions in solution to ions in the gas phase: The mechanism of electrospray mass spectrometry. *Anal. Chem.*, 65:972A, 1993.
- [28] C.G. Enke. A predictive model for matrix and analyte effects in electrospray ionization of singly-charged ionic analytes. *Anal. Chem.*, 69:4885–4893, 1997.
- [29] V. Katta, A.L. Rockwood, and M.L. Vestal. Field limit for ion evaporation from charged thermospray droplets. *Int. J. Mass Spectrom.*, 103:129–148, 1991.
- [30] I.G. Loscertales and J. Fernández de la Mora. Experiments on the kinetics of field evaporation of small ions from droplets. *J. Chem. Phys.*, 103:5041–60, 1995.
- [31] U.A. Mirza and B.T. Chait. Do proteins denature during droplet evolution in electrospray ionization? *Int. J. Mass Spectrom.*, 162:173–181, 1997.
- [32] B.A. Thomson. Declustering and fragmentation of protein ions from an electrospray ion source. *J. Am. Soc. Mass Spectrom.*, 8:1053–1058, 1997.

- [33] S.W. Lee, P. Freivogel, T. Schindler, and J.L. Beauchamp. Freeze-dried biomolecules: FT-ICR studies of the specific solvation of functional groups and clathrate formation observed by the slow evaporation of water from hydrated peptides and model compounds in the gas phase. *J. Am. Chem. Soc.*, 120(45):11758–11765, 1998.
- [34] C.M. Meunier, M. Jamin, and E. De Pauw. On the origin of the abundance distribution of apomyoglobin multiply charged ions in electrospray mass spectrometry. *Rapid Comm. Mass Spectrom.*, 12:239–245, 1998.
- [35] B.A. Mansoori, D.A. Volmer, and R.K. Boyd. ‘Wrong-way-round’ electrospray ionization of amino acids. *Rapid Comm. Mass Spectrom.*, 11:1120–1130, 1997.

Chapter 5 Mobility Measurements of Charged Droplets and Ions

5.1 Introduction

The most important property of an electrostatic spray, from which all its unique features can be attributed, is that it consists entirely of charged droplets that are very near the Rayleigh limit. Each individual droplet in the spray is indistinguishable from the other, and can be traced backward in time through a series of fission events to the original droplets that were formed from the Taylor cone at the spray orifice. Thus, it seems logical that a fundamental study of the mechanism by which ions are produced from electrostatic sprays should focus on the evolution of the first droplets created by the Taylor cone: the rate at which they break apart, the droplets that result from the breakup, the eventual fate of these droplets, and the formation of gas phase ions at some point during the process. This is the approach taken for these investigations. To obtain information on how and when these processes occur requires a technique that can both spatially and temporally resolve the important processes that occur in electrostatic sprays. One way of accomplishing this is to allow the charged droplet to evaporate in the presence of a uniform electric field. As the following chapter will demonstrate, ions and droplets react in different ways to the electric field according to a size- and charge-dependent property called “mobility.” Instruments have been built for the characterization of ions and charged particles based on mobility. For the study of ions, the instrument is called an Ion Mobility Spectrometer (IMS).[1] For the study of charged particles, instruments such as the scanning mobility particle sizer are commonly used.[2] In the discussion that follows, the term “drift cell” will be used when referring to either device, as it best describes the fundamental process that is common to both.

The objective of this chapter is to set forth the theoretical framework for studying electrostatic sprays, through the study of individual charged droplets, using a mobility-based technique. The chapter starts with a review of mobility measurements using drift cells, and the derivation of the mobility of gas phase ions and charged droplets. The results of these calculations are then combined to demonstrate the conditions under which ions and charged droplets can be separated and identified by their mobility. Next, the time evolution of the electrostatic spray process will be considered by investigating evaporation dynamics and the temporal separation of ions from droplets, or offspring droplets from parent droplet, at some axial location in a drift cell. This will serve as the foundation for the long-term objectives of this study.

For the analysis in this chapter, droplets consisting of single, pure solvents with a low concentration of electrolyte will be considered. The choice of single component droplets is made to aid in the theoretical analysis. As the present chapter will demonstrate, for many reasons highly volatile, low surface tension, organic liquids like methanol are better solvents for electrostatic spraying than water. Water, however, has certain advantages over organic solvents such as alcohols, the most important being a higher dielectric constant (relative permittivity of water of 78.38 at 298 K versus 32.66 for methanol) and high solubility, particularly for biological molecules. Because of this, it is most common for researchers using electrospray sources to use a solvent consisting of mixture of water and an organic solvent such as methanol or acetonitrile. Recognizing this, the theoretical analysis presented below will be performed for both water and methanol with the objective being to define limiting behavior for the various phenomena studied. Trends that are described below with pure solvents are expected to be repeated with multi-component solvents.[3]

5.2 A Mobility-Based Technique for Investigating Dynamic Processes Involving Ions and Droplets

In this investigation, there will be repeated use of mobility measurements for studying the dynamics of charged droplet evaporation and ion evaporation. It should be noted that the electrical mobility is implied whenever the term “mobility” is used. A related term, the “mechanical mobility,” is defined as the constant of proportionality between the particle drift velocity and the sum of all external forces. The current section will review some important properties of the drift cell. As presented above, a drift cell is a device in which charged species are made to drift through a buffer gas, usually at atmospheric pressure, under the influence of a constant electric field (Figure 5.1). Within the drift chamber, ions or charged particles will quickly reach a steady-state velocity, v_d , that can be related to the magnitude of the electric field, E , through a constant of proportionality called the electrical mobility, B :

$$v_d = BE. \tag{5.1}$$

The mobility is related to the charge and cross-sectional area of the particle or ion, and will be explored in greater detail in Sections 5.2.1 and 5.2.2. In time, species with differing mobilities will separate longitudinally in the chamber. This separation of ions or charged particles is observed at the outlet of the drift chamber as a series of ion or particle packets that arrive at discrete times. Drift cells are thus useful for separating and identifying ions based on their molecular size (or particles based on their cross-sectional area). Among its most unique features includes its simplicity of design (all that is needed is a series of resistively-coupled rings to create a constant electric field gradient), and the ability to identify molecular species at atmospheric pressure based on their mobility. A brief mention will be made about the basic components of a typical drift cell, as they will be frequently referenced to below and

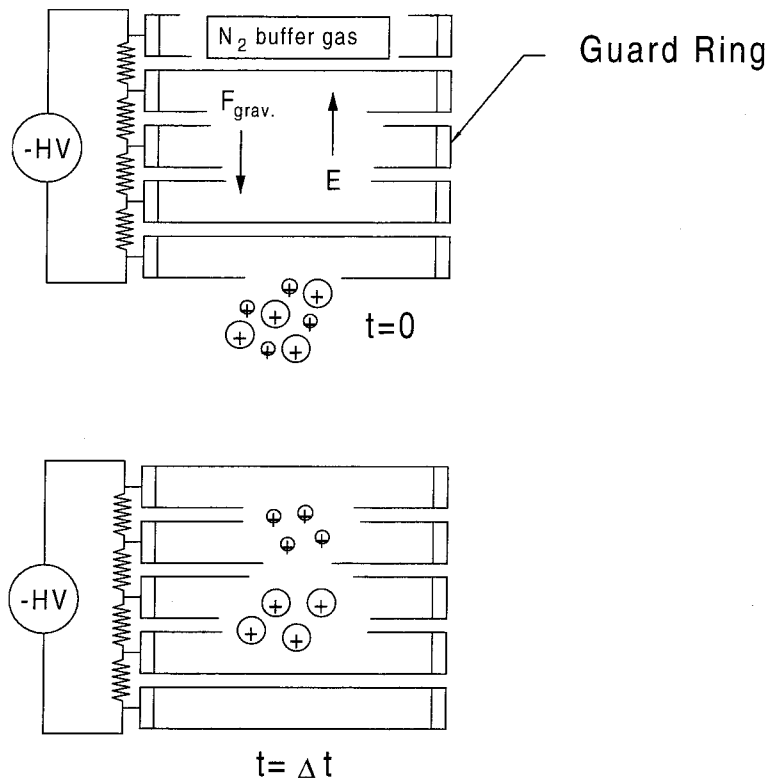


Figure 5.1: Principle of operation for mobility measurements using a drift cell. Ions (or charged droplets) drift through a buffer gas under the influence of an electric field and gravity, quickly achieving steady state and separating into packets based on their size and charge.

in subsequent chapters. Figure 5.1 shows a typical representation of the instrument. The electric field is usually created by a series of stacked metal rings (called “guard rings” in IMS instruments), that are resistively coupled. A high voltage potential is applied to the top and bottom ring. As mentioned in the previous paragraph, the buffer gas is present in the cell, usually at pressures ranging from a few torr to just above one atmosphere. This gas is usually flowed through the cell in a direction counter to the flow of the charged species to assure that the chemical properties are well characterized.

5.2.1 The Mobility of a Charged Droplet

The mobility of a charged droplet in a drift cell is calculated using a force balance and Newton’s Second Law: $\sum F_{ext} = m\dot{v}$, where F_{ext} are the external forces acting on the droplet, m is the droplet mass, and \dot{v} the droplet acceleration. In the following analysis the buffer gas is assumed static and the electric field is in the direction opposite to that of gravity, as shown in Figure 5.1. The forces acting on the droplet also include aerodynamic drag, which is itself dependent on the droplet velocity. The result of the force balance, and subsequent integration,[4] is that at any instant in time a liquid droplet in a constant electric field will reach a steady state drift velocity, v_d , given by:

$$v_d = \left[\frac{C_c(qE - m_p g)}{\frac{\pi}{8} C_D \rho_p D_p^2} \right]^{\frac{1}{2}}. \quad (5.2)$$

Here, q is the droplet charge, E is the electric field strength, m_p , ρ_p and D_p are the mass, density and diameter of the droplet, respectively, C_c is the slip correction factor, and C_D is the drag coefficient. The drag coefficient is itself a function of droplet velocity, so this equation must be solved iteratively. With help from Equation 5.2 we can deduce the lower charge limit for a droplet in the drift chamber. The minimum amount of charge for a droplet is that amount for which the electrostatic force just balances that of gravity, $qE = m_p g$. This is shown in Figure 5.2 for both methanol and water, along with the maximum amount of charge as defined by the Rayleigh instability limit, Equation 4.2 (as there is no limit to the maximum charge level

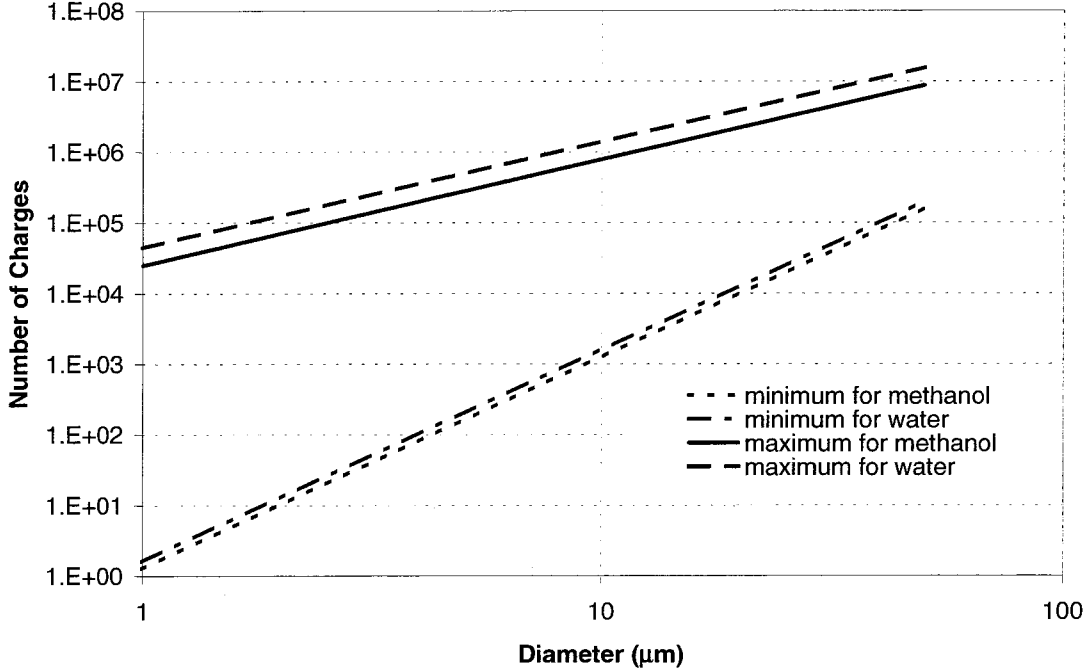


Figure 5.2: Range of charging on droplets of water and methanol for $E=200$ V/cm and a static buffer gas of N_2 at 1 atm. Maximum allowed charge corresponds to Rayleigh limit, minimum allowed charge is for electrostatic forces to just exceed gravitation.

imposed by the drift cell itself). From the figure we can see that droplets which range in charge level by over four orders of magnitude can be analyzed with this technique. The low density and surface tension of methanol compared to water equates to lower charge levels supported in the drift chamber.

The mobility for a charged droplet, from Equation 5.1 is just v_d/E :

$$B_{drop} = \left[\frac{C_c(qE - m_p g)}{\frac{\pi}{8} C_D \rho_p D_p^2 E^2} \right]^{\frac{1}{2}}. \quad (5.3)$$

This result is plotted in Figure 5.3 as a function of droplet diameter. For the purpose of illustration, the droplets are assumed to have 10^5 elementary charges on their surface, and the electric field is set at 200 V/cm. For smaller droplets the electrostatic force, qE , will dominate over the force of gravity and they will acquire higher steady state velocities compared to larger droplets under identical conditions. Another way

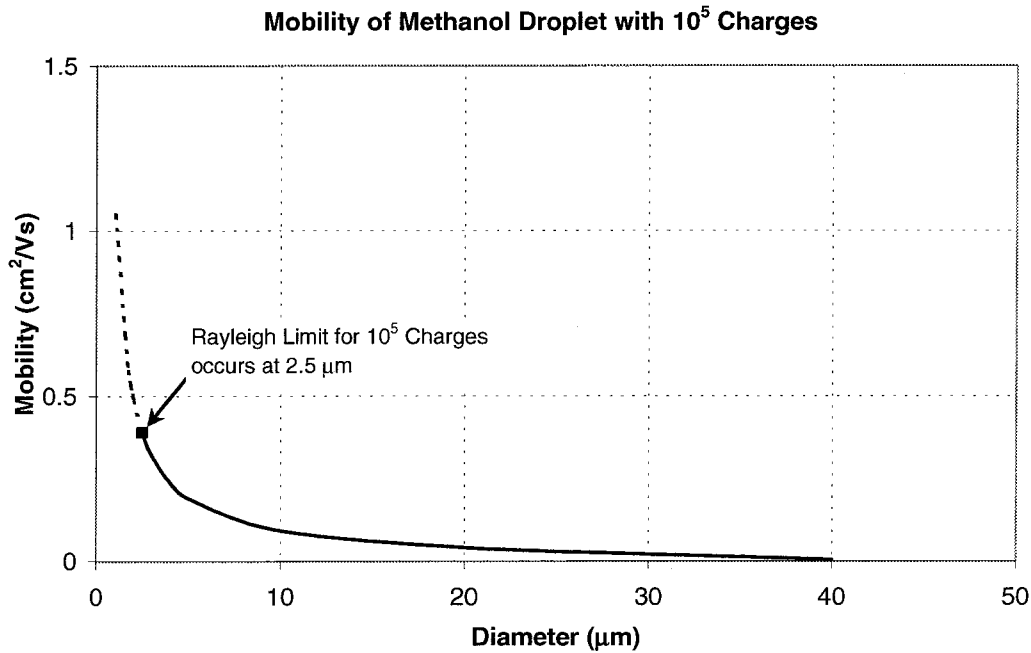


Figure 5.3: Mobility of an evaporating methanol droplet in a drift cell, under the following conditions: $E=200$ V/cm, $q=10^5$ elementary charges, static N_2 buffer gas at 1 atm. Diameter at which Rayleigh instability occurs for methanol and 10^5 charges is indicated.

of interpreting Figure 5.3 is that a droplet within a drift cell that is initially $40 \mu\text{m}$ in diameter will accelerate as it evaporates according to the displayed curve, since droplet charge is conserved during the evaporation process as was pointed out in Section 4.3. The dynamics of the evaporation process will be presented in greater detail in Section 5.3.

5.2.2 The Mobility of a Gas Phase Ion

The calculation of the mobility of an ion in a constant electric field is presented next. The analysis is based on a momentum-transfer analysis,[5] which calculates mobility by applying conservation of momentum and energy to the ion-neutral collisions in the cell. Its most important assumption is the so-called low-field approximation, in which the electric field is so weak that the ions are close to being in thermal equilibrium

Table 5.1: Mobilities of Ions

Ion	Molecular Weight	Average Charge	Hard Sphere Collision Cross-Section (\AA^2)	Reduced Mobility (cm^2/Vs)
Cytochrome-C	12000	+10	2700	0.74
Bradykinin	1060	+2	255	1.83
Na-Fluorescein	376	+1	200	2.02

with the buffer gas molecules. A general rule of thumb is that the field energy is less than the thermal energy if $E/p \ll 2V/cm - torr$. The result of the analysis is:

$$B_{ion} = \frac{q}{16N\bar{\Omega}^{(1,1)}} \sqrt{\frac{18\pi}{\mu k_B T}}, \quad (5.4)$$

where μ is the reduced mass of the ion/buffer gas system, N is the buffer gas number density, and $\bar{\Omega}^{(1,1)}$ is the temperature-dependent momentum transfer cross-section of the ion. It has been shown[6] that, depending on the geometry of the ion, at temperatures above 300 K the momentum transfer cross-section can be approximated by the hard sphere collision cross-section, with resulting errors within 20%. At these temperatures, ion-neutral collisions sample only the repulsive part of the intermolecular potential. Equation 5.4 shows that the mobility of an ion is directly proportional to its “charge-to-size” ratio. The calculated mobilities for different compounds of biological and analytical interest are shown in Table 5.2.2.

With this result, one can plot the mobility of charged droplets and ions under identical conditions within the drift cell. Such a plot best summarizes the effectiveness of the mobility technique in separating ions from droplets, and in addition point out the conditions under which this separation may not be effective. From Figure 5.2 it was observed that a droplet in a drift cell reaches its maximum velocity when it has evaporated to the point where a Rayleigh fission event occurs. In fact, it will be shown later in Section 5.3 that during the complete evolution of the droplet it reaches its maximum velocity just prior to the first fission event, with each subsequent fission event resulting in sequentially lower mobilities. A plot of the maximum mobility of

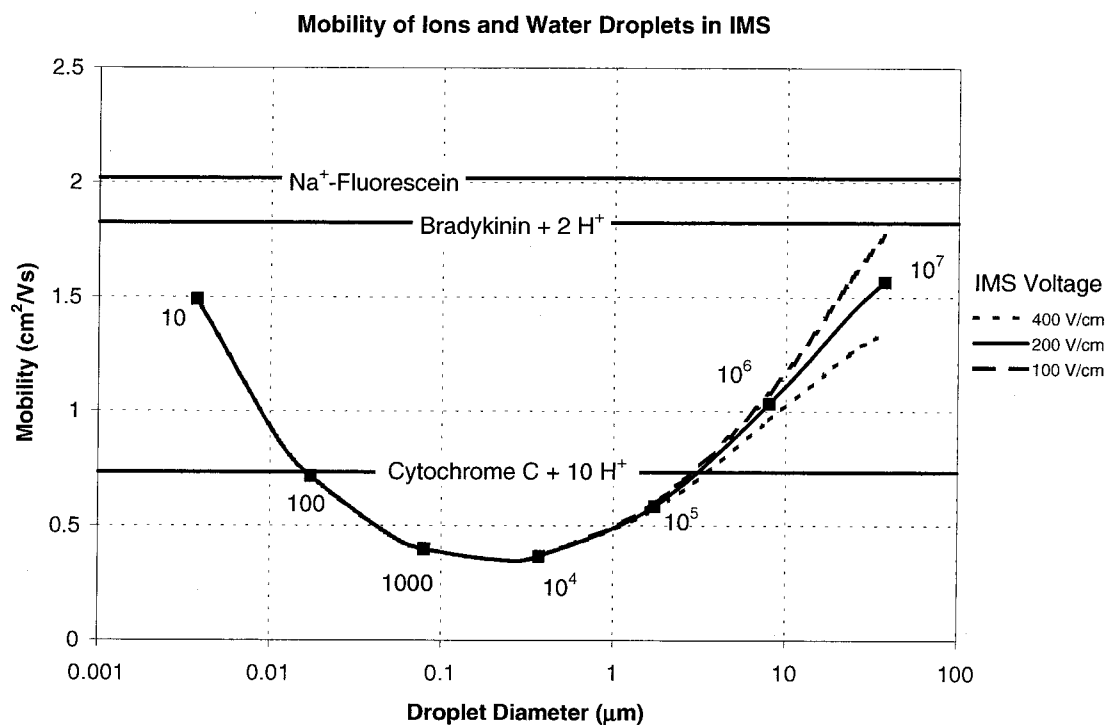


Figure 5.4: Maximum mobility for charged water droplets before onset of Rayleigh instability. Numbers of charges that correspond to the stability limit are shown for selected droplet diameters. Superimposed on graph are drift velocities for bare ions under the same cell conditions. Also shown are mobilities for various electric fields within the drift cell. Other drift cell conditions: static N₂ buffer gas at 1 atm and 293 K.

water droplets in a quiescent N_2 buffer gas at 293 K is shown in Figure 5.4 for different electric fields in the drift cell. Note that, unlike the case of ions given by Equation 5.4, the mobility of a droplet is not always the same at different electric fields. For droplets larger than $2 \mu\text{m}$, higher fields in the cell lead to decreased mobilities due an increase in the drag coefficient, C_D , (see Equation 5.3). Superimposed on the graph are the ion mobilities from the example set in Table 5.2.2. The use drift cell measurements as a tool for achieving both mechanistic and the dynamic information depends upon the degree of separation of the mobilities of a given ion from that of the droplet from which it was formed. A few observations can be made from Figure 5.4. First, the mobility of droplets near the Rayleigh limit is not a unique function of droplet diameter. Instead, there is a minimum in the curve occurring at about $0.3 \mu\text{m}$. Because of this, mobility-based techniques may not be an effective for spatially separating, for example, the parent droplet from smaller offspring droplets in an uneven fission event (see Section 4.3). Depending on the size of the parent droplet, its mobility can be smaller or larger than that of the offspring droplets. A second conclusion can be drawn for the case of pure water droplets and for large analyte ions such as Cytochrome-C. In this instance, the mobilities of both ions and droplets can be similar. Dynamic and mechanistic information on the process of ion formation can still be obtained, since the mobilities of both ions and droplets are measured (e.g., a lower mobility ion can still be traced to its higher mobility droplet source).

A similar analysis can be performed for pure methanol droplets. The major difference between methanol and water as a solvent for electrostatic spraying is that methanol has a much lower surface tension (22.6 dyne/cm, versus 72 for water) and lower density (0.79 g/cm^3 at 298 K vs. 1.0 for water). Thus methanol will have lower mobilities and fission at at smaller droplet diameters when compared to water. Another property of methanol which will be investigated further in the following section adds to its good qualities as a solvent for electrospraying: its vapor pressure is much higher than that of water ($5.1 \times 10^4 \text{ dyne/cm}^2$ versus 9.0×10^3 for water), and will thus evaporate to the Rayleigh limit much more quickly. The maximum mobility of methanol droplets in a drift cell is shown in Figure 5.5, plotted together with that of

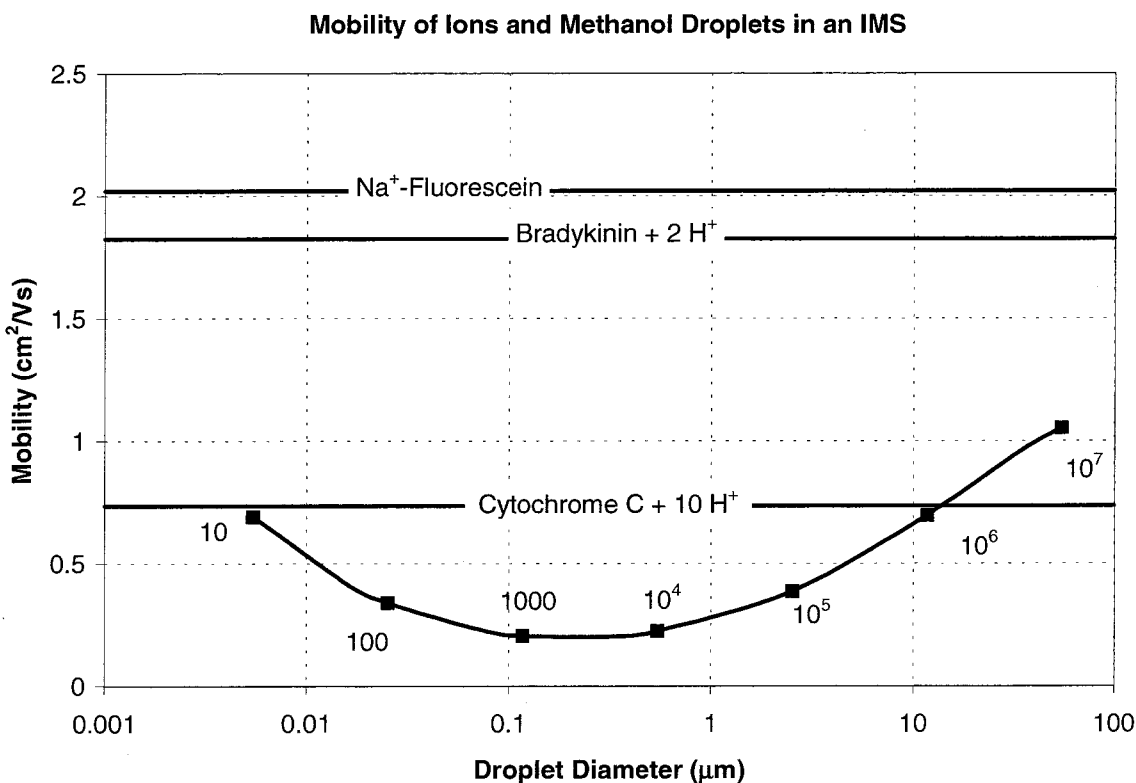


Figure 5.5: Maximum mobility for charged methanol droplets before onset of Rayleigh instability. Numbers of charges that correspond to the stability limit are shown for selected droplet diameters. Superimposed on the graph are drift velocities for bare ions under the same cell conditions. Other drift cell conditions: static N_2 buffer gas at 1 atm and 293 K.

bare ions from Table 5.2.2. While the shape of the curve is similar to that of water, the most significant difference is that there is better separation between droplets and ions. Thus it may be more effective to use methanol droplets where this type of separation is desired. Although not plotted in Figure 5.5 for simplicity, the general trends in Figure 5.4 regarding the effects of electric field strength on mobility are applicable here as well: at higher electric fields droplet mobility would decrease for the droplets larger than a few microns in diameter.

To conclude this analysis of droplet and ion mobility, the results shown in Figures 5.4 and 5.5 indicate that the mobility of a liquid droplet will almost always be less than that of a gas phase ion. If the gas phase ion were relatively small and if

the solution were a volatile organic liquid like methanol, then that difference will be even more significant. If it is true that such a difference exists between the velocity of a drifting droplet in the drift cell and that of an ion desorbed from that droplet, then such an analysis applied to droplet breakup and ion formation might lead to the direct observation of the time in which ions are desorbed from an evaporating, highly charged droplet. This is the driving force for this investigation. One additional analysis has thus far not been performed, and that is of the kinetics of the process. Such an analysis must take into account the evaporation for the charged droplets. The results of this analysis are presented next.

5.3 Modeling the Dynamics of Charged Droplet Breakup and Ion Formation in a Drift Cell

A study of the dynamics of the processes of charged droplet evaporation and breakup focuses primarily on the former, since droplet breakup can be considered instantaneous. Droplet evaporation for uncharged droplets has been studied in detail, and reviews are available in texts on aerosol science.[7, 8] Extension of these theories to charged droplets is supported by studies such as that of Law,[9] who found that high surface charge densities do not affect droplet evaporation rate. An additional finding from Law's study, confirmed by other investigators,[10, 11] is that droplet charge is conserved during the process of evaporation. These two observations allow for a numerical study of rate of charged droplet evaporation. The objective of this modeling study is to predict the time evolution of droplet size and charge within a drift cell.

The most important physical parameters that influence evaporation dynamics of a droplet are its surface area, bulk phase vapor pressure, and partial pressure of droplet solvent in the surrounding air. Other factors are important for volatile droplets. Among these are evaporative cooling of the droplet surface and slight heating of the surface caused by the convective flux that results from the surface-gas temperature differential. The latter convective flow, called Stefan flow, is an important process

for volatile droplets surrounded by a high-temperature buffer gas. For methanol evaporating at room temperature, Stefan flow results in a correction of a few percent in the predicted rate. Other factors to consider in the evaporation of droplets are specific to certain size ranges. These include the “wind effect” and the Fuchs and Kelvin effects. The wind effect is significant for droplet diameters above $50\ \mu\text{m}$, and is applied to compensate for the effect that the droplet settling velocity may have on mass diffusion and thermal conduction at the droplet surface. The Kelvin and Fuchs effects are needed for droplets smaller than 0.1 and $1\ \mu\text{m}$, respectively. The Kelvin effect corrects for the increase in vapor pressure as the droplet becomes smaller, and the Fuchs effect applies a correction when evaporation is no longer governed by diffusion, but instead by the kinetic theory of gases. Since the primary focus of these investigations are on droplets in the $10\text{--}40\ \mu\text{m}$ range, neither the wind nor the Fuchs or Kelvin effects need be considered.

In addition to contributions to droplet evaporation that are easily estimated knowing droplet size and composition, there is an unavoidable effect caused by the presence of analyte compounds in the liquid droplet. As the droplet becomes smaller, these “impurities” can reduce the vapor pressure surrounding the droplet and decrease evaporation rates. In addition, even small amounts of insoluble analyte can form surface films on a droplet that may dramatically decrease evaporation rates.[12] Such contaminant effects can be modeled using multi-component droplet evaporation theory, and a review of suitable models is available in texts on the subject.[3] The following analysis will avoid such complications by modeling the process of evaporation in electrostatic sprays as a single component evaporation process. This approximation is expected to be very good for large droplets, since the concentration of analyte and electrolyte ions in the bulk solution is usually no greater than $10^{-5}\ \text{M}$ (see Section 4.4). As the droplet evaporates to completion, however, the effect of the analyte in solution is expected to become significant. This results in changes in both the rate of evaporation as well as the chemical environment in which gas phase ions are formed. Thus experimental observations of droplet discharge and ion formation from droplets of varying ion concentration would be important.

For droplets that are much larger than the mean free path of the surrounding gas, the rate of evaporation is controlled by the rate at which vapor molecules can diffuse from the surface. The molar flux of vapor A from the surface of a droplet residing in gas B is defined as

$$N_A = -c_A D_{AB} \frac{dx_A}{dr} + x_A (N_A + N_B), \quad (5.5)$$

where N_A and N_B are the molar fluxes of the vapor and gas, respectively, c_A is the molar concentration of the vapor, D_{AB} is the binary diffusivity of vapor A in gas B , and x_A is the mole fraction of the vapor. For a stagnant gas, $N_B = 0$. Equation 5.5 is integrated to obtain the molar flux of the vapor:

$$N_A = -\frac{c_A D_{AB}}{a} \ln \left[\frac{1 - x_{AS}}{1 - x_{A\infty}} \right], \quad (5.6)$$

where a is the droplet radius. The mass balance condition at the droplet surface is

$$\frac{d}{dt} \left[\frac{4\pi a^3}{3} c_p \right] = -4\pi a^2 N_A, \quad (5.7)$$

where c_p is the molar concentration of species A in the liquid phase. Substituting Equation 5.6 into Equation 5.7, integrating over time, and solving for the droplet radius results in the following expression for the droplet radius.

$$a^2 = a_o^2 - 2 \frac{c_A D_{AB}}{c_p} \ln \left[\frac{1 - x_{A\infty}}{1 - x_{As}} \right] t \quad (5.8)$$

Equation 5.8 is valid for droplets in the size range from 1–50 μm in diameter. One effect that must be considered is the drop in temperature at the droplet surface caused by solvent evaporation. This correction is required for all volatile liquids with vapor pressures above 0.1 torr,[7] which includes water and alcohols. The result is obtained by balancing the heat required for evaporation with the heat gained by conduction from the warmer surrounding air. This gives rise to a steady-state temperature de-

pression that is independent of droplet size,

$$T_{\infty} - T_A = \frac{D_{AB}MH}{Rk_v} \left[\frac{p_A}{T_A} - \frac{p_{\infty}}{T_{\infty}} \right]. \quad (5.9)$$

In Equation 5.9, T_{∞} and T_A are the temperatures far from the droplet and at the droplet surface, respectively, p_{∞} and p_A are the partial pressures of the vapor far from the droplet and at the droplet surface, respectively, M is the molecular weight of the vapor A , H is the latent heat of evaporation, and k_v is the thermal conductivity of the surrounding gas. This equation must be solved iteratively, as quantities such as D_{AB} , k_v , H , and p_A are themselves functions of droplet temperature. For droplets evaporating in a vapor-free gas at 293 K, this depression is 15° C for water and increases to 31° C for methanol. The effect of temperature depression is to reduce the partial pressure of the vapor at the surface, thus slowing evaporation.

A plot of droplet diameter versus time is shown in Figure 5.6 for methanol and water droplets, initially 40 μm in diameter, in a vapor-free bath gas of N_2 . The effect of bath gas temperature is also shown in the figure, where water evaporation is portrayed for bath gas temperatures of 30° C and 40° C. The importance of Figure 5.6 is that it sets an approximate upper limit for the lifetime for the evaporating, highly charged droplets that will be produced in these investigations. This will be an important consideration for the design of the drift cell.

The calculation made for Figure 5.6 was made assuming a vapor-free bath gas. In actuality, there may be some residual gas due to incomplete purging of the cell. The effect that a non-zero p_{∞} may have on the rate of evaporation is shown, for the case of water, in Figure 5.7. For vapor concentrations close to zero, the effect is negligible.

At some point in the evaporation of a charged droplet, the diameter will be reached for which the surface charge density approaches the Rayleigh limit. At this point, as was pointed out in Section 4.3, the droplet will shatter (although investigators have found evidence to suggest that the breakup occurs even sooner, at about 75% of the Rayleigh limit). The result of the breakup has not been definitively characterized experimentally, and is in fact a primary objective of this study. Most investigations

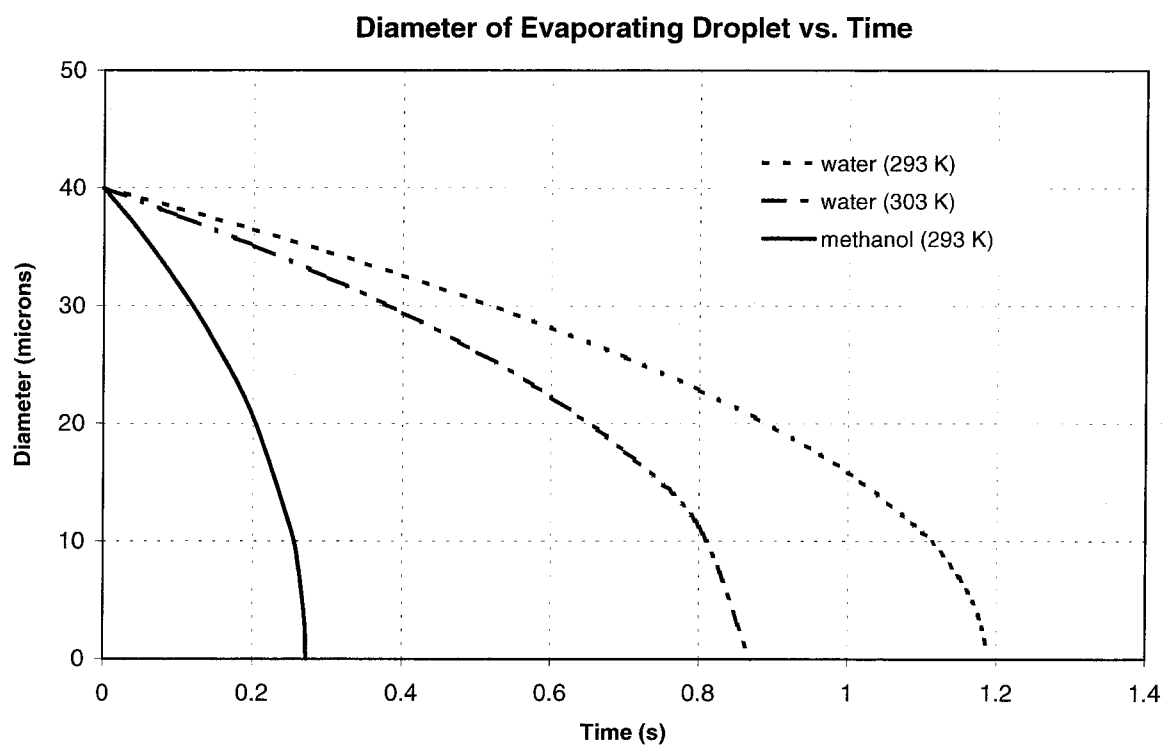


Figure 5.6: Droplet diameter as a function of time for uncharged droplets of methanol and water in vapor-free N_2 gas, from Equation 5.8 with correction for temperature depression. Temperatures of bath gas are indicated.

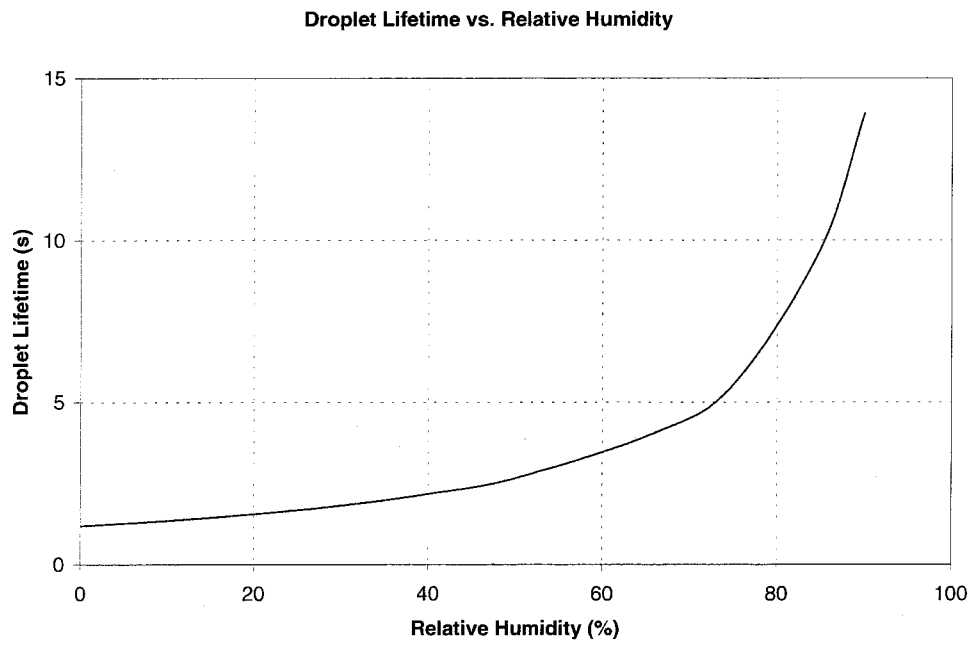


Figure 5.7: Water droplet lifetimes as a function of relative humidity for an initial droplet diameter of $40\ \mu\text{m}$ at 20°C .

have concluded that it is an uneven process, characterized by a loss of about 2% of the droplet mass and 25% of the droplet charge in the form of minute “offspring droplets.”

These findings can now be included in the model of droplet evaporation, and new evaporation curves calculated for the larger “parent droplet” with each successive fission event. The result for a water droplet is shown in Figure 5.8. Included in the figure is the mobility of the parent droplet for the case of an electric field in the drift cell of 200 V/cm. From the plot, it can be seen that the first few fission events result in a successive decrease in droplet mobility. This was, in fact, one of the conclusions drawn from Figure 5.4, which also predicts a point in the breakup process, namely, when the droplet diameter approaches $0.2 \mu\text{m}$, where each successive breakup thereafter leads to an increased mobility. It is also instructive to perform the same calculation for droplets of pure methanol. The result is shown in Figure 5.9.

While the trends are consistent between methanol and water, the much greater evaporation rate of methanol results in a much more rapid evaporation and fission process. Specifically, the time between fission events for an evaporating methanol droplet is on the order of tens of milliseconds, whereas for water it is almost an order of magnitude higher.

A prediction of the behavior of gas phase ions that are desorbed from a small offspring droplet is presented next. For the derivation, we will use the observations of investigators like Gomez,[13] who have found that the uneven fission event results in a large droplet that retains most of its mass as well as numerous sub-micron offspring droplets. The exact determination of the number, size and charge of these offspring droplets is not well known, and represents an important objective of this study. Assuming that dozens of indistinguishable offspring droplets comprise the 2% mass loss of the parent droplet, then the result of this is an average size for these on the order of hundreds of a nanometer. It has been suggested by numerous investigators[14, 15] that these sub-micron droplets are the sole source of desorbing, gas phase ions. The lifetime for the complete evaporation of these minute progeny droplets, although difficult to accurately predict for reasons described earlier in this

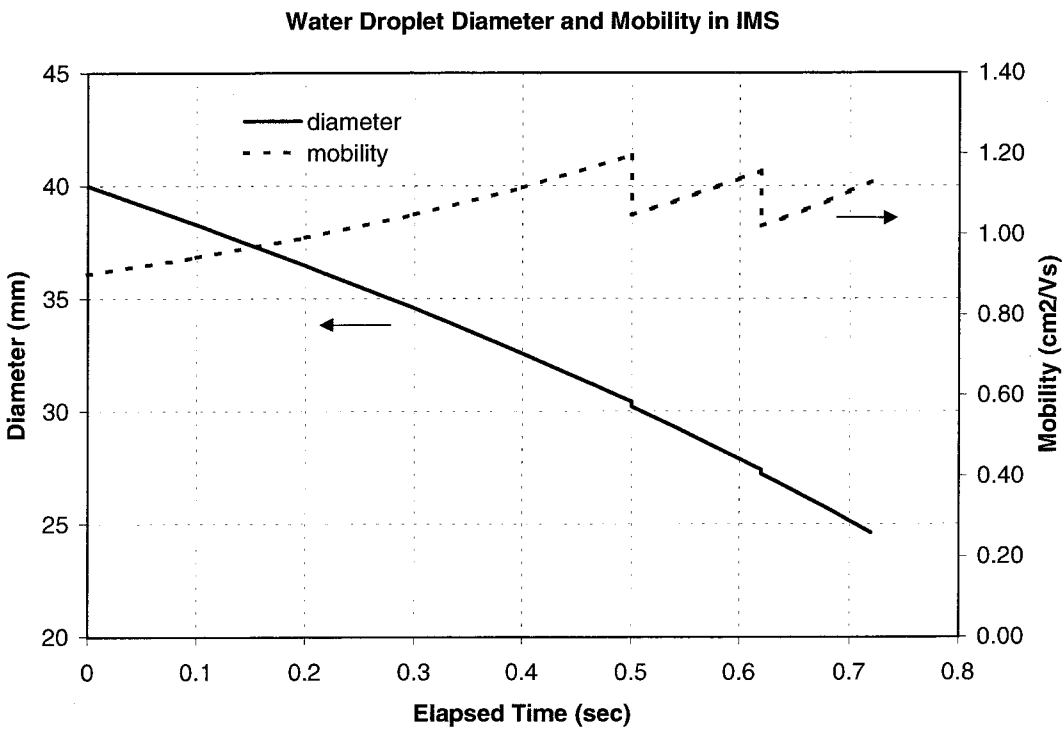


Figure 5.8: Droplet diameter and mobility as a function of time for a water droplet with an initial diameter of $40\ \mu\text{m}$ and with initially one-half of the Rayleigh limit of charge (5.6×10^6 elementary charges). Drift cell conditions: $200\ \text{V/cm}$ electric field; static N_2 buffer gas at $1\ \text{atm}$ and $293\ \text{K}$.

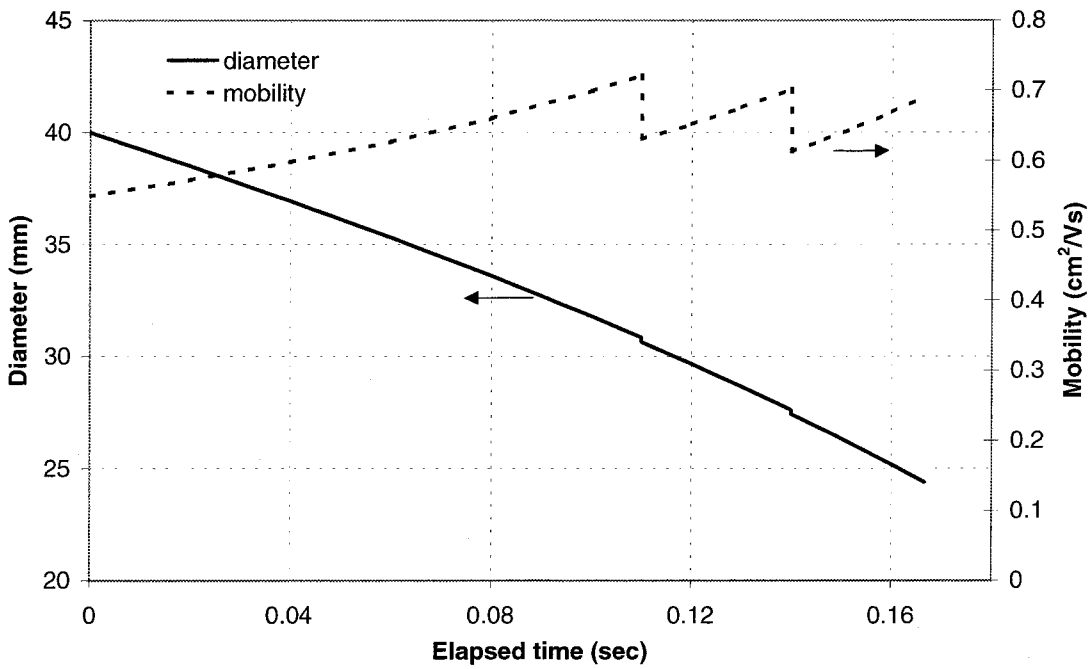


Figure 5.9: Droplet diameter and mobility as a function of time for a methanol droplet with an initial diameter of $40\ \mu\text{m}$ and with initially one-half of the Rayleigh limit of charge (3.1×10^6 elementary charges). Drift cell conditions: $200\ \text{V/cm}$ electric field; static N_2 buffer gas at $1\ \text{atm}$ and $293\ \text{K}$.

section, can nonetheless be estimated using Equation 5.8. The result is a droplet lifetime for these offspring droplets of tens of microseconds. Compared to the time scales of evaporation presented in Figures 5.8 and 5.9 this is instantaneous. Thus, if ions are indeed being produced by these offspring droplets, then they should be observed to originate from these fission events. A “map” of the position of the parent droplet and groups of gas-phase ions that have desorbed from the droplet during each fission event can be created. Such maps are presented in Figures 5.10 and 5.11. For a certain observation point defined in a drift chamber (e.g., the position of a detector), then these plots can be used to determine the relationship between the passage of ions or charge droplets and the mechanism by which they formed. Of particular importance is that information on the time of formation can be obtained by tracing back the motion of a droplet or ion using a measured mobility. The figures have been calculated using certain assumptions regarding the nature of the ion formation process. In practice, this technique can be used to directly observe the mechanism and dynamics of ion formation from highly charged droplets.

5.4 Conclusion

The main conclusion of this analysis of the mobility of droplets and ions is that droplets, in general, have much lower mobilities than ions. Although the analysis was made for methanol and water droplets carrying 10^5 charges in a 200 V/cm field, the result is quite general for the complete set of conditions that are commonly used for drift cells. Droplets will accelerate as evaporation occurs but the velocities of desolvated molecular ions will usually be higher. This conclusion makes possible the separation and detection of these gas phase ions by the proper positioning of a detector or an inlet capillary of a mass spectrometer.

Other conclusions from the current chapter can be made that will aid in the design of a mobility cell for the analysis of droplet breakup and ion formation of highly charged droplets:

- Because the timescales for evaporation are large compared to the time between

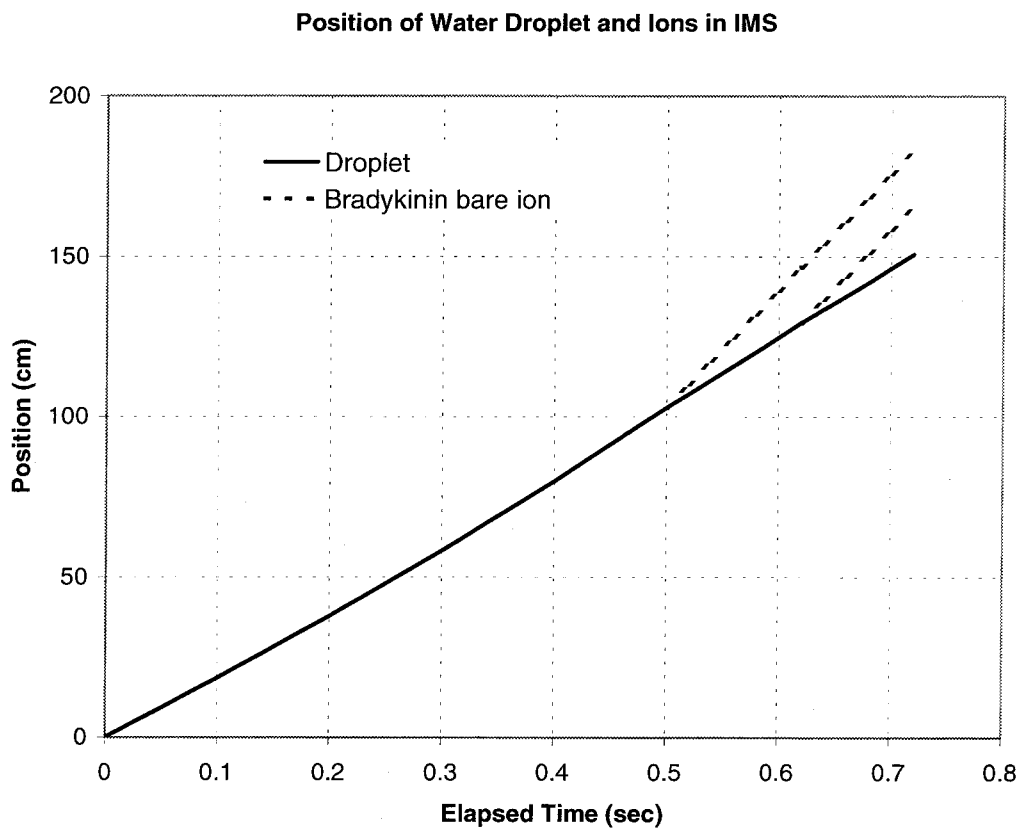


Figure 5.10: Axial position of the $40 \mu\text{m}$ water droplet depicted in Figure 5.8 as a function of time in a drift cell. Also shown is the position as a function of time of bare gas-phase bradykinin ions that are formed instantly at each discharge event. These ions propagate through the cell with a mobility taken from Table 5.2.2.

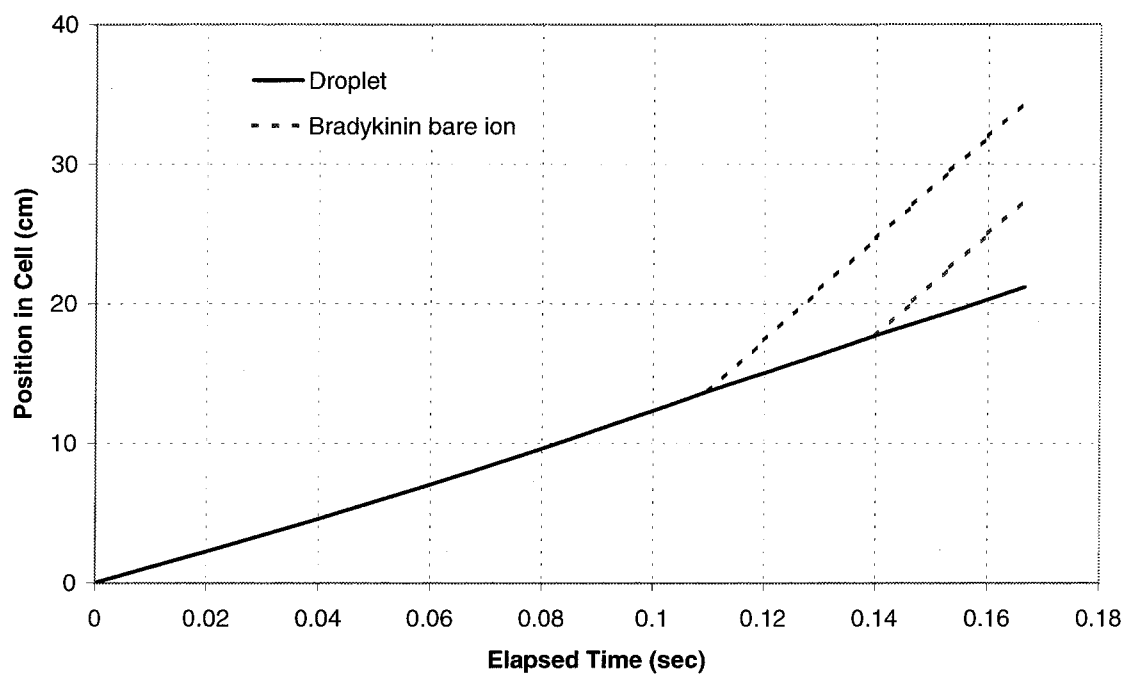


Figure 5.11: Axial position of the $40\ \mu\text{m}$ methanol droplet depicted in Figure 5.9 as a function of time in a drift cell. Also shown is the position as a function of time of bare gas-phase bradykinin ions that are formed instantly at each discharge event. These ions propagate through the cell with a mobility taken from Table 5.2.2.

fission events: order of 100 ms for water (Figure 5.8) and tens of ms for methanol(Figure 5.9), the droplet must be near the Rayleigh limit when it is introduced into the cell. Thus a means of creating charged droplets of water or methanol with at least one-half of the Rayleigh limit of charge is desired.

- From Figure 5.6 it is seen that water evaporates almost an order of magnitude slower than methanol at the same temperature. Increasing the buffer gas temperature by 10° C increases evaporation by 75%. Thus a means of heating the chamber to moderate temperatures is desired. In the absence of heating, the observation time allow for the analysis of the droplet until it has completely evaporated, which can be as long as 1 second.
- Since fission events for methanol can occur as frequently as every 10 ms, measurements performed on the droplet should be capable of high temporal resolution.

Bibliography

- [1] Gary Alan Eiceman. *Ion Mobility Spectrometry*. CRC Press, Boca Raton, 1994.
- [2] S.C. Wang and R.C. Flagan. Scanning electrical mobility spectrometer. *Aerosol Sci. Technol.*, 13:230–40, 1990.
- [3] William A. Sirignano. *Fluid dynamics and transport of droplets and sprays*. Cambridge University Press, Cambridge, 1999.
- [4] R.C. Flagan and J.H. Seinfeld. *Fundamentals of Air Pollution Engineering*. Prentice Hall, New Jersey, 1988.
- [5] E.A. Mason and E.W. McDaniel. *Transport Properties of Ions in Gases*. John Wiley and Sons, New York, 1988.
- [6] A.A. Shvartsburg and M.F. Jarrold. An exact hard-spheres scattering model for the mobilities of polyatomic ions. *Chem. Phys. Lett.*, 261(1-2):86–91, 1996.
- [7] William C. Hinds. *Aerosol technology : properties, behavior, and measurement of airborne particles*. John Wiley and Sons, New York, 2 edition, 1999.
- [8] E. James Davis. Microchemical engineering: the physics and chemistry of the microparticle. In Thomas B. Drew, editor, *Advances in Chemical Engineering*, volume 18. Academic Press, Inc., New York, 1992.
- [9] S.E. Law. Charge and mass flux in the radial electric field of an evaporating charged water droplet: an experimental analysis. *IEEE Trans. Ind. Appl.*, 25:1081–1087, 1989.
- [10] M.A. Abbas and J. Latham. The instability of evaporating charged drops. *J. Fluid Mech.*, 30:663–670, 1967.

- [11] D.G. Roth and A.J. Kelly. Analysis of the disruption of evaporating charged droplets. *IEEE Trans. Ind. Appl.*, IA-19:771–775, 1983.
- [12] D.C. Taffin, S.H. Zhang, T. Allen, and E.J. Davis. Measurement of droplet interfacial phenomena by light-scattering techniques. *AIChE J.*, 34(8):1310–1320, 1988.
- [13] A. Gomez and K. Tang. Charge and fission of droplets in electrostatic sprays. *Phys. Fluids*, 6:404–414, 1993.
- [14] I.G. Loscertales and J. Fernández de la Mora. Experiments on the kinetics of field evaporation of small ions from droplets. *J. Chem. Phys.*, 103:5041–60, 1995.
- [15] J.V. Iribarne and B.A. Thomson. On the evaporation of small ions from charged droplets. *J. Chem. Phys.*, 64:2287, 1976.

Chapter 6 Fundamental Studies of Droplet Evaporation and Discharge Dynamics in Electrospray Ionization

In recent years, electrospray ionization[1] has become one of the most common techniques for analyzing liquid phase samples using mass spectrometry. Important questions still remain, however, regarding the mechanism by which gas phase ions are created from evaporating, highly charged droplets.[2] We report the development of a new technique for studying the time evolution of the size and charge of nascent charged droplets, providing insight into the droplet evaporation and discharge processes which lead to ion formation in electrospray ionization. A brief description of the method is given below, followed by observations made on water, methanol, and acetonitrile, solvents commonly used in electrospray ionization. These studies complement other work in our laboratory, in which the last stages of ion desolvation are investigated using trapped ion FT-ICR methods.[3, 4, 5]

The experimental apparatus is shown in Figure 6.1. The electrospray source comprises a 50 μm inner diameter stainless steel capillary from which charged droplets are injected upward into a cylindrical drift cell with a uniform 51 V/cm electric field. A countercurrent flow of dry N_2 buffer gas at 293 K and atmospheric pressure defines the droplet environment. Liquid flow rate and capillary voltage are adjusted to create droplets ranging from 5–50 μm in diameter. A phase Doppler anemometer (PDA) measures the diameter and axial velocity of individual droplets at the center of the cell.[6, 7, 8] Droplet velocities (mobilities) in a constant electric field are dependent on the size and charge of the droplet, permitting calculation of the droplet charge from the PDA data.[9] After initial detection and characterization, the electric field within the cell is repeatedly reversed to pass the droplet through the measurement volume of

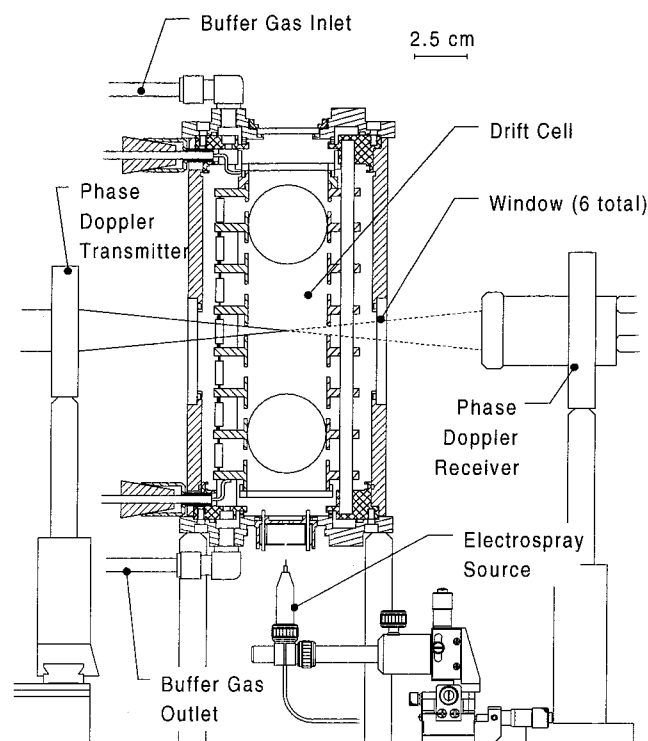


Figure 6.1: Experimental apparatus for studying droplet evaporation and discharge dynamics.

the PDA. This “ping-pong” experiment yields the size and charge of a single droplet as a function of time. The instrument is automated and can collect data for large numbers of droplets in unattended operation.

Solutions studied were spectroscopic grade methanol and acetonitrile, as well as filtered, deionized water to which 10^{-4} M NaCl was added to allow for electro spray at sufficiently low voltages to avoid corona discharges. Size-charge correlations of electro sprayed droplets obtained with the PDA are shown for these solvents in Figure 6.2, where they are compared to the Rayleigh stability limit,[10] which predicts droplet fissioning when electrostatic repulsion overcomes surface tension. Three or more distinct charge-size groupings are apparent in the case of methanol.

The ping-pong experiment directly reveals the droplet evaporation and discharge dynamics of individual droplets after initial detection by the PDA, which occurs

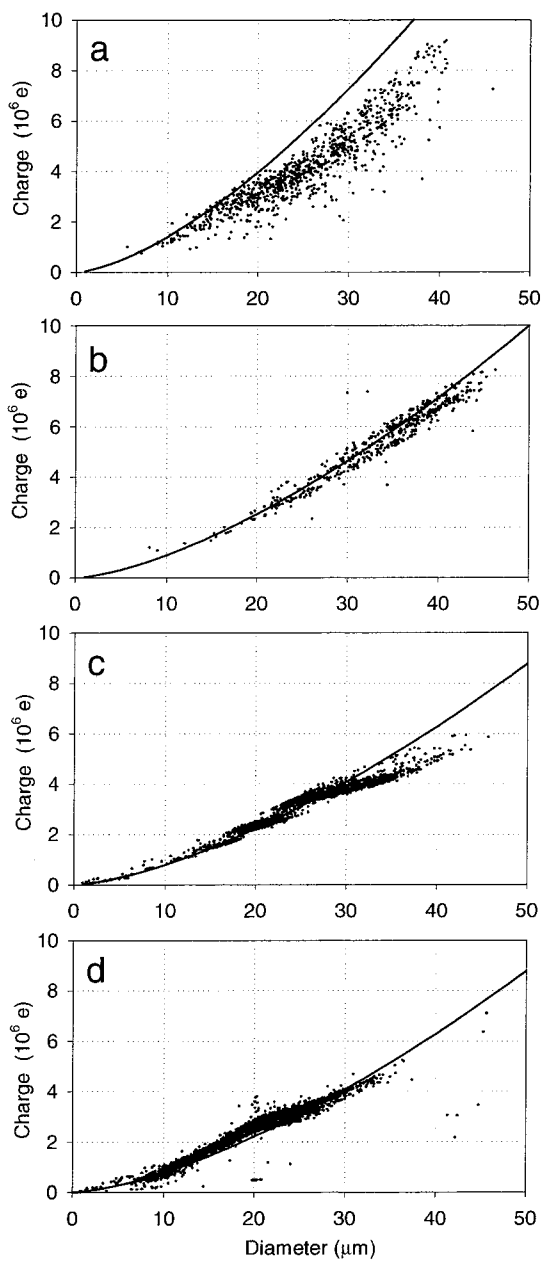


Figure 6.2: Electrospray ionization size-charge correlations for positively charged droplets of (a) water, (b) acetonitrile, (c) methanol, and for (d) negatively charged droplets of methanol with 10^{-4} M NaCl. Also plotted are curves representing the Rayleigh instability limit.

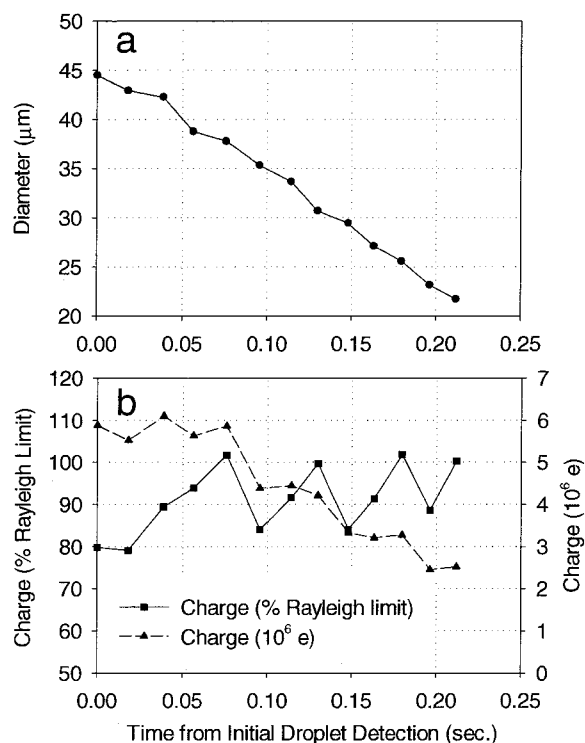


Figure 6.3: Evaporation and discharge of a positively charged methanol droplet in 51 V/cm electric field. (a) Variation of droplet diameter with time. (b) Variation of droplet charge with time, represented as number of elementary charges and as percent of the Rayleigh limit of charge for measured droplet diameter.

after the droplets traverse the 10 cm distance from the source to the PDA (typically 200 ms). Results for methanol are shown in Figure 6.3. The data show that the droplet diameter decreases continuously with time, while charge is expelled from the droplet in discrete events occurring at or slightly above the Rayleigh limit. Three discharge events are evident in the data shown in Figure 6.3, becoming more closely spaced in time as evaporation proceeds. With methanol, discharge events result in a 20% decrease in charge, with no corresponding reduction in diameter in excess of that resulting from solvent evaporation. During evaporation, the overall charge on the droplet is conserved. These results are consistent with the observations of other investigations.[11, 12, 13] Similar data obtained for water and acetonitrile lead to the following generalizations.

(1) The discharge dynamics of droplets with the same initial diameter and charge are highly reproducible for all solvents and analyte/solvent combinations studied to date. (2) Published over a hundred years ago, Rayleigh's analysis of charged droplet instabilities resulting from solvent evaporation is remarkably accurate in predicting observed discharge events for all three solvents. (3) Droplet discharge events occur by loss of 15–20% of the droplet charge in the case of methanol and acetonitrile, and 20–40% in the case of water, with little accompanying loss of solvent. (4) Discharge events occur in a reproducible temporal pattern, with decreasing time intervals between successive events, dictated by solvent evaporation and the approach to the Rayleigh limit. Solvent evaporation and not fissioning is principally responsible for reduction in droplet size. This observation is consistent with photomicrographs of unstable droplets, which show discharge events as sharp conical protrusions with emission of what appear to be much smaller droplets from the tip of the cone.[14, 15] (5) The addition of biomolecules or salt (up to 10^{-3} M) to the solution does not significantly affect the discharge dynamics. The size-charge correlation of negatively charged droplets formed in electrospray ionization of 10^{-4} M NaCl in methanol is displayed in Figure 2d. Discharge dynamics for negatively charged droplets are similar to those observed for positively charged droplets. (6) The life history of a single electrosprayed droplet can be followed through numerous discharge events (up to 5 have been observed) in the absence of radial confinement. This implies that no significant displacement of the droplet arises from discharge events and is inconsistent with any notion of high energy chaotic fission processes. (7) In the case of methanol the size-charge correlation shown in Figure 6.2 suggests nearly monodisperse nascent drop formation. The consistent loss of charge in each discharge event preserves the initial tightly clustered size-charge distribution.

The apparatus in Figure 6.1 has also been operated with two different drop-on-demand generators for producing single highly charged droplets, with results similar to those presented above for a continuous electrospray source. The well-behaved and reproducible droplet discharge dynamics should make it possible to devise methods to efficiently collect and analyze ions produced in successive discharge events from single

charged droplets. Experiments to confirm this exciting possibility are underway in our laboratory.

Acknowledgements

The authors thank the National Science Foundation (CHE-9727566) for support of this work.

Bibliography

- [1] R.B. Cole, editor. *Electrospray Ionization Mass Spectrometry : Fundamentals, Instrumentation, and Applications*. John Wiley and Sons, New York, 1997.
- [2] JB Fenn, J Rosell, T Nohmi, S Shen, and FJ Banks. Electrospray ion formation: Desorption versus desertion. *Biochemical and Biotechnological Applications of Electrospray Ionization Mass Spectrometry*, 619:60–80, 1996.
- [3] S.W. Lee, S.B. Chang, D. Kossakovski, H. Cox, and J.L. Beauchamp. Slow evaporation of water from hydrated salen transition metal complexes in the gas phase reveals details of metal ligand interactions. *J. Am. Chem. Soc.*, 121(43):10152–10156, 1999.
- [4] S.W. Lee and J.L. Beauchamp. Fourier transform ion cyclotron resonance study of multiply charged aggregates of small singly charged peptides formed by electrospray ionization. *J. Am. Mass Spectrom.*, 10(4):347–351, 1999.
- [5] S.W. Lee, P. Freivogel, T. Schindler, and J.L. Beauchamp. Freeze-dried biomolecules: Ft-icr studies of the specific solvation of functional groups and clathrate formation observed by the slow evaporation of water from hydrated peptides and model compounds in the gas phase. *J. Am. Chem. Soc.*, 120(45):11758–11765, 1998.
- [6] W.D. Bachalo and M.J. Houser. Phase doppler spray analyzer for simultaneous measurements of drop size and velocity distributions. *Opt. Eng.*, 23:583, 1984.
- [7] K. Bauckhage. The phase-doppler-difference-method, a new laser-doppler technique for simultaneous size and velocity-measurements .1. description of the method. *Part. Part. Syst. Charact.*, 5(1):16–22, 1988.

- [8] J.N. Smith, J.L. Beauchamp, and R.C. Flagan. The design and calibration of a phase doppler anemometer for instructional and laboratory use. *Rev. Sci. Instrum.*, to be submitted, 2000.
- [9] R.C. Flagan and J.H. Seinfeld. *Fundamentals of Air Pollution Engineering*. Prentice Hall, New Jersey, 1988.
- [10] Lord Rayleigh. On the equilibrium of liquid conducting masses charged with electricity. *Proc. Roy. Soc.*, 14:184–86, 1882.
- [11] E.J. Davis and M.A. Bridges. The rayleigh limit of charge revisited: light scattering from exploding droplets. *J. Aerosol Sci.*, 25:1179–1199, 1994.
- [12] M.A. Abbas and J. Latham. The instability of evaporating charged drops. *J. Fluid Mech.*, 30:663–670, 1967.
- [13] S.E. Law. Charge and mass flux in the radial electric field of an evaporating charged water droplet: an experimental analysis. *IEEE Trans. Ind. Appl.*, 25:1081–1087, 1989.
- [14] A. Gomez and K. Tang. Charge and fission of droplets in electrostatic sprays. *Phys. Fluids*, 6:404–414, 1993.
- [15] D.B. Hager, N.J. Dovichi, J. Klassen, and P. Kebarle. Droplet electrospray mass-spectrometry. *Anal. Chem.*, 66(22):3944–3949, 1994.

Chapter 7 A Study of the Evolution of Droplet Size and Charge in Electrospray Ionization: The Droplet Ping-Pong Experiment

Abstract

We present an experimental technique for probing the mechanism and dynamics of charged droplet breakup in electrosprays. At its core is a novel device that can perform simultaneous, *in situ* measurements of size and charge on individual droplets. Charged droplets from the spray source pass into a drift cell with a 50 V/cm electric field. A phase Doppler anemometer performs a simultaneous diameter and charge measurement on individual droplets at the center of the cell. The field in the drift cell is reversed following the initial size and charge measurements, and the droplet passes again through the measurement region of the phase Doppler anemometer. Using this “ping-pong” technique, the diameter and charge of an individual electro-sprayed droplet can be measured every 10 ms. This results in a sequence of size and charge measurements for individual droplets that, in many cases, span the lifetime of the droplet. The technique can also acquire size-charge correlations of electro-sprayed droplets at a single spatial location in the spray plume. We have applied this technique to electrosprays of pure methanol. The measured size-charge correlation shows that the droplets from the spray fall into discrete groupings that can be attributed to Rayleigh fission events. We have also performed ping-pong measurements of individual electro-sprayed methanol droplets. Most fission events occur near or above the Rayleigh limit of charge, resulting in a negligible mass loss and an charge loss of

approximately 20%.

7.1 Introduction

In 1882, Lord Rayleigh[1] derived a formula for the maximum charge that a droplet can hold before the electrostatic repulsion of surface charges overcomes surface tension. This limiting behavior of an isolated droplet provides the starting point for our present understanding of the mechanism of droplet breakup in electrospray ionization sources for mass spectrometry. In the century that has passed since Lord Rayleigh's derivation, numerous investigators have attempted to chronicle the life history of a charged droplet that has evaporated to Rayleigh's stability limit. This has received particular attention in the past decade, due in part to the enormous success of electrospray ionization for creating large, multiply charged ions of biological interest. An understanding of the processes of droplet evaporation and discharge in electrosprays is crucial to deducing the physical and chemical environments under which gas phase ions are produced by these highly charged droplets. This has implications both in the design of highly efficient ion sources and in correlating the peaks in a mass spectrum with the nature and concentration of the analyte in solution.[2]

We report a new experimental technique for determining the time evolution of the size and charge of individual droplets from an electrospray source. In this method, charged droplets produced by an electrospray are introduced into a cylindrical drift cell with a uniform electric field of approximately 50 V/cm. At the center of the cell, an individual droplet passes through the measurement volume of a phase Doppler anemometer (PDA). The PDA measures its diameter and velocity, from which the charge can be deduced. After a short delay, the electric field within the cell is reversed and the droplet passes again through the measurement volume of the PDA for another size and charge measurement. The process repeats itself, with the trajectory of the droplet resembling that of a ping-pong ball in play, until the droplet can no longer be detected. These measurements provide a time sequence of size and charge for each droplet that passes through the PDA measurement region. A plot of the parameters

for the first measurement in each sequence provides a size-charge correlation of the droplets in the spray.

Below is a detailed description of the apparatus, followed by an investigation of methanol electrosprays. A size-charge correlation reveals a unique structure whereby droplets fall into distinct groupings. Rayleigh fission events are the primary mechanism for the formation of these groups. Evidence of Rayleigh fission processes in the spray from these size-charge correlations is confirmed by analysis of the time series plots of size and charge of individual electrosprayed droplets using the ping-pong technique described above.

7.2 Background

Although research in the field of charged droplet breakup and electrostatic sprays began well before Lord Rayleigh's derivations in 1882,[3] his result is the theoretical foundation for our current understanding of these processes. Rayleigh deduced that a droplet of a given radius, R_R , can sustain a maximum level of charge when electrostatic repulsion of surface charges is exactly balanced by surface tension. A further decrease in droplet diameter results in disruption, often referred to as Rayleigh instability. Rayleigh's result for this critical charge, Q_R , is as follows:

$$Q_R = 8\pi\sqrt{\epsilon_o\gamma R_R^3}, \quad (7.1)$$

where ϵ_o is the permittivity of free space and γ is the liquid surface tension. Although Rayleigh's work simply and elegantly predicts the instabilities observed for a highly charged droplet, it provides no insights into the nature of the products of the fission event. In the past century, numerous studies have attempted to complete the history of a charged droplet that has evaporated to Rayleigh's stability limit. The current study combines salient features from the two most popular experimental approaches. The first approach employs an instrument called an electrodynamic balance to trap a charged droplet in an alternating electric field for study, usually by sensitive optical

techniques. The second approach performs *in situ* measurements of size and velocity in electrosprays by the optical technique of phase Doppler anemometry.

The first set of measurements to provide a detailed description of the mechanism of charged droplet evaporation and discharge relied on a device that bears a close resemblance to that used by Millikan[4] to measure the charge on the electron. This device consists of parallel plates that are used to produce a uniform electric field to trap charged droplets. Early investigators, such as Abbas and Latham,[5] used this device to continuously measure the size and charge of evaporating water droplets. Recently a modern version of the Millikan apparatus, the electrodynamic balance (EDB),[6] has improved the quality of these measurements by providing a radial trapping field. The EDB has been employed in numerous studies on the breakup of highly charged droplets, a review of which can be found in a recent study.[7] These investigations provide a picture of the disruption process. A charged droplet evaporates without loss of charge as it approaches the Rayleigh stability limit, at which point the droplet undergoes a disruption which results in a 15–30% loss in the charge residing on the droplet and a negligible to 5% loss in mass. Most EDB investigators report disruptions occurring from 10–20% below the Rayleigh stability limit, prompting debate as to whether the techniques used to study the phenomena of droplet breakup are somehow perturbing the droplet and initiating a premature fission event.

Although the EDB provides accurate and continuous measurements of size and charge of evaporating droplets, sample introduction is a major challenge for investigators studying volatile solutions used in electrosprays. As a result, most EDB studies to date have been performed on slowly evaporating droplets such as water in a saturated bath gas[5] or dodecanol.[7] Phase Doppler anemometry[8, 9] has been frequently employed to perform *in situ* measurements of the size and velocity of electrosprayed droplets, providing more realistic information about the physical properties of electrosprays. In this technique, shown in Figure 7.1, two beams originating from a single laser intersect to create an interference fringe pattern. A droplet residing in the fringe pattern acts like a small lens, expanding the fringe pattern in an inverse relationship

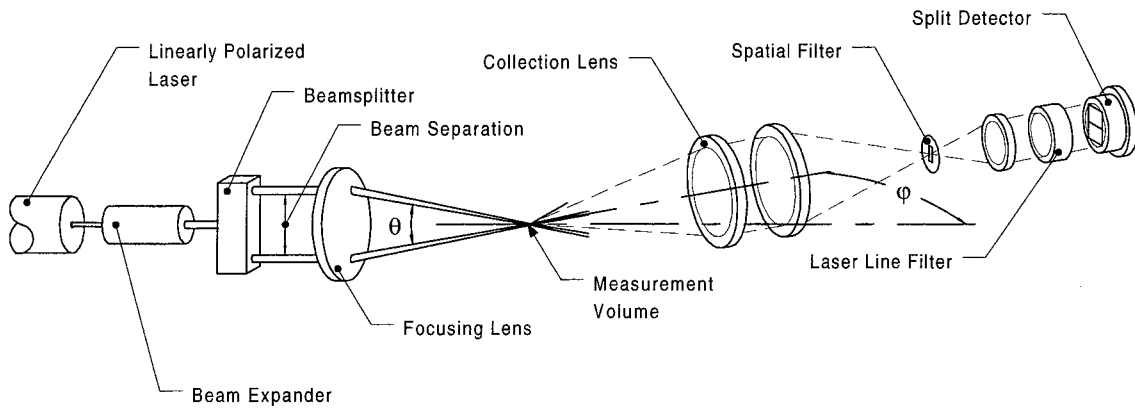


Figure 7.1: PDA system optical arrangement.

to the droplet's diameter. This diverging pattern will sweep by a stationary optical receiver at a velocity proportional to the speed of the droplet in the direction perpendicular to the fringes. If the collection aperture of the receiver is split into two regions, as shown in Figure 7.1, the divergence of the sweeping fringe pattern will cause the signal detected by one region to be phase-lagged with respect to the signal detected in the other. The direction of the phase shift is dependent upon the flow direction of the droplet and whether the droplet is refracting or reflecting the light. The frequency of the signal seen at each detector is proportional to particle velocity, and the phase shift proportional to particle size; the instrument performs both measurements simultaneously. Figure 7.2 shows a typical pair of signals (which are inverted by a pre-amplifier in the receiver) from the instrument used in these experiments. The essential features of the measurement technique can be seen in the figure: the frequency of both signals are equal, and one can detect a small phase shift between signals.

Gomez and Tang[10] used phase Doppler anemometry to study electrospays of heptane, motivated by the combustion applications of electrostatic spraying. They used spray conditions similar to those in the current study and obtained size and average charge measurements for the electrospayed droplets using the average diameter determined by a phase Doppler measurement and a total current measurement from a

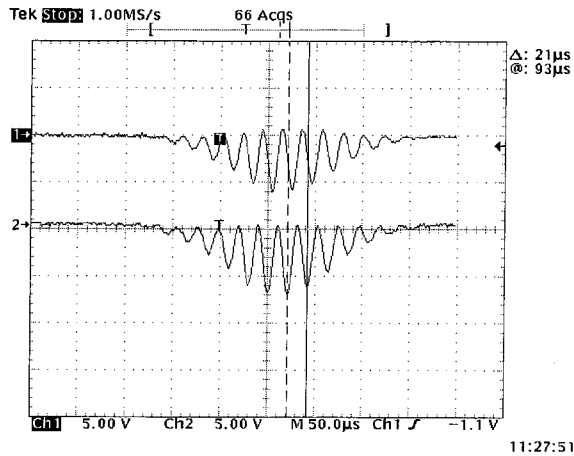


Figure 7.2: Typical signals from a phase Doppler receiver.

mesh upon which the droplets impinge. They concluded that droplet breakup occurs at about 70–80% of the Rayleigh limit, attributing the low threshold for breakup to aerodynamic effects that stress the droplet into premature fissioning. In measurements of droplet size at various locations downstream from the source, they noted a shift in the distribution towards smaller sizes and attribute it to droplet evaporation. At large distances from the source, however, their size distributions feature a secondary group of droplets with diameters around $5 \mu\text{m}$, which they conclude are the products of fission events. In this region of the spray, they took photographs of droplets in the process of disruption. These photographs showed the distortion of the droplet into a small conical protrusion out of which even smaller droplets appeared to be emitted.

In this region of the spray, the Gomez and Tang experienced some difficulty in applying the phase Doppler technique because their commercial system invalidated measurements of non-spherical droplets. Recently, Doicu and co-workers have presented theoretical and experimental evidence that the phase Doppler technique can be effective in characterizing some forms of non-spherical particles.[11] In their study of monodispersed, randomly oriented spheroids with eccentricities as large as 2.2, they observed a distinct peak in the size measurement that is quite close to that of

the volume equivalent sphere. The measured size distributions for these spheroids are quite broad, however, and feature extensions out to large diameters. We have confirmed this observation with PDA measurements of droplets during disruption. These data are discussed in detail below.

Other phase Doppler studies of the electrospray process have focused on correlating the droplet size and velocity distributions with solution properties such as conductivity.[12] Naqui and co-workers[13] performed phase Doppler measurements on solutions of sulfuric acid and octanol, and presented a plot of size versus velocity for one such spray. It shows a clear correlation of size with velocity, as well as discrete groupings resembling those found in the current investigation. Since the measurements were performed in diverging electric field surrounding the capillary, they could not make quantitative estimates of the droplet charge. They do, however, hint that the size and velocity capabilities of the phase Doppler technique can be employed to gather much more information on the mechanism of the electrospray process. Their claim is supported by our investigation.

7.3 Instrumentation

Figure 7.3 shows a diagram of the apparatus used in this study. The main components are the electrospray source, drift cell, phase Doppler anemometer (PDA), and the data acquisition and instrument control system. We present the theoretical basis for obtaining charge from a PDA measurement below. Following this, we provide a description of each component of the experiment.

7.3.1 Theory

The excess charge on a droplet can be calculated by performing a simultaneous measurement of a droplet's size and velocity within a uniform electric field. This result emerges from a force balance calculation on an isolated droplet and subsequent integration.[14] After a relaxation time, a liquid droplet within a constant electric

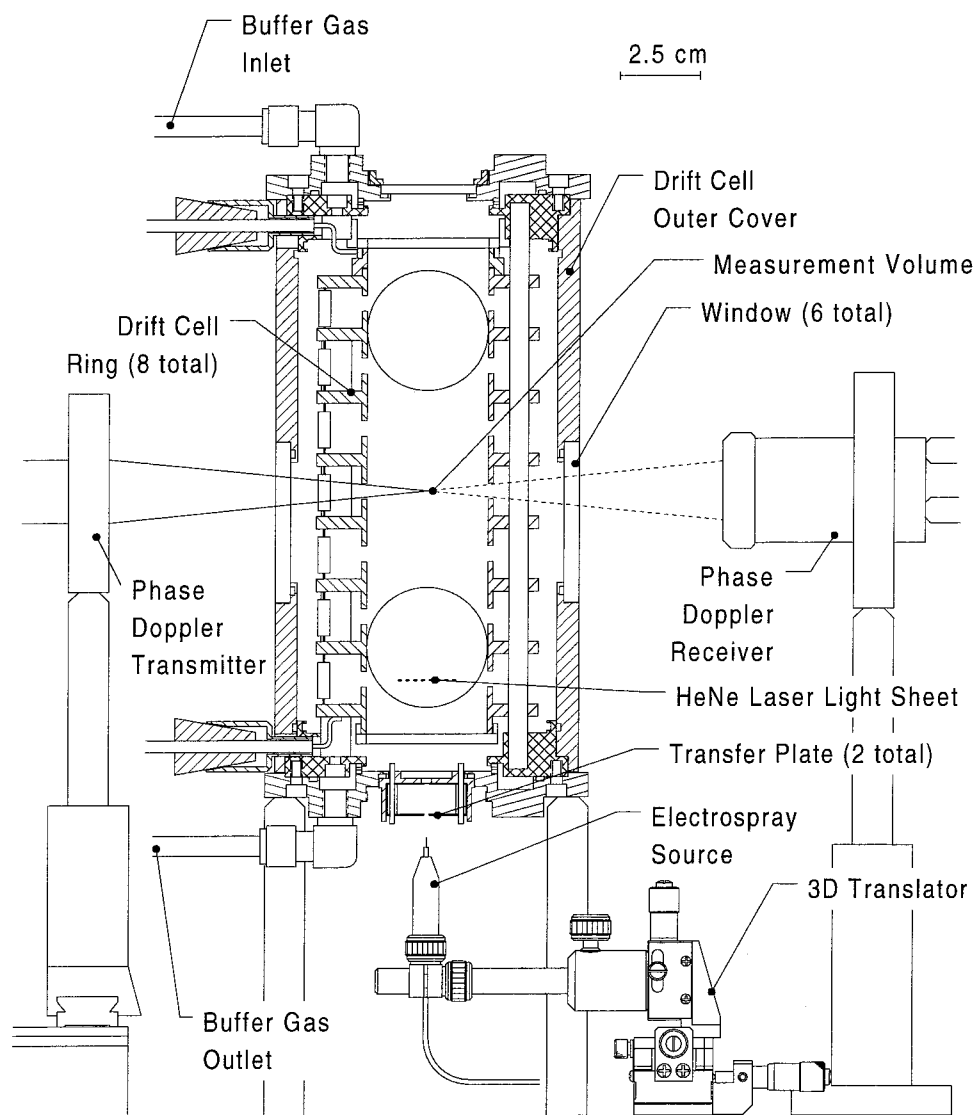


Figure 7.3: Experimental apparatus for studying droplet evaporation and discharge dynamics.

Table 7.1: Calculated charge and diameter for methanol droplets at the Rayleigh instability limit. Also shown are droplet velocities in a 50 V/cm electric field and droplet relaxation times.

Droplet Charge (#e)	Diameter at Rayleigh Limit (μm)	Velocity at Rayleigh Limit (cm/s)	Relaxation Time (s)
1×10^3	0.08	20.13	6.7×10^{-8}
5×10^3	0.23	17.63	2.9×10^{-7}
1×10^4	0.37	18.57	6.1×10^{-7}
1×10^5	1.72	30.25	1.0×10^{-7}
1×10^6	7.99	57.41	2.0×10^{-4}
5×10^6	23.35	85.30	1.5×10^{-3}
1×10^7	37.07	97.77	3.6×10^{-3}

field of strength E will achieve a steady state drift velocity v_d given by

$$v_d = \left[\frac{C_c(qE - m_p g)}{\frac{\pi}{8} C_D \rho_p D_p^2} \right]^{\frac{1}{2}}. \quad (7.2)$$

Here, q is the droplet charge, m_p , ρ_p and D_p are the mass, density and diameter of the droplet, respectively, C_c is the slip correction factor, and C_D is the drag coefficient. Solving Equation 7.2 for the droplet charge, q , results in:

$$q = \frac{\pi C_D \rho_p D_p^2 v_d^2 + 8 C_C m_p g}{8 C_C E}. \quad (7.3)$$

In the equation above, C_D and C_C are known for a given droplet size and velocity.[15]

If, after a measurement is taken of droplet size and charge, the electric field is reversed, then the droplet's response to this change in field will not be instantaneous. This response time determines the minimum time resolution of the experiment. Table 7.1 shows calculated relaxation times[14] for droplets near the Rayleigh limit in conditions similar to those of this study. The table also shows the critical diameter at which Rayleigh instability occurs, the velocity of the droplet just prior to the instability, and the droplet relaxation time in a 50 V/cm electric field.

7.3.2 Electrospray Source

The electrospray source for these investigations was built in-house, and is identical to one that is being employed as an ion source in the investigators' laboratories at the Beckman Institute Center for High Performance Mass Spectrometry.[16] The source consists of a stainless steel capillary of 50 μm inside and 115 μm outside diameters biased in the range ± 900 to ± 1200 V, depending on the polarity of the droplets produced. A syringe pump (model 22; Harvard Apparatus, Inc.) delivers sample solution through tubing made of PEEK plastic (Vicatex PLC) at flow rates of approx. 0.2–1 $\mu\text{l}/\text{min}$. A three-dimensional translator (OptoSigma Corp.) positions the capillary at the entrance aperture to the drift cell. The tip of the electrospray needle is located approximately 2 mm from the first transfer plate with a 1.5 mm aperture in the center. This plate is biased at ∓ 100 V. A second, identical plate is located 1 cm above the first and electrically grounded. These two transfer plates inject charged droplets from the spray source into the drift cell, while limiting the sampled droplets to those that are nominally co-axial with the drift cell. Modular electrostatic lens components (Kimball Physics, Inc.) comprise the transfer plates. The current arrangement was chosen following numerous tests of different transfer plate arrangements. An inspection microscope (Edmond Scientific Corp.) allows one to monitor the spray. A HeNe laser light sheet located at the entrance to the drift cell allows one to determine if droplets are entering the drift cell.

We adjust liquid flow rate and capillary voltage within the range listed above in order to create droplets of approximately 40 μm in diameter, as measured by the PDA at a location 10 cm above the source (see Figure 7.3). This creates droplets large enough to be monitored with optical techniques, and long-lived enough to observe evaporation and discharge processes. We found no correlation between the measured droplet size and the observed evaporation and discharge processes when examining droplets between 5 and 50 μm in diameter. These droplets are larger than those commonly associated with electrospray ionization, which are about 1–2 μm in diameter at the source.[13] However, if the observed absence of correlation between

size and discharge dynamics holds, our results describe processes in the plumes of typical electrospray sources. The size range studied is comparable to those used in some applications of electrostatic spraying.[10, 3] The procedure for establishing the spray conditions is to operate the source initially at conditions used in creating ions for mass spectrometry. In this mode of operation, the droplets that enter the region between the transfer plates are smaller than a few microns in diameter, so they volatilize completely in this region before they can pass into the drift cell. Following this, we then move the needle away from the first plate using the vertical adjustment of the translator until droplets of 20–40 μm are detected by the PDA. The result is an electrospray that is operating in the “cone-jet” mode, emitting a fine stream of droplets with a nearly monodispersed size distribution.[17]

7.3.3 Drift Cell

The drift cell allows for a variety of studies of disruption and ion formation processes from charged droplets. We have provided abundant optical access to the center of the drift cell, since optical detection is employed throughout the chamber for most of the planned investigations. The electric field is as uniform as possible over the entire flight path of droplets and over most of the cross-section. To ensure that a vapor-free gas surrounds the evaporating droplet, a pressure and temperature controlled counter-flowing buffer gas is introduced into the cell. In addition, the cell is adaptable to different methods of droplet generation and different detection schemes.

A uniform electric field is provided by eight resistively-coupled, stainless steel rings. The interior of the cell is 13.8 mm in length and 3.8 mm in diameter. The rings have a “T”-shaped cross-section to shield the drift cell from field perturbations caused by the walls of the cell and to create uniform buffer gas flow conditions. Wire grids can be mounted at both ends of the cell to ensure field uniformity, although they are not employed in the present investigation. We used a PC-based ion optics simulation program, SIMION,[18] to simulate the electric field within the drift cell. The result, displayed in Figure 7.4, verifies that the field gradient is constant over

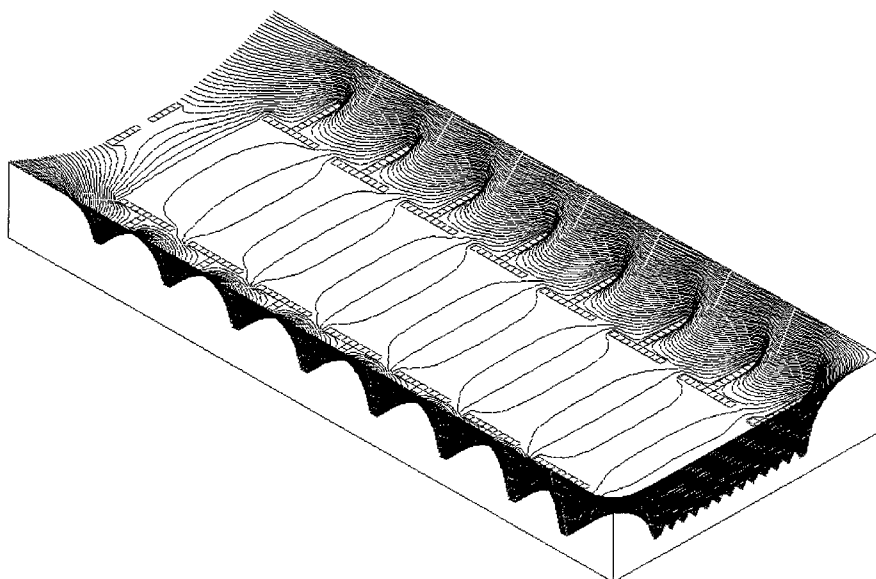


Figure 7.4: IMS electrostatic field calculated with SIMION. Charging electrode is located in the upper left of the figure, and outlet is on the lower right.

the length of the cell and the field is uniform to within 1% over the area enclosed by one-half the inner radius.

A flow of nitrogen is typically provided at a rate of 0.3 l/min. The gas first enters an annular chamber at the top of the instrument before flowing into the drift cell through a porous ring. The flow in the drift cell is laminar at this flow rate: the calculated axial velocity of the gas in the cell is 3 cm/s and the Reynolds number is 76. The flow conditions of the buffer gas were also modeled to assure uniformity using FIDAP, a fluid mechanics simulation program.[19] An example of the modeled flow velocity contours at the inlet to the cell is shown in Figure 7.5.

Gaps of 5 mm gaps between the rings provide optical access to the drift cell. Windows made from UV grade fused silica (Suprasil 312; Heraeus Amersil, Inc.) on the outer cover of the cell provide access to these gaps. An additional window can be mounted at the top of the instrument for viewing the cell axis. Buffer gas temperature can be monitored by inserting thermocouple probes at the top and bottom of the cell. As these probes perturb the gas flow and electric fields, they are usually inserted and removed for periodic monitoring. The cell can be heated to a maximum temperature

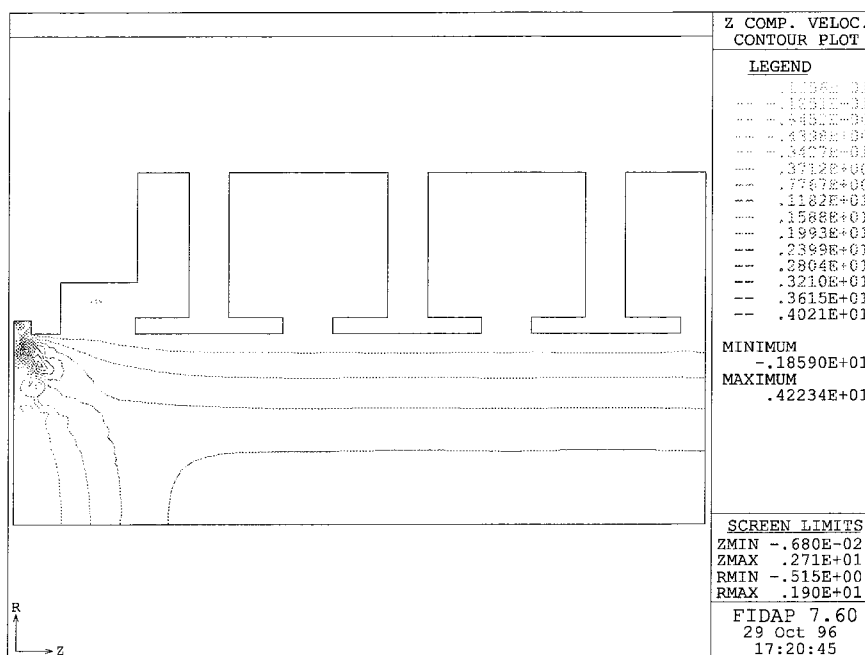


Figure 7.5: IMS fluid flow field calculated with FIDAP. Gas inlet is located to the left of the figure, which shows a small region of the drift cell.

of 328 K with foil heating elements bonded to the outer cover (Thermofoil; Minco Products, Inc.). The outer cover is o-ring sealed and can maintain a vacuum with the inlet sealed of 0.1 torr. All experiments in this study were performed at atmospheric pressure.

Figure 7.6 shows a schematic of the electrical circuit used to reverse the field in the cell for the ping-pong experiment. Two high voltage relays (model WV102VX-50; Magnecraft, Inc.) switch the polarity. Although reliable and inexpensive, these relays exhibit slower response times (1.5 ms) than high voltage transistor switches (1 ns). In addition, contact bounce in the relays creates large electrical interference in all nearby circuitry, so nearby electronics and wiring are carefully shielded. The effect of the slow relay response is to increase the minimum time resolution above the theoretical resolution limit (Table 7.1).

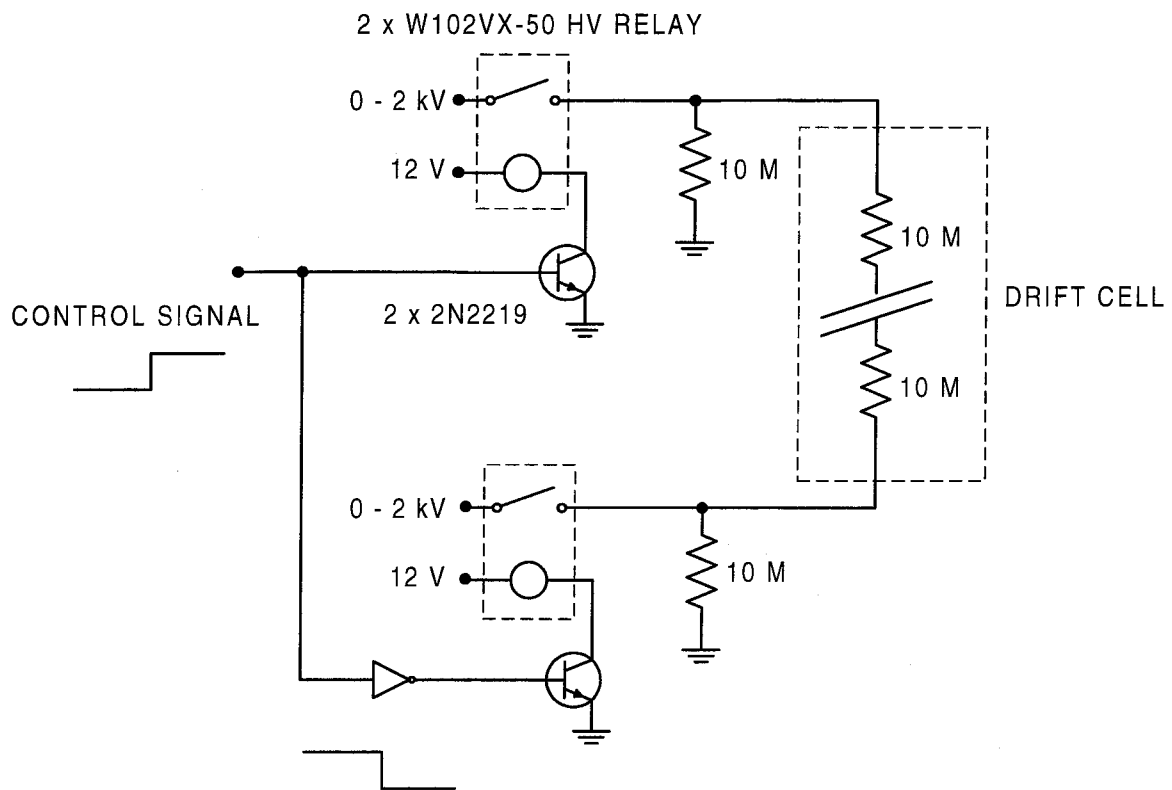


Figure 7.6: Electrical circuit for reversing field in the drift cell.

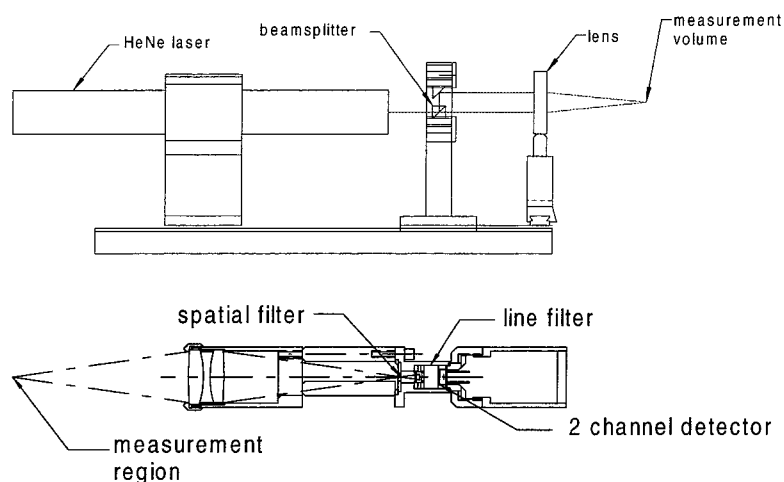


Figure 7.7: Phase Doppler anemometer transmitter (above), and receiver (below). Transmitter baseplate is 45 mm in length and the receiver is 3.3 cm in diameter by 24 cm in length.

7.3.4 Phase Doppler Anemometer

Figure 7.7 shows scale diagrams of the phase Doppler transmitter and receiver. A detailed description of the design and calibration can be found in a recently submitted paper.[20] Here we mention a few key features that are relevant to the interpretation of the experimental measurements.

A table of the optical arrangement is provided in Table 7.2. The optical system was not adjusted or moved since an extensive calibration procedure in the size range from 10–40 μm was performed.[20] The well-established theory of phase Doppler anemometry allows the calibration to be extrapolated to the 1–10 μm range.[8] We employed SCATAP,[21] a phase Doppler simulation program based on Mie theory, to verify the linearity of the phase shift–diameter relationship in the diameter range 1–40 μm . From the calibration procedure, the measurement of diameter should be accurate to either $\pm 5\%$ of the measured droplet diameter or $\pm 1 \mu\text{m}$, whichever is larger. The velocity measurement is inherently more accurate, to $\pm 0.2\%$ based on literature values for similarly configured phase Doppler systems.[22]

Since the instrument performs sequential measurements of an evaporating droplet,

Table 7.2: Phase Doppler Anemometer optical configuration for the current investigation.

Transmitter:	
Beam separation	22.4 mm
Focusing lens focal length	250 mm
Measurement volume diameter ($1/e^2$)	155 μm
Fringe separation	7.1 μm
Receiver:	
Collection lens focal length	100 mm
Detector geometry	Two half-circles split at scattering plane
Detector radius at collection lens	12.5 mm
Collection off-axis angle	30°

the sensitivity of the receiver should increase as the droplet became smaller. To accomplish this task, we built an adjustable signal amplifier circuit and installed it between the receiver pre-amplifier and the sample digitizer. Figure 7.8 shows a schematic of this circuit. A peak detector circuit measures the peak intensity of the phase Doppler burst from one of the detectors. A comparator is then used to compare the peak voltage to pre-set values. The digital data produced by the comparator are then transferred to the computer for analysis. The programmable gain amplifiers (model PGA102; Burr-Brown Corp.) receive digital programming data from the computer based on the comparator data. Additional details regarding the integration of this circuit into the overall data acquisition and control system are presented in the next section.

A LeCroy 9450A digital oscilloscope in sequential acquisition mode digitizes the phase Doppler signals. In this operating mode, high data rates are possible without the intervention of the control computer. The trigger time for each phase Doppler signal in the ping-pong sequence is stored in the memory of the oscilloscope with the raw data from the PDA. A GPIB interface then transfers these data to the computer once the digitizer acquires the full sequence of ping-pong measurements. A software algorithm processes the PDA signals. First, each PDA signal is directed through a digital band pass filter. Following this, an FFT-based algorithm determines

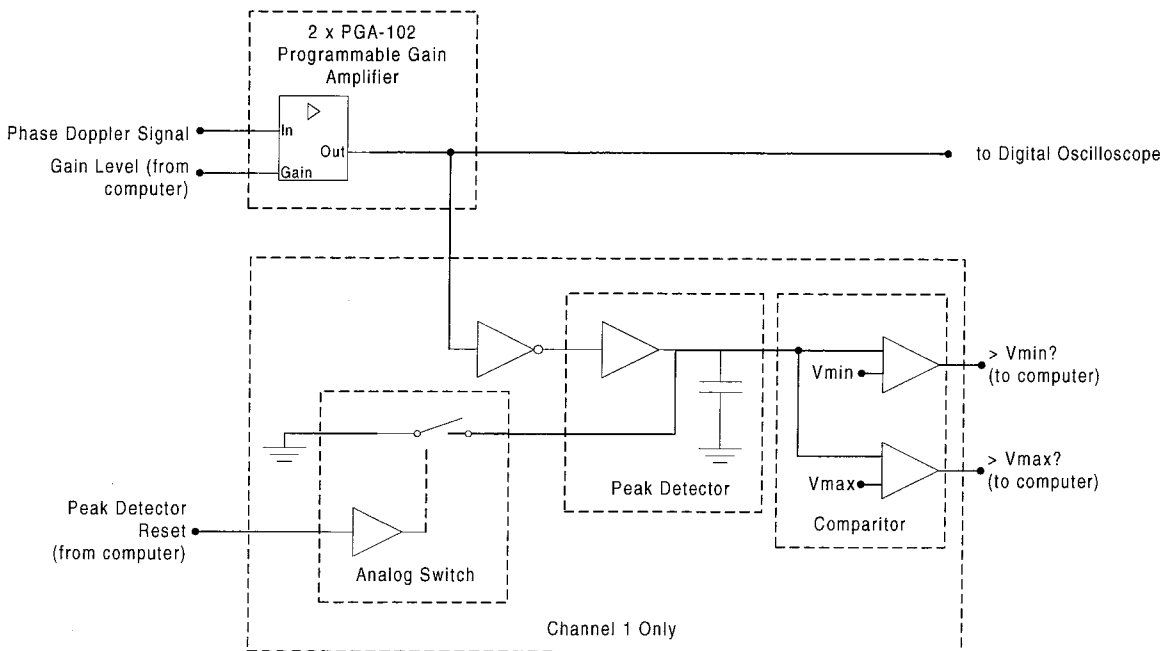


Figure 7.8: Programmable gain amplifier circuit for phase Doppler receiver.

the average frequency of the PDA signals and the phase shift between them. The processed results, along with the raw signals, are stored to disk before the next sequence is acquired.

7.3.5 Data Acquisition and Instrument Control System

A personal computer equipped with a GPIB interface (model PCI-GPIB; National Instruments, Inc.), a multifunction data acquisition board (model Lab-PC+; National Instruments, Inc.) and a digital input/output board (model DIG-100; BSOFT Software, Inc.) controls data acquisition, gain programming, processing of the phase Doppler signals, and the control and timing of the field reversal process in the drift cell. The LabVIEW programming language[23] was used for all for data acquisition and instrument control programs. The result is an automated data acquisition system that can operate without user intervention. This facilitates the analysis of a large number of droplets: thousands of individual droplets can be trapped and analyzed for each spray configuration.

In the discussion that follows, the term “acquisition sequence” is defined as a set of PDA measurements that are acquired using the ping-pong technique. This results in “time series plots” of size and charge for the droplet that has passed through the PDA measurement volume. Figure 7.9 shows a flow chart detailing one acquisition sequence.

Most of the control of the experiment, which includes reading the status of the comparators, resetting the peak detector, controlling the programmable gain amplifiers, and regulation of the field reversal process, requires digital input and output operations. The handshaking features of two 8255A programmable peripheral interface circuits, one located on the data acquisition board and the other on the digital input/output board, are employed for these data transfer operations. In a handshaking operation, a digital output or input port waits until the arrival of a “handshake” pulse before it writes or reads data. This allows for precise timing and synchronization of data.

The major steps involved with the reversal of the field, along with a timing diagram of the process, are shown on the right side of Figure 7.9. The field reverses after a predetermined delay, triggered by the arrival of a signal from the PDA. The arrival time of the PDA signal is provided by a “trigger out” pulse from the oscilloscope. The predetermined delay time is generated digitally using the 8253 counter/timer chip located in the data acquisition board, configured as a delayed pulse generator. This delayed pulse is the handshake signal for the digital output port that controls the relays for field reversal, described in Figure 7.6. An acquisition sequence is terminated when this handshake pulse does not arrive to the output port after a predetermined “timeout” period.

7.4 Experiment

Spectroscopic grade methanol (OmniSolv, EM Science, Inc.) was pumped to the electrospray source at a rate of $.5 \mu\text{l}/\text{min}$. Positively charged droplets were created by applying +800 V to the electrospray source with respect to the first transfer plate.

We adjusted the position of the source obtain the desired initial size distribution according to the procedure described in Section 7.3.2. The nominal distance from the source tip to the first transfer plate was 2.5 mm. A 50.6 V/cm electrostatic field directed the charged droplets upward through the PDA measurement volume, and a buffer gas of nitrogen flowed downward at a rate of 0.3 l/min. Data acquisition proceeded for a period of 4.5 hours and resulted in the trapping and measurement of 2,372 individual electrosprayed droplets.

7.4.1 Size-Charge Correlation of Electrosprayed Droplets

Figure 7.10A–D presents the results of the measurement of size and charge for each droplet that passed through the PDA measurement volume. Each point represents the first measurement in the acquisition sequence obtained for each droplet. Plot C is a correlation of size and charge for these droplets, and demonstrates the high degree of correlation that exists between the size and charge of electrosprayed droplets. Most investigators who have applied PDA measurements to electrosprays have observed correlations between the size and velocity for electrosprayed droplets, but since their measurements were not performed in a uniform field they were unable to make definitive statements on the size-charge correlation. The remarkable feature of Plot C is that the droplets fall into groupings in size-charge space. These groupings are even more apparent when the charge is represented as the percentage of the Rayleigh limit, shown in Plot D. Each group appears to be separated by a charge level that corresponds to approximately 20% of the Rayleigh limit.

7.4.2 Time Evolution of Droplet Size and Charge

The ping-pong technique was employed to obtain a time history of size and charge for each data point in Figure 7.10. Figure 7.11 shows typical time series plots of size and charge. Plots A and B show the measurements of size and velocity made with the PDA, and Plot C shows the the time series of charge which was calculated using Equation 7.3. Plot D shows the sequence of signals from one channel of the PDA.

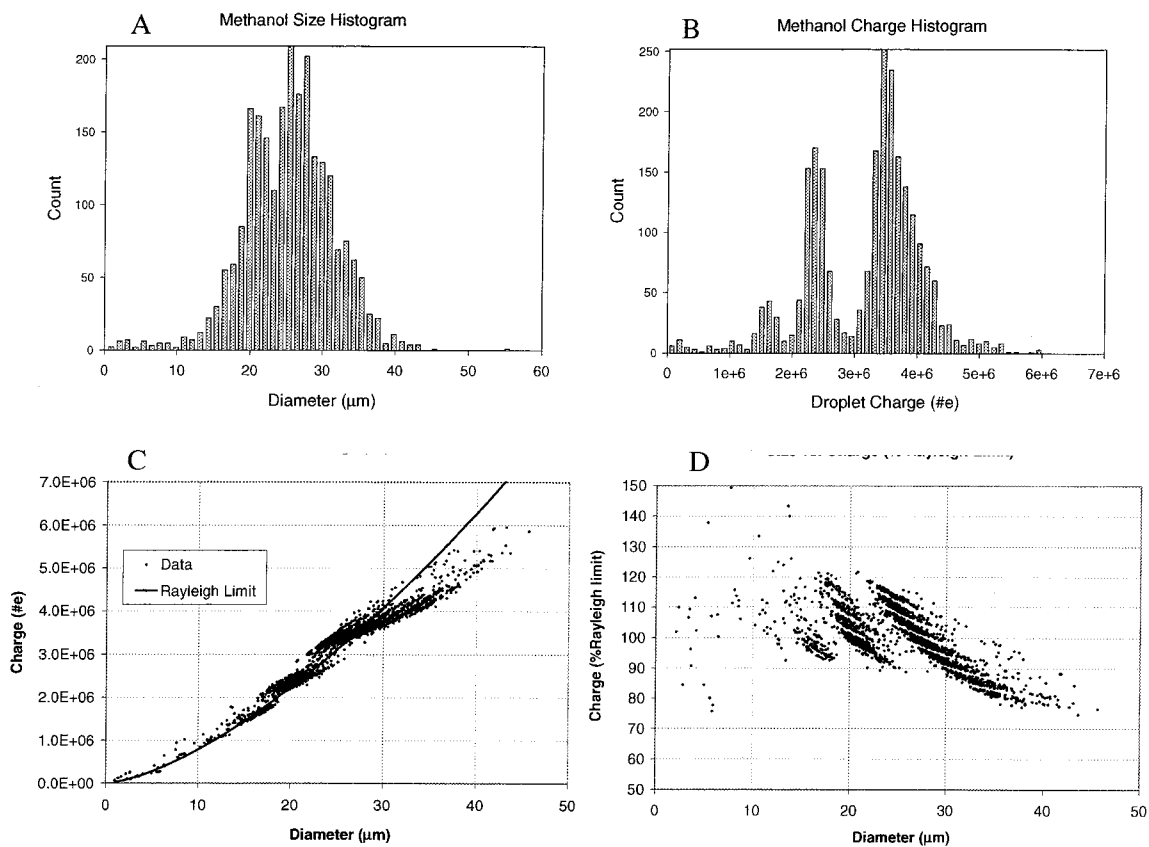


Figure 7.10: Plots of size and charge measurements of individual droplets in a methanol electrospray. A: Droplet diameter histogram; B: Droplet charge histogram; C: Diameter versus charge, plotted alongside the Rayleigh stability limit curve; D: Diameter versus charge, with charge represented as the percentage of the Rayleigh limit.

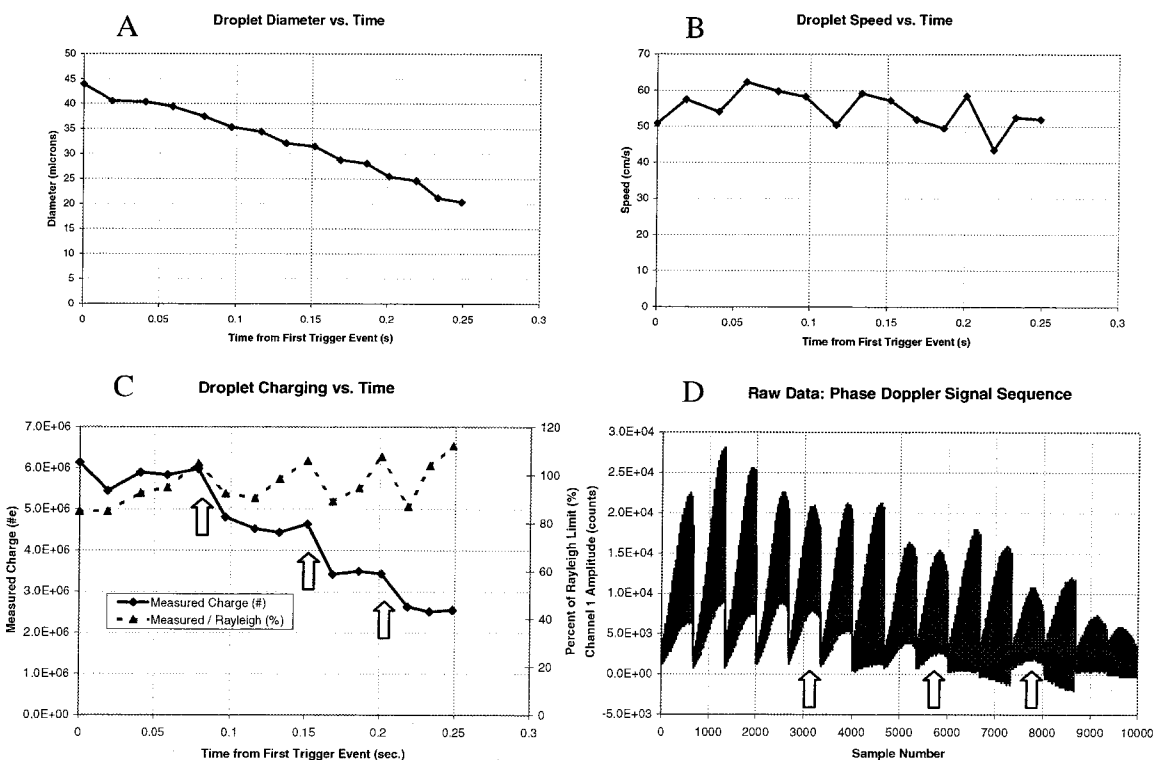


Figure 7.11: Time series plots for a methanol droplet in a 51 V/cm field. A: Time series of droplet diameter; B: Time series of droplet axial speed; C: Time series of droplet charge, presented in number of elementary charges and in percent of the Rayleigh limit of charge. Arrows indicate discrete discharge events; D: Channel 1 raw signal.

Each burst in Plot D corresponds to a datum in the time series plots, and is similar in structure to those in Figure 7.2 but contains a large number of fringes that cannot be resolved in the figure.

During the measurement period, the droplet underwent three discharge events, each indicated with arrows in Plot C and characterized by a step-wise decrease in charge. The onset of these discharge events correspond to a Rayleigh limit of charge that is 105%, 106%, and 108%, respectively, of that predicted by the Rayleigh limit equation (Equation 7.1). The actual value may be greater, as the delay in the field reversal process determines the interval for PDA measurements. Thus, the PDA measurements may not correspond to the precise time at which these discharge events

occur. The time between discharges decreases with each successive event.

The times for corresponding to droplet discharge are marked on the plot of the raw PDA signals in Plot D. The lower envelope of the PDA signals changes at times close to these discharge events. This effect is quantified by defining the signal “visibility” as follows: if the amplitude of the upper envelope is A , and that of the lower envelope is B , then the visibility V is defined as $V = (A - B)/A$. If a droplet is large compared to the fringe separation in the interference pattern of the measurement region, then $V < 1$. A droplet that is smaller or equal to the fringe separation will scatter signals with “high visibility,” such as in Figure 7.2 where $V \cong 1$. The changes in visibility displayed in Plot D are thus inconsistent with the continuous decrease in size shown in Plot A. Note that, for the second and third discharge events, the visibility goes back to one following each event.

On occasion a small, non-evaporating particle was trapped and observed with a characteristic time series like that shown in Figure 7.12. In other tests using solutions with higher salt concentrations, the probability of detecting these particles increased. One interpretation of this observation is that solution droplets are drying to solid residues before detection. Another interpretation is that these non-volatile particles may form over time as the electrospray source accumulates residue from evaporation at the source tip. Such small, non-volatile droplets might be the source of the secondary peak observed by Gomez and Tang[10] in their studies of heptane, to which they added an agent to increase conductivity.

Since the time steps for these sequences are large compared to the characteristic time of disruption, which is thought to be nearly instantaneous, a single series can only supply occasional glimpses of the processes of disruption and discharge. In order to provide a more complete picture of the process, we have searched the database of all acquired series to find the largest number of matches in the initial diameter measurement made by the PDA. The search identified 200 individual time series that start with a diameter of $25.2 \pm 0.5 \mu\text{m}$. Figure 7.13 shows the superposition of all subsequent size and charge measurements that follow from this narrow range of initial droplet size. Plot A shows the composite diameter time sequences, characterized by

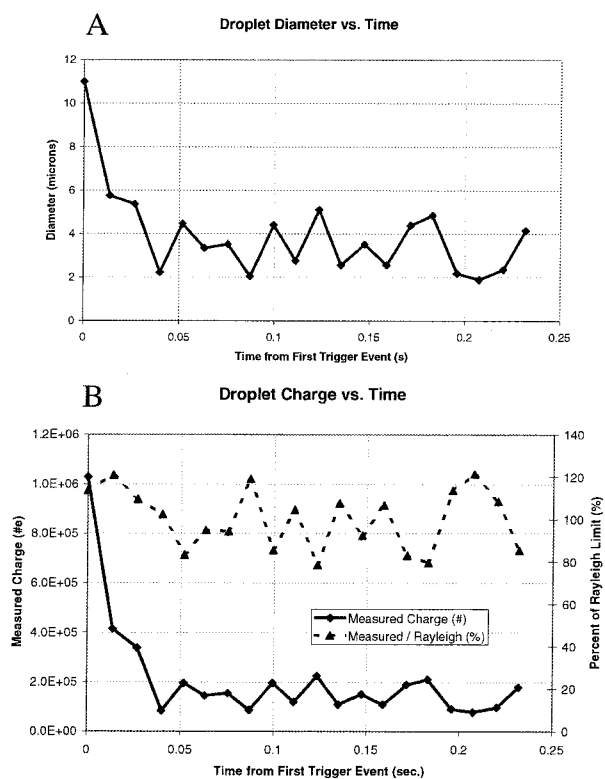


Figure 7.12: Time series plots of (A) diameter and (B) charge from an electrospray of spectroscopic grade methanol, showing a non-volatile particle charged at the Rayleigh limit.

large variability in the measured diameter that falls outside the $\pm 1 \mu\text{m}$ estimated error for PDA measurements of spherical particles. The theoretical evaporation rate of an $25.2 \mu\text{m}$ droplet in a vapor-free gas is also plotted in Figure 7.13A. In this size range, the evaporation rate of a pure droplet consisting of species A is proportional to droplet surface area:

$$a^2 = a_o^2 - 2 \frac{c_A D_{AB}}{c_p} \ln \left[\frac{1 - x_{A\infty}}{1 - x_{As}} \right] t, \quad (7.4)$$

where a is the droplet radius, a_o is the droplet radius at time $t = 0$, c_A is the molar concentration of the species A in the vapor phase, D_{AB} is the binary diffusivity of vapor A in the surrounding gas B , x_{As} and $x_{A\infty}$ are the mole fractions of species A at the droplet surface and far from the droplet, respectively, and c_p is the molar concentration of species A in the liquid phase. The Fuchs, Kelvin, wind effects are negligible in this size range and were therefore excluded.[6] We used a steady-state temperature depression model[6] to calculate evaporative cooling of the droplet surface. This results in a 31°C decrease in the methanol droplet surface temperature. Plot A shows close agreement between observed diameter decrease and that predicted using evaporation theory. Figure 7.13B displays the composite droplet charge time series, and includes charge histograms for the first five groups of measurements. The histograms show some dispersion in the droplet charge, but at most times the droplets are well-behaved and fall into two groupings centered at approximately 90% and at 115% of the Rayleigh limit.

The droplet diameter time series shown in Figure 7.13 display large variability. The same database of time series can be searched for sequences for which the initial diameter and charge are more closely matched to determine the degree of repeatability of the ping-pong measurements. Figure 7.14 shows the superposition of eight time series of size, velocity, and charge for which the initial diameter is $27.2 \pm 0.05 \mu\text{m}$ and the initial charge is $3.49 \pm 0.08 \times 10^6 \text{e}$. In Plot A, the small variations in the measured droplet diameter are repeated with each time sequence. This repeatability is more evident in the measured droplet velocity (Plot B). The reason is that that

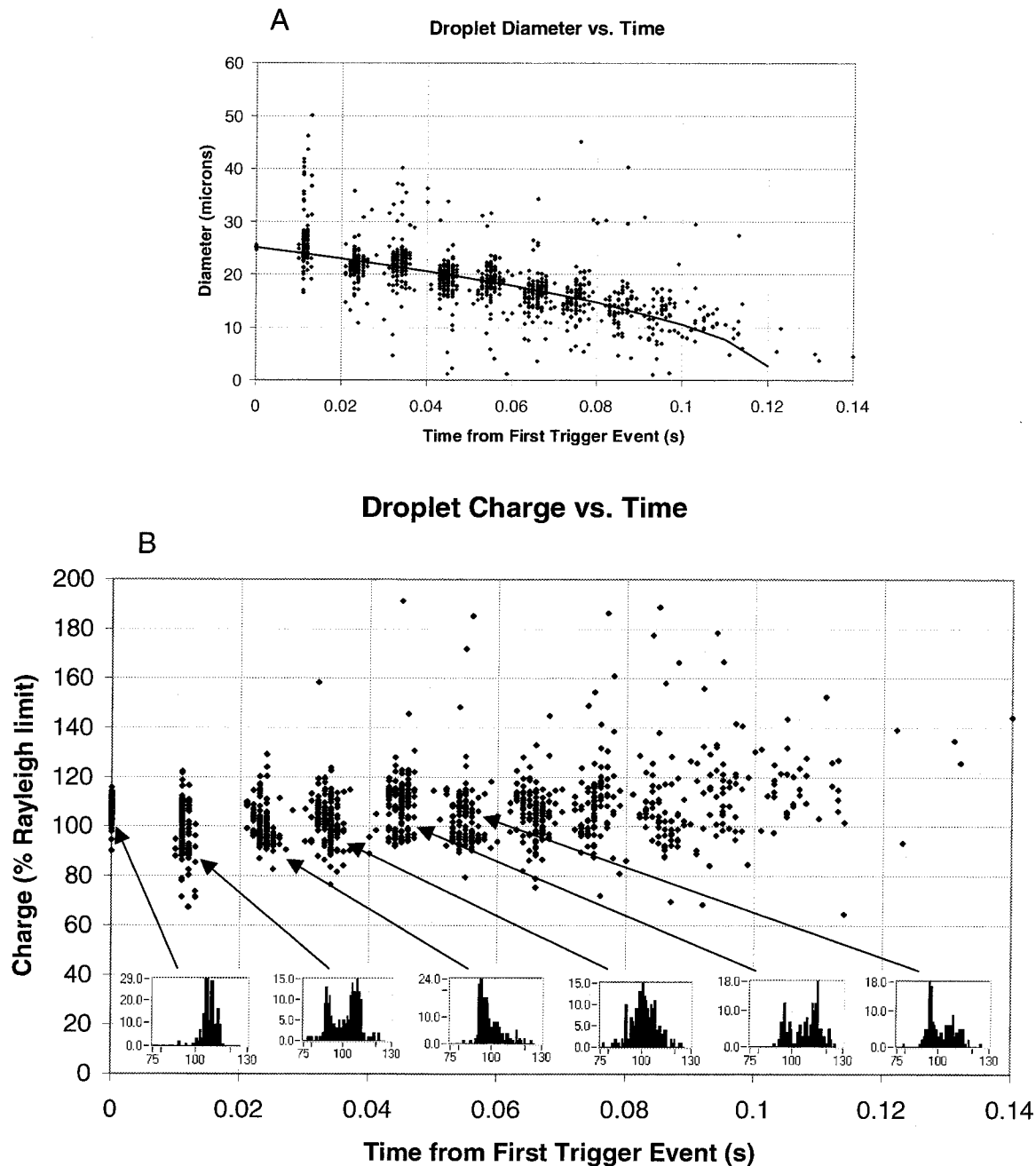


Figure 7.13: Summary of time series plots for methanol droplets with initial diameter of $25.2 \pm 0.5 \mu\text{m}$ in a 51 V/cm field. A: Superposition of diameter time sequences. Also plotted is the predicted evaporation dynamics of a neutral droplet in a vapor-free gas. B: Superposition of droplet charge time sequences, presented as percent of the Rayleigh limit of charge. Shown also are charge histograms for selected groups of measurements.

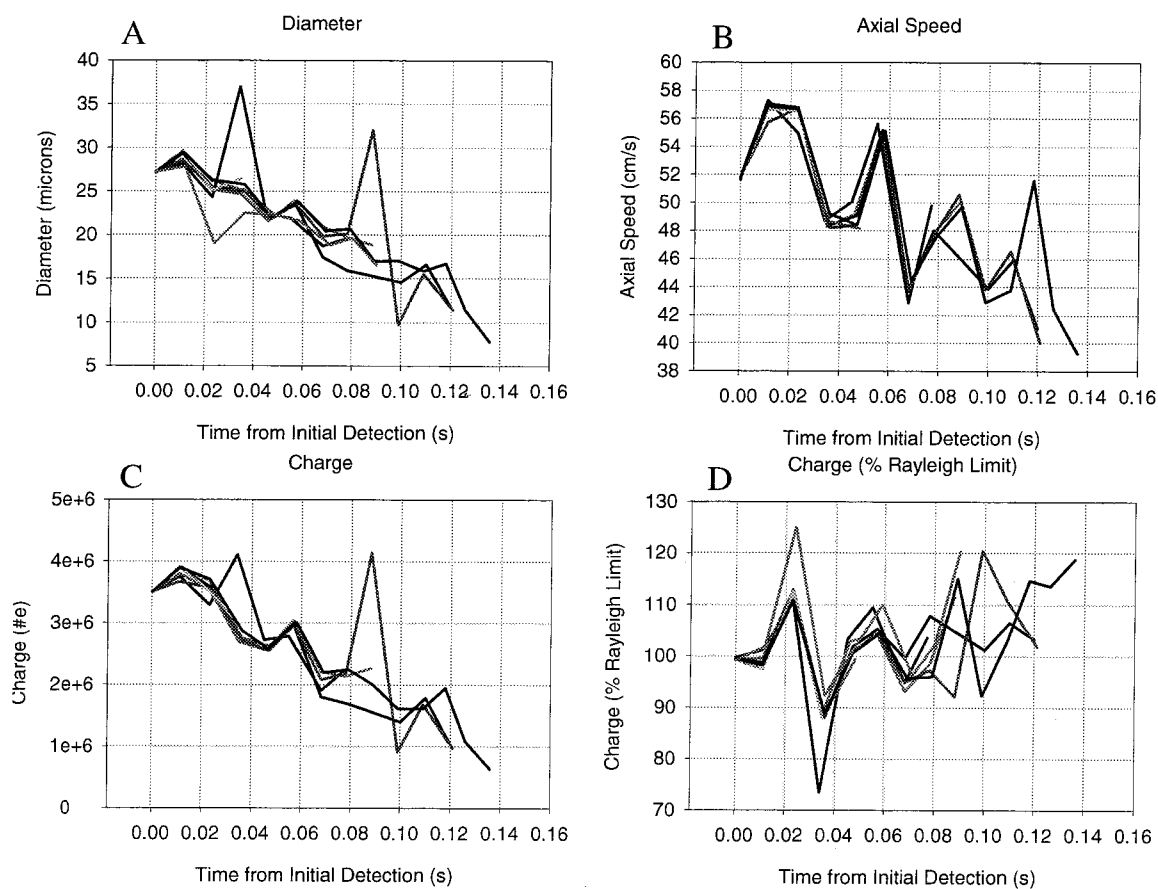


Figure 7.14: Superposition of eight measurements of positively charged methanol droplets with an initial charge of $3.49 \pm 0.08 \times 10^6 e$ and an initial diameter of $27.2 \pm 0.05 \mu\text{m}$.

the velocity measurement is insensitive to droplet morphology. The resulting droplet charge time sequences are shown in Plots C and D. From Figure 7.14, one can see that the seemingly random fluctuations in the measured droplet diameter and charge are in fact repeatable for droplets with the same initial size and charge.

7.5 Analysis

The time series plots of individual droplets and the size–charge correlation for the first droplet measurement in every series represent temporal and spatial representations, respectively, of the electrospray plume. In the case of electrosprays of methanol,

which when operated in cone-jet mode create nearly monodispersed droplet size distributions, each point in the size-charge correlation in Figure 7.10 can be thought of as originating from an identical “parent droplet.” If a true monodispersed distribution were produced at the tip, then a spatial measurement such as that provided by the size-charge correlation would not show distinct groups from Rayleigh fissioning – a temporal measurement would be required to see this effect. For a spatial measurement like that in Figure 7.10 to display droplets that are in varying stages of Rayleigh fissioning, a narrow (but not too narrow) distribution of droplets is needed. In this case, a measurement of size and charge at a single spatial location is quite similar in form to a time series of a single charged droplet.

The data in Figures 7.10 and 7.13 confirm the observations of many studies performed with a variety of liquids: that discharge events caused by Rayleigh instability lead to a reduction in charge of approximately 20%. During evaporation, the overall charge on the droplet is conserved, also consistent with the observations of other investigators.[5, 24] Since our measurement technique measures droplet diameter, it is not expected to detect the 1–2% decrease in mass (0.4–0.7% change in diameter for 20 μm diameter droplets), that investigators using the EDB have been able to observe. The close agreement between the observed decrease in droplet diameter and that predicted using a model of droplet evaporation implies that solvent evaporation is principally responsible for reduction in droplet size.

One interesting result of this study is that droplet discharges are commonly observed which exceed the Rayleigh limit by as much as 20%. This observation contradicts those of Davis and Bridges[7] and others who have examined the process with electrodynamic balances. If one uses the bulk surface tension of methanol to calculate the Weber number (defined as the ratio of inertial to surface tension forces) for a 20 μm droplet, the result, 2×10^{-5} , is five orders of magnitude lower than that required for droplet breakup. However, as Gomez and Tang point out,[10] the surface tension of a droplet near the Rayleigh limit approaches zero so that even the smallest external disturbance can bring about a disruption regardless of Weber number. In light of these observations of high surface charge densities associated with droplet breakup,

we plan to study whether the onset of fissioning may be related to environmental parameters, such as droplet acceleration and gas phase solvent concentration.

The discrepancy between the large changes in visibility and the continuous change in droplet diameter, shown in Figure 7.11, can be explained in a number of ways. One possible interpretation is that the droplet remains approximately spherical but with a conical protrusion similar to those photographed by Hager and co-workers in their study of highly charged methanol droplets,[25] and Gomez and Tang in their study of electrosprays of heptane.[10] Another possible explanation is that the droplet is distorted from its normally spherical shape so as to reduce the signal visibility, but that the distortion is not detected by a phase shift measurement from a PDA. This possibility is consistent with photomicrographs taken of unstable droplets, which show discharge events as sharp conical protrusions from an otherwise spherical droplet.[10, 25]

7.6 Conclusion

We have presented an experimental technique for measuring droplet size and charge of individual electrosprayed droplets using phase Doppler measurements of these droplets as they reside in a uniform electric field. Using the ping-pong technique, one can obtain time series of droplet size and charge. These time series plots complement the observed distribution of size and charge from the electrospray source measured at a single spatial location. The results indicate that the droplets from an electrospray source fall into discrete groupings of size and charge which are representative of successive generations of Rayleigh fissioning events. This quantization of droplet size and charge is unique to operating conditions that are characterized by a narrow, monodispersed distribution in droplet size from the source, an important mode of operation for both electrospray ionization sources and for most electrostatic sprays.

From the analysis of over 2000 individual positively charged droplets from an electrospray of methanol, we observe that disruption taking place at charge levels that

can vary from 100–120% of the Rayleigh limit. This represents higher charge densities than those reported in electrodynamic balance experiments. Investigations are currently underway to understand the degree to which factors such as the concentration of the vapor surrounding the droplet or aerodynamic forces contribute to the onset of Rayleigh instability. In the analysis of the decrease in droplet size as a result of disruption, no noticeable change is observed in excess of normal evaporative loss. Since our measurement technique measures droplet diameter and not mass, we do not expect to be able to detect the 1–2% decrease in mass that other investigators have observed as a result of disruption.

The success of the ping-pong technique, in spite of having no radial restraining force, implies that the process of droplet breakup can be quite gentle, rather than a chaotic explosion. This aspect of mechanism of droplet breakup and discharge can be useful in the design of a high efficiency electrospray sources, since it appears that the droplet trajectory remains stable throughout the discharge process.

Acknowledgements

The authors thank the following agencies for funding this work: National Science Foundation (CHE-9727566), Defense Advanced Research Projects Agency, and the Office of Naval Research.

Bibliography

- [1] Lord Rayleigh. On the equilibrium of liquid conducting masses charged with electricity. *Proc. Roy. Soc.*, 14:184–86, 1882.
- [2] P. Kebarle and L. Tang. From ions in solution to ions in the gas phase: the mechanism of electrospray mass spectrometry. *Anal. Chem.*, 65:972A, 1993.
- [3] Adrian G. Bailey. *Electrostatic Spraying of Liquids*. Electrostatics and electrostatic applications. John Wiley and Sons, Ltd., Somerset, 1988.
- [4] R.A. Millikan. *Electrons (+ and -), Protons, Photons, Neutrons and Cosmic Rays*. Cambridge Univ. Press, 1935.
- [5] M.A. Abbas and J. Latham. The instability of evaporating charged drops. *J. Fluid Mech.*, 30:663–670, 1967.
- [6] E. J. Davis. Microchemical engineering: the physics and chemistry of the microparticle. In Thomas B. Drew, editor, *Advances in Chemical Engineering*, volume 18. Academic Press, Inc., New York, 1992.
- [7] E. J. Davis and M. A. Bridges. The Rayleigh limit of charge revisited: light scattering from exploding droplets. *J. Aerosol Sci.*, 25:1179–1199, 1994.
- [8] W.D. Bachalo and M.J. Houser. Phase Doppler spray analyzer for simultaneous measurements of drop size and velocity distributions. *Opt. Eng.*, 23:583, 1984.
- [9] K. Bauckhage. The phase-Doppler-difference-method, a new laser-Doppler technique for simultaneous size and velocity-measurements. 1. Description of the method. *Part. Part. Syst. Charact.*, 5(1):16–22, 1988.
- [10] A. Gomez and K. Tang. Charge and fission of droplets in electrostatic sprays. *Phys. Fluids*, 6:404–414, 1993.

- [11] A. Doicu, J. Koeser, T. Wriedt, and K. Bauckhage. Light scattering simulation and measurement of monodisperse spheroids using a phase Doppler anemometer. *Part. Part. Syst. Character.*, 15:257–262, 1998.
- [12] Z. Olumee, J.H. Callahan, and A. Vertes. Droplet dynamics changes in electrostatic sprays of methanol-water mixtures. *J. Phys. Chem.*, 102(46):9154–9160, 1998.
- [13] A.A. Naqwi, R.P.A. Hartman, and J.C.M. Marijnissen. Basic studies of electrohydrodynamic atomization process using phase Doppler measurement technique. *Part. Part. Syst. Character.*, 13(2):143–149, 1996.
- [14] Richard C. Flagan and John H. Seinfeld. *Fundamentals of Air Pollution Engineering*. Prentice Hall, New Jersey, 1988.
- [15] John H. Seinfeld and Spyros N. Pandis. *Atmospheric Chemistry and Physics*. John Wiley and Sons, New York, 1998.
- [16] S.-W. Lee and J.L. Beauchamp. Fourier transform ion cyclotron resonance study of multiply charged aggregates of small singly charged peptides formed by electrospray ionization. *J. Am. Soc. Mass Spectrom.*, 10:347, 1999.
- [17] J.M. Grace and J.C.M. Marijnissen. A review of liquid atomization by electrical means. *J. Aerosol Sci.*, 25(6):1005–1019, 1994.
- [18] Ion Source Software. SIMION, 1998.
- [19] Fluent, Inc. FIDAP, 1996.
- [20] J.N. Smith, J.L. Beauchamp, and R.C. Flagan. The design and calibration of a phase Doppler anemometer. *Rev. Sci. Instrum.*, to be submitted, 2000.
- [21] T. Wriedt, Z. Jiang, J. Rheims, N. Warncke, and F. Duersterbeck. SCATAP for windows, 1996. May be downloaded from the website of the Institute of Material Science at the University of Bremen at <http://imperator.cip-iw1.uni-bremen.de/fg01/scatap.html>.

- [22] Norman A. Chigier, editor. *Combustion Measurements*, volume XIV of *Combustion: An International Series*. Hemisphere Pub. Corp., Washington, 1991.
- [23] National Instruments Corp. Labview, 1998.
- [24] S.E. Law. Charge and mass flux in the radial electric field of an evaporating charged water droplet: an experimental analysis. *IEEE Trans. Ind. Appl.*, 25:1081–1087, 1989.
- [25] D.B. Hager, N.J. Dovichi, J. Klassen, and P. Kebarle. Droplet electrospray mass-spectrometry. *Anal. Chem.*, 66(22):3944–3949, 1994.

Chapter 8 The Design and Calibration of a Phase Doppler Anemometer

Abstract

We describe the design and calibration of a benchtop one-dimensional phase Doppler anemometer. Its distinguishing features include a simple yet highly configurable design, low cost, and dependence on off-the-shelf optics and mechanical parts. Its design makes it suitable for instructional use as well as laboratory applications where high data acquisition rates are not needed. We calibrated the instrument and tested its performance by measuring the terminal velocities of 10–40 micron diameter falling water droplets. The resulting calibration is compared to theoretical curves that were calculated using Mie theory and the geometrical optics approximation. Calibration was found to be excellent in the size range studied.

8.1 Introduction

The Phase Doppler Anemometer (PDA)[1, 2] enables the simultaneous measurement of size and velocity of spherical, homogeneous particles in the size range from $0.5 \mu\text{m}$ to several millimeters. Measurements are made at a single spatial location and can be performed in real time with the potential for high data acquisition rates. Moreover, the *in situ* measurements enable detailed characterizations in difficult-to-reach or sensitive flow fields. The measurement does not depend on the intensity of the scattered signal, so one can probe environments where clouding and degradation of elements within the optical path preclude the use of intensity-based techniques.

In spite of these great advantages, the high cost of commercial systems makes this technology unavailable to many. We describe here a simple, highly configurable PDA

system that can be built at low cost (less than \$7000) with a minimum of custom-built parts. The simple, flexible mechanical design and robust signal processing algorithms make it an attractive option for those applications where a commercial instrument is not affordable or provides substantially more performance than is needed, as for example as a demonstration instrument in a laboratory course. A complete parts list, machine drawings, system software, and an operations manual are freely available and can be downloaded from the Electronic Physics Auxiliary Publication Service.[3]

We designed the instrument described here for the study of the evaporation dynamics of charged droplets within an electric field to aid in understanding ion generation in electrosprays. The present instrument can measure droplets moving in a single pre-defined direction, although a Bragg cell or rotating grating could readily be added. A two-element silicon PIN photodiode with a frequency response of 1 MHz is used as the detector for this instrument, since the intended application did not require fast response times. A digital oscilloscope is used to digitize the signals acquired by the receiver and software algorithms are employed for all data processing.

Following a review of the phase Doppler technique, we describe below the optical components, data acquisition system, and signal processing method. We also present a calibration method for droplet diameters in the 10–40 μm range. This calibration technique uses the highly accurate velocity measurements acquired with the PDA to infer droplet diameter from polydisperse water droplets sedimenting in a quiescent gas. Variations of the observed phase shift with the size deduced from the terminal settling velocities are compared to theoretical predictions based on Mie theory.

8.2 Background

A review of the history and basic principles of the phase Doppler technique can be found in the literature.[4] A brief description is provided here, while a more detailed presentation of phase Doppler theory can be found in early studies of the technique.[1, 2] Figure 8.4 shows a schematic diagram of the optical arrangement for a phase Doppler anemometer (PDA). The measurement volume is defined by the intersection

region of two phase-matched laser beams, created by splitting a single beam from a laser and re-focusing. The intensity profile at this intersection region is shown in Figure 8.2a, and is comprised of a sinusoidal fringe pattern with a period, δ , that is a function of the laser wavelength, λ , the beam separation before re-focusing, s , and the Focusing Lens focal length, F .

$$\delta = \frac{\lambda F}{s} \quad (8.1)$$

As a particle passes through the measurement volume (Figure 8.2b), it scatters a time-varying pattern, called a “Doppler burst,” identical in form to the intensity profile shown in Figure 8.2a but with a period, τ , defined by the velocity of the particle in the plane perpendicular to the fringes, v .

$$\tau = \frac{\delta}{v} \quad (8.2)$$

Figure 8.2c shows how the same optical arrangement is used to determine the diameter of a spherical, homogeneous particle. The figure traces the wavefront from each beam as it passes through a purely refracting particle, such as a droplet of water, and reaches an external detector. Each beam is phase-delayed by a different amount due to the surface curvature of the particle. For a reflecting particle, the beams are similarly phase delayed since surface curvature causes them to travel slightly different distances in the surrounding medium (usually air) to the detector. The instrument described here uses two detectors, arranged as shown in Figure 8.1. The difference in the phase delay recorded by each detector results in signals that are phase-shifted in time. This temporal phase shift is linearly related to the particle diameter, d , according to[2]

$$d = \frac{1}{2b} \left(\frac{\lambda_o}{\pi n_c} \right) \Phi, \quad (8.3)$$

where n_c is the particle refractive index, λ_o is the wavelength of the laser, Φ is the measured phase shift between two detectors, and b is a “geometrical factor” that is a function of the experimental arrangement and droplet properties.

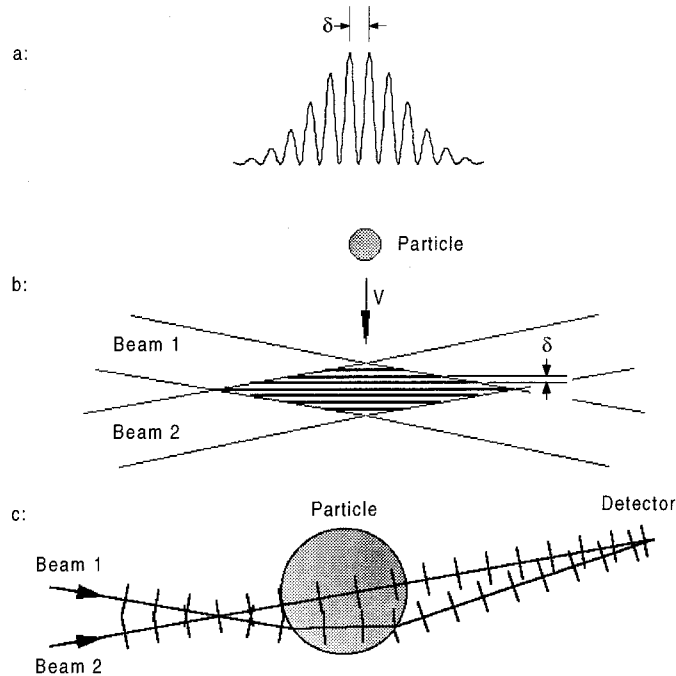
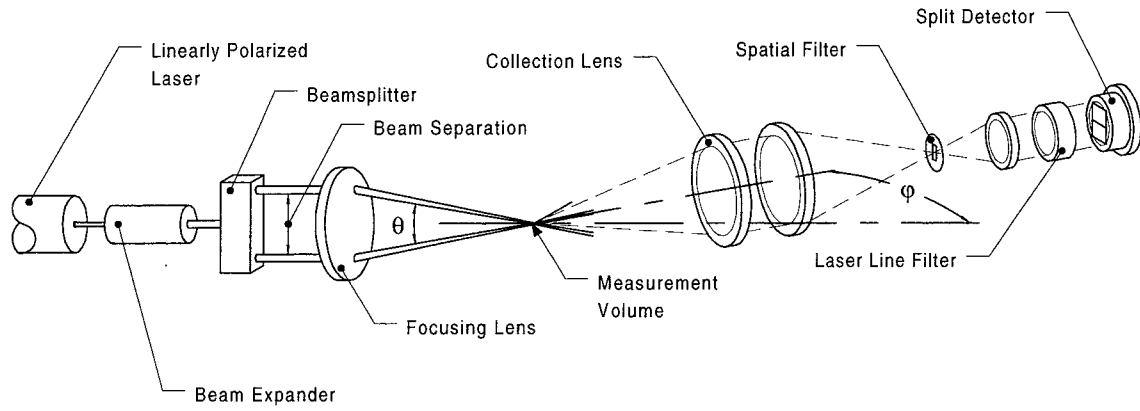


Figure 8.2: Theory of PDA measurements. (a) Radial intensity profile at the measurement volume. (b) The measurement volume, defined by the intersection of two phase-matched laser beams. (c) Schematic diagram of path of each beam through a refracting particle and to an external detector.

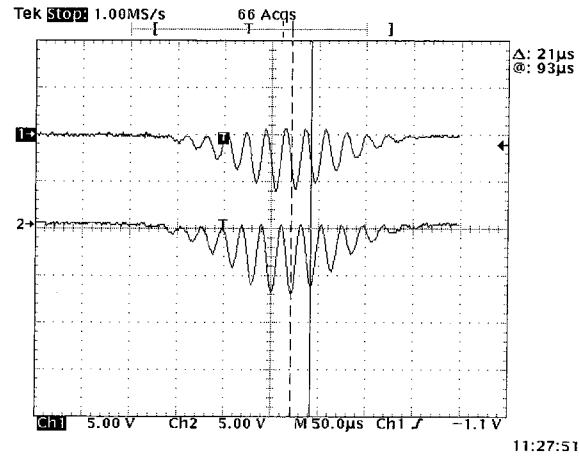


Figure 8.3: Typical signals from a phase Doppler receiver.

A typical set of signals from the instrument is shown in Figure 8.3 (inverted by detector pre-amplifiers). In the figure, the essential features of the measurement technique can be seen: the period of both signals can be seen as equal, and a small phase shift between signals can be detected.

8.3 System Description

Figure 8.4 shows a schematic diagram of the basic system components, which are described in detail below. In designing the PDA, the primary objectives included low cost, the use of off-the-shelf optics and hardware whenever possible, and the ability to easily modify the system configuration to accommodate changing measurement requirements.

8.3.1 Optical Components

Figure 8.1 shows the optical configuration for the PDA and identifies the major components of the transmitter and receiver. Table 8.1 demonstrates how the configuration of the transmitter and receiver can be adjusted to accommodate a wide range of sizes and velocities. The simple two detector design of the receiver leads to phase

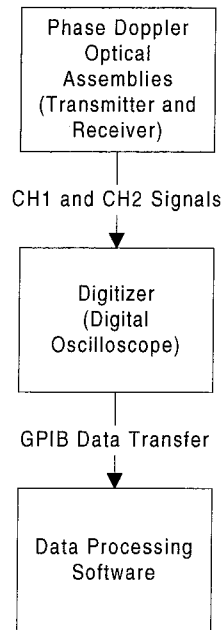


Figure 8.4: PDA system schematic.

wrap-around at 2π that defines the maximum measurable diameter for a given configuration. The velocity range is defined by the digitization rate and the detector frequency response.

Transmitter

The phase Doppler transmitter generates a pair of equal intensity laser beams from a single source beam and focuses them to an intersection point, thus forming the measurement volume. Figure 8.5 shows an assembly diagram of the transmitter. All transmitter optical components are mounted on an optical rail (model URL-18; Newport Corp.), allowing great flexibility in the optical arrangement while maintaining some degree of portability. The present instrument employs a 10 mW, polarized red HeNe laser (model 05LPH991; Melles Griot, Inc.) as the radiation source. Recent advances in the size and performance of laser diodes make this a viable option that would reduce the size of the transmitter considerably. Depending on the requirements for the measurement volume, a beam expander can be placed in the beam directly

Table 8.1: Estimated PDA system maximum particle size and velocity.

Transmitter Focal Length (mm)	Focused Beam Waist Diameter (μm)	Beam Separation (mm)	Fringe Spacing (μm)	Maximum Velocity ¹ (m/s)	Theoretical Maximum Diameter ²	
					200 mm Collection Lens (μm)	100 mm Collection Lens (μm)
250	296.2	10	15.8	15.8	417.0	208.5
		20	7.9	7.9	208.5	104.3
125	148.1	20	4.0	4.0	208.5	104.3
		40	2.0	2.0	104.3	52.1

1. 1 MHz detector limit

2. Maximum diameter corresponds to water droplets and a 2π phase shift.

after the laser, using off-the-shelf mounting hardware compatible with the optical rail. An unpolarized beamsplitter and turning mirror split the original beam into two parallel beams of equal intensity. Although the current system does not employ frequency shifting, a Bragg cell can be placed in the path of one of the beams after the beamsplitter assembly. A spherical achromat focuses the beams to form the measurement volume. For the experiments presented below, a 250 mm focal length achromat is used (model PAC-079; Newport Corp.).

Receiver

The receiver contains two detectors for measuring the velocity and phase shift. An assembly diagram is shown in Figure 8.6. A pair of lenses collects laser light scattered by particles in the beam and refocuses it to a spatial filter slit. Only light scattered from the measurement volume passes through the slit. This light is recollimated and passes through a laser line filter (model 35-5990; Coherent, Inc.) to improve signal quality by reducing exposure of the detector to ambient light. The scattered light then illuminates the detectors comprising a two-element silicon PIN photodiode (model UV-140BQ-2; EG&G Canada Ltd.). The detector splits the light collected by the receiver into two equal regions: one above the scattering plane and one below. The geometry of this split detector is shown in the upper right of Figure 8.1. It consists of a square region that is divided into two equal-sized rectangles. For

Table 8.2: PDA transmitter parts list.

Location in Figure 8.5	Description	Quantity
Machined Parts:		
1	laser mounting bracket	1
Off-the-Shelf Parts:		
2	laser mount	1
3	adapter plate	3
4	optical rail: 457 mm length	1
5	10 mW, polarized HeNe laser head	1
6	micro optical rail: 76.2 mm length	1
7	micro series spacer set	1
8	compact carrier with channel	2
9	kinematic mirror mount: 25 mm	2
10	micro optical rail: 152 mm length	2
11	base	1
12	beamsplitter cube: 12.7 mm	1
13	right angle prism with Aluminum hypotenuse	1
14	lens mount: 76.2 mm diameter	1
15	achromat: 250 mm focal length x 38.1 mm diameter	1
16	post: 50 mm length	1
18	compact carrier, flat	1
19	holder: 50 mm	1

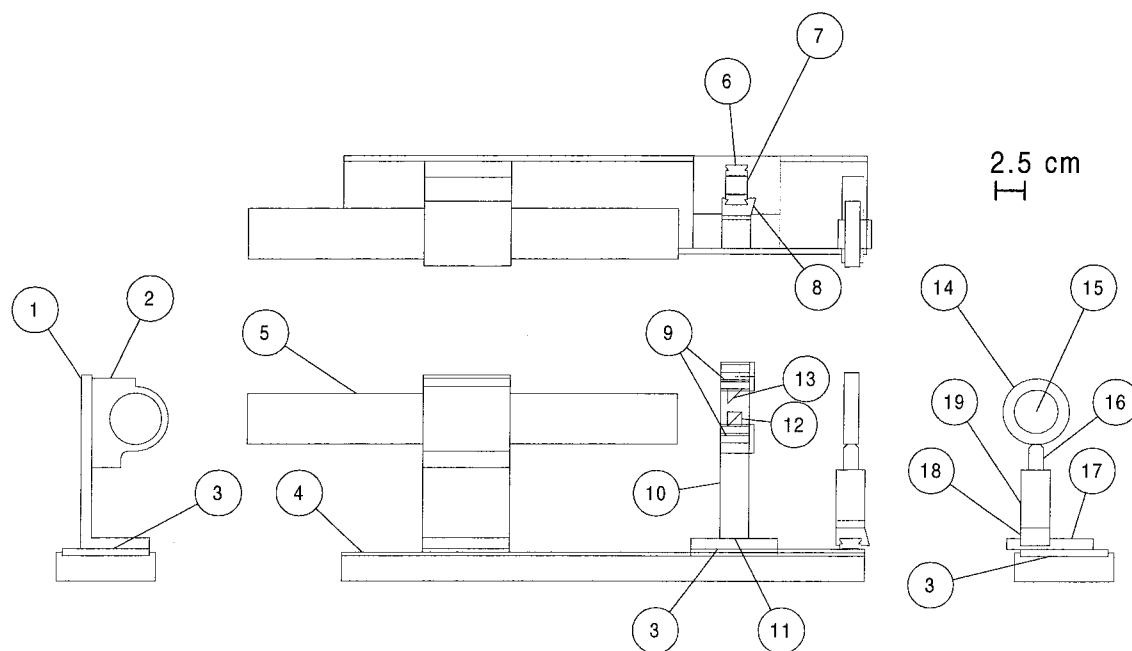


Figure 8.5: PDA transmitter assembly diagram. See Table 8.2 for parts identification.

the present investigations, the photodiodes are operated in photovoltaic mode that produces extremely low noise levels but slow response times. Biased mode operation of the photodiodes would yield higher frequency response. For the shortest response times of several MHz, the photodiodes can be replaced with a bifurcated fiber optic bundle linked to two external avalanche photodiodes or photomultiplier tubes.

A preamplifier is located within the rear cover of the receiver. It consists of two transimpedance amplifier circuits for converting the current output of each photodetector to a voltage. Figure 8.7 illustrates this circuit. External programmable gain amplifiers (model PGA-102; Burr-Brown Corp.), also shown, are located in a separate enclosure 1 meter from the receiver to enable amplification of the signals from the preamplifiers of up to two decades. Two digital lines from the control computer provide gain control. The signals from the amplifier stage are then digitized for processing, as described next.

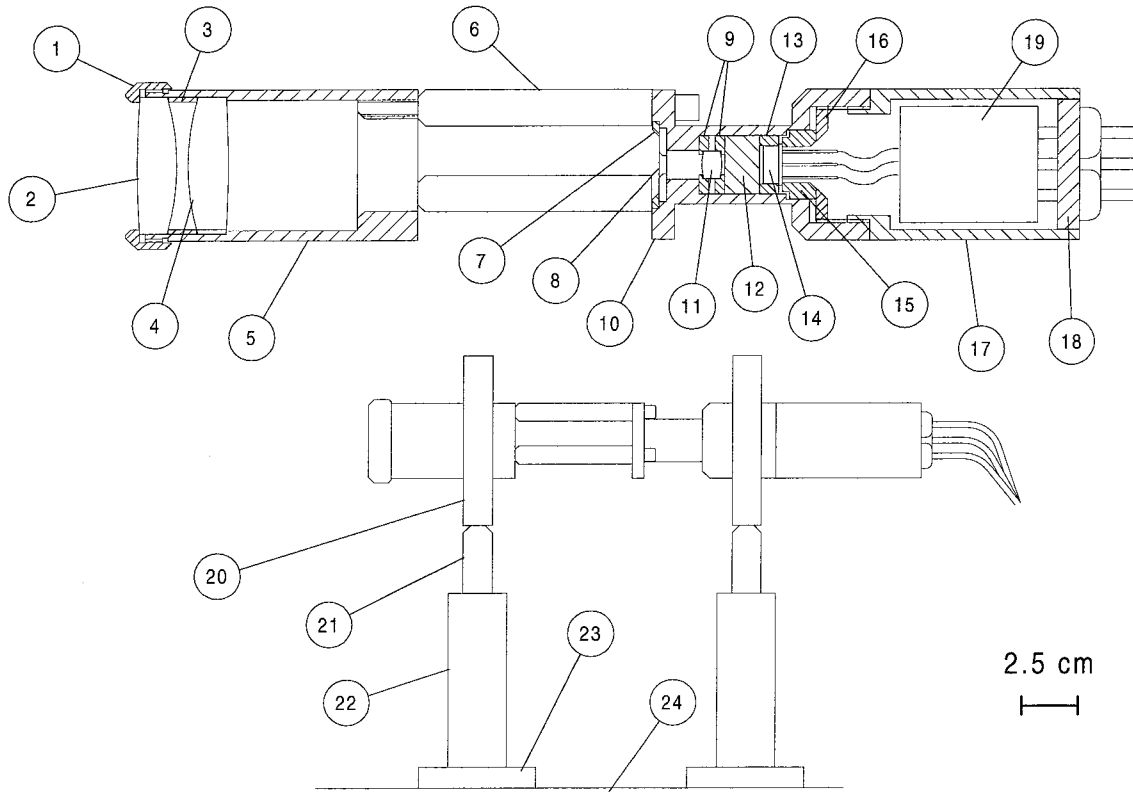


Figure 8.6: PDA receiver assembly diagram. See Table 8.3 for parts identification.

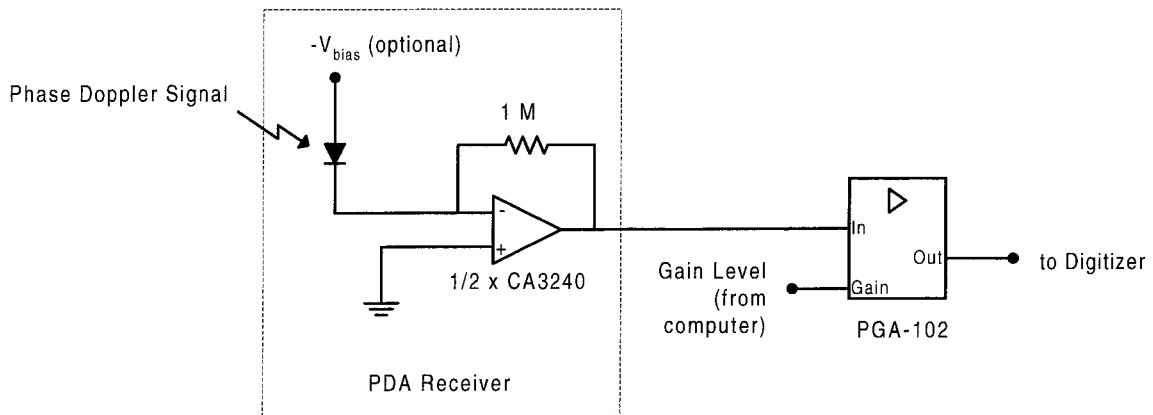


Figure 8.7: PDA pre-amplifier and programmable gain amplifier circuit.

Table 8.3: PDA receiver parts list.

Location in Figure 8.6	Description	Quantity
Machined and Custom-Built Parts:		
1	front lens retainer	1
3	receiver lens spacer	1
5	front tube	1
7	spatial filter ring	1
9	lens ring	2
10	receiver rear tube	1
14	detector holder	1
16	detector retainer	1
17	rear cover	1
18	receiver end cap	1
19	preamplifier	1
Off-the-Shelf Parts:		
2	achromat: 100 mm focal length x 30 mm diameter	1
4	achromat: 100 mm focal length x 30 mm diameter	1
6	micro post: 50 mm length	3
8	100 m mounted slit	1
11	achromat: 10 mm focal length x 6 mm diameter	1
12	633 nm interference filter	1
14	silicon PIN photodiodes	1
20	adjustable radius chuck	2
21	post: 50 mm length	2
22	holder: 50 mm length	2
23	base	2
24	optical rail: 457 mm length	1

8.3.2 Signal Digitization

We employ a model 9450A digital oscilloscope (LeCroy SA) to digitize the phase Doppler signals. Other digitization methods that have been successfully employed include the model TDS410A digital oscilloscope (Tektronix, Inc.), and a waveform acquisition board (model WAAGII; Markenrich Corp.) that plugs directly into a ISA slot within the personal computer. The digital oscilloscope communicates with the control computer via a GPIB interface (model PCI-GPIB; National Instruments, Inc.).

The choice of digitization method is the primary factor in determining the data acquisition rate. For real-time measurements in which each acquired signal is processed and displayed before the next is acquired, the maximum data acquisition rate is determined primarily by the time required to transfer the signal from the oscilloscope to the computer, nominally 8 ms. For faster acquisition times, the model 9450A oscilloscope can be operated in sequential mode. In this mode, up to 200 PDA signal pairs are acquired and stored in segmented memory for later retrieval with a minimum delay time of 100 μ s between signals. Recent advances in plug-in digital oscilloscope boards make these an attractive option. Modern oscilloscope boards feature fast data transfer rates and large memory sizes that enable higher data acquisition rates with real-time presentation of data.

8.3.3 Signal Processing

Signal processing for the PDA is performed exclusively in software using LabVIEW.[5] The processing algorithm performs two basic operations on each digitized signal:

- Separation of the higher frequency sinusoidal signal from the low frequency Gaussian pedestal to enable measurement of the frequency of that sinusoid from which the velocity of the particle is calculated.
- Measurement of the phase difference between the two signals to obtain the particle size.

In the past several years the method of Fast Fourier Transforms (FFT) has become one of the most widely used algorithms for performing both of these operations, and it is the method adopted here. The processing algorithm is based on the FFT followed by an interpolation step,[6] and is summarized next.

The discrete Fourier transform X_n of the sampled signal x_k from each detector is given by:

$$X_n = \frac{1}{N} \sum_{k=0}^{N-1} x_k e^{-j2\pi kn/N}, \quad 0 \leq n \leq N-1 \quad (8.4)$$

Here, N is the number of sampling points. The frequency resolution of the measurement is related to the sampling interval, Δt , as follows:

$$\Delta f = \frac{1}{N \cdot \Delta t}. \quad (8.5)$$

The interpolation step is needed because the true signal frequency will very rarely coincide with a spectral line, $f_n = n \cdot \Delta f$. Rajaona and co-workers derived this deviation of the true frequency from the nearest spectral line X_m . The result is given below:

$$f_m = \frac{m + \varepsilon_m}{N \cdot \Delta t}, \quad (8.6)$$

$$\varepsilon_m = \text{Im} \left(\frac{j(B-1)}{B+1} \right), \quad (8.7)$$

$$B = \frac{X_m - X_{m+1}}{X_m - X_{m-1}}. \quad (8.8)$$

The corresponding phase for each signal is given by:

$$\Phi_m = \arg(A_m), \quad (8.9)$$

$$A_m = (2X_m - X_{m+1} + X_{m-1}) \frac{Z_m(Z_m^2 + 4\pi^2)}{8\pi^2(1 - e^{-Z_m})}, \quad (8.10)$$

$$Z_m = \frac{j2\pi(B-1)}{B+1}. \quad (8.11)$$

The phase for each signal is, therefore, derived using Equations 8.9–8.11. The difference between the two phases is the phase shift. This phase difference is adjusted by

2π as needed in accordance with the expected direction of the phase shift (derived from the refractive index of the droplet and the indicated flow direction). For the signal frequency, Equations 8.6–8.8 are applied to the signals from both detectors and the values for f_m subsequently averaged.

Validation checks are applied to each sample to insure a reliable frequency and phase shift measurement. Signal rejection will occur if any of the following are not satisfied: (1) The measured frequency of both signals must agree to within 1%. (2) The peak amplitude power of the Fourier-transformed signals must agree to within 25%. (3) The measured phase shift lies in the ranges 0° – 1° or 359° – 360° (added to reduce the occurrence of phase wrap-around).

8.3.4 Software Interface

Figure 8.8 shows a flowchart of a single acquisition performed by the system software. As the flowchart for the data acquisition module shows, the display of processed data is made after all the data are acquired by the oscilloscope. This is done in order to minimize the time between successive data points. All settings that control data processing are entered at the front panel of the control software, pictured in Figure 8.9.

8.4 Particle Size Calibration

The geometrical factor, b , in Equation 8.3 can be calculated in the geometrical optics regime for purely refracting, homogeneous particles (e.g., liquid water droplets), [2] resulting in:

$$\begin{aligned}
 b_{refract.} &= 2 \left[1 + n'^2 - \sqrt{2}n' \left(1 + \sin \frac{\theta}{2} \sin \psi + \cos \frac{\theta}{2} \cos \psi \cos \varphi \right)^{1/2} \right]^{1/2} \\
 &- 2 \left[1 + n'^2 - \sqrt{2}n' \left(1 - \sin \frac{\theta}{2} \sin \psi + \cos \frac{\theta}{2} \cos \psi \cos \varphi \right)^{1/2} \right]^{1/2} \quad (8.12)
 \end{aligned}$$

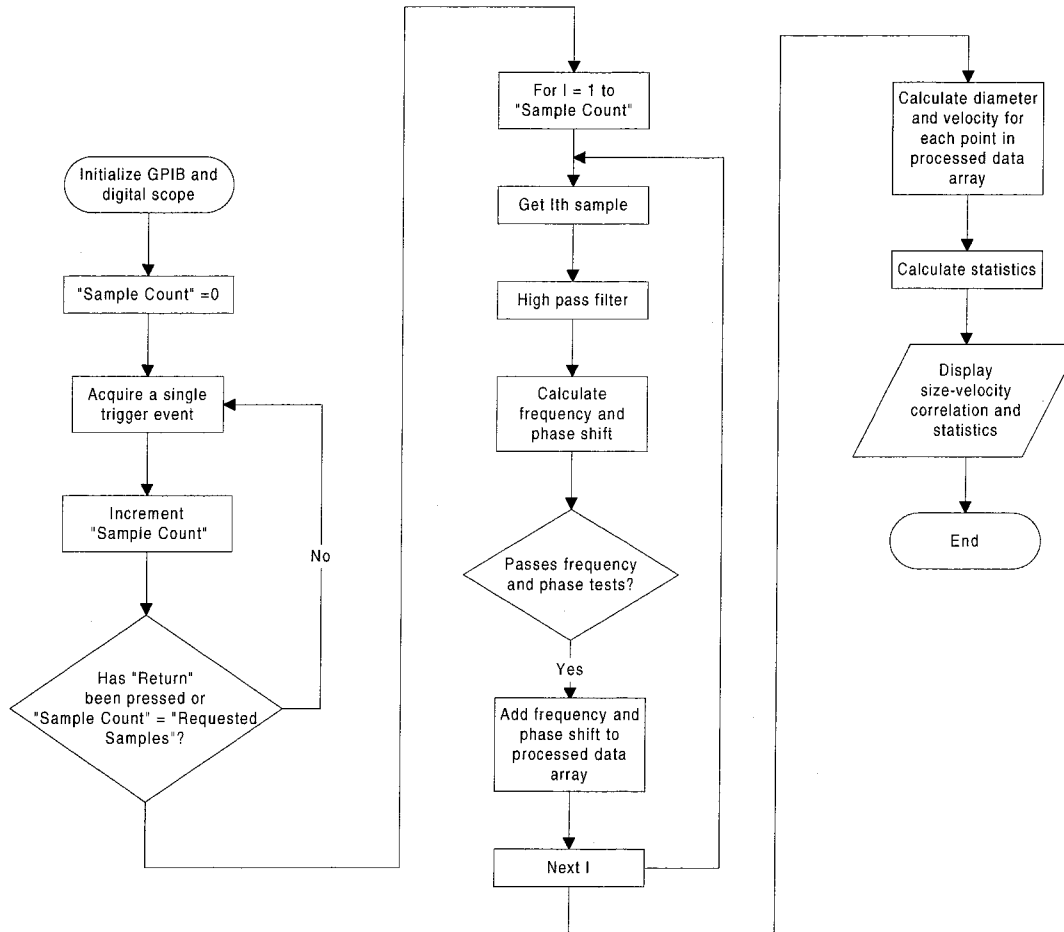


Figure 8.8: Flowchart for PDA calibration and data acquisition modules.

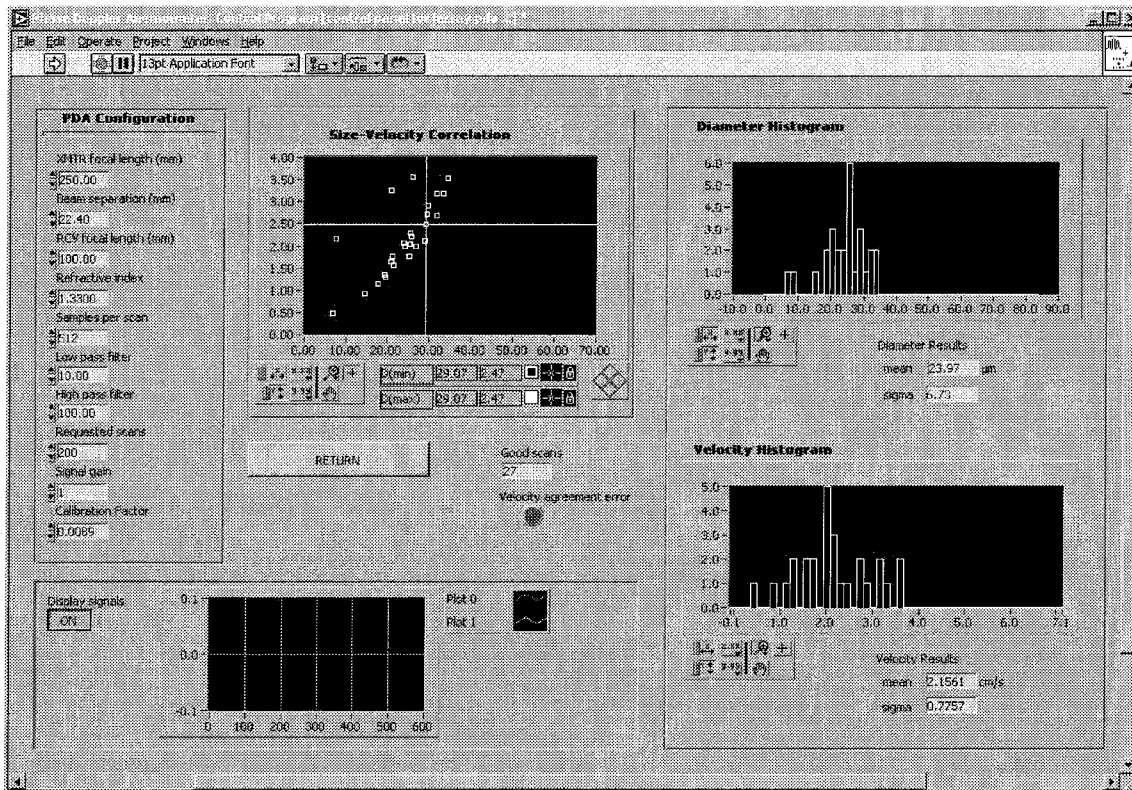


Figure 8.9: Data acquisition panel for PDA control software.

where $n' = n_d/n_c$, and is the ratio of the refractive indices of the surrounding medium (n_d) to that of the particle. In Equation 8.12, θ and ψ are the beam intersection angle and the off-axis collection angle and are shown in Figure 8.1. ϕ is the elevation angle of the projection of the detectors on the collection lens (measured to the centroid of each detector region) relative to the plane defined by the axes of the transmitter and receiver. The geometrical optics approximation used in generating Equation 8.12 is quite accurate to droplet sizes as small as $5 \mu\text{m}$. [1] For smaller droplet sizes, Mie theory must be invoked. In cases involving pure refractive scatter the Mie theory solution preserves the linear “diameter- Φ ” calibration relationship and well as the dependence of the geometrical factor on instrument configuration.

Although Equation 8.12 and the more rigorous Mie theory solution are a quite valid means of generating the geometrical parameter, b , in Equation 8.3, in practice this is not done since the angles θ , ψ , and ϕ may not be known to the necessary accuracy. Instead, the instrument must be calibrated by performing numerous measurements on particles of known diameter and refractive index to obtain the constant, b . A subsequent measurement of phase shift can then be corrected for a relative change in optical setup using the dependencies in Equation 8.12.

Calibration of any optical particle sizing system is often the most challenging aspect in its operation. Most commonly, calibrated polystyrene latex spheres (PSL) or some form of the vibrating orifice (“Berglund-Liu”)[7] droplet generator is used, although recently some success has been reported using a microlens affixed to a glass plate.[8] None of these techniques can be used to obtain a continuous size span of calibrated aerosol over a broad range of diameters. None of the techniques can be applied with ease in the size range from $5\text{--}50 \mu\text{m}$, a range of great importance for characterizing sprays such as those produced by pressure atomizers. To address this need, we have made use of the unique quality of a phase Doppler to make a simultaneous measurement of size and velocity. By measuring the terminal velocity of a falling droplet and inferring the droplet diameter from this this highly accurate measurement of velocity, the measured phase shift can be correlated with the droplet’s aerodynamic diameter. The droplets can be formed from a variety sources, and the

Table 8.4: Optical configuration for Instrument Calibration.

Transmitter:		
Beam Separation		22.4 mm
Front Lens Focal Length		250 mm
Measurement Volume Diameter		155 μm
Fringe Separation		7.1 μm
Receiver:		
Collection Lens Focal Length		100 mm
Geometry of Detector at Collection Lens	Two Half-Circles, Split at Scattering Plane	
Detector Radius at Collection Lens		12.5 mm
Collection Off-Axis Angle		30°

size span of the generated droplets determines the size range of the calibration. For our investigations, which primarily focus on the size range from 1–50 μm , a household ultrasonic humidifier was used (model 696; Sunbeam Corp.).

The optical configuration of the PDA is listed in Table 8.4 for these calibration studies. Using these parameters, a theoretical prediction of the calibration curve for water droplets can be made. Since the prediction is based only the design parameters of the instrument, it is not expected to match perfectly with the experimentally derived calibration, but will instead be linearly proportional according to Equation 8.3. The calculations were made using both the geometrical optics approximation (Equations 8.3–8.12), and using Mie theory. The program SCATAP[9] was used for the Mie theory calculations. The result is shown in Figure 8.10. As the results in the figure show, the geometrical optics approximation provides quite a good representation of the calibration curve. The Mie theory calculation of the diameter– Φ relationship in the size range from 1–50 μm shows that this relationship is not precisely linear, but exhibits a superimposed low intensity, slowly-varying oscillation. Although this is a small correction to the calibration curve, it is not undetectable and emphasizes the importance of calibrating under conditions most closely resembling the planned experiments. A sixth-order polynomial fit is made on the theoretical curve to reduce calibration errors caused by this oscillation. This polynomial is plotted in Figure 8.10.

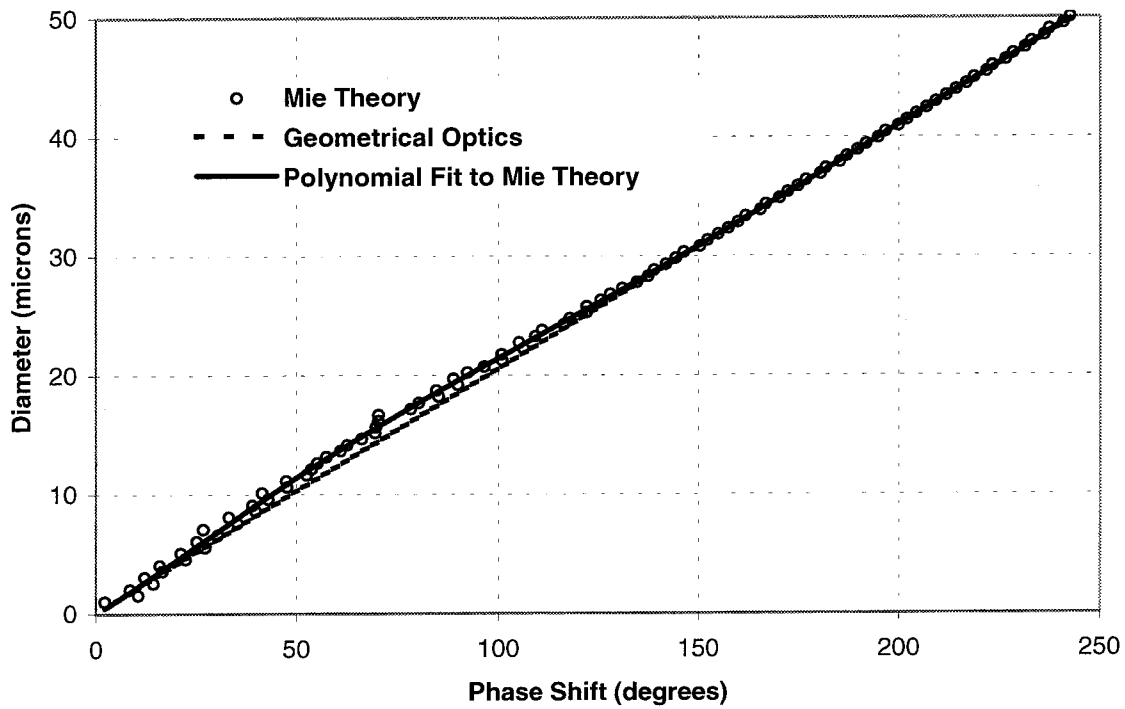


Figure 8.10: Theoretical calibration curves obtained with geometrical optics theory (Equations 8.3–8.12) and with Mie theory (SCATAP results), using design parameters for optical configuration. Also plotted is a 6th order polynomial least squares fit to the Mie theory data.

For the size range from 5–50 μm , Stokes flow around the droplet can be assumed. In this regime, the relationship between the droplet diameter, D_d , and its terminal velocity, v_t , is given by the following expression:[10]

$$D_p = \sqrt{\frac{18\mu v_t}{\rho_p g}}, \quad (8.13)$$

where μ is the viscosity of the surrounding gas, ρ_p is the droplet density, and g is the gravitational constant. The primary difficulty in calibrating by this technique can be demonstrated using Equation 8.13 by calculating the range of velocities for water droplets at atmospheric pressure. The size range from 5–50 μm corresponds to a range in velocities from less than 0.1 to 7.4 cm/s. Such low velocities can be easily perturbed by convection in the surrounding gas. Even small temperature differences can have a great effect. Thus special effort was made to protect the measurement region from air currents in the lab. A diagram of the calibration apparatus is shown in Figure 8.11. The measurement volume was located inside an o-ring sealed chamber filled with air at atmospheric pressure. A water reservoir located at the base of the chamber was used to collect the falling droplets and to humidify the air within the chamber to reduce the rate of evaporation. Droplets from the source fall into the chamber through a 22 cm long ceramic tube with a 1.6 mm inner diameter, which eliminates the influence of laboratory air currents. Since water droplets cool as they evaporate, convection due to temperature gradients in the cell can develop. This is remedied by providing sealed insulation over the area of the chamber that is exposed to the droplets from the source. Thermocouples placed in contact with the upper and lower end caps of the chamber verified that no temperature gradient existed in the cell when the droplet generator was running.

An example of the data generated from this experiment can be seen in Figure 8.9, where a clear correlation can be seen between the droplet diameter and velocity. Since the purpose of the measurement is to establish the calibration of the instrument, it is more appropriate to plot the “raw data”: the measured velocity versus the phase shift. This is presented in Figure 8.12, which contains approximately 1000 individual droplet

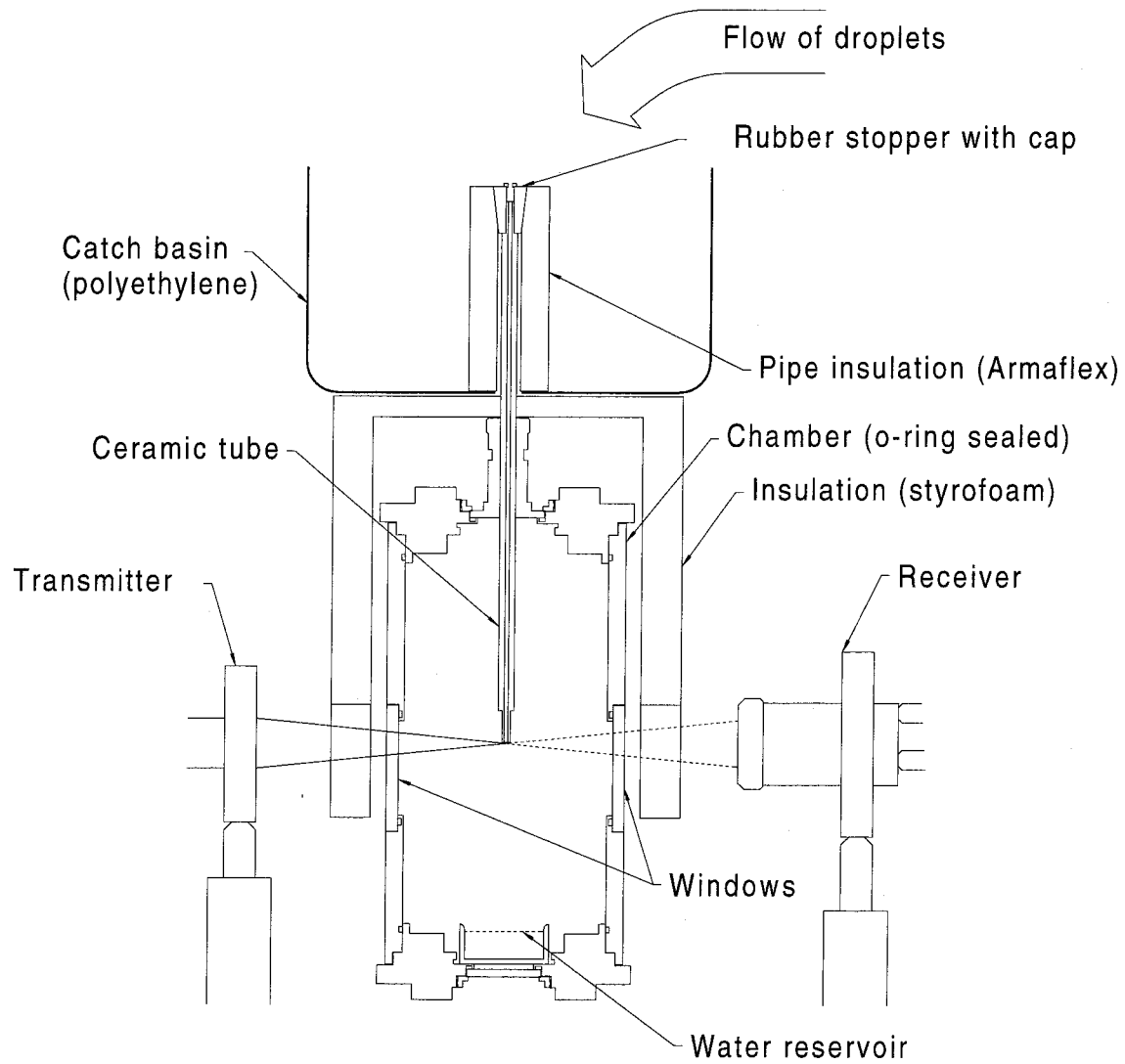


Figure 8.11: Experimental arrangement for testing and calibration of PDA. Distances of transmitter and receiver to measurement volume are not to scale.

measurements. Although more data were acquired from slower, smaller droplets, a general trend is observed in the dispersion in the data, which is greater for these smaller droplets. This is attributed to a number of factors. As the droplet becomes smaller, the phase shift decreases and the uncertainty associated with measuring such a small phase shift increases. Smaller droplets would also be most likely influenced by very small perturbations in the surrounding gas, and thus slightly more scatter can be expected. The SCATAP predictions for our optical arrangement in Figure 8.10 show that the phase shift-size relationship exhibits some oscillatory behavior as the droplets become smaller, and this too will contribute to the dispersion. In spite of this, the correlation is quite good and the data can now be used to establish the calibration of the instrument.

A calibration curve, shown in Figure 8.13, is computed using the raw data in Figure 8.12 and Equation 8.13. The measured terminal velocity of the droplet is used to calculate the droplet diameter, and this is plotted on the abscissa of Figure 8.13. The ordinate on the plot is the same as that in Figure 8.12. The graph shows the approximate linear relationship between the measured phase shift and the droplet diameter. Superimposed on the plot is the least squares fit of the polynomial fit to the calibration curve from Figure 8.10. A constant factor of 0.91 was applied to the polynomial to achieve the fit. The close agreement of the experimental and theoretical calibration functions provides additional confidence in the validity of our experimental approach.

8.5 Conclusion

We have presented the design and calibration of a phase Doppler anemometer for measuring diameter and a single velocity component of spherical, homogeneous particles in the size range $0.5 \mu\text{m}$ to several millimeters. The design is unique in its flexibility and ease in manufacture, relying primarily on easily-obtained off-the-shelf components. It is also economical, costing less than \$7000, and can be suitable for a variety of applications that do not require the high data rates obtained with com-

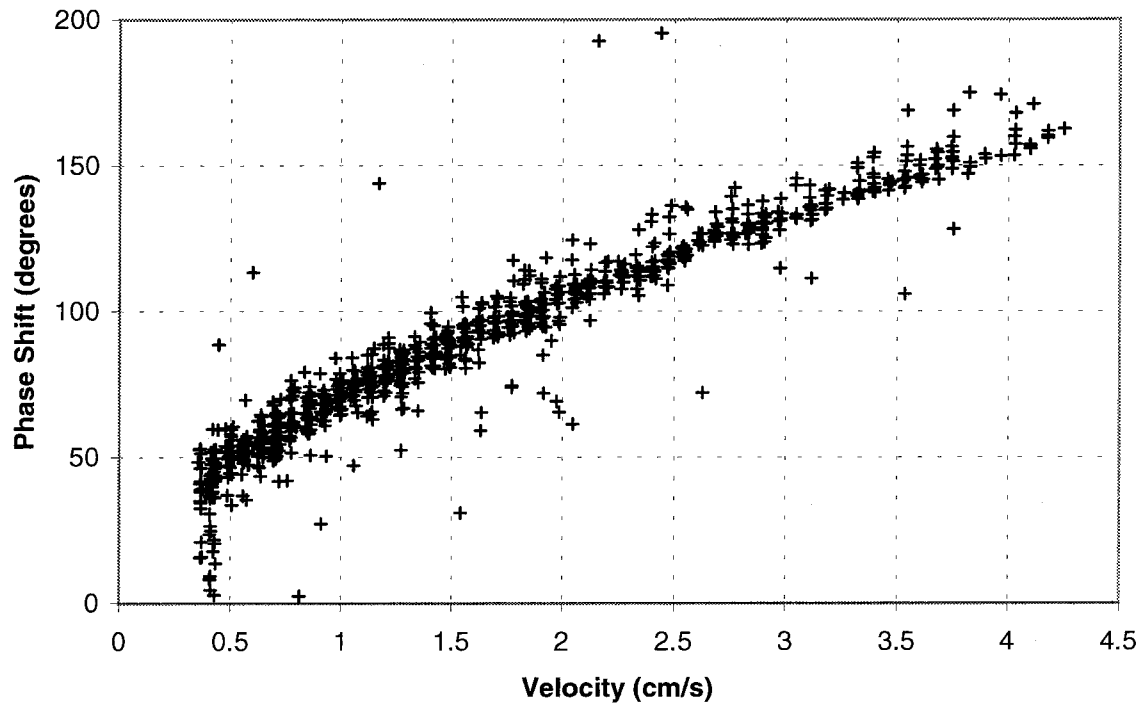


Figure 8.12: Velocity-phase shift correlation for water droplets falling at terminal velocity.

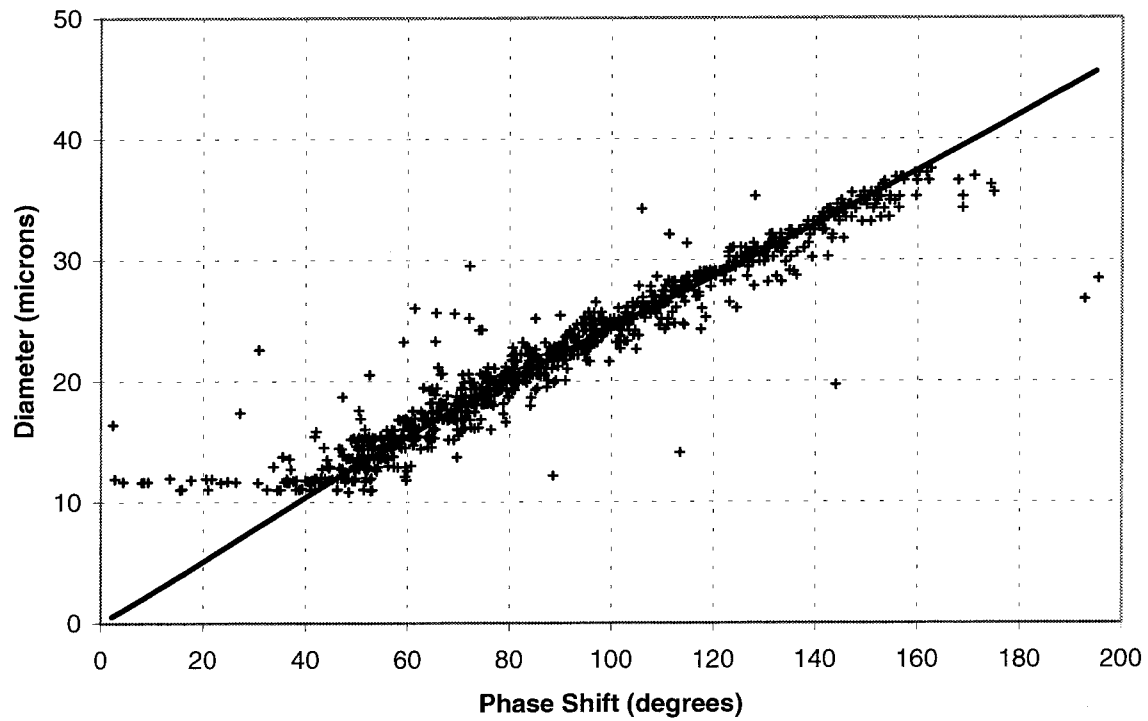


Figure 8.13: Calibration curve for PDA. Droplet diameter is determined from the measured terminal velocity. Also plotted is the theoretical calibration curve obtained with SCATAP using “design” parameters for optical configuration.

mercial systems. Data acquisition rates for our configuration are approx. 100 Hz, and were dictated primarily by data transfer rates from the digitizer to the control computer. The processing algorithm is performed in software, and will benefit from future improvements in the speed of personal computers and data processing algorithms. Calibration of the system has been performed by measuring the terminal velocity of falling water droplets in a chamber adapted for this application. The apparatus made possible the calibration of the instrument over a range of diameters from 10–40 μm - a difficult range to achieve by other calibration procedures currently in use. The procedure makes use of theoretical calculations for the shape of the calibration curve, which predicts low frequency oscillations in the calibration curve that cannot be modeled in the geometrical optics approximation. When this function is fit to the the measurements of terminal velocity of water droplets, excellent agreement is observed.

Acknowledgements

The authors thank the following agencies for funding this work: National Science Foundation (CHE-9727566), Defense Advanced Research Projects Agency, and the Office of Naval Research.

Bibliography

- [1] W. D. Bachalo and M. J. Houser. Phase Doppler spray analyzer for simultaneous measurements of drop size and velocity distributions. *Opt. Eng.*, 23:583, 1984.
- [2] K. Bauckhage. The phase-Doppler-difference-method, a new laser-Doppler technique for simultaneous size and velocity-measurements. 1. Description of the method. *Part. Part. Syst. Character.*, 5(1):16–22, 1988.
- [3] Electronic Physics Auxiliary Publication Service. May be accessed at their home page: <http://www.aip.org/pubservs/epaps.html>.
- [4] E.D. Hirleman. History of development of the phase-Doppler particle-sizing velocimeter. *Part. Part. Syst. Character.*, 13(2):59–67, 1996.
- [5] National Instruments Corp. Labview, 1998.
- [6] R. D. Rajaona and P. Sulmont. A method of spectral analysis applied to periodic and pseudoperiodic signals. *J. Comput. Phys.*, 61:186–193, 1985.
- [7] R. N. Berglund and B. Y. H. Liu. Generation of monodispersed aerosol standards. *Environ. Sci. Technol.*, 7:147–153, 1973.
- [8] S.J. Bever and E.A. Hovenac. Reticle for verification of the correct operation of the phase Doppler particle analyzer. *Opt. Eng.*, 38(10):1730–1734, 1999.
- [9] T. Wriedt, Z. Jiang, J. Rheims, N. Warncke, and F. Duersterbeck. SCATAP for windows, 1996. May be downloaded from the website of the Institute of Material Science at the University of Bremen at <http://imperator.cip-iw1.uni-bremen.de/fg01/scatap.html>.
- [10] R.C. Flagan and J.H. Seinfeld. *Fundamentals of Air Pollution Engineering*. Prentice Hall, New Jersey, 1988.

Chapter 9 The Mechanism of Droplet Discharge in Electrospray Ionization: Solvent and Buffer Gas Composition Effects

9.1 Introduction

Chapter 6 concludes with a number of statements regarding the effects that solvent choice, electrolyte concentration, and charge polarity may have on charged droplet evaporation and discharge dynamics in electrospray ionization. Some of the conclusions from that study are listed here.

- The discharge dynamics of droplets with the same initial diameter and charge are highly reproducible for all solvents and analyte/solvent combinations studied to date.
- Electrosprays of positively charged methanol, acetonitrile, and water were characterized to investigate the effect that solvent choice may have on droplet discharge dynamics. No significant differences are observed in the mechanism of droplet discharge between these solvents, indicating the evaporation alone is primarily responsible for observed differences in the time evolution of droplet size and charge.
- The effect of electrolyte concentration on droplet discharge dynamics was also investigated. Tests were performed on electrosprays of positively charged methanol to which 10^{-6} – 10^{-4} M NaCl was added. No significant differences were observed in the mechanism of droplet breakup for individual droplets for these

solutions.

- Measurements were made of electrosprays of negatively charged droplets. The results show that the polarity of the electrosprayed droplets does not affect the mechanism by which they break up.

This chapter provides supporting data for these conclusions. Below, we provide a brief description of the experimental technique. We then present results for each investigation of solvent effects in droplet discharge processes. Following this, we present some recent results that suggest that the droplet environment may play an important role in determining the extent of charge loss resulting from discharge.

9.2 Experimental Arrangement

Chapter 7 provides a detailed discussion of the experimental apparatus. These investigations make use of a recently-developed technique for obtaining temporal and spatial distributions of the diameter and charge of electrosprayed droplets. Figure 9.1 summarizes this “ping-pong” technique. Charged droplets produced by an electrospray are injected into a cylindrical drift cell with a uniform electric field of approximately 50 V/cm. At the center of the cell, an individual droplet passes through the measurement volume of a phase Doppler anemometer (PDA). The PDA measures its diameter and velocity, from which the charge can be deduced. After a short delay, the electric field within the cell is reversed and the droplet passes again through the measurement volume of the PDA for another size and charge measurement. The process repeats itself, with the trajectory of the droplet resembling that of a ping-pong ball in play, until the droplet can no longer be detected. These measurements provide a time sequence of size and charge for each droplet that passes through the PDA measurement region. A plot of the parameters for the first measurement in each sequence provides a size-charge correlation for the droplets in the spray.

Figure 9.2 shows a diagram of the apparatus used in these investigations. For most experiments, a counter-flowing buffer gas of nitrogen purges the drift cell at

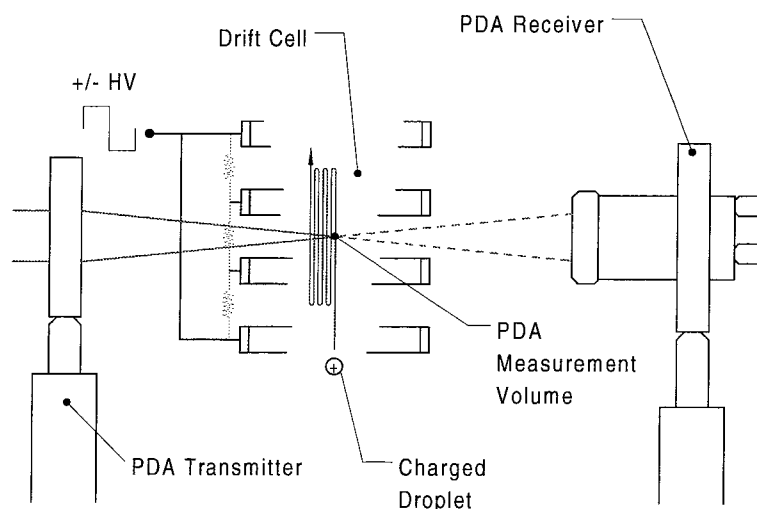


Figure 9.1: The droplet ping-pong experiment: measurement concept.

a flow rate of 0.25–0.3 l/min. We conduct all tests at atmospheric pressure and at a temperature of 293 K. A syringe pump supplies the spray solution to the needle of the electrospray source. This pump operates at a flow rate of 0.2–0.5 $\mu\text{l}/\text{min}$. A description of each experiment follows, including any modifications made to these operating parameters.

9.3 Solvent Effects: Electrosprays of Methanol, Acetonitrile, and Water

We have studied the effect that choice of solvent may have on the mechanism and dynamics of droplet discharge using the ping-pong experiment. The solvents studied were spectroscopic grade methanol and acetonitrile, as well as filtered, deionized water to which 10^{-4} M NaCl was added to allow for electrospray at sufficiently low voltages to avoid corona discharges. We acquired size and charge distributions and size–charge correlations at a single spatial location located on the spray axis, 10 cm above the source. The electrospray source operates in positive-ion mode, resulting in positively charged droplets. Figures 9.3–9.5 show the results of these measurements.

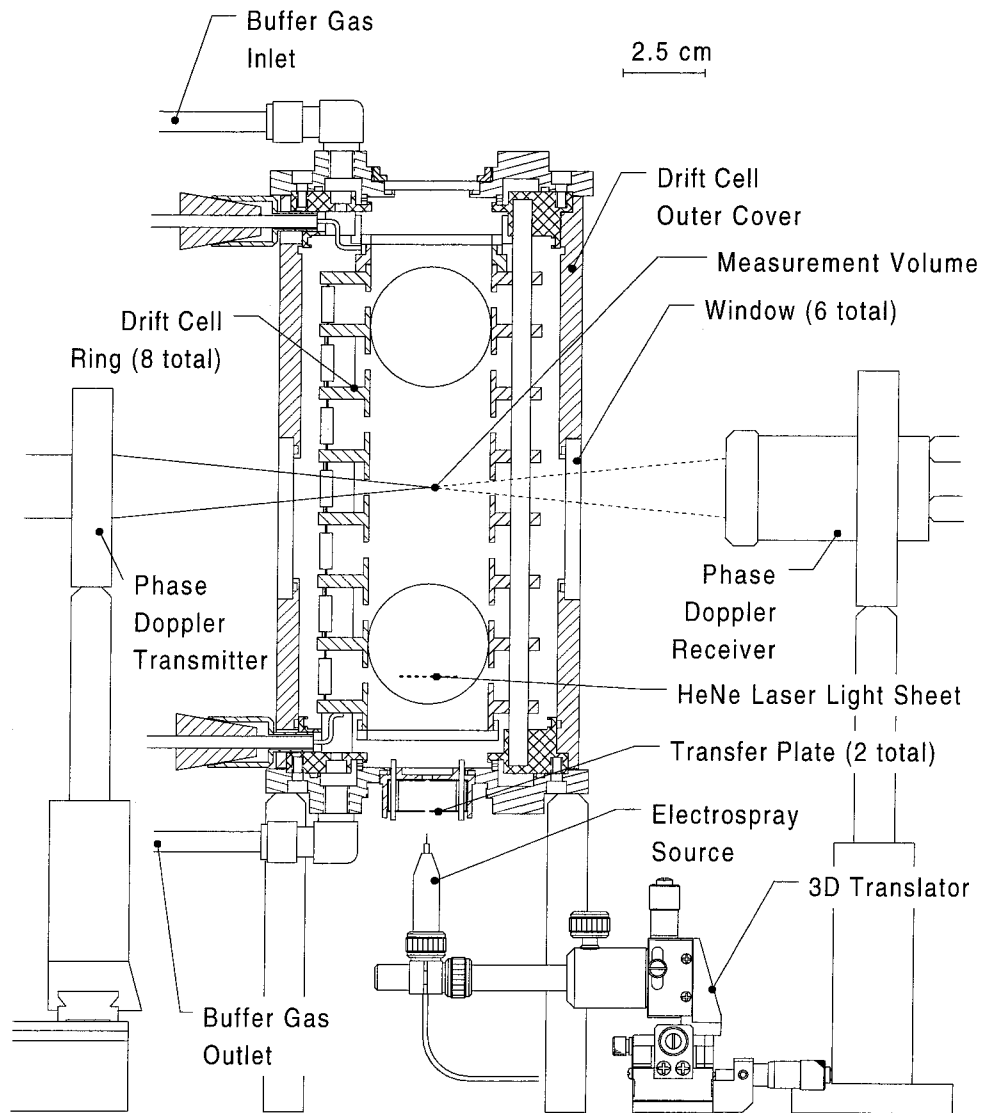


Figure 9.2: Experimental apparatus for studying droplet evaporation and discharge dynamics.

Figure 9.3 shows the data for water droplets. The distributions shown in the figure are typical of those obtained for droplets that are still approaching Rayleigh limit through solvent evaporation, which reduces droplet size while conserving surface charge. The size-charge correlation, Figure 9.3C, shows that the smaller droplets are closer to the Rayleigh limit. This occurs because the rate of evaporation increases as droplet diameter decreases. Figure 9.4 shows the data for acetonitrile droplets. The charge and size histograms display some structure, although they are not well defined due to poor statistics. Figure 9.4C shows the size-charge correlation for acetonitrile, where one sees that all of the droplets are near the Rayleigh limit of charge. Presumably, these droplets are in the process of evaporating and disruption, and may have undergone several fission events prior to this measurement. Figure 9.5 shows the results of spatial measurements for an electrospray of pure methanol. Structures in the size and charge distributions are now clearly seen. The size-charge correlations, shown in Figures 9.5C and D, suggest a mechanism that originates with a nearly monodispersed stream of droplets created at the source. These droplets subsequently undergo evaporation-discharge cycles. The small variation in nascent droplet size and charge result in similar fates for each droplet in the spray. This appears in the size-charge correlation as three or more distinct groupings of droplets, which can be interpreted as three or more “generations” resulting from discharge processes. Another feature seen clearly in Plot D is that each group of data has a characteristic striped pattern. We attribute these streaks to the digitization of the signals from the PDA.

The distributions shown in Figures 9.3–9.5 suggest the following mechanism for droplet discharge in electrospray ionization. Droplets are formed at the source with a narrow distribution of size and charge. They subsequently evaporate until the surface density is high enough to cause the droplet to discharge. This happens close to the Rayleigh limit, generally just above, as evident in Figures 9.4C and 9.5C–D where the data exceed the Rayleigh limit in charge by 10–20%. Once a disruption event occurs, the charge loss amounts to approximately 20% of the total droplet charge prior to breakup. This is seen in Figures 9.4C and 9.5C, where the range of charge for a given droplet diameter can be directly measured. This charge loss can also be observed in

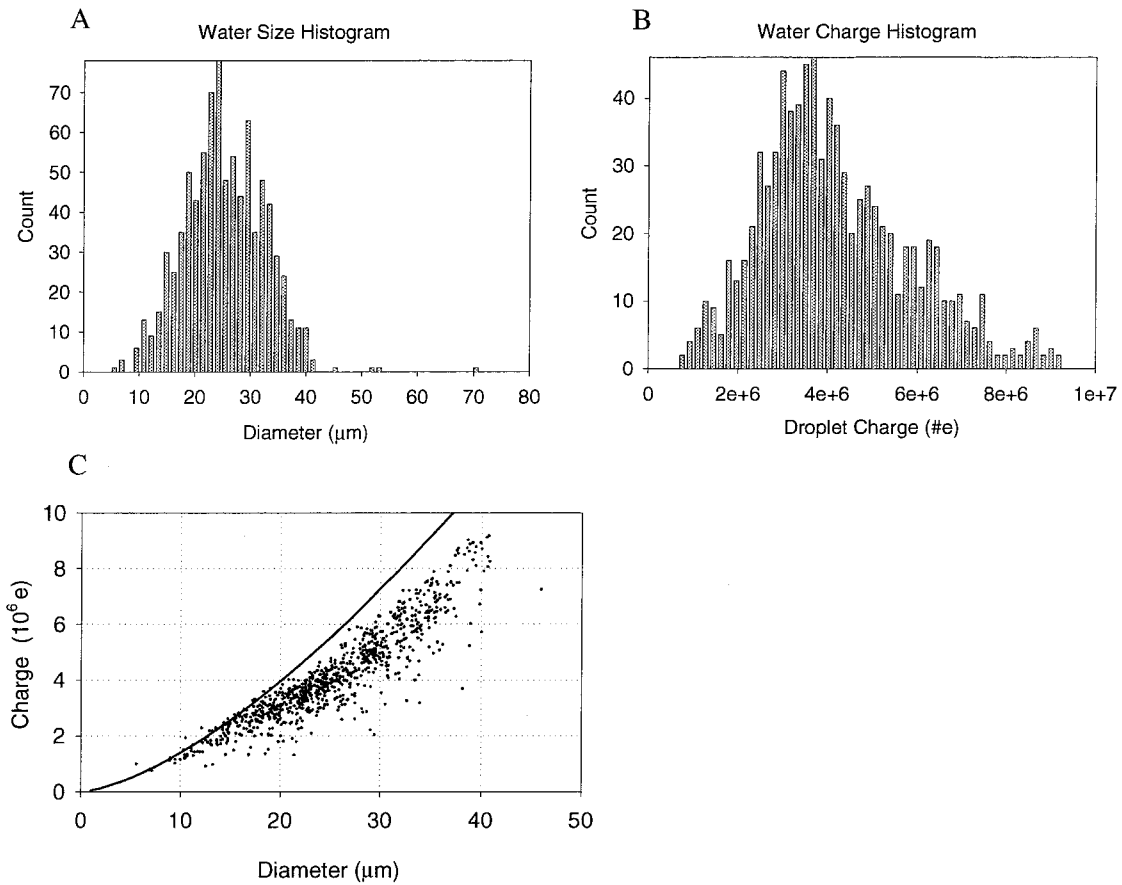


Figure 9.3: Plots of size and charge measurements of individual droplets in a positive-ion electrospray of 10^{-4} M NaCl in water. A: Droplet diameter histogram; B: Droplet charge histogram; C: Diameter versus charge, plotted with a curve representing the Rayleigh stability limit.

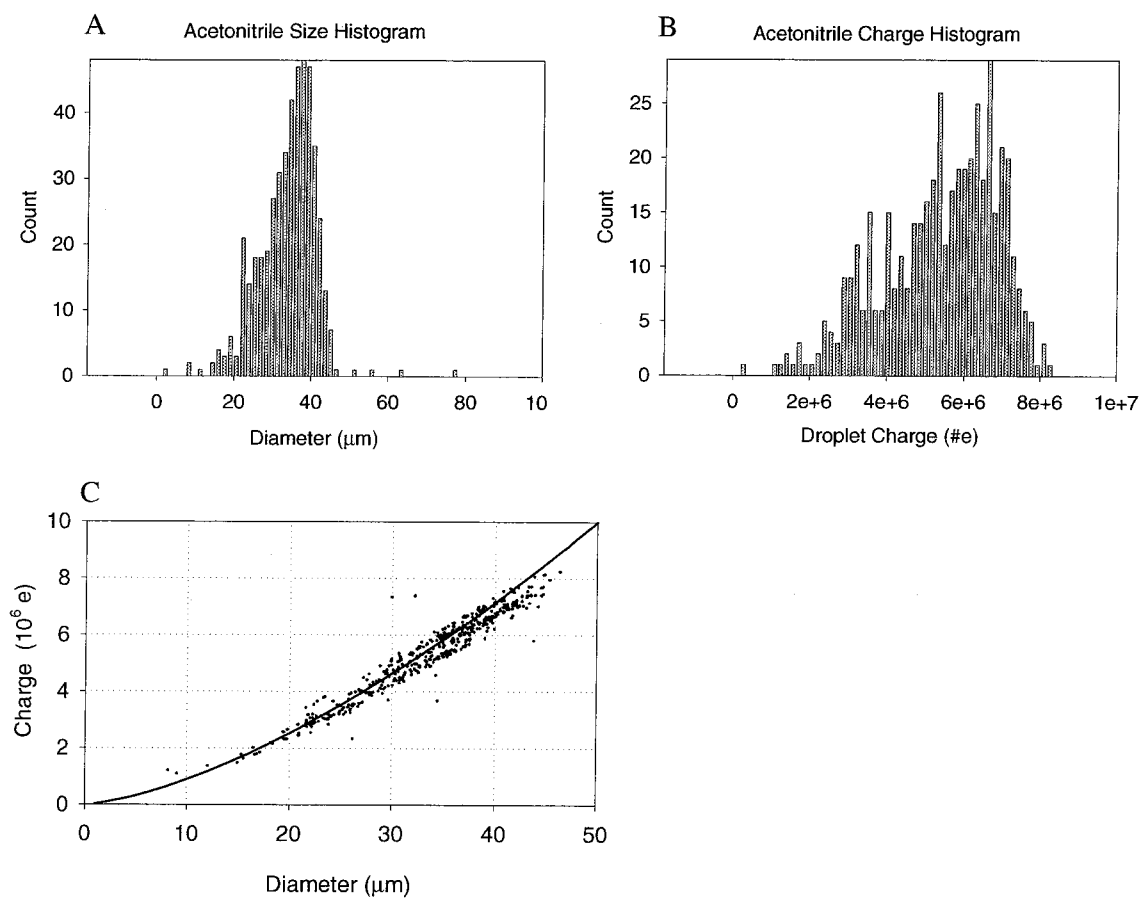


Figure 9.4: Plots of size and charge measurements of individual droplets in a positive-ion electro spray of pure acetonitrile. A: Droplet diameter histogram; B: Droplet charge histogram; C: Diameter versus charge, plotted with a curve representing the Rayleigh stability limit.

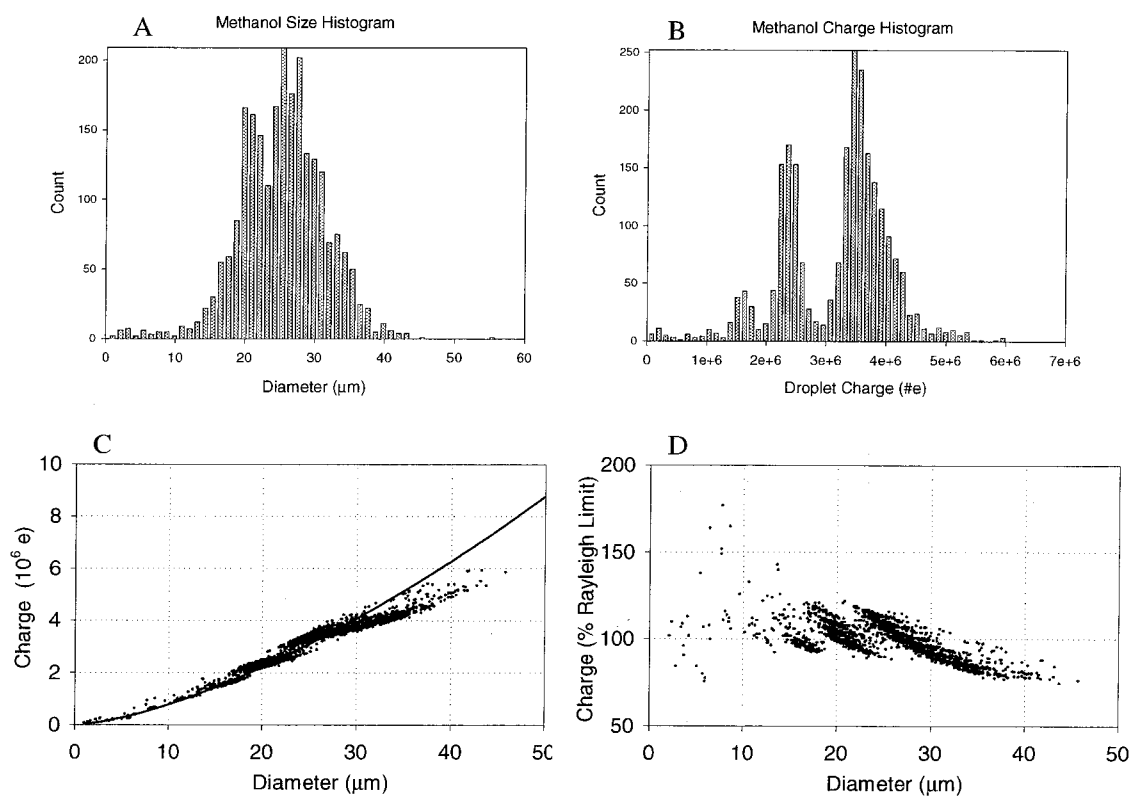


Figure 9.5: Plots of size and charge measurements of individual droplets in a positive-ion electro spray of pure methanol. A: Droplet diameter histogram; B: Droplet charge histogram; C: Diameter versus charge, plotted with a curve representing the Rayleigh stability limit; D: Diameter versus charge, with charge represented as the percentage of the Rayleigh limit.

Figure 9.5D as the vertical spaces that separate the three larger groups of data.

Although the explanation provided above is consistent with observed size-charge correlations, no dynamic information can be obtained from these measurements. For this, the ping-pong technique can be employed to obtain the time evolution of size and charge of individual electrosprayed droplets. Three such time sequences are shown in Figures 9.6–9.8 for electrosprays of water, acetonitrile, and methanol. The plots confirm the mechanism of droplet discharge in electrosprays proposed above, and add the observation that evaporative processes dictate the dynamics of droplet discharge.

We have developed a model for the evaporation dynamics of a volatile droplet, which is discussed in greater detail in Section 5.3. Spherically symmetric vaporization of the droplet defines the approach of this model. Stefan convection and diffusion in the gas phase sum to equal convection in the solution phase of the droplet to create the mass balance condition at the droplet surface. This results in Equation 5.8 for droplet diameter as a function of time. Energy conservation at the interface allows for the calculation of evaporative cooling on the droplet surface, and results in Equation 5.9 for this temperature depression.

Figure 9.6 shows the result of this model for an evaporating water droplet. To allow for observations of multiple discharge events for this less volatile water solution, the N_2 buffer gas in the drift cell was heated to 317 K. Plot A shows the change in droplet diameter as a function of time. Superimposed on the experimental results are the model results for 317 K. Excellent agreement can be seen in the figure, providing strong evidence that evaporation plays a primary role in determining droplet mass loss. In Plot C, one can see that the droplet has undergone a series of three or more fission events during the course of the measurement. The discharge events depicted in Plot C result in a charge loss of 20–30% of the total charge, and exhibit some variation between successive events.

Similar droplet ping-pong sequences for acetonitrile and methanol are provided in Figures 9.7 and 9.8, respectively. We include the results of our evaporation model in the plots of droplet diameter as a function of time (Plots A). The theoretical curves of evaporation dynamics slightly over-predict droplet mass loss in these two examples.

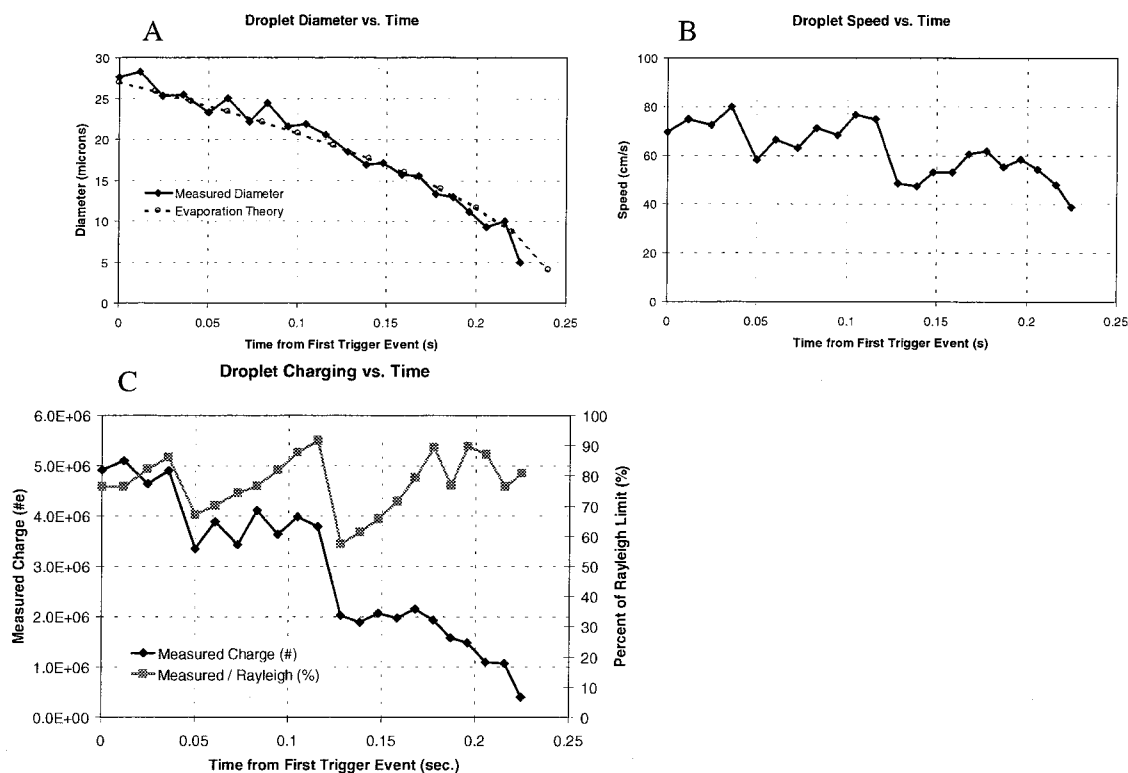


Figure 9.6: Evaporation and discharge of a positively charged water droplet in a 317 K N_2 buffer gas and a 51 V/cm electric field. A: Variation of droplet diameter with time. Also plotted is the predicted evaporation dynamics of a water droplet in a vapor-free N_2 gas at 317 K. B: Variation of droplet axial speed with time. C: Variation of droplet charge with time, represented as number of elementary charges and as percent of the Rayleigh limit of charge for measured droplet.

Several factors can contribute to this. First, the model is a relatively simple one that assumes that a vapor-free gas surrounds the droplet and that the temperature is constant throughout the droplet. In addition, the experimental evaporation rates may be slower due to solvent evaporation that results in small amounts of impurities in the droplet. The discrepancies are nonetheless minor for all solvents studied, and support the assertion that evaporative processes dictate the dynamics of droplet mass loss.

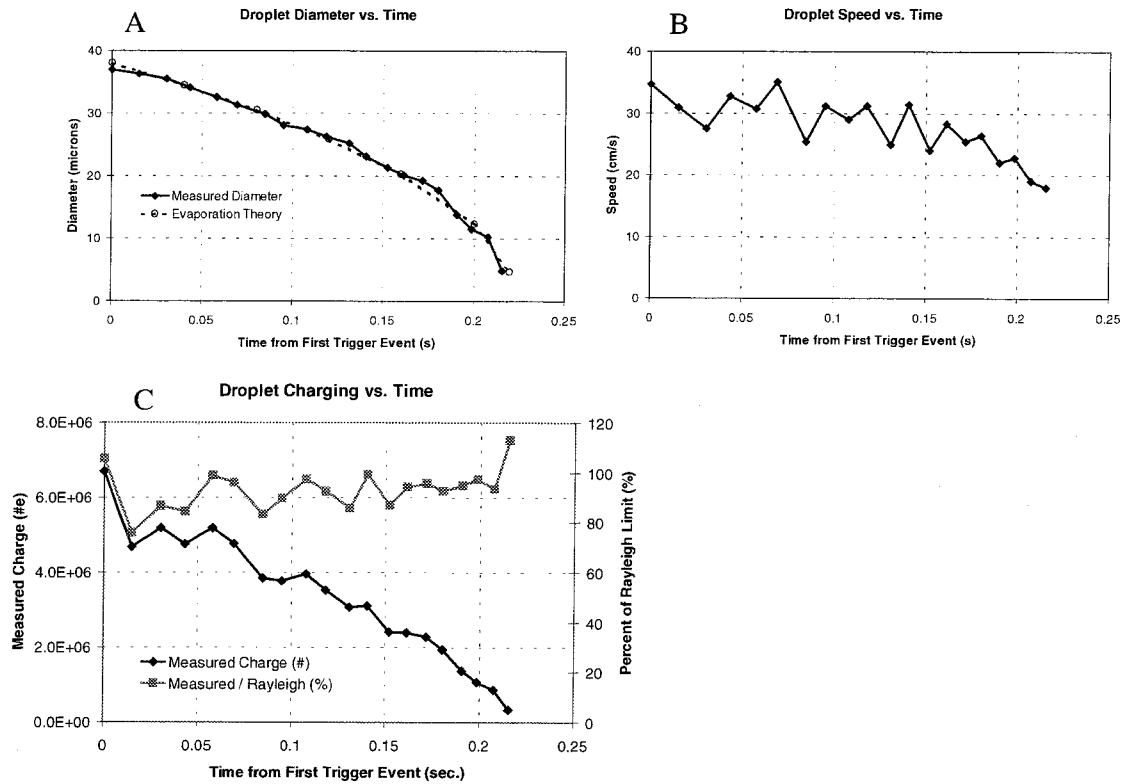


Figure 9.7: Evaporation and discharge of a positively charged acetonitrile droplet in a 51 V/cm electric field. Also plotted is the predicted evaporation dynamics of a acetonitrile droplet in a vapor-free N_2 gas. A: Variation of droplet diameter with time; B: Variation of droplet axial speed with time; C: Variation of droplet charge with time, represented as number of elementary charges and as percent of the Rayleigh limit of charge for measured droplet.

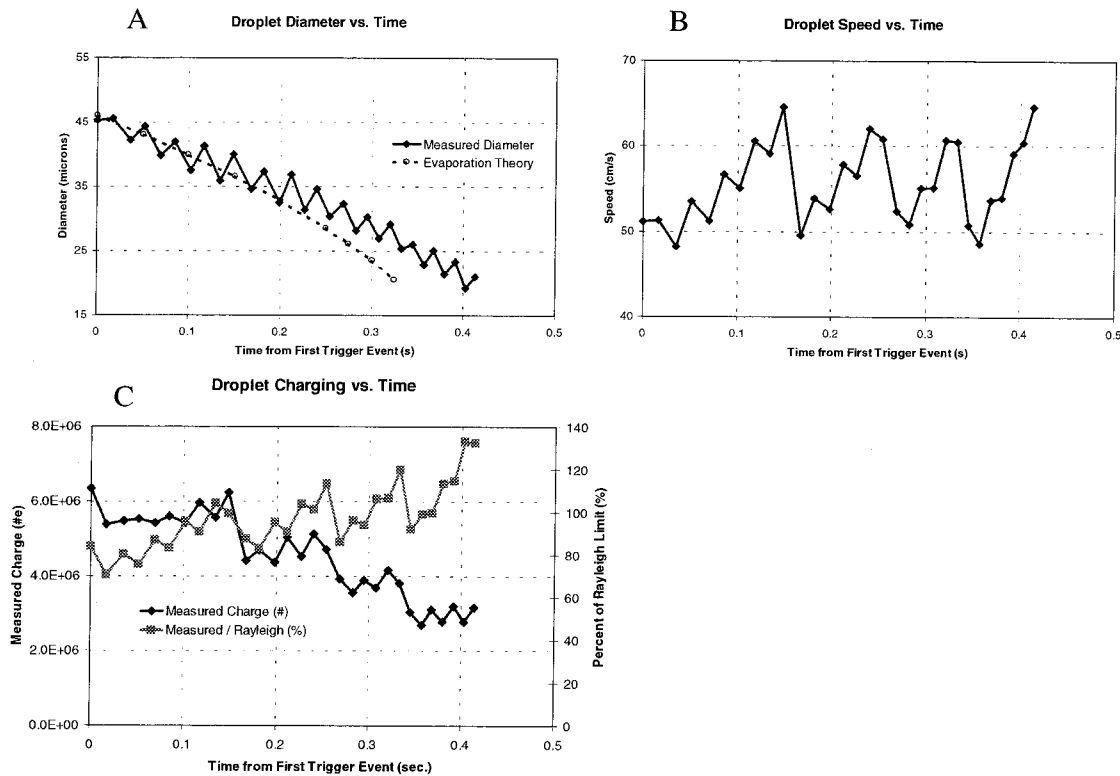


Figure 9.8: Evaporation and discharge of a positively charged methanol droplet (10^{-6} M NaCl added) in a 51 V/cm electric field. Also plotted is the predicted evaporation dynamics of a neutral methanol droplet in a vapor-free N_2 gas. A: Variation of droplet diameter with time; B: Variation of droplet axial speed with time; C: Variation of droplet charge with time, represented as number of elementary charges and as percent of the Rayleigh limit of charge for measured droplet.

9.4 Droplet Charge Polarity Effects

Most practitioners of electrospray apply a positive voltage to the needle with respect to the front aperture plate of the mass spectrometer. This creates positively charged droplets and gas phase cations. The popularity of positive-ion electrospray is due in part to the numerous applications involving protonated species of biological interest. There are several applications for creating negative ions with electrospray, however, and few studies exist on the properties of negative-ion electrospray. We have applied the droplet ping-pong experiment to the study of negative-ion electrosprays of various solvents. The goal of these studies is to determine the influence of droplet charge polarity on the mechanism and dynamics of droplet evaporation and discharge.

In Figure 9.9 are size and charge histograms as well as size-charge correlations for a negative-ion electrospray of 10^{-4} M NaCl in methanol. The charge distribution (Plot A) features a broad shoulder at smaller charge levels. The size-charge correlation in Plot C suggests that this shoulder is caused by Rayleigh fission processes, as droplets with charge less than $3 \times 10^6 e$ correlate well with the curve representing the Rayleigh limit of charge. The size distribution (Plot B) is skewed towards the smaller sizes due to evaporation. Figure 9.9D shows the droplet size-charge correlation, with charge represented as the percentage of the Rayleigh limit. At the smallest detected sizes, one notes a group of data with charge corresponding to 50–100% of the Rayleigh limit of charge. These droplets are non-volatile, with characteristic size and charge dynamics resembling those in Figure 7.12. A comparison of Figures 9.9D and 9.5D leads to the following observations. No groupings exist in the size-charge correlation of this negative-ion electrospray, unlike the case for positive-ion mode. Negatively charged methanol droplets reach a maximum charge level corresponding to 125–130% of the Rayleigh limit of charge, slightly higher than that attained by positively charged droplets (120%).

To investigate the dynamics of droplet evaporation and disruption in negative-ion electrospray, we conducted ping-pong measurements using a solution of spectroscopic grade methanol mixed with an equal volume of filtered, de-ionized water. Figure 9.10

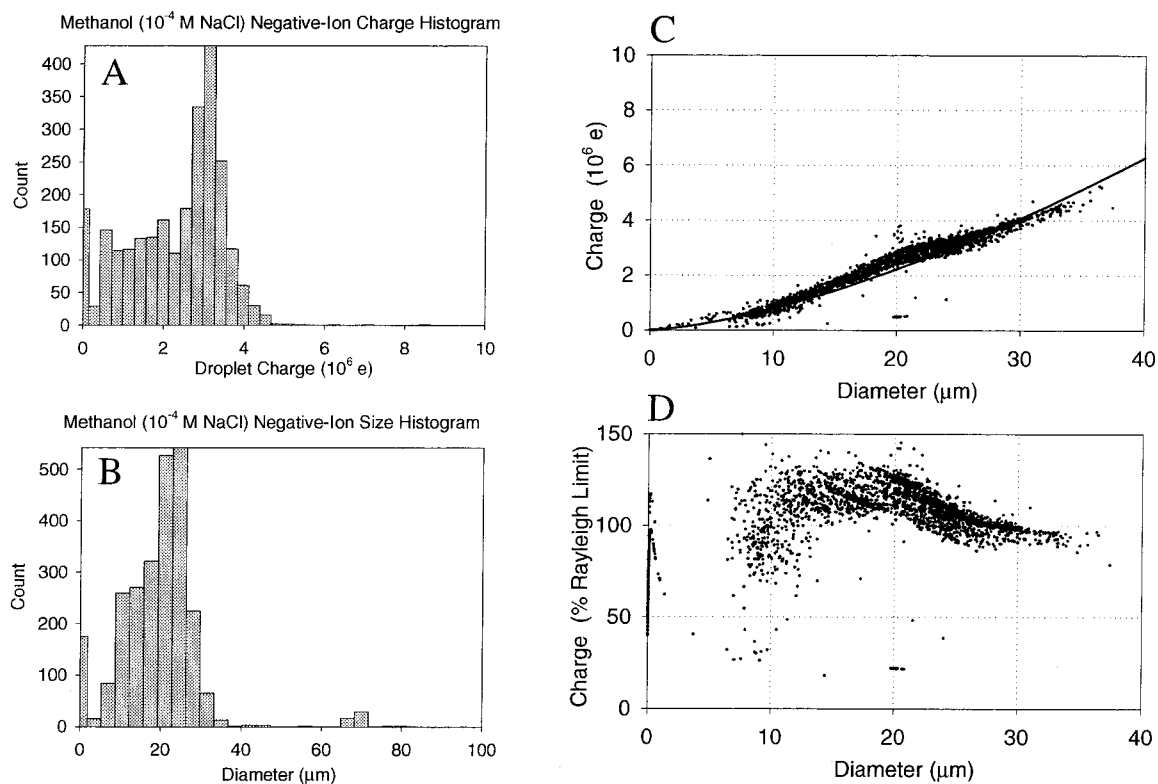


Figure 9.9: Diameter versus charge for a negative-ion electrospray of 10^{-4} M NaCl in methanol. A: Droplet charge histogram; B: Droplet diameter histogram; C: Diameter versus charge, plotted with a curve representing the Rayleigh stability limit; D: Diameter versus charge, with charge represented as the percentage of the Rayleigh limit.

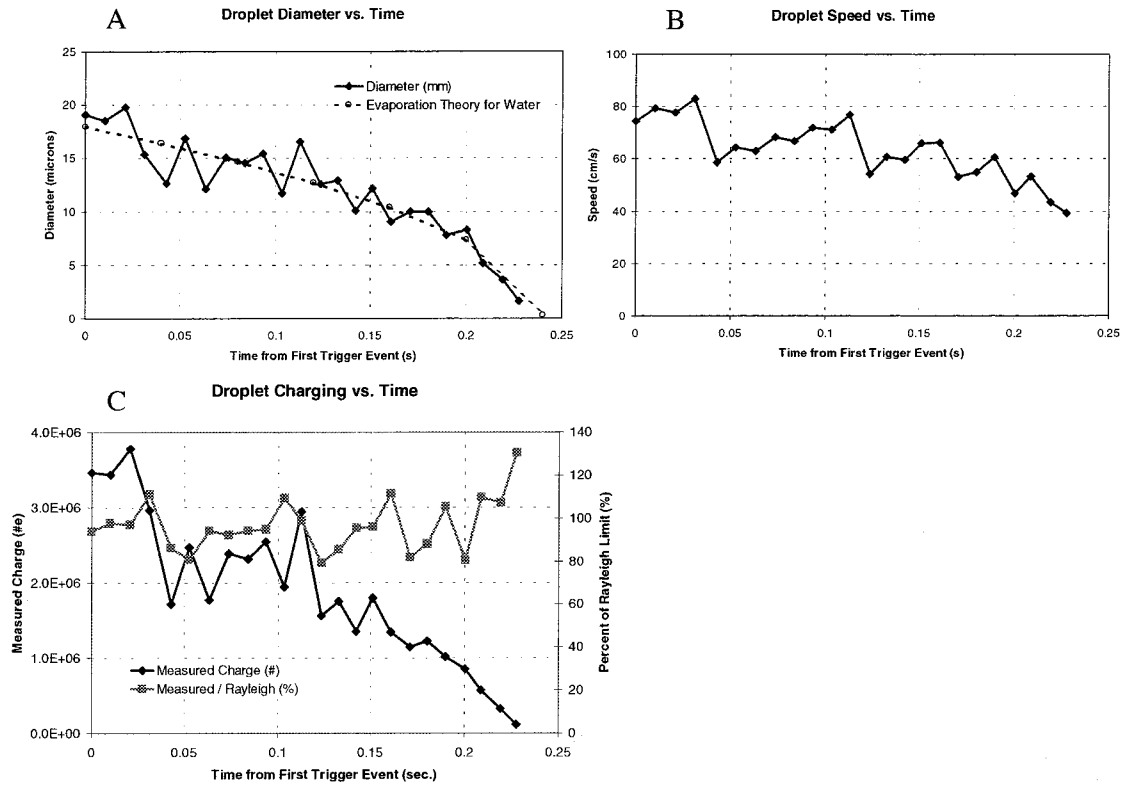


Figure 9.10: Evaporation and discharge of a negatively charged droplet of comprised of equal volumes of methanol and water in a 51 V/cm electric field. Also plotted is the predicted evaporation dynamics of a water droplet in a vapor-free N_2 gas. A: Variation of droplet diameter with time; B: Variation of droplet axial speed with time; C: Variation of droplet charge with time, represented as number of elementary charges and as percent of the Rayleigh limit of charge for measured droplet.

shows one ping-pong sequence of size and charge for this mixture. Plotted alongside the droplet diameter curve (Plot A) is the modeled evaporation curve assuming the droplet is composed of water. This approximation can be justified by the observation that a binary mixture of a volatile and a non-volatile solution will, after a period of evaporation, reach a state where it is primarily comprised of the non-volatile component. In Plot A, one notes excellent agreement between the observed and modeled droplet diameters. Plot C depicts the time evolution of droplet charge. As in Plot A, the physical parameters for water were used to generate the charge curve and to calculate the Rayleigh limit of charge.

9.5 Electrolyte Concentration Effects

Electrolyte concentrations in electrospray ionization typically span the range from 10^{-6} M to 10^{-4} M. We report here an investigation of droplet discharge processes in positive-ion electrosprays salt-methanol solutions. The goal of this study is to determine if electrolyte levels influence the mechanism or dynamics of droplet discharge. NaCl was added to spectroscopic grade methanol to create solutions with 10^{-6} , 10^{-5} , and 10^{-4} of the electrolyte. During these investigations, we found that the weaker salt solutions were more stable and easier to characterize. Figure 9.11 shows the size-charge correlations for these electrosprays. In Plot A, corresponding to 10^{-6} M NaCl, one can observe the same groupings that were seen above in Figure 9.5D. Such structure is not seen for the higher salt concentrations in Plots B and C.

In spite of the differences in the structures of the size-charge correlations, the results of ping-pong measurements show little difference in evaporation and discharge dynamics for varying salt concentrations. Figure 9.12 demonstrates this point. To create the plots shown in Figure 9.12, we have searched the databases of ping-pong measurements made for all three electrolyte concentrations to find the best match in the first size and charge measurement. This search resulted in the identification of two ping-pong sequences for each concentration level with initial measured diameters lying within $26 \pm 0.5 \mu\text{m}$ and charges within $3.2 \pm 0.5 \times 10^6 e$. Figure 9.12A shows the superposition of droplet diameter versus time, and does not reveal a correlation between electrolyte level and evaporation rate. The plot of the time evolution of droplet charge (Plot C), shows large variability in the times at which the droplets undergo discharge. However, the charge level at which fission occurs is approximately equal for all three electrolyte levels (115–120% of the Rayleigh limit of charge). We attribute the difference in the time at which fissioning occurs to the criteria we establish for locating these “matched” sequences. Better statistics would allow for a better initial size and charge match for all three charge levels. Nevertheless, the data in Plot C do not reveal a correlation between electrolyte concentration and droplet discharge dynamics.

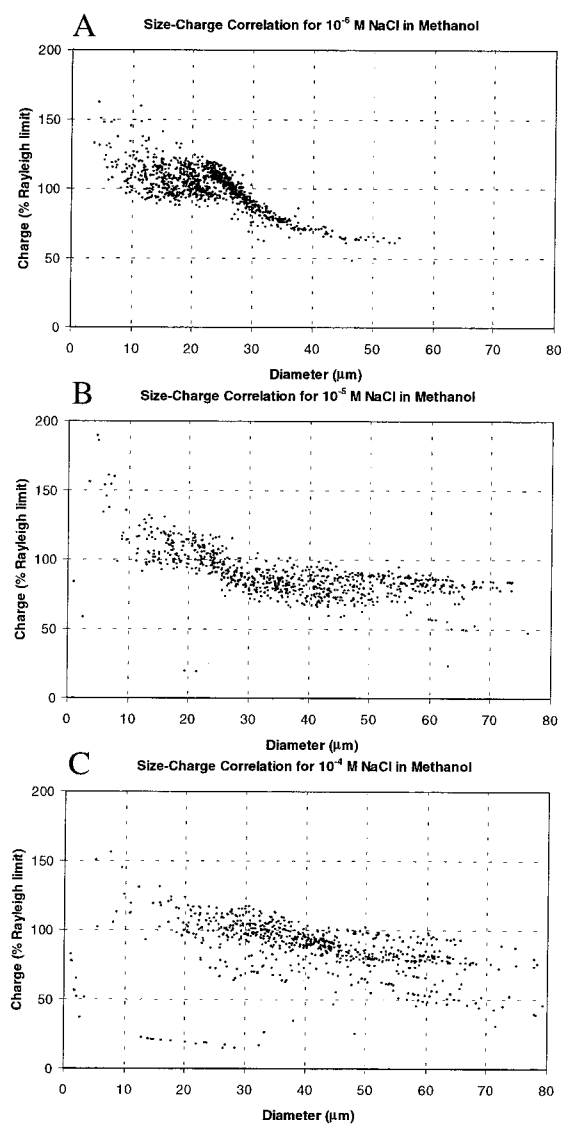


Figure 9.11: Diameter versus charge, with charge represented as the percentage of the Rayleigh limit, for a positive-ion electrospray of methanol with the following concentrations of NaCl: A. 10^{-6} M; B. 10^{-5} M; C. 10^{-4} M.

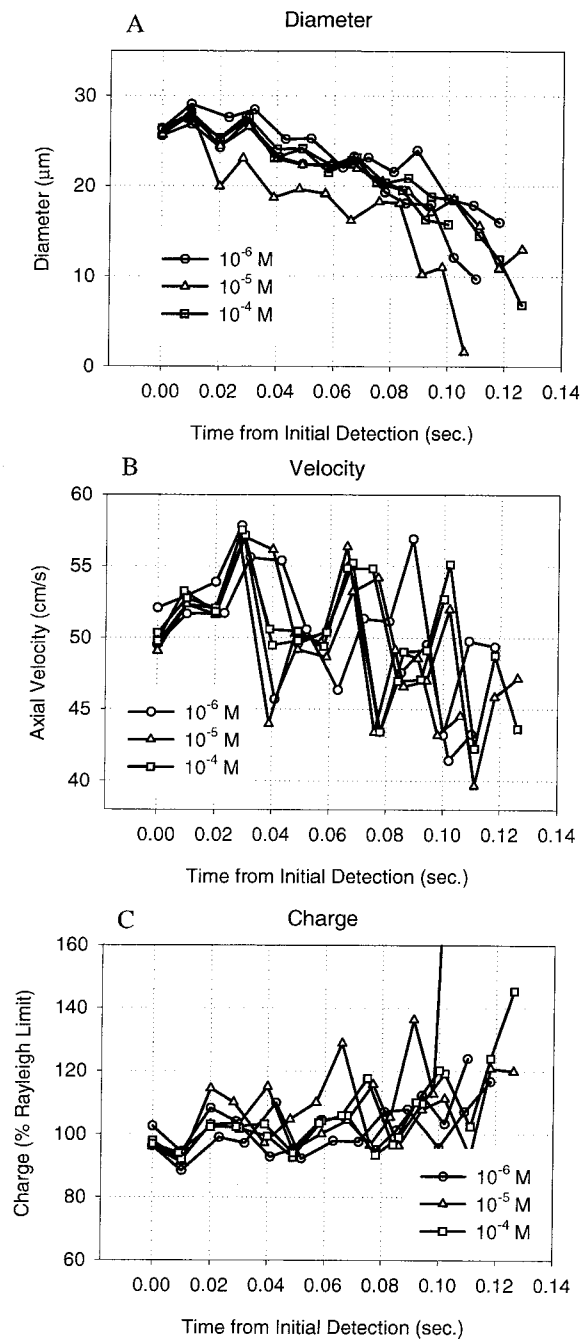


Figure 9.12: Evaporation and discharge of positively charged droplets of 10^{-6} – 10^{-4} M NaCl in methanol in a 51 V/cm electric field. A: Variation of droplet diameter with time; B: Variation of droplet axial speed with time; C: Variation of droplet charge with time, represented as percent of the Rayleigh limit of charge for measured droplet size.

9.6 Buffer Gas Composition Effects

This section presents data from some on-going experiments studying the effect of buffer gas composition on the discharge mechanism of charged droplets in electro-sprays. We started these investigations after experiments in which the drift cell buffer gas was turned off resulted in ping-pong measurements like that shown in Figure 9.13. The time evolution of charge in this example of positive-ion electrospray of spectroscopic grade methanol features disruption events that correspond to unusually high charge levels. These events occur at charge levels of more than 150% of the Rayleigh limit of charge (Plot C). This observation is repeatable, and correlates with a quiescent buffer gas. Plot A shows the time evolution of droplet diameter, plotted alongside the predicted evaporation rate for a methanol droplet in a vapor-free buffer gas. The discrepancy between the observed and modeled evaporation rates suggest that there may be a significant amount of methanol vapor surrounding the droplet, thus slowing the rate of evaporation.

To test the effect that vapor concentration in the buffer gas may have on the charge levels corresponding to disruption, the nitrogen buffer gas was passed through the headspace of a container filled with methanol prior to entering the drift cell. This saturated gas then flowed into the drift cell at a rate of 0.3 l/min. Figure 9.14 shows a representative ping-pong measurement for a positively charged methanol droplet. Although the concentration of methanol in the buffer gas is not known precisely, one can conclude from the long observation time shown in Plot A (1.4 seconds) that the gas must be close to fully saturated. The application of the evaporation model (Equation 5.8 leads to the prediction of approximately 80% saturation for this example. As Plot C shows, the observed fission events correspond to charge levels of about 110% of the Rayleigh limit of charge. Thus a high vapor concentration in the buffer gas cannot be the cause of the high charge levels associated with fissioning in Figure 9.13.

We performed an additional test using the ping-pong technique for positively charged methanol droplets evaporating in a pure oxygen (O_2) buffer gas. The presence

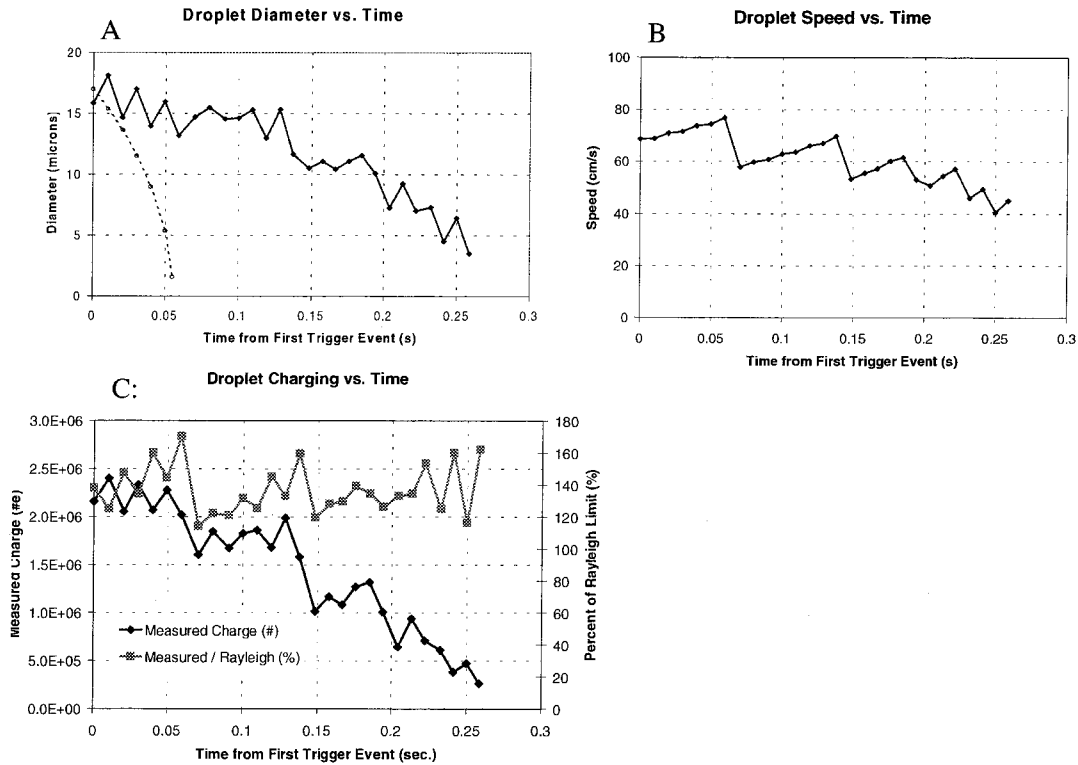


Figure 9.13: Evaporation and discharge of a positively charged methanol droplet in a quiescent buffer gas and a 51 V/cm electric field. Also plotted (dashed line) is the predicted evaporation dynamics of a neutral methanol droplet in a vapor-free N_2 gas. A: Variation of droplet diameter with time; B: Variation of droplet axial speed with time; C: Variation of droplet charge with time, represented as number of elementary charges and as percent of the Rayleigh limit of charge for measured droplet.

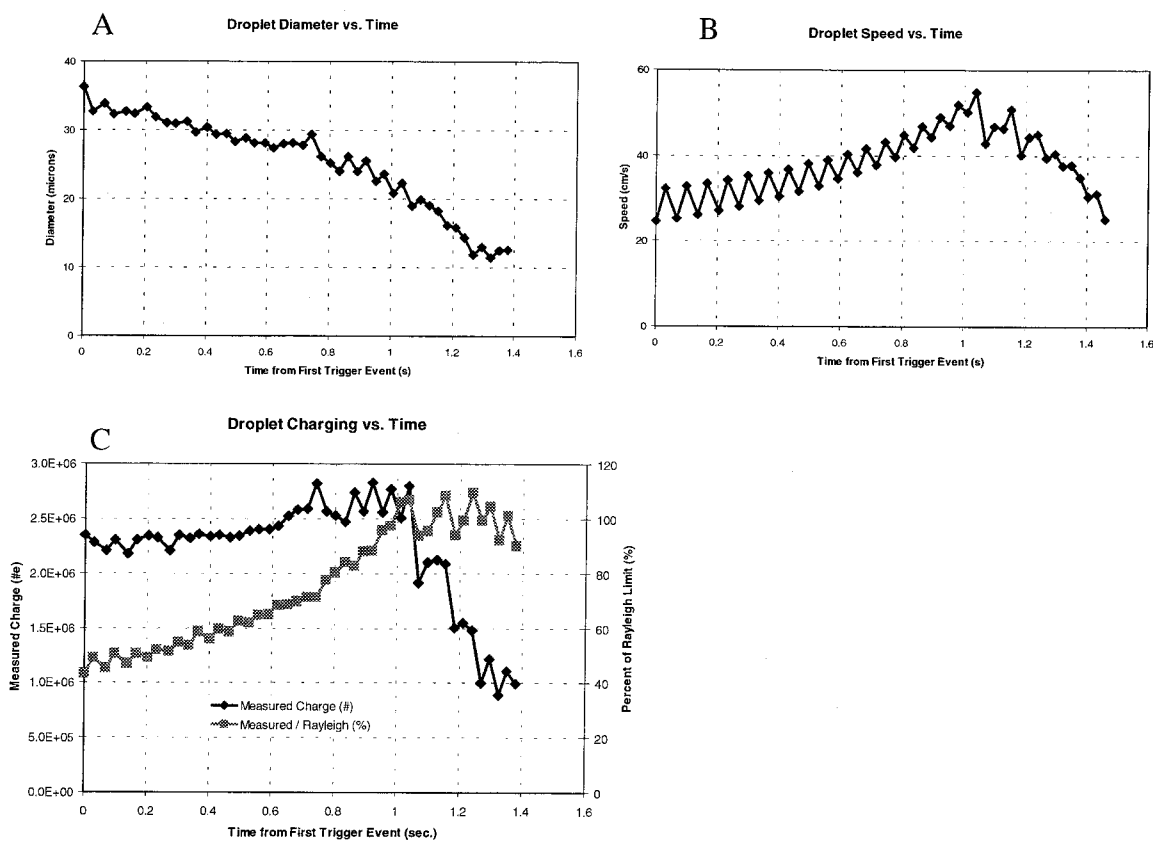


Figure 9.14: Evaporation and discharge of a positively charged methanol droplet in a nearly saturated buffer gas and a 51 V/cm electric field. A: Variation of droplet diameter with time; B: Variation of droplet axial speed with time; C: Variation of droplet charge with time, represented as number of elementary charges and as percent of the Rayleigh limit of charge for measured droplet.

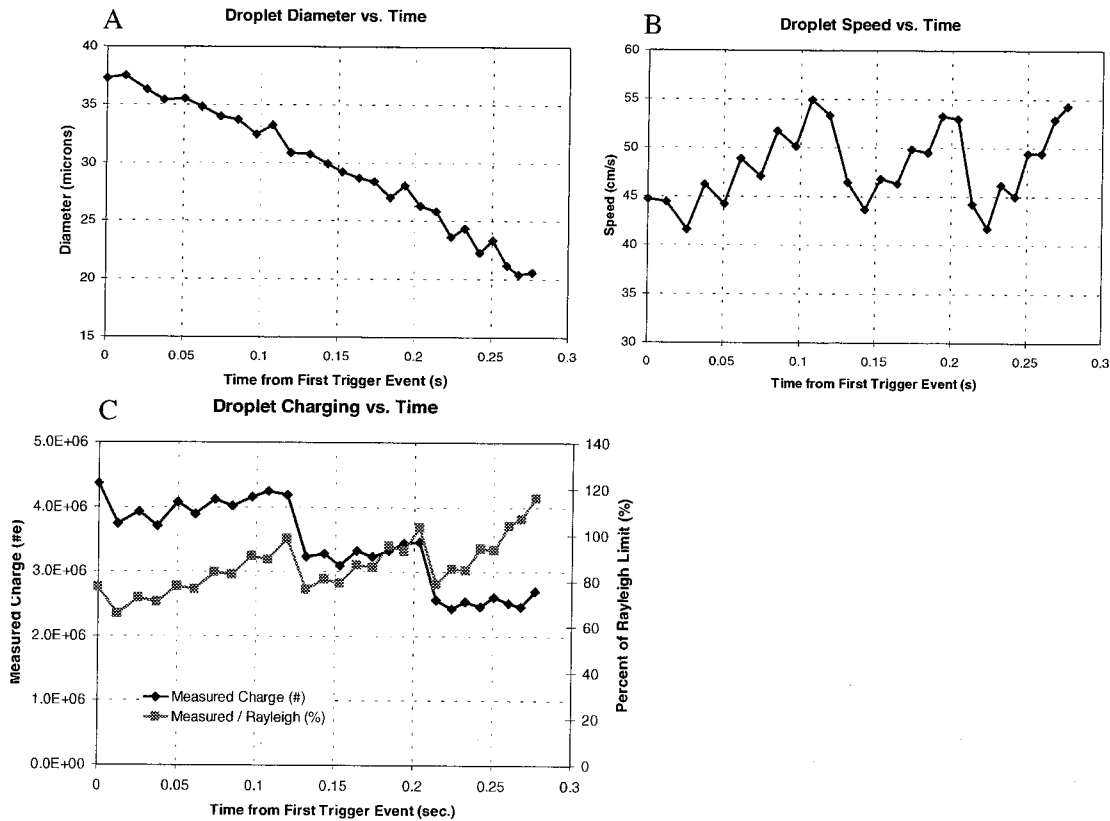


Figure 9.15: Evaporation and discharge of a positively charged methanol droplet in an O_2 buffer gas and a 51 V/cm electric field. A: Variation of droplet diameter with time; B: Variation of droplet axial speed with time; C: Variation of droplet charge with time, represented as number of elementary charges and as percent of the Rayleigh limit of charge for measured droplet.

of oxygen may influence discharge processes, since it forms a stable anion in the gas phase by electron attachment. Oxygen is often introduced to reduce arcing. It is thus interesting to compare the results of ping-pong experiments performed in a buffer gas of oxygen with those using pure nitrogen. Figure 9.15 shows a representative sample. In Plot C, one observes two fission events that correspond to charge levels of 100% of the Rayleigh limit of charge. Thus an electron scavenger in the buffer gas does not contribute to the high charge levels observed in Figure 9.13.

Chapter 10 Recommendations for Future Work

The droplet ping-pong experiment is a simple and effective technique for obtaining time sequences of size and charge for individual droplets in an electrospray. With this technique, it is possible, in theory, to remotely measure many droplet properties at rates as fast as 100 Hz. This theoretical maximum sampling rate is dictated by droplet relaxation times, as was shown in Section 7.3.1. The current instrument, however, allows for measurements at a rate of approximately 10 Hz due to the use of mechanical relays for reversing the field within the drift cell. While this has not posed great problems for observing fission events for the first few disruption cycles, an analysis of time sequences such as that shown in Figure 6.3 demonstrates that the current set-up is unable to resolve higher order events.

Theoretical calculations of droplet evaporation and discharge dynamics in the drift cell confirm this observation. In Figure 10.1, the model developed in Chapter 5 is employed using typical drift cell conditions: 50 V/cm electric field, 0.3 l/min flowing nitrogen buffer gas, and 293 K buffer gas temperature. In the figure, the discharge dynamics for a 40 μm diameter methanol droplet with initially 80% of the Rayleigh limit of charge are followed at 10 ms intervals through 3 fission events. As evaporation proceeds, fewer data are available to characterize each generation of evaporation and discharge. Figure 10.2 shows the time between fission events for the same methanol droplet. The model results shown in Figure 10.2 show that the fifth generation of droplet discharge would be characterized by only two measurements. Clearly, the characterization of these higher order fission events can benefit from a reduction in the measurement step size. The theoretical time resolution is also plotted in Figure 10.2. In theory, it is possible to characterize these higher order fission events with as many as 10 measurements.

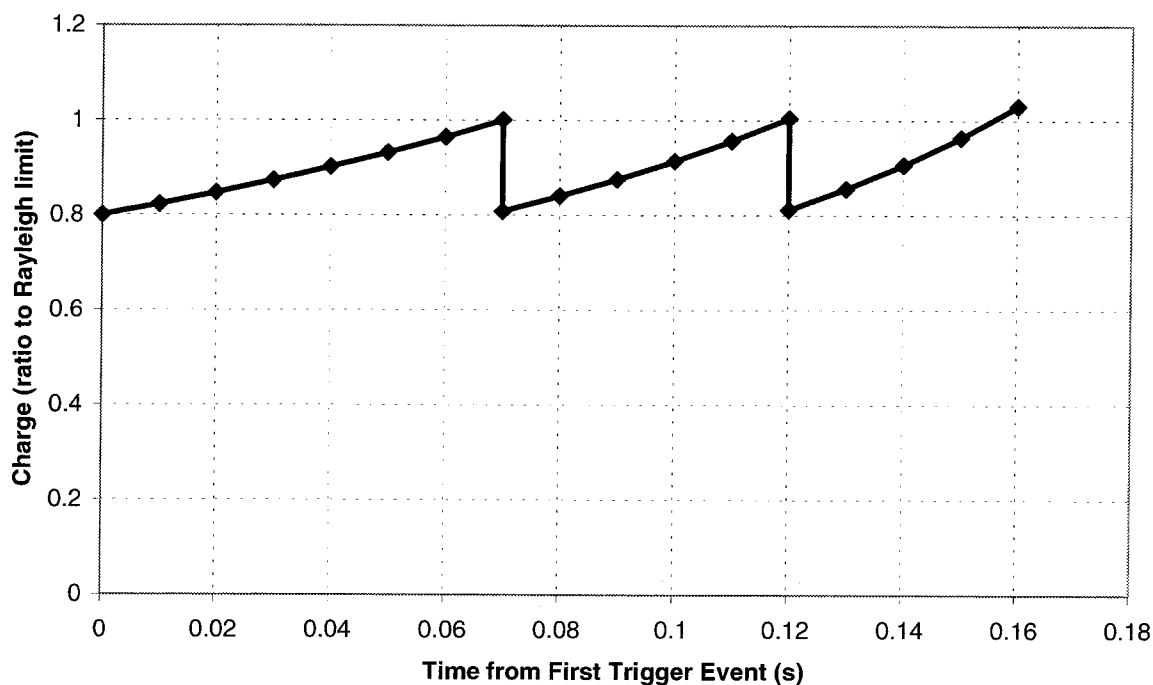


Figure 10.1: Modeled time series of droplet charge for an evaporating methanol droplet with initially 80% of the Rayleigh limit of charge.

A reduction of the measurement step size can be accomplished with minimal modifications to the existing apparatus by replacing the high voltage relays with solid state transistor switches. Modern high voltage switches (such as those manufactured by Eurotek, Inc.) are capable of switching high voltages (up to 65 kV DC) and high peak currents (up to 5 kA DC) with nanosecond response times. However, these are not necessary for the current experiment if the region of the switched field is reduced. As the analysis below will demonstrate, the oscillating droplet in the ping-pong experiment occupies a very small portion of the cell. Thus a much smaller region of the cell can be isolated for trapping the droplet, and much lower potentials used in reversing the electric field. This will allow the use of standard “high voltage” transistor switches such as the MTP1N100 MOSFET switch.

The model used in creating Figure 10.1 can predict the position of an evaporating charged droplet within the drift cell during the course of a ping-pong measurement. This analysis can then be used to predict the effectiveness of the ping-ping tech-

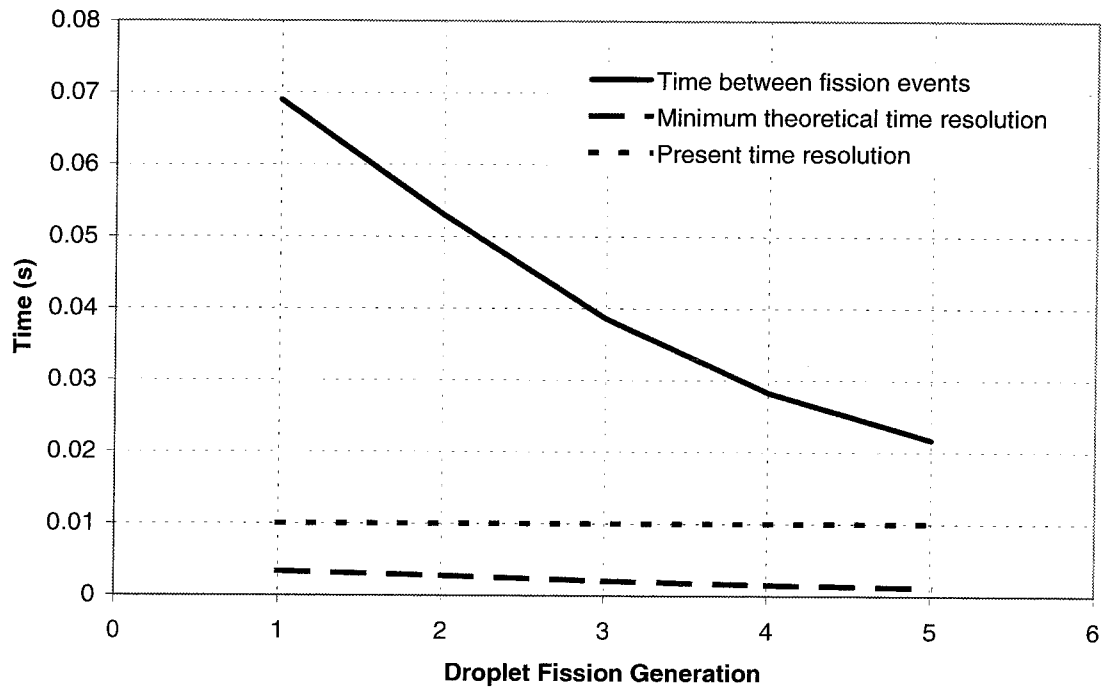


Figure 10.2: Time between fission events for the $40 \mu\text{m}$ methanol droplet portrayed in Figure 10.1. Also plotted is the theoretical minimum sampling time for the same droplet, based on its aerodynamic response time.

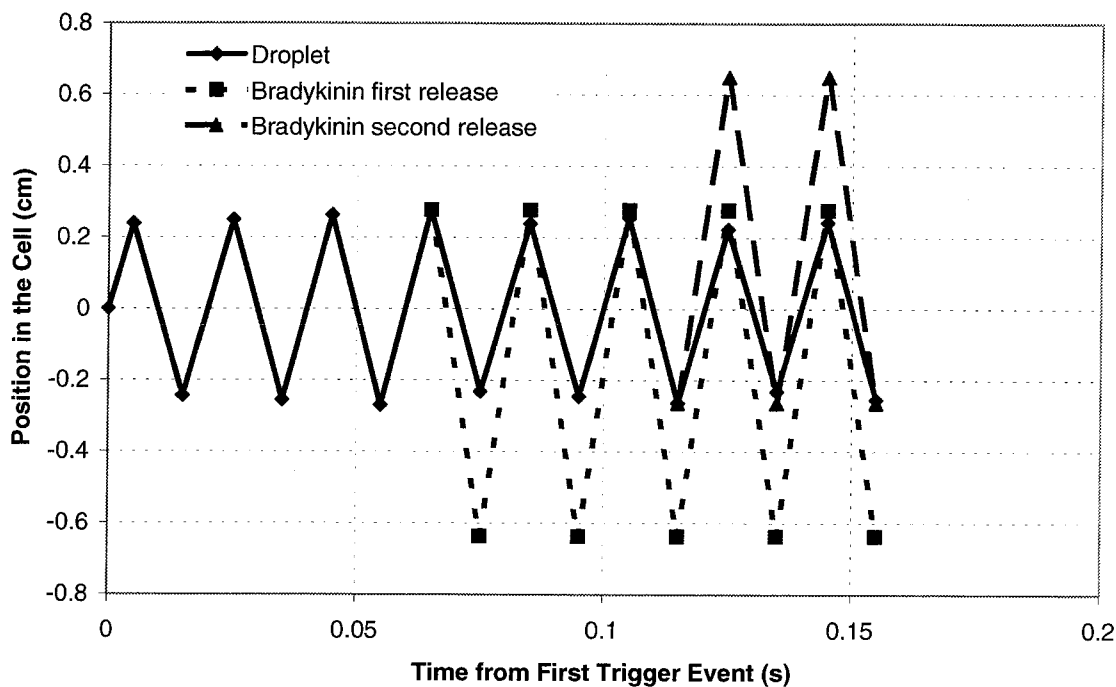


Figure 10.3: Modeled position of the charged droplet from Figure 10.1 during the ping-pong experiment, in a 50 V/cm electric field. Also plotted is the position of a bare gas phase Bradykinin ion in a +2 charge state.

nique for separating gas phase ions from the parent droplet for analysis using mass spectrometry, a Faraday cup detector, or by optical means such as laser induced fluorescence. Figure 10.3 shows the position of the methanol droplet from Figure 10.1 during the ping-pong experiment. The trajectory of the droplet is not influenced significantly by the fission events, and executes periodic motion over a range of about 5 mm. A simple model of ion release has been added to the plot, similar to that presented in Chapter 5. In the model, a bare ion of Bradykinin (in a +2 charge state) is released promptly as a result of droplet discharge. For this model, ion release from the droplet occurs that the extrema of the droplet trajectory. Bradykinin has a mobility approximately twice that of the droplet portrayed in the figure, so its motion is characterized by a range that is approximately twice that of the parent droplet from which it is formed.

The trajectory plot in Figure 10.3 demonstrates the challenges of detecting the

release of ions during the process of droplet breakup using the ping-pong technique. The plot shows that the motion of the ions can be very similar to that of the parent droplet, thus making it difficult to separate the two phases. This observation is consistent with the conclusions from Chapter 5, specifically, the data presented in Figure 5.5. The proper choice of ion can help to resolve this separation issue, since smaller ions would have a higher mobilities that scale to first order according to cross-section. For example, protonated methylamine, with a reduced mobility of $2.65 \text{ cm}^2/\text{Vs}$, [1] would travel a distance of 0.9 cm for the condition in Figure 10.3.

Additional difficulties in separating nascent ions from these charged droplets would be incurred if the ions are partially solvated. If solvated ions are produced, as suggested by numerous investigators, [2] then their mobilities can be reduced significantly. In addition, Figure 5.5, indicates that nanometer sized charged droplets with the Rayleigh limit of charge may have mobilities similar to that of large biomolecules such as Cytochrome-C (+10 charge state). Thus it would be difficult to insure that only gas phase ions are separated from the charge droplet during discharge.

All of the above factors must be accounted for in designing an experiment for analyzing ion formation using the ping-pong experiment. Although these are significant issues if one wishes to observe the formation of large gas phase compounds such as Bradykinin or Cytochrome-C, an appropriate starting point for these investigations is to analyze low molecular weight compounds with much higher mobilities. In view of the analysis presented above, a slight modification of the apparatus is needed in order to separate and analyze desorbed ions. Figure 10.4 shows one possible design. The proposed drift cell has been modified slightly. Specifically, the guard rings within the drift cell are electrically isolated into three groups. The lower ring stack is biased to inject droplets from the electrospray source into the measured volume of the PDA. This field can be reversed to stop the flow of droplets in order to flush the chamber, as is done currently. At the center of the chamber are two rings that form the trapping cell. These are biased separately from the other rings and covered with high transmission mesh grids to insure uniform field conditions. The field in this region can be reversed using off-the-shelf high voltage transistor switches such as the previously

mentioned MTP1N100 MOSFET switch. Above the trapping cell is the upper ring stack, which is biased to inject ions that exit from the trapping cell up into the exit port to the inlet of a mass spectrometer. Control of the fields on the upper and lower ring stacks can be done using the high voltage relays used in the current design, as these do not need to be rapidly switched. Note that, on average, this technique will be successful in detecting ions from half of the fission events, since they have equal probability of occurring when the droplet is moving upward as they do while it is moving downward.

For the study of the desorption of biomolecules from these droplets, the mobility issues presented above create challenges in separating these ions from the droplet. One approach that circumvents this separation issue is to tag the biomolecules with a fluorescent dye and use laser induced fluorescence (LIF) of these dye-tagged molecules to detect them in the gas and solution phases. Sensitive fluorophores are available with moieties that form covalent bonds with common biomolecules (Molecular Probes, Inc.). The possibility of optically detecting these ions eliminates many of the challenges discussed above, and can further be used to probe the chemical properties of these highly charged droplets as has been reported recently for measurements of solvent fractionation in an electrospray plume[3]. A high-efficiency optical receiver for LIF measurements on these droplets has been developed, and schematic of this instrument is shown in Figure 10.5.

An additional use of the LIF receiver is to probe the measurement volume of the PDA in search of evidence of small progeny droplets that result from fissioning. These progeny droplets cannot be detected with the PDA, as they are expected to have diameters less than one micron. The LIF would be well suited for such a sensitive measurement, as it utilizes photomultiplier detectors that can be configured in photon counting mode.

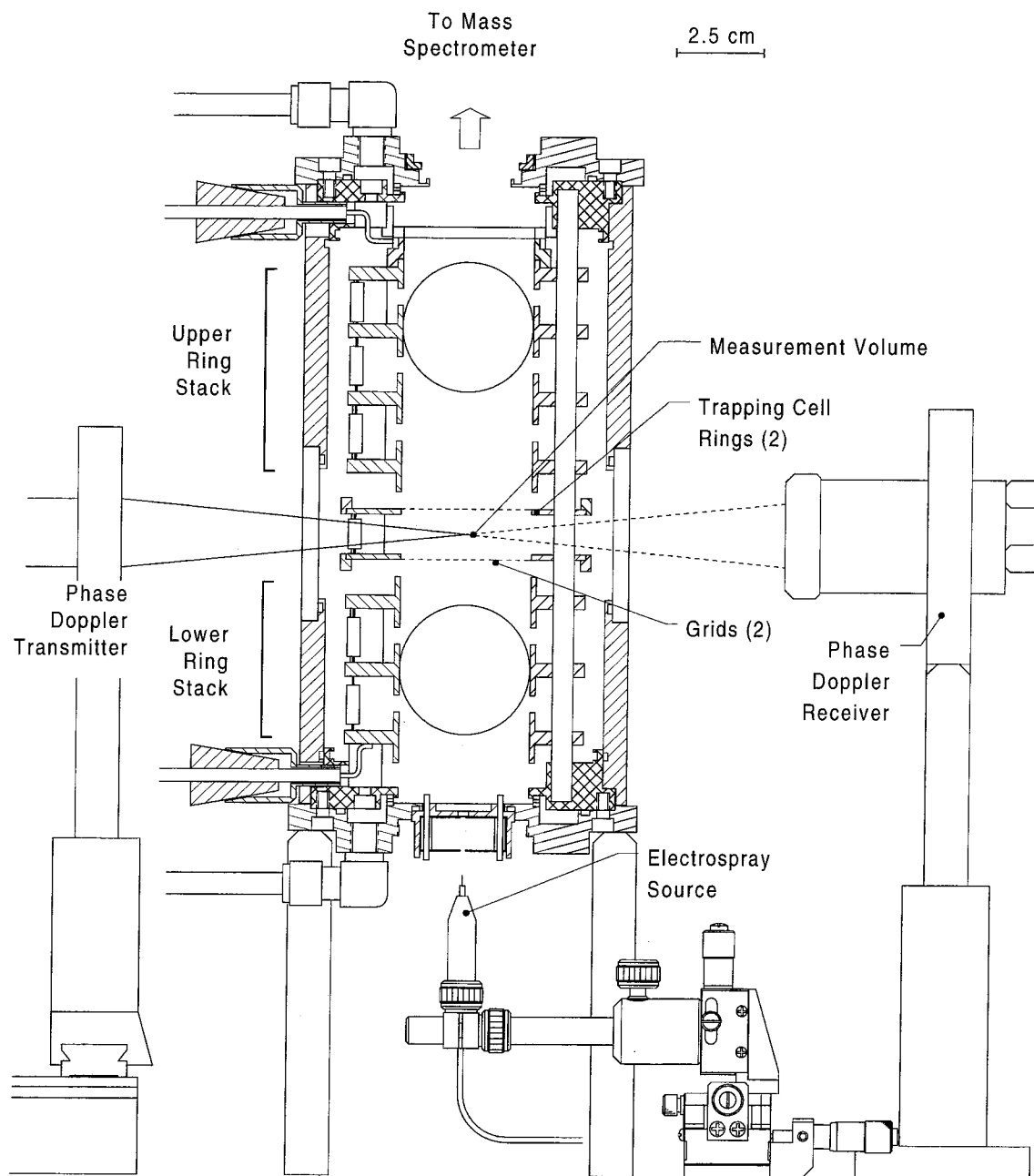


Figure 10.4: Proposed modification of the drift cell to allow for the injection of desorbed ions from the oscillating trapped droplet into a mass spectrometer.

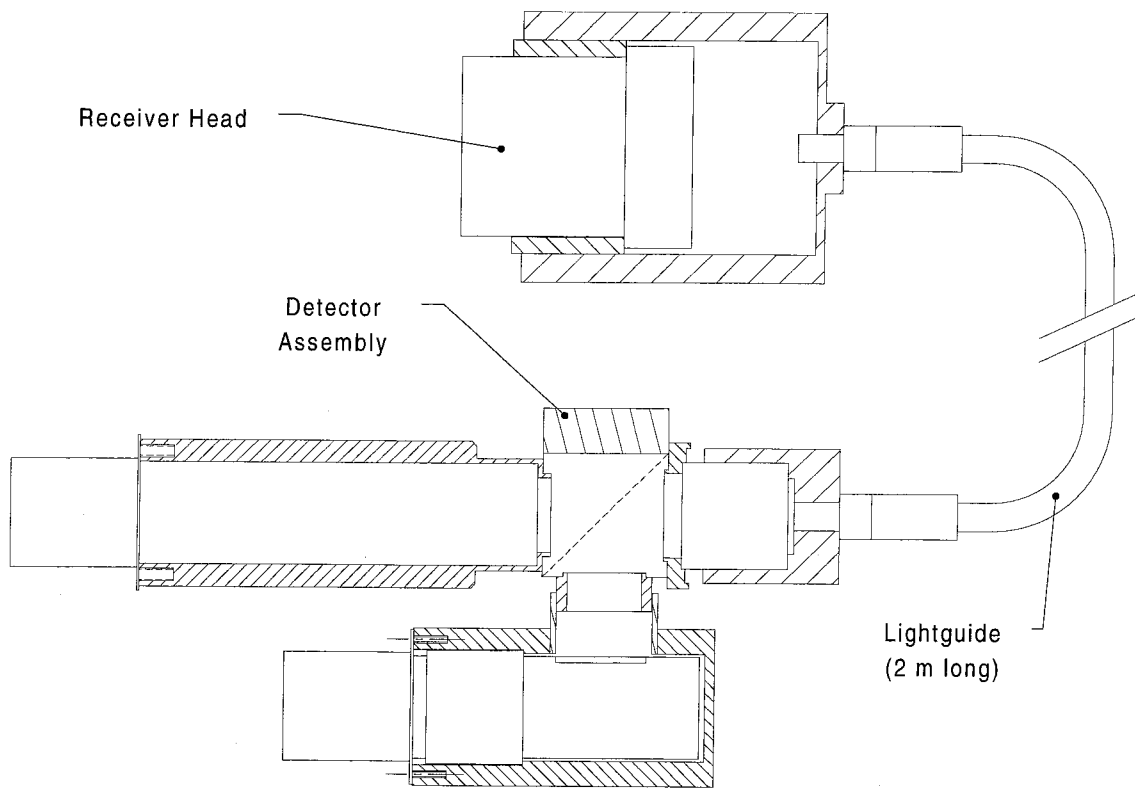


Figure 10.5: Overview of LIF receiver system showing primary components.

Bibliography

- [1] Gary A. Eiceman and Karpas Zeev. *Ion Mobility Spectrometry*. CRC Press, Boca Raton, 1994.
- [2] J.V. Iribarne and B.A. Thomson. On the evaporation of small ions from charged droplets. *J. Chem. Phys.*, 64:2287, 1976.
- [3] S. Zhou and K.D. Cook. Probing solvent fractionation in electrospray droplets with laser-induced fluorescence of a solvatochromic dye. *Anal. Chem.*, 72:963–969, 2000.

Appendices

Appendix A Phase Doppler Anemometer Operations Manual

A.1 Introduction

The Phase Doppler Anemometer (PDA) is an instrument that can be used to obtain simultaneous size and velocity measurements on individual spherical particles in the size range from $0.5\ \mu\text{m}$ to several millimeters. Measurements are made at a single spatial location and can be made in real time with data acquisition rates limited only by the choice of processor and optical arrangement. In addition, measurements are made *in situ* and thus allow for detailed measurements in difficult-to-reach or sensitive flow fields.

The following manual has been written to provide the user with some elementary background on the technique and instructions as to proper setup, alignment, calibration, and operation. This manual assumes an elementary knowledge of optics and lasers. In the absence of this, a good introductory book on optics is recommended.[1]

A.1.1 Phase Doppler Theory

A review of the history and basic principles of the phase Doppler technique can be found in the article by Hirleman.[2] A detailed description of the theory that underlies the technique can be found in a number of references.[3, 4] A review of the technique is given here to provide the user with enough information in order to make simple measurements. The optical system for the PDA is similar to that of the laser Doppler anemometer, and is shown in Figure A.1. The measurement volume is defined by intersection of two identical beams from a polarized HeNe laser. The profile at this cross-over point is shown in Figure A.2a, and consists of two major

frequency components: a Gaussian low frequency pedestal and a sinusoidal higher frequency fringe pattern. The distance between fringes, δ , is a function of the laser wavelength, λ , the distance between the two beams before they are focused by the front lens, s , and the front lens focal length, F , and can be approximated for small beam intersection angles as:

$$\delta = \frac{\lambda F}{s}. \quad (\text{A.1})$$

The diffraction-limited waist diameter of the measurement volume, D_w , is derived from Gaussian optics theory:

$$D_w = \frac{4\lambda F}{\pi D_{in}} \quad (\text{A.2})$$

where D_{in} is the diameter of each beam before it is focused by the front lens and is determined by the laser beam diameter and the configuration of the beam expander.

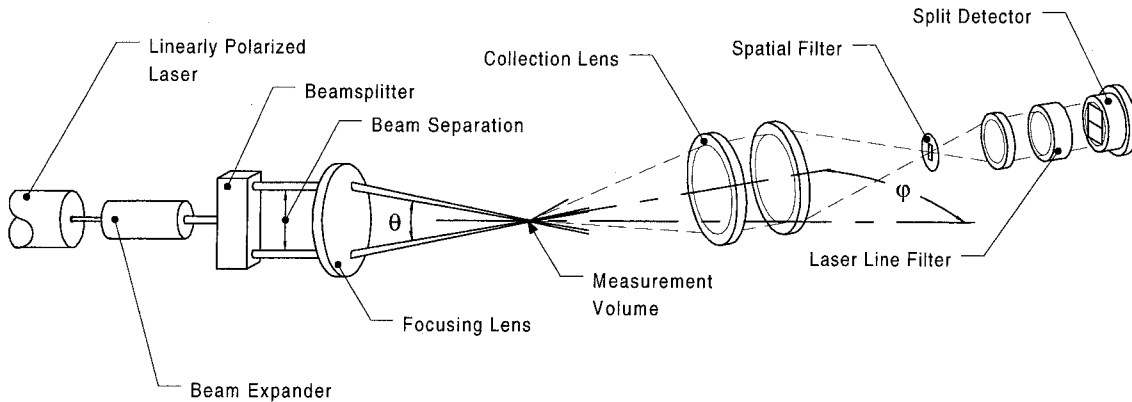


Figure A.1: PDA system optical arrangement.

As a particle passes through the beam crossover, shown schematically in Figure A.2b, it refracts or reflects the light from this region into the surrounding space. An optical receiver is situated to collect this scattered light and to image it onto a pair of detectors. Each detector will record a time-varying signal that looks identical to the measurement volume profile shown in Figure A.2a. These signals will be referred to throughout this manual as “Doppler bursts” and possess two features that comprise the essential elements of the technique. The first is that the time, τ , that

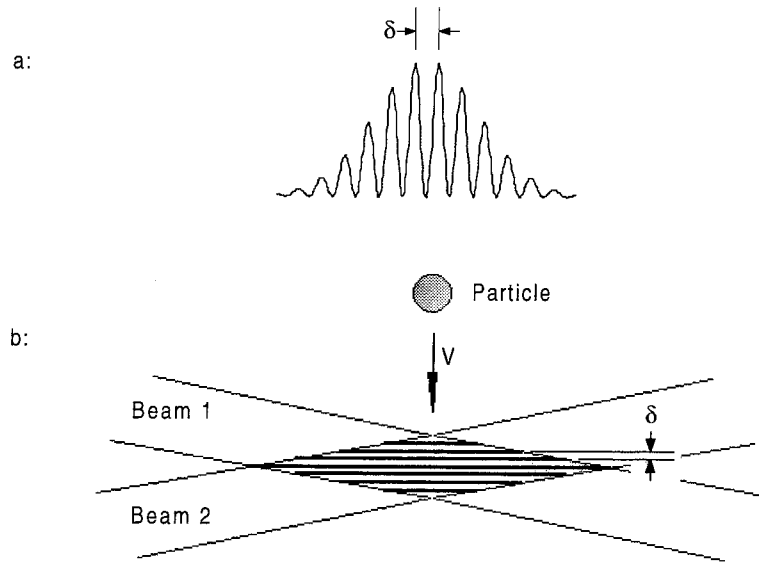


Figure A.2: Theory of PDA measurements. (a) Radial intensity profile at the measurement volume. (b) The measurement volume, defined by the intersection of two phase-matched laser beams.

is recorded between any two fringes in a Doppler burst will be determined by the relative velocity of the particle in the plane perpendicular to the fringes. The particle velocity, v , is

$$v = \frac{\delta}{\tau} = \delta\nu \quad (\text{A.3})$$

where ν is the signal frequency. The second feature of the signals collected by the two detectors is that there will be a phase shift between them. This phase shift is directly proportional to the particle diameter. The origin of this phase shift can be understood by thinking of the particle as a small lens or mirror that is refracting or reflecting light as it falls through the fringe planes of the measurement region. If one were to freeze the motion of the particle “lens” as it passes through the measurement region, the particle will then project an image of the fringes into surrounding space. The smaller the particle’s diameter (or, by analogy, the smaller the effective focal length of the lens), the more expanded the projected fringes will be in the surrounding space. It is this spatial frequency of the projected fringe pattern that is measured by the phase

shift between two detectors. The analogy of a particle as a lens suggests two important properties that particles must satisfy in order that they may be measured with the phase Doppler technique: they must be homogeneous and spherical. This has been verified in both theory and experiment, and several studies have been undertaken to determine how each affects the accurate determination of particle size.[5, 6, 7]

The most common arrangement for the two detectors in a PDA receiver is shown in Figure A.1. In this arrangement, the collection lens of the receiver is divided into two equal areas. The plane that separates these two areas is that which contains the transmitter and receiver axes, and is called the scattering plane. As the diagram shows, the image is inverted by the receiver lens system so light that is incident upon the top half of the collection lens is transmitted to the lower detector. As a refracting particle passes through the measurement region, the projected image of the fringes will sweep in front of the collection lens. Thus the signal at the lower detector will lead the signal at the upper detector. A reflecting particle will create the opposite effect: in this case, the fringes will sweep in space in the opposite direction as the particle's motion, and the signal from the lower detector will lag in phase from that of the upper detector.

The relationship between the phase shift and particle size has been derived in the geometrical optics approximation.[3, 4] More exact Mie theory can also be employed, and numerical solutions are available to derive this relationship for any given choice of particle refractive index and transmitter and receiver configuration.[8] If careful attention is paid to the optical arrangement so that the scatter is the result of pure refraction or reflection, this "calibration curve" (phase shift versus size relationship) will be a straight line passing through the origin. Scatter resulting from a combination of reflection and refraction will be described by a nonlinear calibration curve.

The use of numerical simulation programs for PDA such as SCATAP[8] (which is freeware and can be downloaded from website of the Institute of Material Science at the University of Bremen at <http://imperator.cip-iw1.uni-bremen.de/fg01/scatap.html>) is strongly recommended as a tool for verifying the linearity of this relationship. For

example, Figure A.3 shows the result from SCATAP of the phase shift/particle size relationship for pure water droplets measured with the optical arrangement listed in Table A.1. Also shown in Figure A.3 is the calibration curve that was generated experimentally by using a vibrating orifice aerosol generator (VOAG, which will be explained in greater detail in Section A.2.3) and using the optical configuration listed in Table A.1. As the graph shows, there is excellent agreement between experiment and theory. An interesting feature of Figure A.4 is that the calculated calibration curve begins to fall off from a straight line at about $100\ \mu\text{m}$. This suggests that, for the optical configuration used in the example, there may be some inherent inaccuracies associated with extending the measurement to the full $0 - 2\pi$ in phase shift. Thus a modification of the parameters listed in Table A.1 may be needed for carrying out measurements of particles that are larger than $100\ \mu\text{m}$. As we will see in Section A.3, an adjustment in the transmitter or receiver optics is easily implemented.

Table A.1: Typical optical configuration for PDA.

Transmitter:	
Beam Separation	6.8 mm
Front Lens Focal Length	250 mm
Receiver:	
Collection Lens Focal Length	200 mm
Geometry of Detector at Collection Lens	Two Half-Circles, Split at Scattering Plane
Detector Radius at Collection Lens	12.5 mm

SCATAP can also be employed as a tool for carrying out sensitivity analyses for various optical parameters of the PDA or the aerosol under study. An example is shown in Figure A.4, which shows how a $\pm 10^\circ$ variation of the collection angle for the receiver, θ (see Figure A.1), results in a variation in the slope of the calibration curve. This would result in a $\pm 10\ \mu\text{m}$ uncertainty for particles at around $100\ \mu\text{m}$.

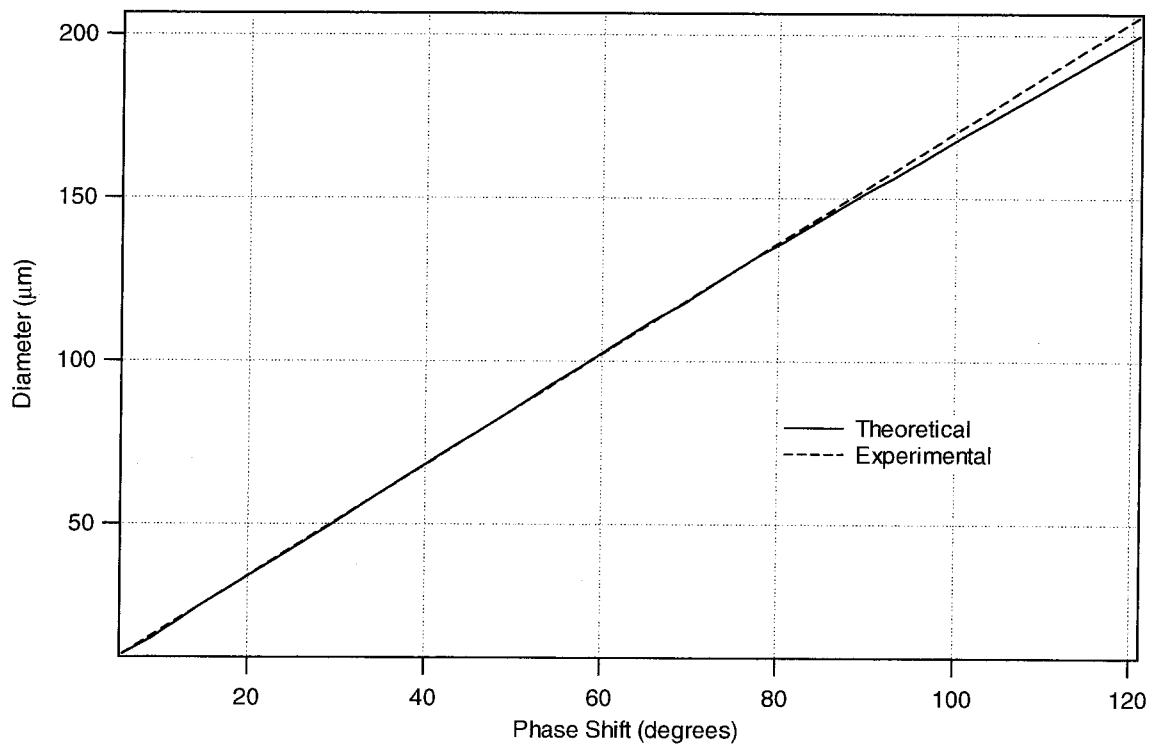


Figure A.3: Calibration for PDA, showing phase shift versus particle size relationship using SCATAP and the experimentally obtained relationship resulting from calibration with a VOAG. For optical configuration see Table A.1.

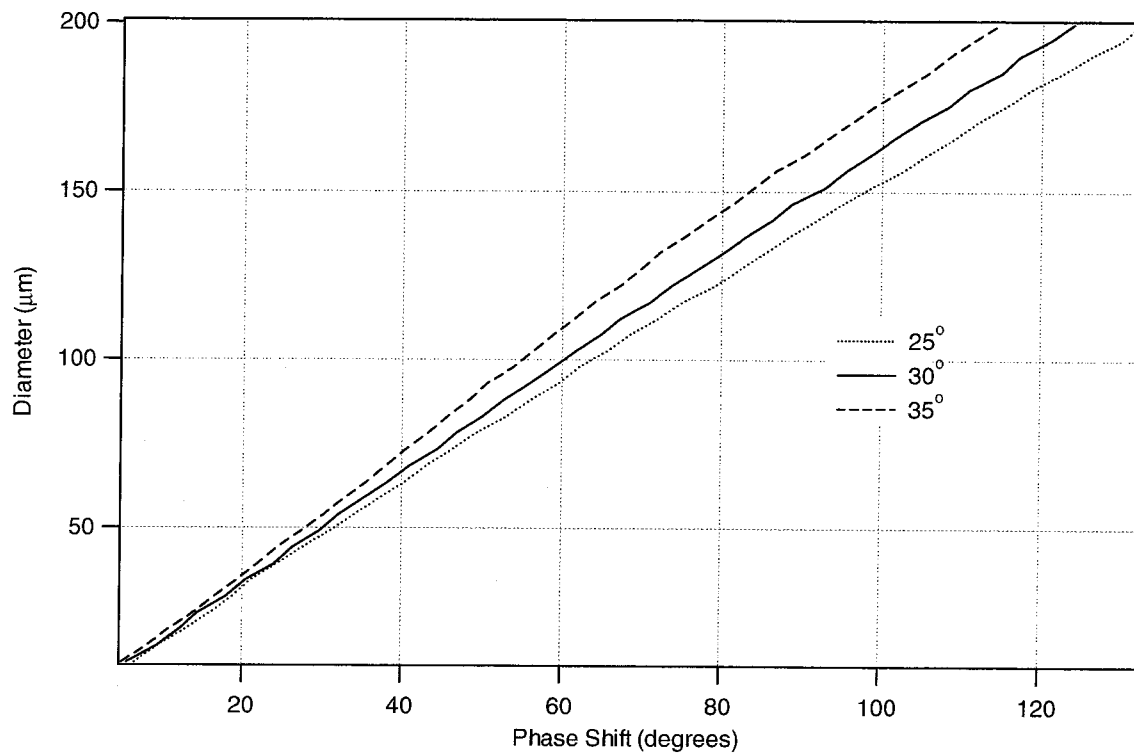


Figure A.4: Calibration curves for various collection angles, showing the effect that an uncertainty in the angle might have in the particle size measurement. For optical configuration see Table A.1.

A.1.2 Adjustments to Instrument that Affect Measurement Range

As the data in Figure A.4 suggest, one of the ways to change the size range of the PDA is to change the receiver collection angle, θ . The complete list of parameters for changing the size and velocity range are listed below (see Figure A.1 for the definition of these parameters):

- Beam Separation
- Transmitter Focusing Lens Focal Length
- Receiver Collection Lens Focal Length
- Receiver Collection Angle, θ

The first two parameters change the fringe separation, according to Equation A.1, and thus can be used to change both the size and velocity ranges. The last two parameters modify the size and location of the two detector regions of the receiver. Modification of these parameters would not affect the velocity range, which is a temporal measurement and so would not depend upon the location of the detectors, but would have an effect on the size range.

Table A.2 shows typical values for maximum particle size and velocity as a function of the three of the parameters (excluding collection angle, for reasons that will be divulged later) listed above. The maximum velocity that can be recorded with the technique is directly proportional to the fringe separation and is limited only by the maximum frequency response of the photodetector and associated electronics. For the current photodetector arrangement the frequency bottleneck resides in the silicon PIN photodiodes, which have a maximum frequency response of 1 MHz. Biased mode operation of the photodiodes would yield higher frequency response. For the shortest response times of up to 100 MHz, the photodiodes can be replaced with a bifurcated fiber optic bundle linked to two external avalanche photodiodes or photomultiplier tubes. This will most likely shift the bottleneck in the overall system frequency

response to the processing electronics, which currently consist of a Tektronix TDS 410A digital oscilloscope with a 100 MS/s sampling rate.

Table A.2: Estimated PDA system maximum particle size and velocity.

Transmitter Focal Length (mm)	Focused Beam Waist Diameter (μm)	Beam Separation (mm)	Fringe Spacing (μm)	Maximum Velocity ¹ (m/s)	Theoretical Maximum Diameter ²	
					200 mm Collection Lens (μm)	100 mm Collection Lens (μm)
250	296.2	10	15.8	15.8	417.0	208.5
		20	7.9	7.9	208.5	104.3
125	148.1	20	4.0	4.0	208.5	104.3
		40	2.0	2.0	104.3	52.1

1. 1 MHz detector limit

2. Maximum diameter corresponds to water droplets and a 2π phase shift with $\beta=97.6$, $n_{\text{calib}}=1.33$, $\text{BeamSep}_{\text{calib}}=6.8$, $\text{XMTLens}_{\text{calib}}=250$

The measurement of particle size, like that of velocity, is dependent upon the fringe separation at the measurement region. In addition the size range can be affected by the location of the receiver and the solid angle over which the two detectors collect the scattered light. Under conditions where the calibration curve is linear and passes through the origin,

$$D \propto \frac{n \times \text{XMTlens} \times \text{RCVlens}}{\text{BeamSep}}, \quad (\text{A.4})$$

where n is the refractive index of the sample, XMTlens is the transmitter lens focal length, RCVlens is the collection lens focal length, and BeamSep is the transmitter beam separation. For example, if one were to double the beam separation, the result would be to halve the resulting diameter range. Doubling the beam separation will also affect the maximum velocity that the instrument can measure, halving that as well. These trends can be seen in Table A.2.

The effect of changing the collection angle is not included in Equation A.4. The reason for this is that the relationship between collection angle and the slope of the calibration curve cannot be easily calculated. Additionally, a change in the collection angle can result in the collection of light that is the result of multiple scattering modes (such as partial refraction and partial reflection). SCATAP is recommended

for investigating the effect of collection angle on particle size range. An example is shown in Figure A.5, which continues the calculations of Figure A.4 for increasing collection angles using the representative PDA optical configuration in Table A.1. At 90° off-axis, the linear relationship between phase shift and particle size completely breaks down as reflective scatter from the surface of the droplet mixes with refractive scatter. For the other collection angles, the results of these SCATAP calculations can be used to directly modify the constant of proportionality between the phase shift and particle size as described in Equation A.4. It is, however, recommended that large changes in collection angle be followed by a re-calibration of the instrument to insure that the results are accurate. This calibration process is described in the next section.

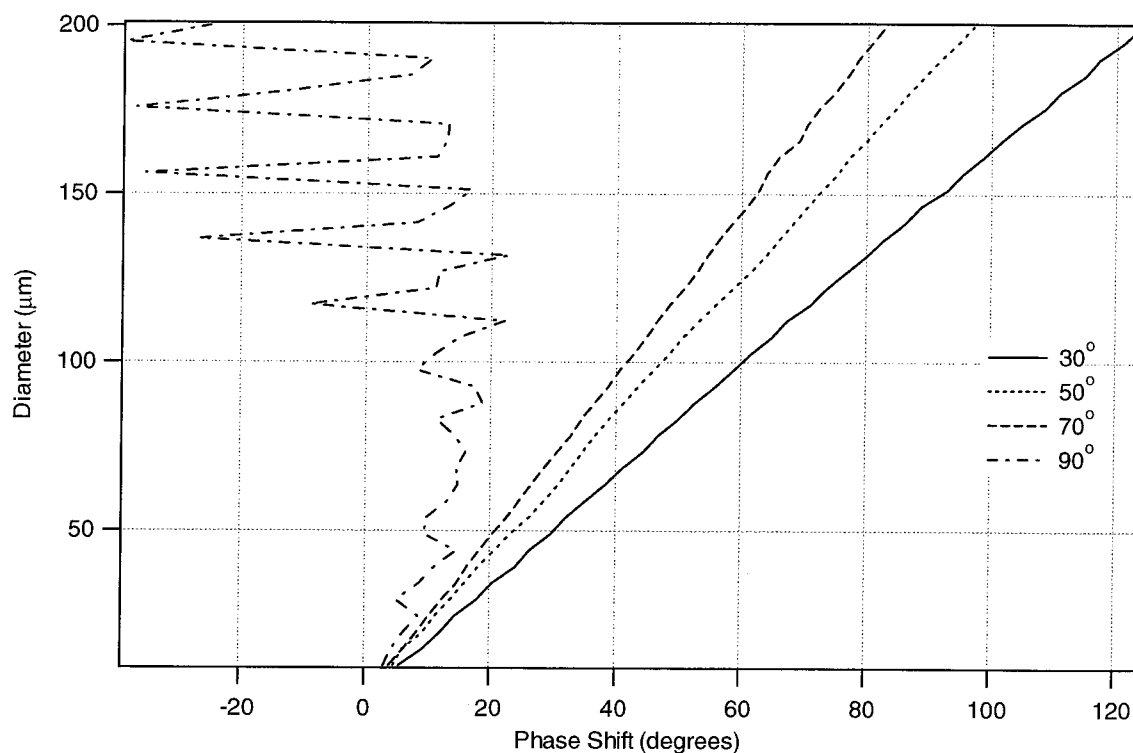


Figure A.5: PDA calibration curves for pure water as a function of collection angle. For optical configuration see Table A.1.

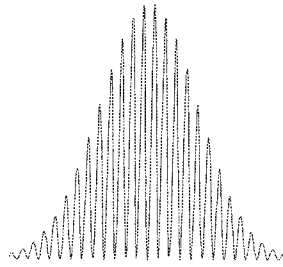
Two additional comments are worthy of note in considering the suitability of an optical configuration to a particular size measurement range. The first comment

regards the minimum size sensitivity of the PDA method. In general, the PDA method is considered to be valid for particle diameters that are greater than the wavelength of the light used to measure them. For most systems this results in an absolute minimum diameter of about $0.5 \mu\text{m}$. Recent experimental investigations[9] have shown this to be the case provided careful attention is paid to the optical configuration. In addition to the previously mentioned fringe separation and receiver location, another factor that needs to be considered when attempting measurements of very small particles is the sensitivity of the receiver to the collection of the low light levels that are associated with these small particles. Here, the measurement volume diameter plays an important role in determining the incident light intensity on the scattering particle. As Equation A.2 shows, the measurement volume is determined by the focal length of the transmitter front lens and the beam diameter of each beam incident upon the lens. A beam expander can be used to modify the diameter of each beam without affecting any of the other parameters in the transmitter system. Since the measurement region diameter is inversely proportional to the incident beam diameter, a beam expander that increases the size of the beams will result in a measurement volume diameter that is smaller than the original size. This results in a higher light flux incident on the particle and better sensitivity to smaller sizes.

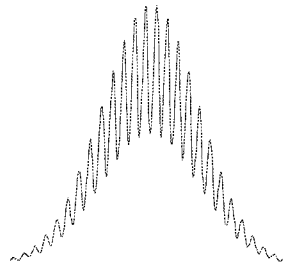
In considering large particles, two issues should receive particular attention. As a general rule, the measurement volume should be equal to or greater than the largest particles that are likely to be measured. As the particle becomes larger than the measurement volume diameter, it becomes more and more likely that low level scatter from other modes begin to compete with the major scattering mode. Another phenomenon that is often encountered when measuring large particles is that the visibility of the signal begins to degrade as the particle diameter becomes much larger than the fringe separation. The visibility of a Doppler burst is defined as the difference between the upper and lower envelopes of the sinusoidal part of the signal, as shown in Figure A.6. A simple reason for this effect is that a particle that is much larger than the fringe separation will always be scattering light from multiple fringes as it passes through the measurement region so the resulting scattered fringes will

be “washed out” as a result. It is interesting to note that the visibility can itself be used as a method for measuring particle size.[10] SCATAP results for the size of water droplets as a function of visibility are shown in Figure A.7. A reduction in visibility results in the attenuation of the amplitude of oscillation in the sinusoidal component of the scattered signal. Thus the signal-to-noise ratio of the signal may actually decrease for these larger particles, even though the intensity of the scattered light will certainly increase as the particle size increases.

100%:



50%:



33%:

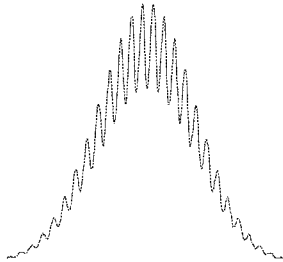


Figure A.6: Visibility of PDA signals. As a scattering particle becomes large in relation to the fringe separation the visibility will decrease.

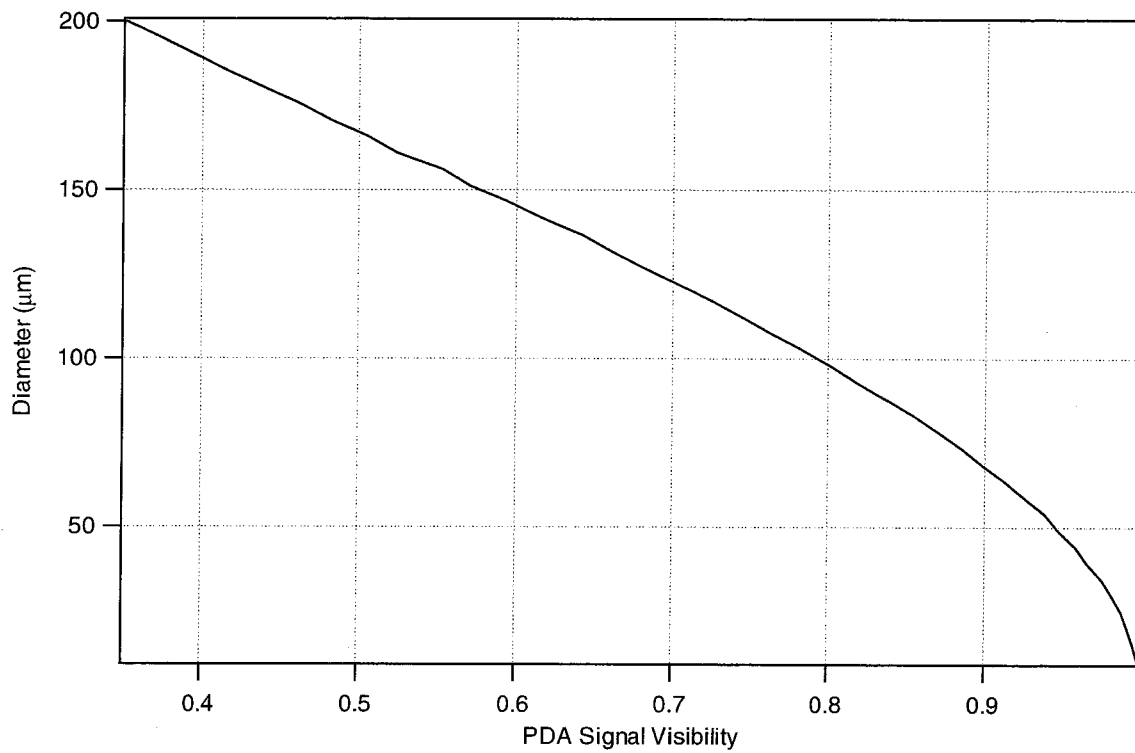


Figure A.7: Particle size versus PDA signal visibility for water droplets ($n = 1.33$), using the optical configuration in Table A.1.

A.2 Calibration

Calibration of the PDA is important for determining the exact relationship between phase shift and particle diameter, i.e., the constant of proportionality for Equation A.4. The following sections will address such issues as when to re-calibrate the instrument, how the instrument makes use of the calibration in normal operation, and the procedure for performing the calibration.

A.2.1 When to Calibrate

Calibration of the PDA is not normally required for day-to-day operation. This is one of the features that has made phase Doppler anemometry so successful in a variety of research and industrial applications. It is due to the fact that the type of measurements required for the technique, namely the frequency and the phase shift of the two collected signals, are independent of detector or electronic gain and therefore do not vary from one day to the next. Calibration is necessary whenever you suspect that a change in the transmitter or receiver optics or particle type might result in a change in the calibration curve that cannot be predicted by the relations that will be presented in Section A.2.2. Calibration is recommended for situations such as the following:

- The location of the receiver has changed relative to the transmitter. The most common example of this is a change in the collection angle from its typical position in the scattering plane at 30° off-axis in the forward direction. This is the most common reason to recalibrate, as there is no guarantee that the resulting calibration curve is linear for changes in collection angle.
- A modification has been made to the receiver that might have resulted in a change in the effective area for each detector (i.e., the effective area of the two detectors when projected onto the front lens of the receiver). This might include disassembly of the rear of the receiver for cleaning or repair. It would not be necessary to recalibrate, however, if either the spatial filter or collection lens is

changed. A description of these components will be given in Section A.3.3.

- A particle with dramatically different scattering properties is being measured. This would not include a change from, for example, pure water droplets ($n = 1.33$) to DES ($n = 1.44$) or PSL ($n = 1.59$). It might be necessary to recalibrate if the original calibration was done with water and one wishes to study particles that may have some absorptive properties (i.e., an imaginary refractive index). If unsure about the need to calibrate, it is always best to perform the calibration.
- A significant change is made to the transmitter optics that calls into question the linearity of the calibration curve.

A.2.2 Calibration Fundamentals

The ultimate goal of the calibration process is to obtain the calibration factor, γ , which is defined by the following product:

$$\gamma = \beta \times \frac{BeamSep_{calibr}}{n_{calibr} \times XMTlens_{calibr} \times RCVlens_{calibr}}, \quad (A.5)$$

where the subscript *calibr* indicates the parameters for the system at the time of calibration and *XMT* is the transmitter lens focal length, *BeamSep* is the transmitter beam separation, *RCVlens* is the receiver collection lens focal length, and n is the sample refractive index. The first two parameters are directly measured on the transmitter. The sample refractive index is taken from the sample used in calibration. β is the constant of proportionality between the measured phase shift, ϕ_{calibr} , and the particle diameter, D_{calibr} :

$$D_{calibr} = \beta \times \Phi_{calibr} \quad (A.6)$$

When subsequent PDA measurements are taken, the particle diameter is obtained from the measured phase shift using the relationship:

$$D_{meas} = \gamma \times \frac{n_{meas} \times XMTlens_{meas} \times RCVlens_{meas}}{BeamSep_{meas}} \times \Phi_{meas}. \quad (A.7)$$

As an example, the PDA is calibrated with water droplets from a VOAG (described below). During the calibration, the transmitter beam separation is 6.8 mm and the transmitter lens is 250 mm. The receiver lens has a 200 mm focal length. As a result of the calibration process, β is found to be 98.9. This results in the following calibration factor: $\gamma = 98.9 \times 6.8 / (200 \times 250 \times 1.33) = 0.01011$. For a subsequent measurement of PSL particles ($n = 1.59$), the transmitter beam separation is changed to a new value of 10 mm. The new relationship between the measured phase shift and the particle size is therefore: $D_{meas} = 0.01011 \times (1.33 \times 250 \times 200/10) \times \Phi_{meas}$.

A.2.3 Methods for Producing Calibrated Particles

To perform the calibration, a means of producing homogeneous particles or droplets of a known diameter must be found. One means of providing calibration aerosol is by using monosized polystyrene latex spheres (PSL). Another method is to create liquid droplets using a vibrating orifice aerosol generator (VOAG). The method chosen for producing these monosized particles will depend upon the particle size range over which one wishes to calibrate. Dispersing PSL with a nebulizer is a viable method for producing particles smaller than 50 μm . For large particle sizes of approximately 500 μm to 1 mm, the use of liquid droplets becomes problematic owing to their tendency to distort when injected into the measurement region under normal flow conditions. Thus the use of glass or plastic beads is recommended for calibration of large particle sizes. For the range of the particle sizes from 3 to 500 μm , the use of the VOAG is recommended. Since this covers the range for most measurements with the PDA, the remainder of this section will be devoted to issues related to calibrating the PDA with the VOAG.

The VOAG[11] is an instrument for generating a monodisperse aerosol jet. A description of the instrument and a guide to its operation is beyond the scope of this manual, and the interested user is directed to the instruction manual for the TSI model 3050 Berglund–Liu Vibrating Orifice Monodispersed Aerosol Generator for an excellent description of both. There are two modes of operating the VOAG that are

pertinent to the calibration of the PDA. The first technique, the solvent evaporation technique, uses a solution for the aerosol comprised of a non-volatile solute in a volatile solvent. After the aerosol is created from the generator, the volatile solvent is allowed to evaporate leaving the non-volatile particles whose size is a function of the operating conditions of the VOAG and the mixing ratio of the solution. This technique is described in detail in the TSI model 3050 instruction manual, and it is recommended that this instrument be used for this mode of aerosol generation. Once injected into the measurement volume, calibration can be performed according to the principles described above. Specific instructions on the operation of the system software are given in Section A.4.3. The particles produced by this technique range in size from 3 to 10 μm in diameter. As droplets become larger it becomes more likely that they will be lost to the walls of the VOAG before they reach the measurement volume.

For particles in the range of 10–300 μm , the jet of monodispersed liquid droplets from the VOAG is allowed to pass directly into the PDA measurement volume. The solution for these aerosols is usually water, although this can be varied to more closely match to the eventual measurement application of the PDA. For this mode of operation, a simple device has been made to replace the TSI model 3050, consisting of a small piece of thin-walled metal tubing upon which a piezoelectric plate has been glued. At one end of the tube is a fitting for the introduction of the sample liquid and at the other is a fitting for a precision pinhole. The monodispersed droplets that exit the pinhole are produced at a frequency equal to the driving frequency of the piezoelectric crystal, usually at about 1 to 5 kHz. This droplet production rate is crucial to a successful measurement using the PDA. As mentioned in the introduction to this manual, the PDA is a single particle counting technique. If the droplet production rate is too high such that multiple particles are scattering light in the measurement volume at any one time, then the instrument will not be able to resolve individual signals from the particles. The resulting signals will have very low visibility, and an accurate measurement of the phase shift will not be possible. It is therefore crucial that the user pay close attention to the measurement volume

diameter when calibrating. In general, for piezo driving frequencies from 1 to 5 kHz corresponding to a size range from about 100 to 200 μm , no beam expander should be used. The operating parameters in Table A.1 have been found to work well for this particle size range from the VOAG. An example of the result of a calibration of the PDA is shown in Figure A.8

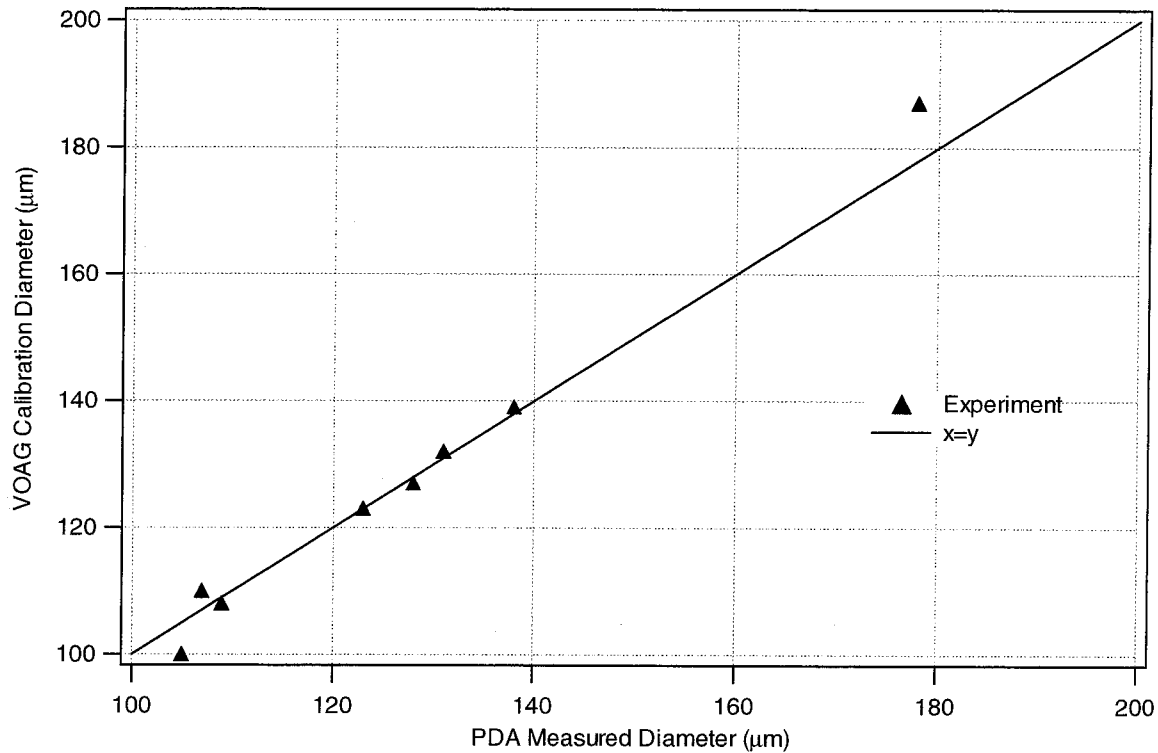


Figure A.8: PDA calibration with a VOAG: Measured diameter vs. VOAG calibration diameter.

A.2.4 Laser Safety

The laser is a source of extremely intense light having characteristics that are very different from light emitted from conventional sources. Many of these unique properties can be a source of danger to the uninitiated. For example, light from a laser is collimated over a great distance from the source, and thus the energy density of a beam can be high and dangerous even at large distances from the laser. The laser

that is used in most implementations is a polarized, 10 milliwatt Helium Neon laser. This laser has been rated by the U.S. Bureau of Radiological Health as a Class IIIB laser product. The beam from the laser head can be blocked by sliding the shutter near the outlet of the laser head, as indicated in the instructions that accompany the laser.

What follows are some recommendations for the operation of any laser experiment. Rather than being an exhaustive list, it is meant to encourage safe thinking when working with laser systems.

- Find the manufacturer's instructions for the operation of the laser. Follow the manufacturer's recommendations for safe handling.
- While the laser is operating, limit access to the immediate area. During alignment of the optical system, when stray laser beams might pass out of the immediate area, clear the room of unnecessary personnel and use extreme caution to limit exposure.
- Use caution when operating the laser in the presence of flammable, explosive, or volatile substances such as alcohols and other similar organic compounds.
- Always block the beam in an experiment with a laser power meter or some other non-reflective, nonflammable object. A folded piece of metal, painted black, works well. Also, set up shields to prevent strong reflections from leaving the experiment.
- Never look directly into either the main laser beam or any stray beams. Never sight down a beam towards its source.
- Do not allow reflective objects to be placed in the laser beam. Even objects such as rings and watch crystals can reflect dangerous levels of laser light.
- Protective eyewear should always be available in the area of the experiment.

A.3 Optical System Description

The PDA consists of two major optical assemblies, a transmitter and a receiver. The transmitter and receiver can be configured in a variety of ways. These will be discussed below.

A.3.1 Transmitter

The transmitter is designed to generate a pair of equal intensity laser beams and focus them to an intersection point that forms the measurement region. A schematic of the transmitter assembly, showing the major components, is shown in Figure A.9. A photograph of the transmitter, without a beam expander, is shown in Figure A.10. For a detailed list of the components in the transmitter, including drawings for machined parts, see Section A.5.

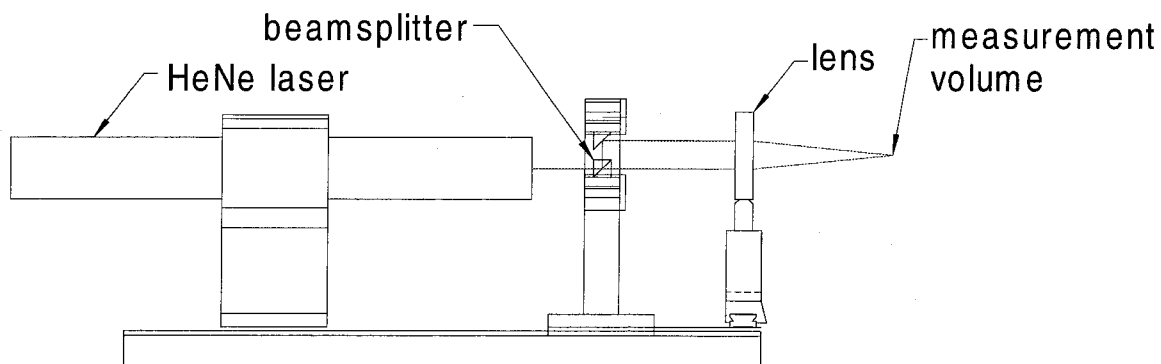


Figure A.9: PDA transmitter.

As described in Section A.1.2, the transmitter beam separation and the front lens focal length can be easily changed. The front lens is replaced by removing the 1.5 inch diameter lens in its cell and replacing it with another. The beam separation is modified by moving the turning mirror until the proper separation is achieved. This procedure is outlined in greater detail in the next section.

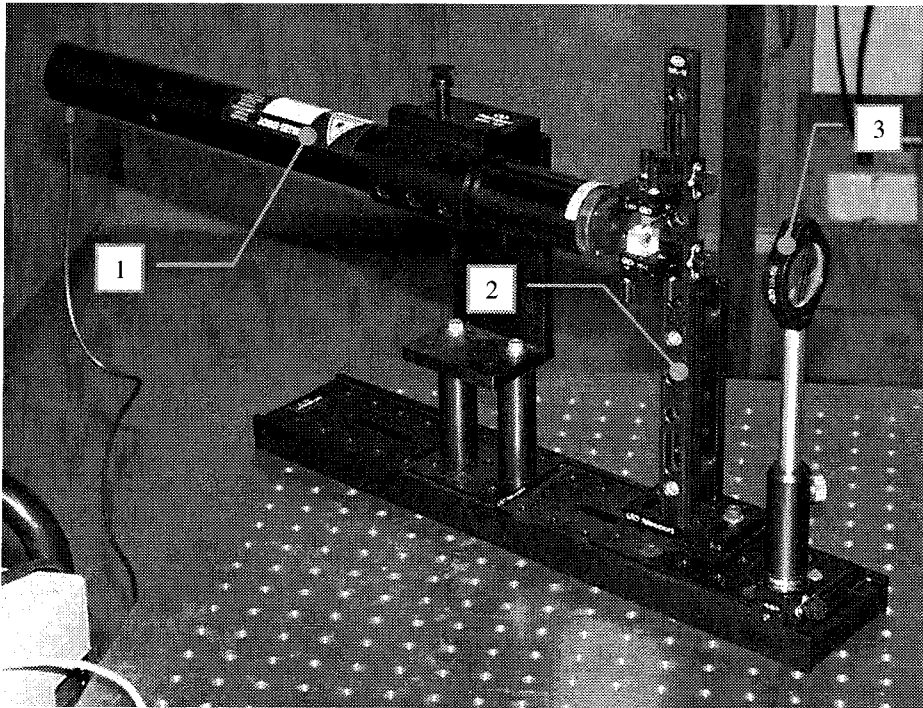


Figure A.10: Photograph of the PDA transmitter showing the main parts. 1: Polarized HeNe laser, 2: Beamsplitter assembly, 3: Front lens.

A.3.2 Alignment of Transmitter Optics

Alignment of the transmitter optics requires a few special tools that can be built from materials commonly found in an optics lab. A tape measure and a ruler are needed to measure the beam separation. To reduce risk of eye injury from scattered light a small neutral density filter or polarizing filter is also recommended to attenuate the laser beam. A microscope objective or short focal length lens, mounted with an optical base and post at the same height as that of the measurement volume, is used to check beam intersection. Finally, a scattering target needs to be made for locating the point of beam intersection and, later, for aligning the receiver to this point. The simplest way to create this target is with a length of transparent tape attached at one end to an optical post with the free end placed in the path of the beam.

The procedure for aligning the transmitter is as follows:

- A. Remove the beamsplitter and turning mirror from the vertical rail of the beamsplitter assembly, shown in Figure A.11. This is done by loosening the knobs that lock each carriage to the vertical rail. Remove beam expander lenses, if present, and front lens from their post holders, leaving the post holders mounted on the transmitter rail. Anchor the transmitter rail to an optical breadboard.
- B. Allow the beam to strike a wall several meters away (making sure to follow the rules for laser safety outlined in Section A.2.4). Make a small mark on the wall at the location of the laser spot.
- C. Align the beam from the laser so that it is horizontal and at the proper height. Choose a height for the measurement volume based upon your requirements, keeping in mind that the output from the laser forms the lower of the two parallel beams which are then focused to the measurement volume. This is shown in Figure A.9.
- D. If a beam expander is required for the measurement, it must be installed and aligned next. The most common beam expander is pair of coated achromatic doublet lenses (each in their own mount), selected so that the ratio of their focal

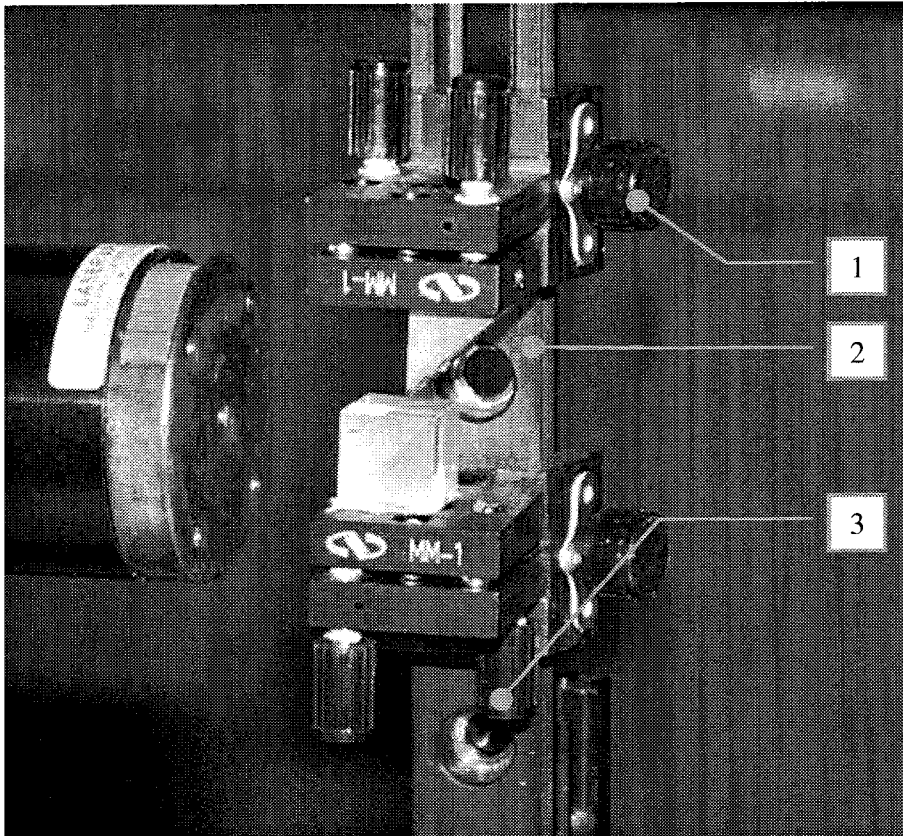


Figure A.11: Close-up of the beamsplitter assembly, showing the beamsplitter and turning mirror. 1: Locking knob for turning mirror carriage. 2: Vertical rail. 3: Adjustment knob for tilting beamsplitter mount.

lengths is equal to the amount of expansion or contraction desired.[1] Drop the first lens in place on the transmitter rail as close to the laser as possible. Make adjustments to the lateral position of the lens, insuring that the laser spot on the wall is not shifted from its original position. To correct for the tilt of the lens, observe the low-intensity beam that is reflected back to its source and insure that the beam is reflected back upon itself. After the first lens is aligned and secured, place the second lens at the appropriate distance. Observe the spot on the distant wall to assure that the beam is well collimated. Following the same guidelines as for the first lens, adjust the lateral position and tilt of the lens and secure it to the rail.

- E. The beamsplitter assembly is installed next. Slide to beamsplitter into position and lock it in place using the locking knob on the carriage. Adjust the tilt on the beamsplitter mount, observing the low intensity beam that is reflected back as with the lens adjustment. Next, slide the turning mirror into position, and lock into place so that the desired beam separation is achieved. Observe the two spots on the distant wall and adjust the tilt of the mirror so that the beams are parallel and are oriented vertically.
- F. Drop front focusing lens into the post holder, and adjust lateral position and tilt according to the instructions in D.
- G. Verify that the beams are intersecting completely using the mounted microscope objective or small lens. Place the objective in the path of the intersecting beams and view the projected image of the beams at a far wall. As the objective is slid towards and away from the transmitter one should observe the projected spots of the beams as they approach and then overlap. If the beams do not perfectly overlap, make slight adjustments to the tilt mount of the turning mirror. At the point at which the two beams overlap, you should be able to observe the interference fringes. This forms the measurement volume.
- H. Place the transparent tape scattering target at the point of beam intersection.

Measure the distance from the beam intersection point to a distant wall with a tape measure. Also measure the beam separation at the distant wall. The beam separation is measured using the following relationship:

$$\frac{\text{Beam Separation}}{\text{Front Lens Focal Length}} = \frac{\text{Separation of Beams at a Distant Target}}{\text{Distance from Beam Intersection to Distant Target}}$$

. Verify that the beam separation that is derived using the above relation corresponds to the separation that can be directly measured (but with less accuracy) in the transmitter.

A.3.3 Receiver

The receiver, shown schematically in Figure A.12 and pictured in Figure A.13, collects laser light scattered by particles at the measurement volume and directs it first to a spatial filter slit. The role of the slit is to block out all the light scattered by particles that are outside of the measurement volume. Light scattered from the measurement volume passes through the slit, is recollimated, and passes through a laser line filter. The laser line filter is an optical filter that is designed to pass only light with wavelength near the $0.6328 \mu\text{m}$ wavelength of the HeNe laser. Its purpose is to improve signal quality by reducing exposure of the detector to ambient light. Finally the scattered light illuminates the detectors. The detectors are silicon PIN photodiodes mounted in a single assembly. The assembly effectively splits the light that is collected by the receiver into two equal regions: one above the scattering plane and one below. The geometries of the two collection regions are shown to the far right in Figure A.1. Also located within the rear cover of the receiver is a preamplifier circuit for converting the current output of the photodetectors to a voltage. This circuit is powered by an external power supply. The signals from the preamps exit the rear of the receiver through two coaxial cables that are plugged into the two channels of the digital oscilloscope for recording. A detailed description of the components in the transmitter, including drawings for machined parts, can be found in Section A.5.

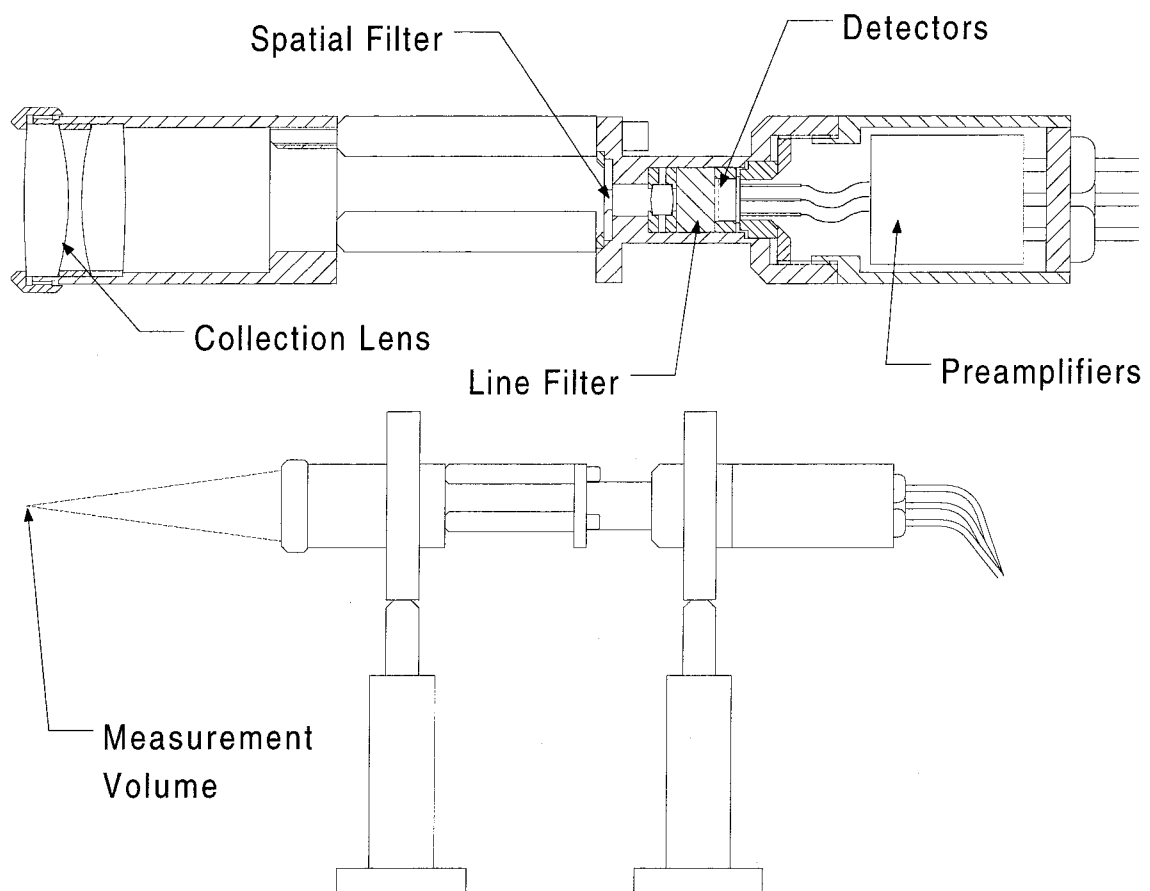


Figure A.12: PDA receiver.

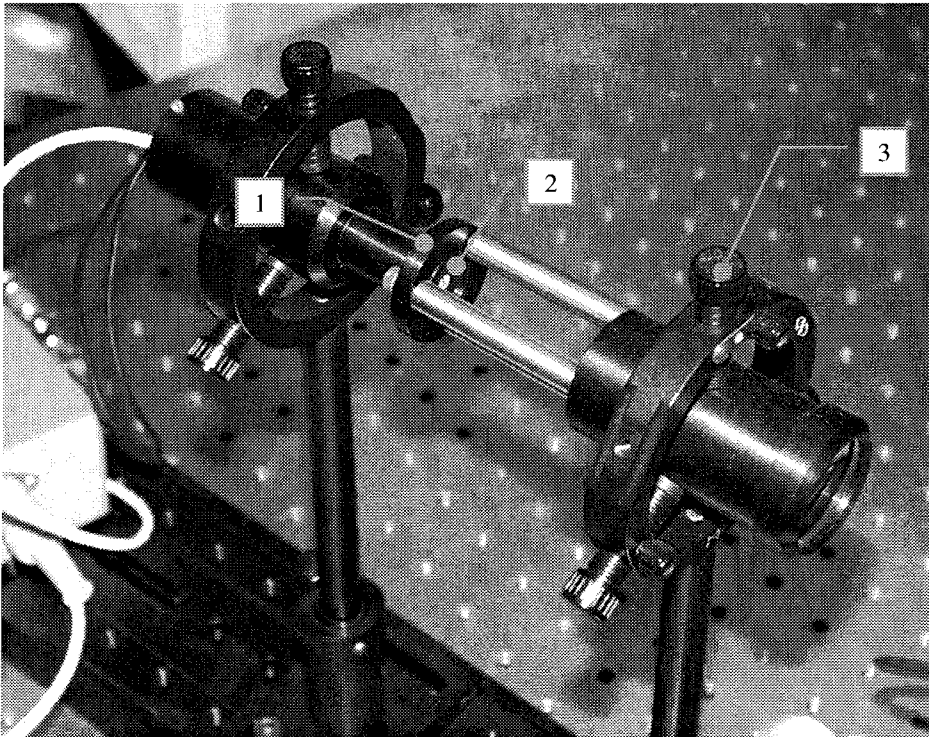


Figure A.13: Photograph of PDA receiver showing key elements. 1: Rear tube, 2: Spatial filter, 3: Adjustment knob for tilt adjustment, 4: Collection lens and retainer ring.

As described in Section A.1.2, one way to change the range of the particle size measurement without affecting the velocity range is by changing the receiver collection lens. This is a simple operation, performed by removing the retainer ring pictured in Figure A.13 and grasping the outside edge of the lens. The lens is a 30 mm diameter coated achromatic doublet, and can be replaced with a number of different off-the-shelf lenses.

The spatial filter slit can also be easily replaced. This might be necessary when data rates are either too high or too low. For high particle concentrations where there may be a danger of near-simultaneous scatter events reaching the detector from multiple particles, a smaller slit can be installed to reduce the length of the beam crossover region that is imaged onto the detector. The geometry of the measurement volume is shown in Figure A.14. The slit width defines the length of the measurement volume according to:

$$t = SlitWidth \times \frac{RCVlens}{100mm} \quad (A.8)$$

where 100 mm corresponds to the focal length of the lens located between the collection lens and the spatial filter. For the example in Table A.2, the length of the measurement volume for a 100 μm slit is $100 \times 250/100 = 250 \mu\text{m}$. For occasions where low particle concentrations are encountered, a larger slit will help to improve statistics. Use caution that the measurement volume length as determined by Equation A.8 does not exceed the overlap region of the two beams. The result would be poor signal quality for those particles that pass outside of the overlap region, and will be evident by the characteristic shape of the lower envelope of the sinusoid. The relationship between alignment and signal quality will be explored further in the following section.

Referring again to Figure A.14, the area of the measurement volume projected on the scattering plane, A , depends also on the collection angle, θ , and is given by:

$$A = \frac{D_w \times SlitWidth}{\sin \theta} \quad (A.9)$$

Equation A.9 suggests an important capability of the PDA: the ability to measure

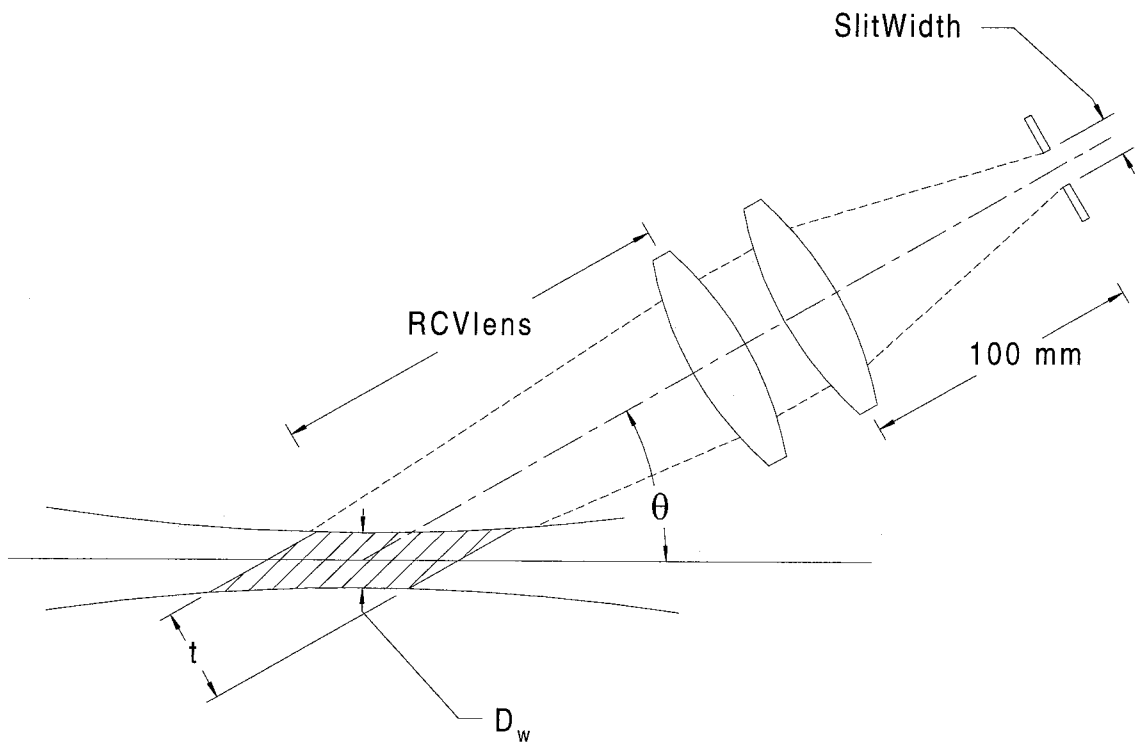


Figure A.14: Image of slit projected across laser beams (diagram not to scale).

particle mass flux or number density. If the measured particles are known to be tracers for the surrounding fluid, then the swept volume, V , which contained the particles during a measurement of time duration, t , is:

$$V = \bar{u} \times t \times A \quad (\text{A.10})$$

where u is the mean velocity of the particles. The particle number density, C_n , is therefore:

$$C_n = \frac{N}{V} \quad (\text{A.11})$$

Before replacing the slit, first mark the orientation of the existing one. At present there is no keying mechanism for orienting the slit, which can rotate freely in its mounting surface until locked in place. Next, remove the three bolts that attach the rear tube assembly to the 0.5 inch posts. The posts serve to retain the ring that holds the mounted slit in place, so removing the posts will allow the ring and spatial filter to fall out. New spatial filter slits can be purchased off-the-shelf, and information on this can be found in Section A.5. Once the filter is replaced, carefully orient it by dropping it into place and making small adjustments by applying pressure with your finger. Then replace the retainer ring and re-attach the rods.

With the exception of the collection lens and spatial filter, no other elements of the receiver can be changed without affecting the instrument calibration. If, for example, the user wishes to use the receiver with a light source other than a HeNe laser, then the laser line filter located inside the rear tube will need to be removed and replaced. The laser line filter is accessed from the back of the rear tube. The drawings in Section A.5 can assist the user in accessing this area.

A.3.4 Positioning of Receiver

Once the proper collection angle has been selected by using a program such as SCATAP, the process of aligning the receiver is straightforward. This process, described below, assumes that the user has access to the region in which the beam

crossover is located. In some situations involving *in situ* measurements it is not always possible to have access to the measurement region, so the alignment complicated by this. In the most inaccessible environments the system must be aligned by allowing particles to pass through the beams and viewing the signal quality on the digital oscilloscope.

Before starting the process of positioning the receiver, check to make sure that the tilt adjustment knobs (see Figure A.13) are in their centered position and that the receiver is level and at the same height as the transmitter.

If the user has access to the beam intersection point, place a scattering target, such as tape target described in the first paragraph of Section A.3.2, at the exact beam intersection. The more transparent the tape is, the easier it will be to locate the beam intersection point. It is also a good idea to have a mostly transparent scattering target so that you are not forced to stare at a bright scattering point. Looking at the spatial filter slit (see Figure A.15), locate the spot of light against the white background of the slit surface. This is the image of the point of light from the scattering target. In order to see the image spot it might be necessary to translate the entire receiver assembly (including the rail upon which the receiver is mounted) by sliding it on the tabletop. After the spot of light is located and focused onto the surface of the spatial filter, the next task is to position the receiver at the correct collection angle. An adjustable triangle of the type used in mechanical drawing is ideal for measuring the angle between the transmitter and receiver. In most normal PDA applications this angle will be 30° . Once the receiver is moved to the proper collection angle and the image spot from the scattering target can still be viewed near the slit, affix the rail to the surface of the table. A final small adjustment to the receiver can be made with the tilt adjustment knobs without making a significant difference in the collection angle. If the receiver rail is mounted at the proper angle and the light from the scattering target is passing into the spatial filter, then this first phase of the alignment is complete.

The next phase of the alignment involves checking the quality of the signals from the receiver. It therefore assumes that some source of particles can be found that can

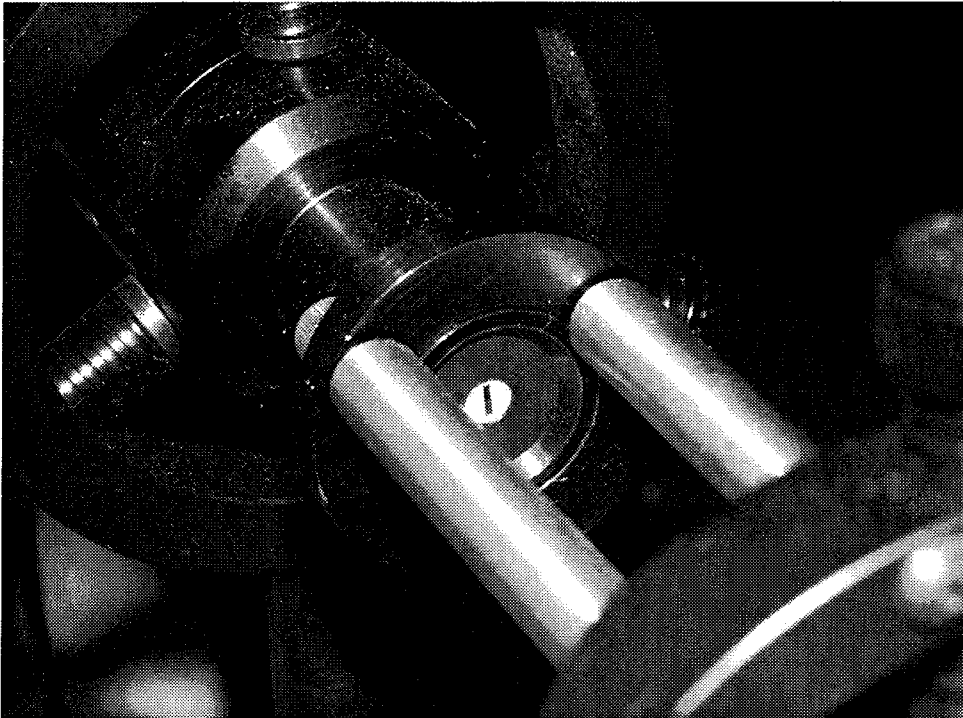


Figure A.15: Close-up of receiver spatial filter slit.

be directed through the measurement region. An ultrasonic household humidifier is ideal for this purpose. With a source of particles passing through the measurement volume, turn on the power supply for the receiver preamplifier and observe the signals on the digital oscilloscope. Figure A.16 shows three examples of signals that would be viewed on the digital oscilloscope. The caption describes how each signal indicates something about the alignment between the transmitter and the receiver. When the receiver is well aligned the upper and lower envelope of the signal is symmetric and Gaussian-shaped. When this criterion is met, the alignment procedure is complete.

A.4 Data Acquisition and Signal Processing

The data acquisition and signal processing system is comprised of a transient recorder and the PDA system software. At present the transient recorder can be either a Tektronix model 410A or a LeCroy model 9450 digital oscilloscope. In the following

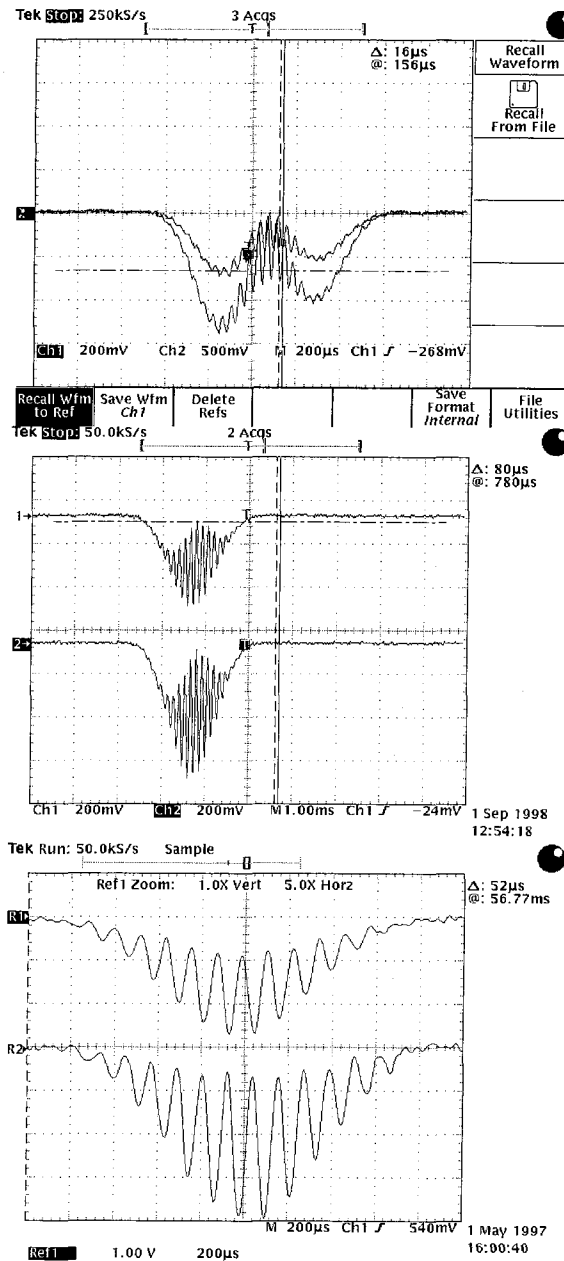


Figure A.16: Actual signals from the PDA receiver (signals are inverted due to the use of an inverter amplifier as the preamp). Top: A badly misaligned receiver, particle is scattering outside the crossover region, as evident by the presence of two Gaussian bursts. Middle: Receiver is close to being aligned, since the top envelope of the sinusoid is Gaussian. However, lower part of envelope is not Gaussian, which indicates particle is not passing through exact intersection point. Bottom: A well-aligned system, showing a Gaussian profile for both upper and lower envelopes.

sections the Tektronix digital scope will be discussed, but most instructions can be extended to the LeCroy without difficulty. The transient recorder interfaces with the system software via a GPIB bus, using the IEEE 488 communications standard. The signal processing system at present is entirely software-based using LabVIEW.[12] Below, the signal processing technique is presented. Following this, a brief explanation of specific issues related to the setup of the digital oscilloscope is provided. This section concludes with a description of the PDA system software.

A.4.1 Signal Processing

Signal processing for the PDA is performed exclusively in software using LabVIEW. This limits data acquisition rates to the time needed to transfer data from the transient recorder to the computer (via the GPIB interface), which for the current system limits acquisition rates to about 100 Hz. For those instances where higher data rates are desirable, a hardware-based technique that makes use of digital signal processors would be a better solution. Such a system would most likely make use of the same algorithms that are presented below, however.

The PDA processor must make the following two measurements from the signals that arrive from the receiver:

- It must separate the higher frequency sinusoidal signal from the low frequency Gaussian pedestal and measure the frequency of that sinusoid to obtain the velocity of the particle.
- It must measure the phase difference between the two signals in order to obtain the particle size.

In the past several years the method of Fast Fourier Transforms (FFT) has become the most widely used algorithm for performing both of these operations, and it is the method adopted here. The exact processing algorithm is based on the FFT followed by an interpolation step,[13] which is summarized next.

The discrete Fourier transform X_n of the sampled signal x_k from each detector is

given by:

$$X_n = \frac{1}{N} \sum_{k=0}^{N-1} x_k e^{-j2\pi kn/N}, \quad 0 \leq n \leq N-1 \quad (\text{A.12})$$

Here, N is the number of sampling points. The frequency

$$\Delta f = \frac{1}{N \cdot \Delta t} \quad (\text{A.13})$$

The interpolation step is needed because the true signal frequency will very rarely coincide with a spectral line, $f_n = n \cdot \Delta f$. Rajaona derived this deviation of the true frequency from the nearest spectral line X_m . The result is given below:

$$f_m = \frac{m + \varepsilon_m}{N \cdot \Delta t} \quad (\text{A.14})$$

$$\varepsilon_m = \text{Im} \left(\frac{j(B-1)}{B+1} \right) \quad (\text{A.15})$$

$$B = \frac{X_m - X_{m+1}}{X_m - X_{m-1}}. \quad (\text{A.16})$$

The corresponding phase for each signal is given by:

$$\Phi_m = \arg(A_m) \quad (\text{A.17})$$

$$A_m = (2X_m - X_{m+1} + X_{m-1}) \frac{Z_m(Z_m^2 + 4\pi^2)}{8\pi^2(1 - e^{-Z_m})} \quad (\text{A.18})$$

$$Z_m = \frac{j2\pi(B-1)}{B+1} \quad (\text{A.19})$$

The phase for each signal is, therefore, derived using Equations A.17–A.19. The difference between the two phases is the phase shift. This phase difference is adjusted by 2π as needed in accordance with the expected direction of the phase shift (derived from the refractive index of the droplet and the indicated flow direction). For the signal frequency, Equations A.14–A.16 are applied to the signals from both detectors and the values for f_m subsequently averaged.

Validation checks are applied to each sample to insure a reliable frequency and

phase shift measurement. Signal rejection will occur if any of the following are not satisfied: (1) The measured frequency of both signals must agree to within 1%. (2) The peak amplitude power of the Fourier-transformed signals must agree to within 25%. (3) The measured phase shift lies in the ranges $0^\circ - 1^\circ$ or $359^\circ - 360^\circ$ (added to reduce the occurrence of phase wrap-around).

A.4.2 Data Acquisition using a Digital Oscilloscope

Once the system is completely aligned as described in Section A.3.4 and signals can be observed on the scope, most of the task of setting up the oscilloscope is completed. There are however a few issues that must be emphasized regarding the setup of the oscilloscope:

- The GPIB device address for the Tektronix scope should be set at “1.”
- The trigger mode should be set at “normal.”
- The trigger delay and level should be set so that the signals are centered on the screen.
- The time scale should be set according to the “samples per scan” that is set in the software (see the next section). For the Tektronix scope, the total number of points across the screen is 500. If 256 samples per scan are requested, then the record for each signal will cover a little over half the screen.
- The voltage scale should be set so that signal from neither channel ever goes past the limits of the screen in magnitude.
- The baseline for both channels should be set at 0 volts.

Once the settings on the oscilloscope satisfy the above requirements, you are ready to acquire data using the PDA system software.

A.4.3 System Software

The PDA system software consists of three individual modules:

- Signal Monitor
- Data Acquisition

These modules can either exist as a complete program or they may be embedded in some other application where a PDA measurement is needed as part of a larger experiment. In either case the instructions for setting up and using the modules are the same, and each will be described in the following paragraphs.

Monitoring Signals from Oscilloscope

One of the first operations that needs to be performed prior to processing the data is to view the acquired signals from the scope. This option is called “Monitor” in the system software, and consists of the two parts shown in the lower panel in Figure A.17. A flowchart for this software module is shown in Figure A.18. The top graph on the panel, labeled “Raw Data,” simply shows the data that were transferred from the oscilloscope. This is used to verify that that the oscilloscope is configured properly; the signals should be well centered, of the proper magnitude, and the time base set to an appropriate value. If this any of these parameters need adjustment then that modification can be made by exiting from this module and making the necessary changes in the PDA Configuration Menu. You must close the Monitor panel in order to make the changes either in the PDA Configuration Menu or the oscilloscope. To exit from the Monitor panel, click on the “Return” button located just above the Raw Data graph.

The second graph on the panel, labeled “Filtered Data,” shows the result of a high pass filtering of the data. The filtering of the Doppler burst is done in software using a digital elliptic IIR filter. The cutoff frequency for this filter is set by adjusting the “Low Pass Filter” parameter in the PDA Configuration Menu, shown in Figure A.17. As you increase the value of this parameter the Gaussian pedestal component of the

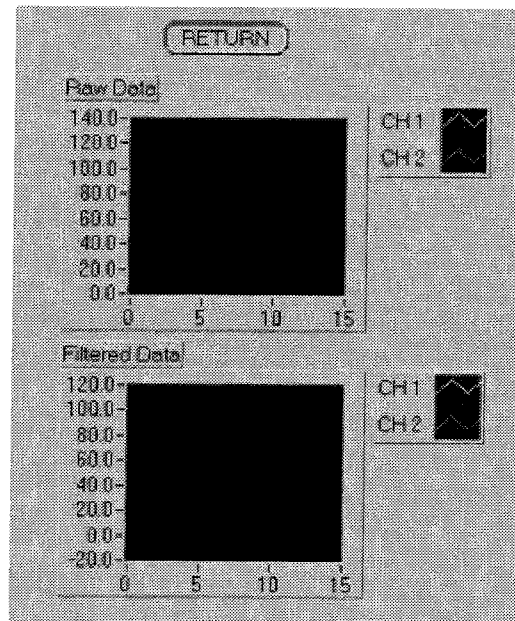
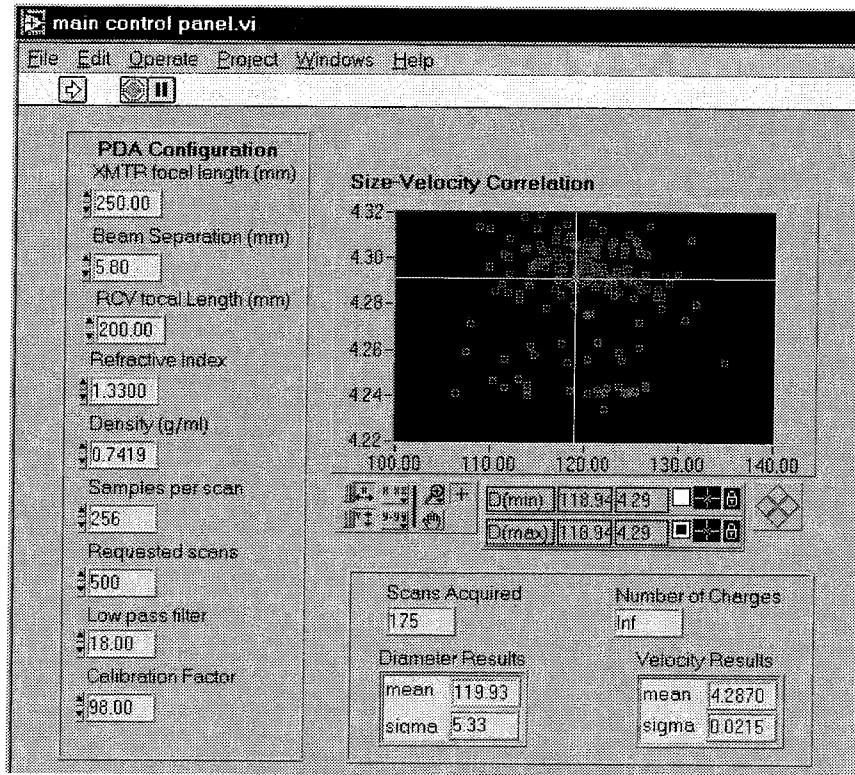


Figure A.17: Panels from the PDA system software. Top: PDA parameters and data on the front panel. Bottom: Signal monitor panel.

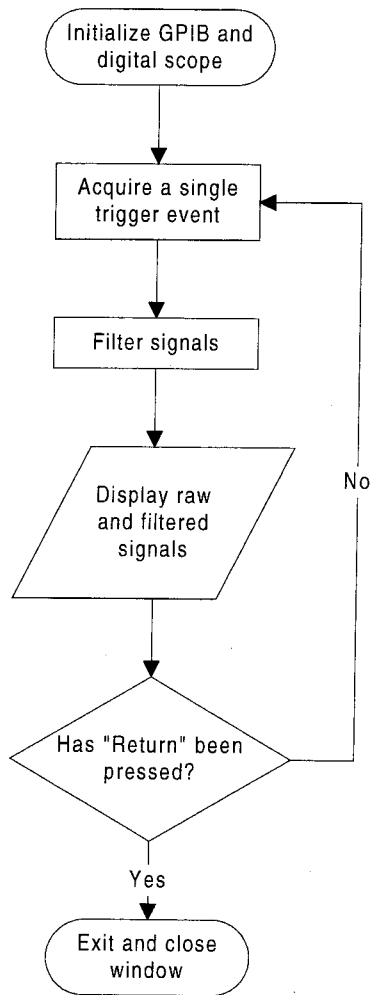


Figure A.18: Flowchart for monitor module.

signal is gradually removed, leaving only the sinusoidal pattern centered at 0 volts. Performing filtering in this way helps to improve the quality of signal processing by removing a major component to the power spectrum of the Doppler burst. Another parameter on the PDA Configuration Menu that can be used to modify the acquired signal is “Samples per Scan.” This parameter was already referred to in Section A.4.2, and is used to vary the record length of each acquired signal. It should be limited to a power of two, since this helps to speed up the Fourier transform operation that is applied to the signal in during processing. A large value such as 256 results in more accurate results, but at the expense of longer processing times and therefore lower data acquisition and processing rates. Once the signals appear to be well-centered, of the proper magnitude, and properly filtered, then it is time to acquire data. This option is described next.

Running the Data Acquisition Module

A flowchart showing the procedure invoked with the “Acquire PDA Data” command is pictured in Figure A.19. The process begins by acquiring sample data from the digital scope and storing the data in memory. During this process of data acquisition the user is able to abort acquisition and proceed with processing the acquired points by selecting the “Return” button which appears on the screen during this time. The total number of data points that are acquired by the scope is determined by the “Requested Scans” input box in the PDA Configuration Menu. After all of the points are acquired, the two Doppler bursts which comprise each data point are then high pass filtered as described in Section A.4.3 and processed according to the equations in Section A.4.3 to obtain the phase shift (measured in radians) and the average frequency. The particle diameter is computed from the phase shift using the calibration factor, γ , described in Section A.2.2 and the actual values for the optical configuration according to Equation A.7. Once this measurement is completed, average size and velocity along with the standard deviations are displayed in the Data Summary Panel shown in Figure A.17. Also displayed in this panel is the number of scans that were actually processed: “Scans Acquired.” This is the number of sample points for which the

criterion was met. Finally, the size-velocity correlation, which is a plot of the particle diameter versus its velocity, is displayed.

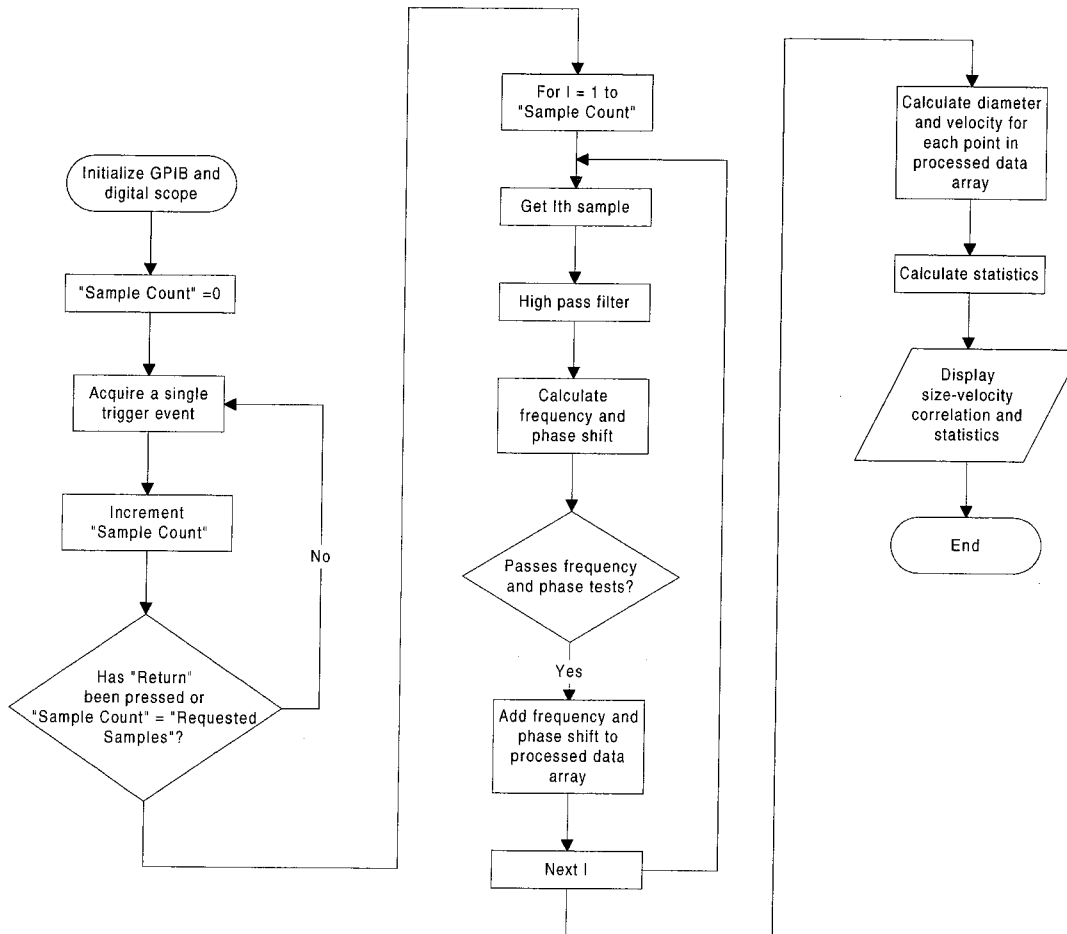


Figure A.19: Flowchart for PDA calibration and data acquisition modules.

A.5 Machine Drawings and Parts Lists

A.5.1 Transmitter

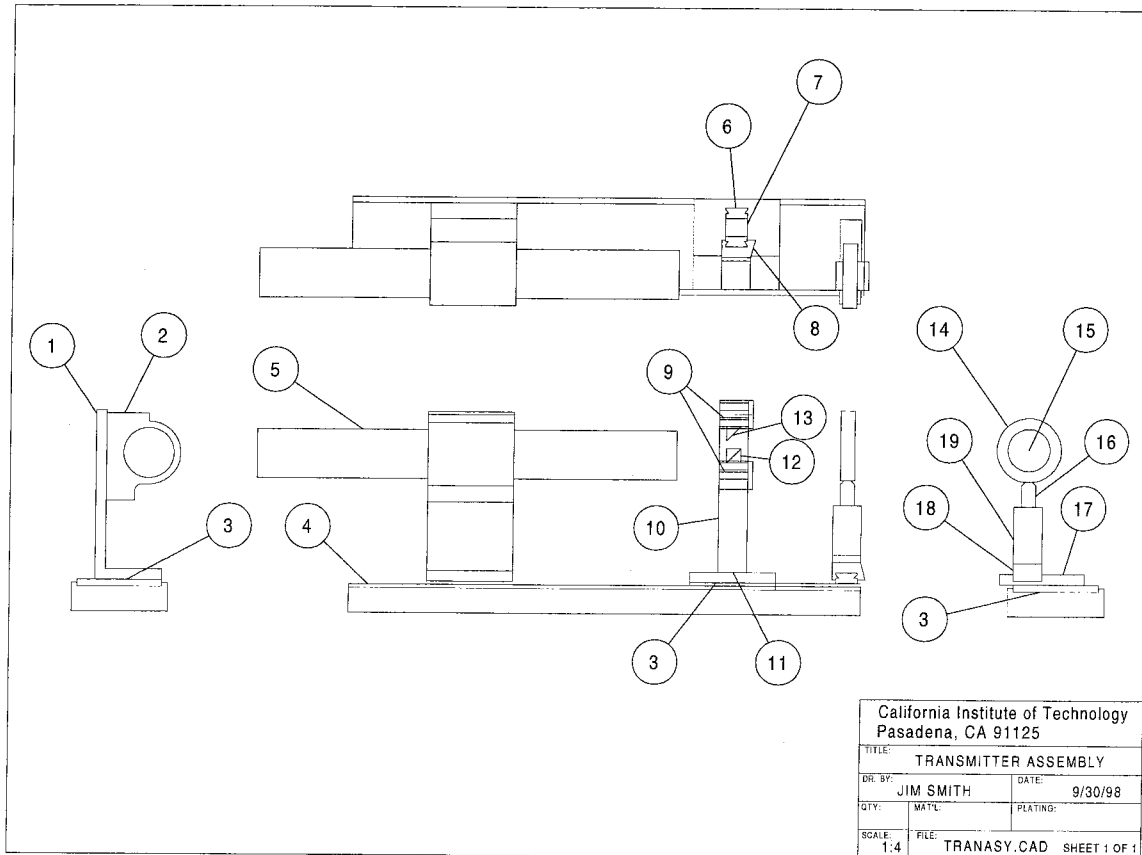
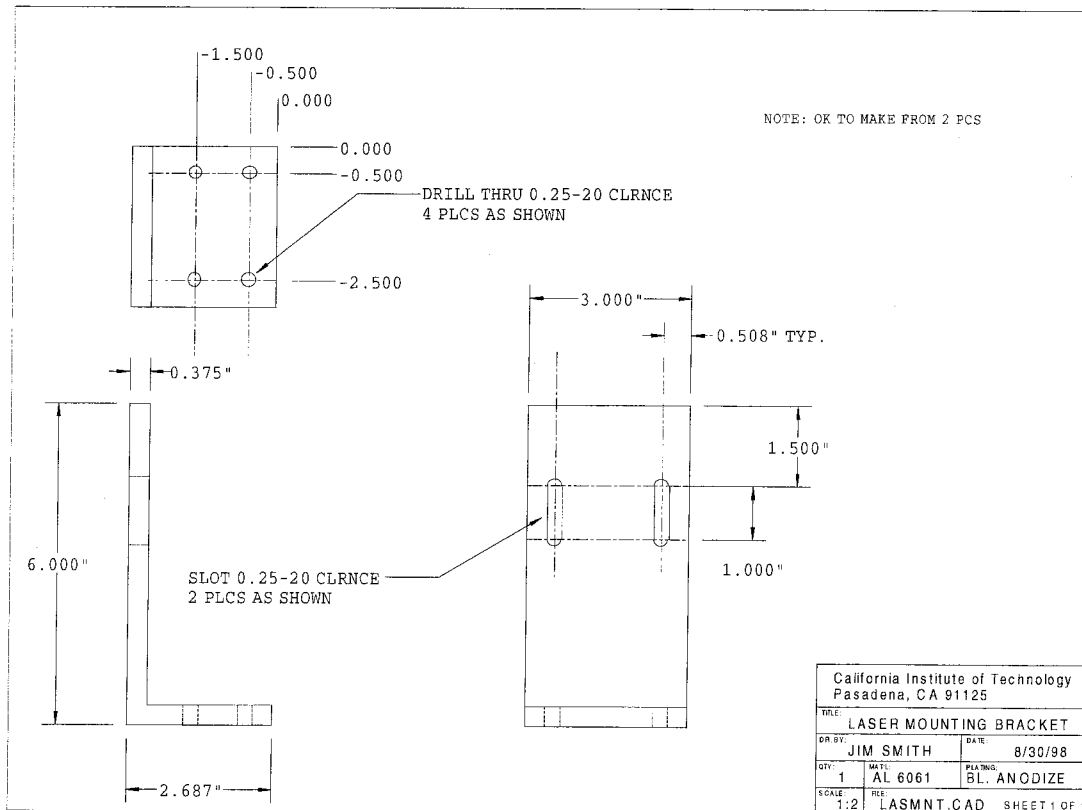


Figure A.20: Assembly diagram for PDA transmitter.



California Institute of Technology Pasadena, CA 91125			
TITLE: LASER MOUNTING BRACKET			
DR BY:	JIM SMITH	DATE:	8/30/98
QTY:	1	MATL:	AL 6061
		FINISH:	BL. ANODIZE
SCALE:	1:2	REV:	LASMNT.CAD
			SHEET 1 OF

Table A.3: PDA transmitter parts list.

Description	Location on Assembly Diagram	Vendor ¹	Part Number	Qty	Unit Price ²	Extended Price
<u>Off-the-Shelf Parts:</u>						
optical rail - 18"	4	N	URL-18	1	127.00	127.00
adapter plate	3	N	B1-A	3	22.00	66.00
micro optical rail - 6"	10	N	MRL-6	2	35.00	70.00
micro optical rail - 3"	6	N	MRL-3	1	23.00	23.00
compact carrier w/ channel	8	N	MCC	2	18.00	36.00
compact carrier, flat	18	N	MCF	1	19.00	19.00
kinematic mirror mount - 1"	9	N	MM-1	2	41.30	82.60
micro series spacer set	7	N	SS-2	1	11.00	11.00
250/38.1 mm achromat	15	N	PAC-079	1	113.00	113.00
lens mount - 1.5"	14	TL	LMR1.5	1	20.00	20.00
post - 2"	16	N	SP-2	1	4.95	4.95
holder - 2"	19	N	VPH-2	1	10.80	10.80
base	11	N	B-2	1	11.85	11.85
beamsplitter cube - 12.7 mm	12	MG	3BSC005	1	68.00	68.00
right angle prism w/ Al hypotenuse	13	MG	01PRA001	1	39.30	39.30
HeNe laser head	5	MG	05LHP991	1	987.00	987.00
laser power supply		MG	05LPL370-065	1	229.00	229.00
laser mount	2	N	ULM	1	140.00	140.00
<u>Machined Parts:</u>						
Laser Mounting Bracket	1			1	124.00	124.00

total: 2,182.50

1. Vendor Key: N: Newport Corp.; MG: Melles Griot; E: Ealing; TL: ThorLabs

2. Prices are from 1992 price lists.

A.5.2 Receiver

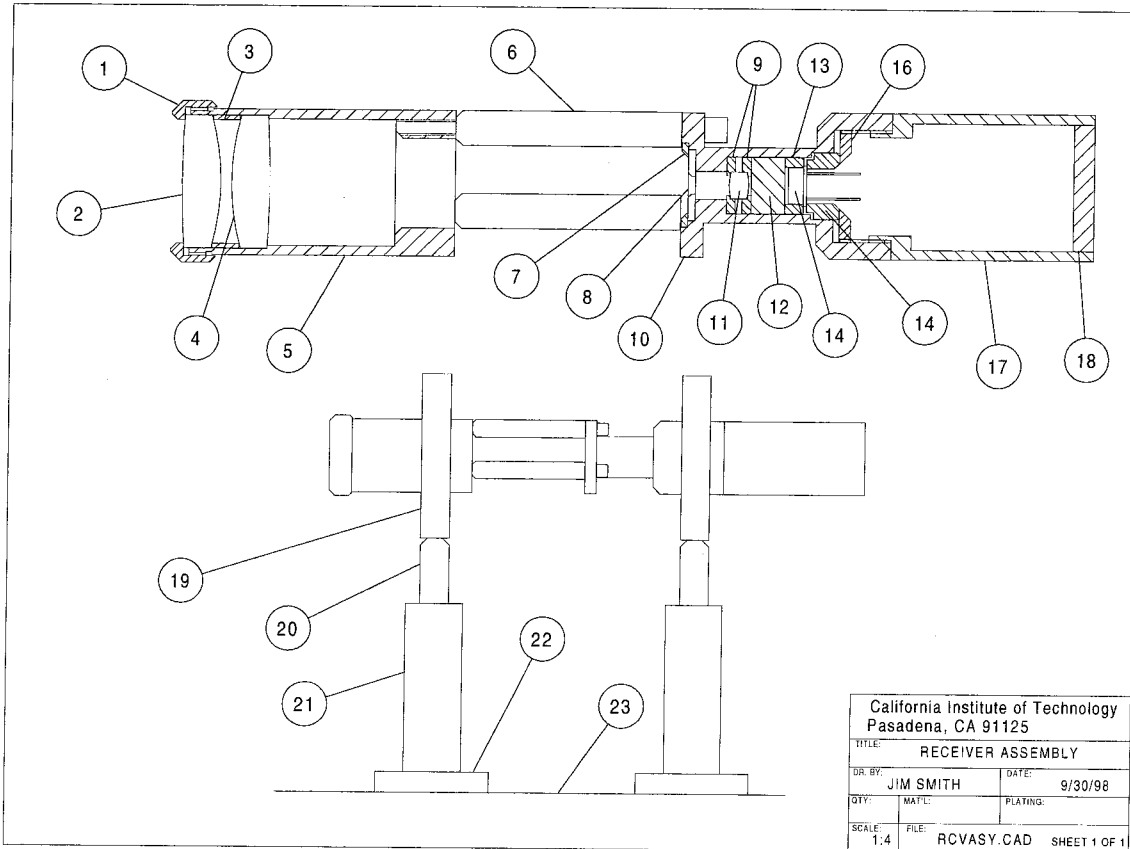
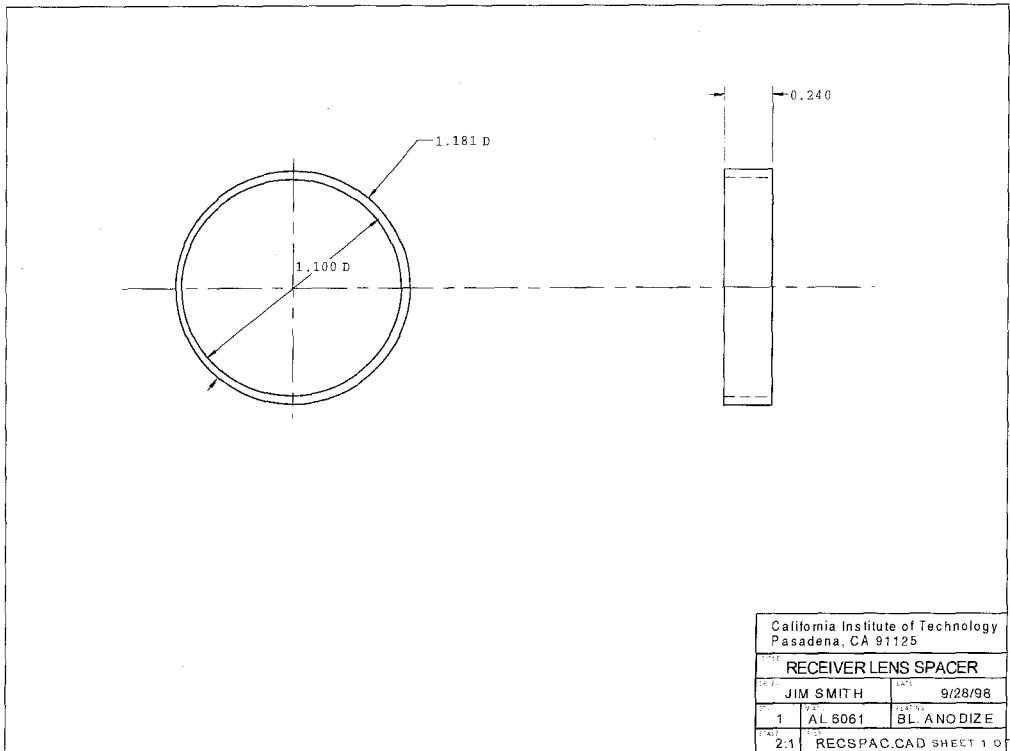
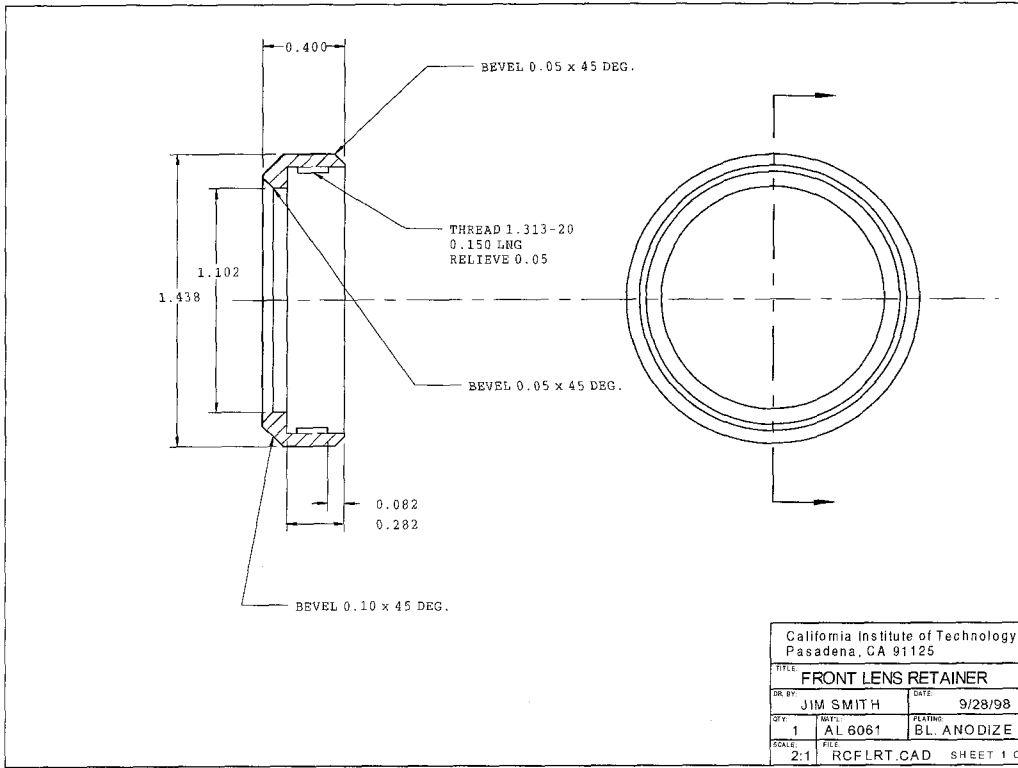


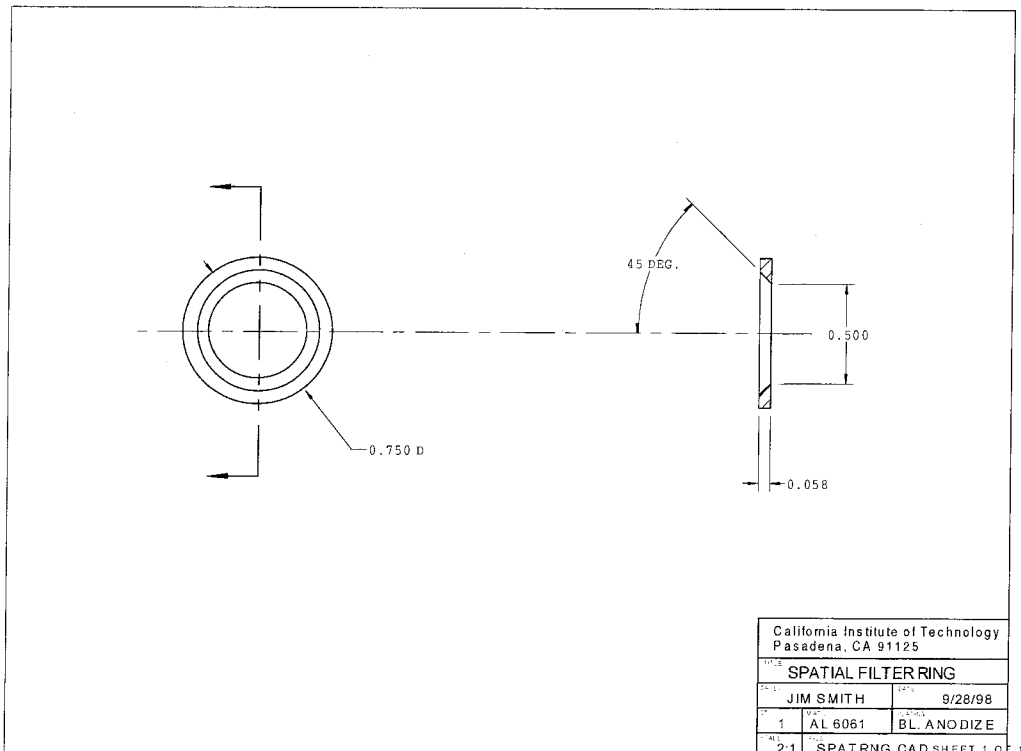
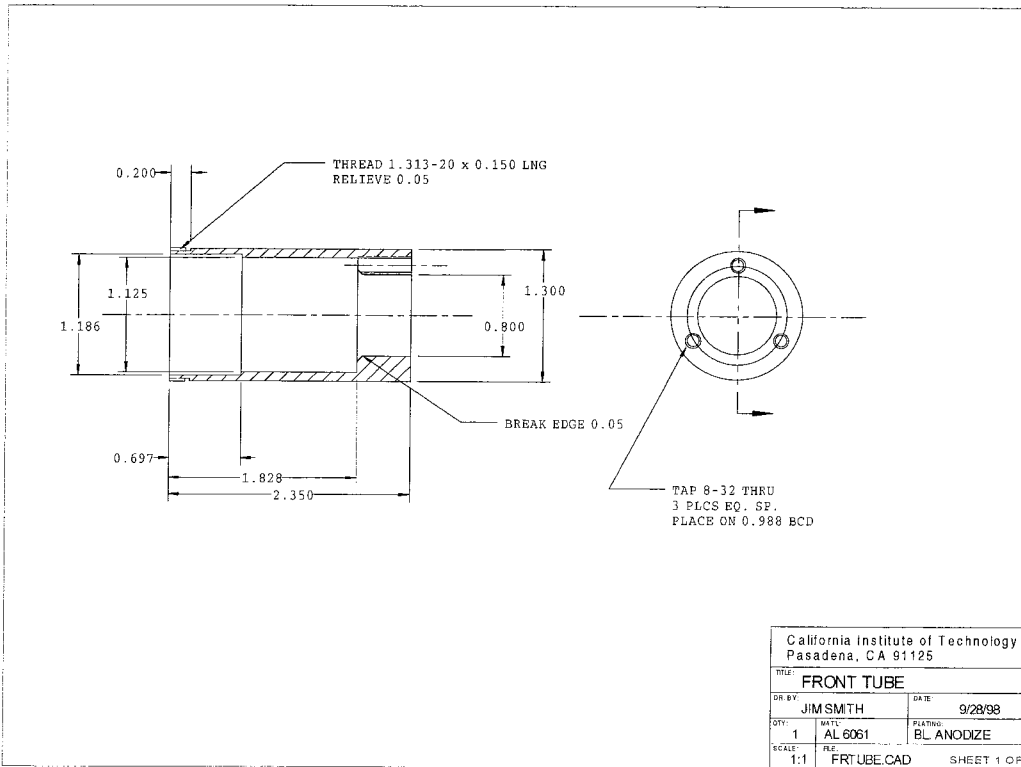
Figure A.21: Assembly diagram for PDA receiver.

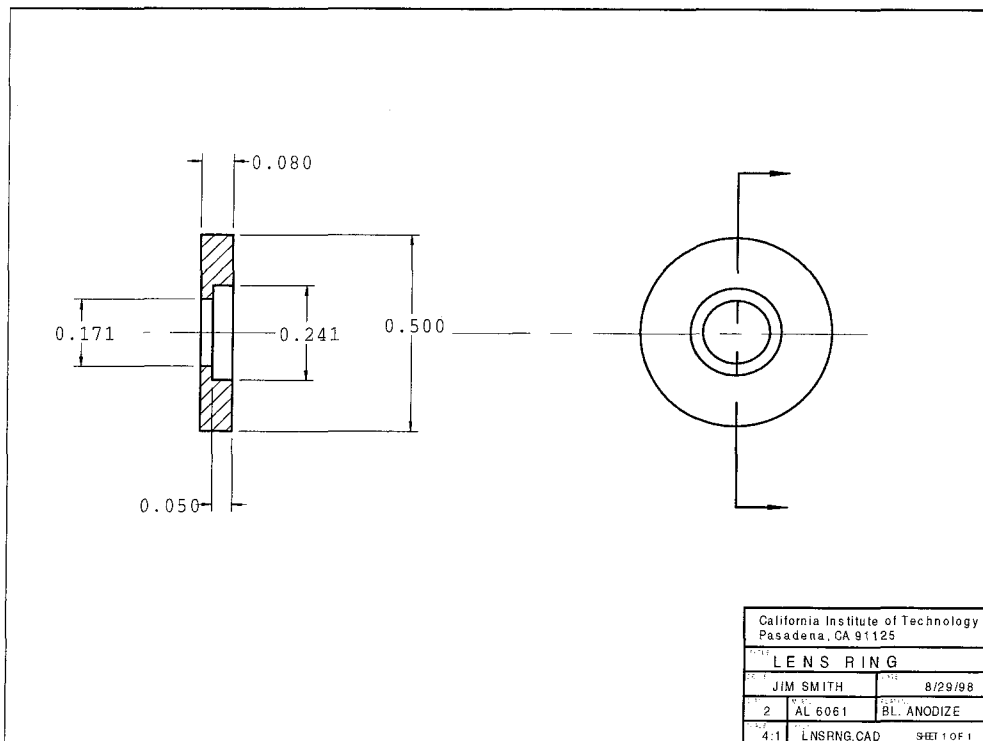
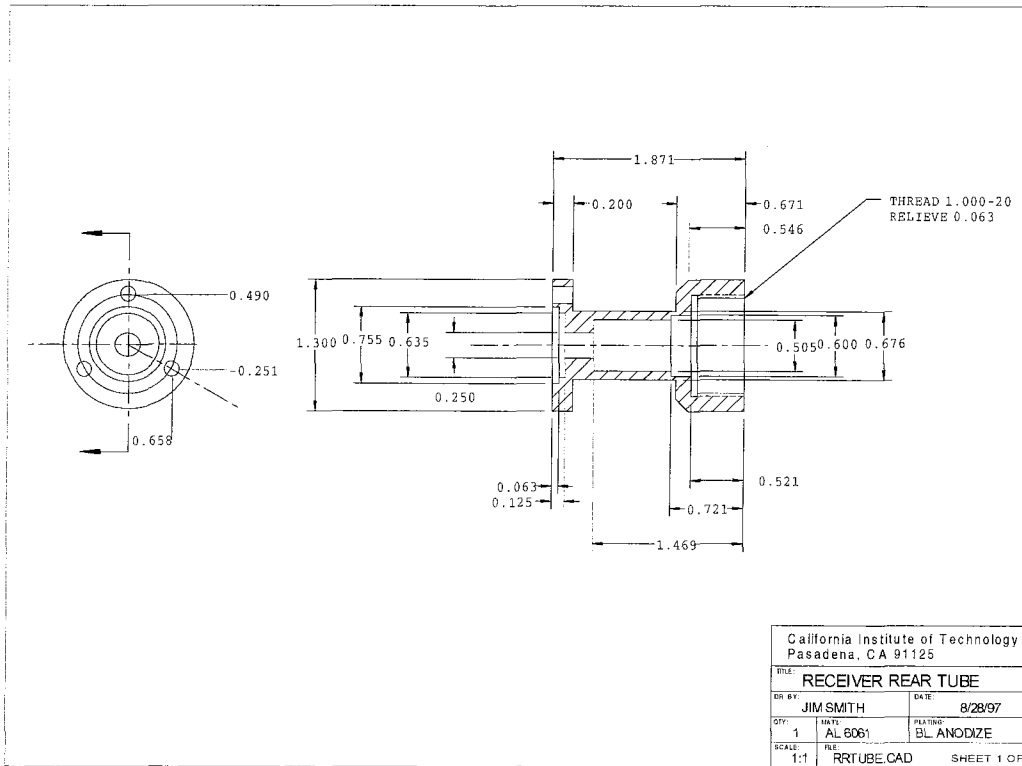
Table A.4: PDA receiver parts list.

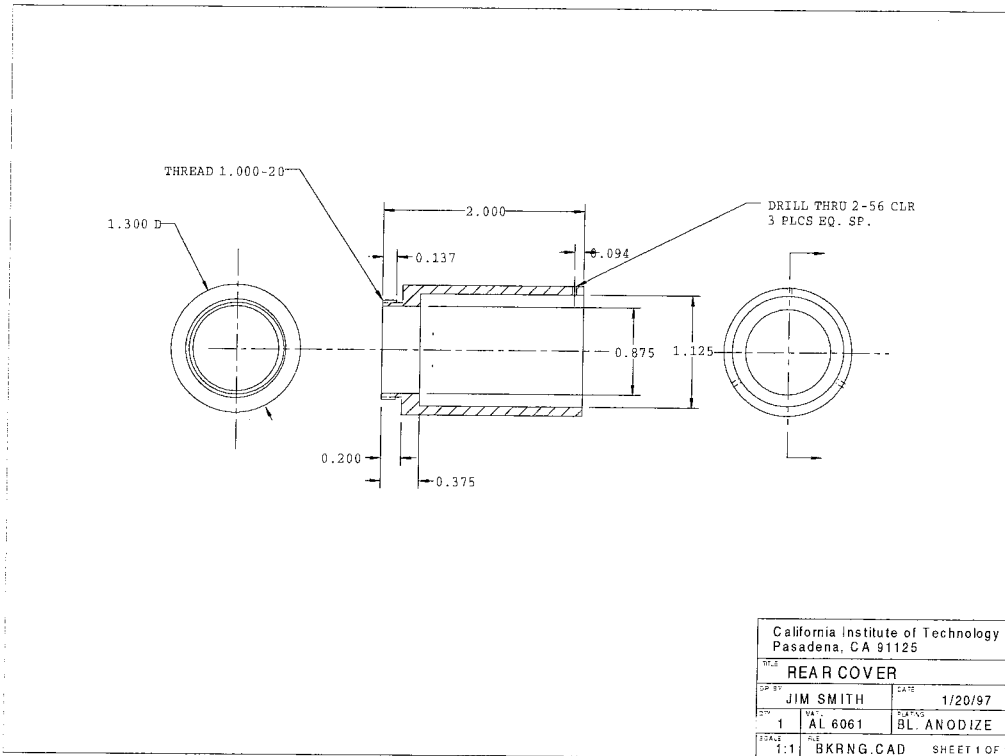
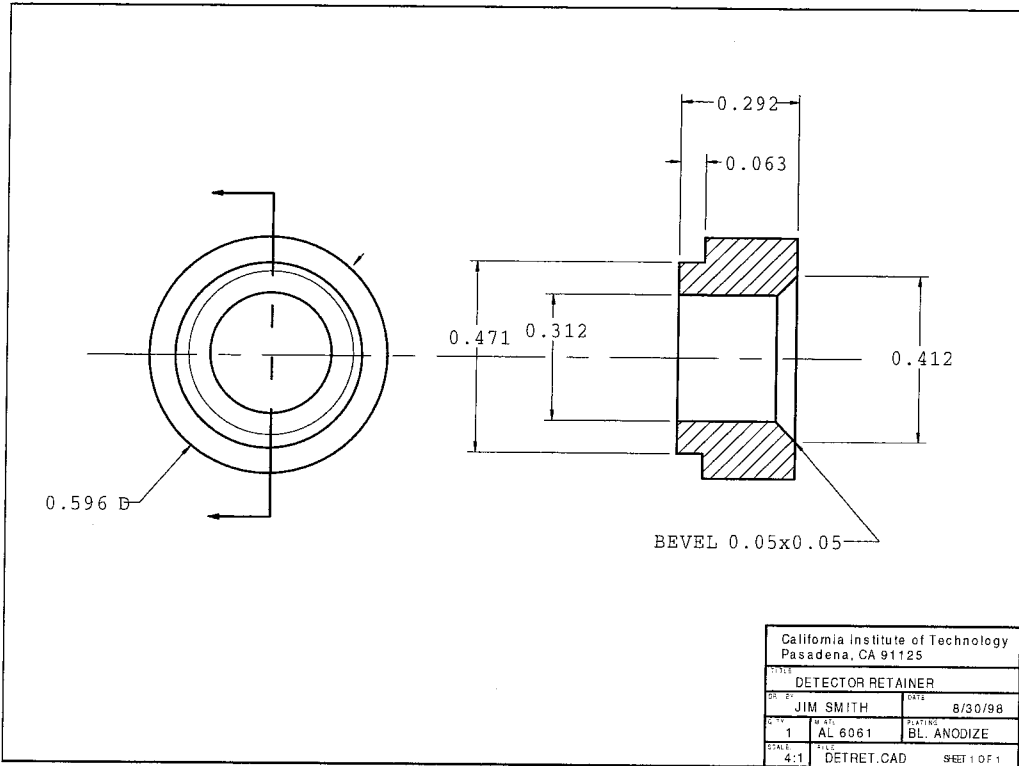
Description	Location on Assembly Diagram	Vendor ¹	Part Number	Qty	Unit Price ²	Extended Price
<u>Off-the-Shelf Parts:</u>						
100/30 mm achromat	4	MG	01LAO124	1	83.80	83.80
200/30 mm achromat	2	MG	01LAO189	1	89.00	89.00
100 μ m mounted slit	8	MG	04PSM006	1	71.00	71.00
10/6 mm achromat	11	MG	01LAO001	1	73.00	73.00
633 nm interference filter	12	E	35-5990	1	82.00	82.00
micro post - 2"	6	N	MSP-2	3	7.00	21.00
post - 2"	20	N	SP-2	2	4.95	9.90
holder - 2"	21	N	VPH-2	2	10.80	21.60
base	22	N	B-2	2	11.85	23.70
optical rail - 18"	23	N	URL-18	1	127.00	127.00
adjustable radius chuck	19	N	AC-2	2	63.00	126.00
silicon PIN photodiode	14	EGG	UV-140BQ-2	1	49.00	49.00
<u>Machined Parts:</u>						
front lens retainer	1			1	95.00	95.00
receiver lens spacer	3			1	35.00	35.00
front tube	5			1	168.00	168.00
spatial filter ring	7			1	24.00	24.00
receiver rear tube	10			1	214.00	214.00
lens ring	9			2	21.00	42.00
detector holder	14			1	39.00	39.00
detector retainer	16			1	82.00	82.00
rear cover	17			1	155.00	155.00
receiver end cap	18			1	116.00	116.00
					total:	1,747.00

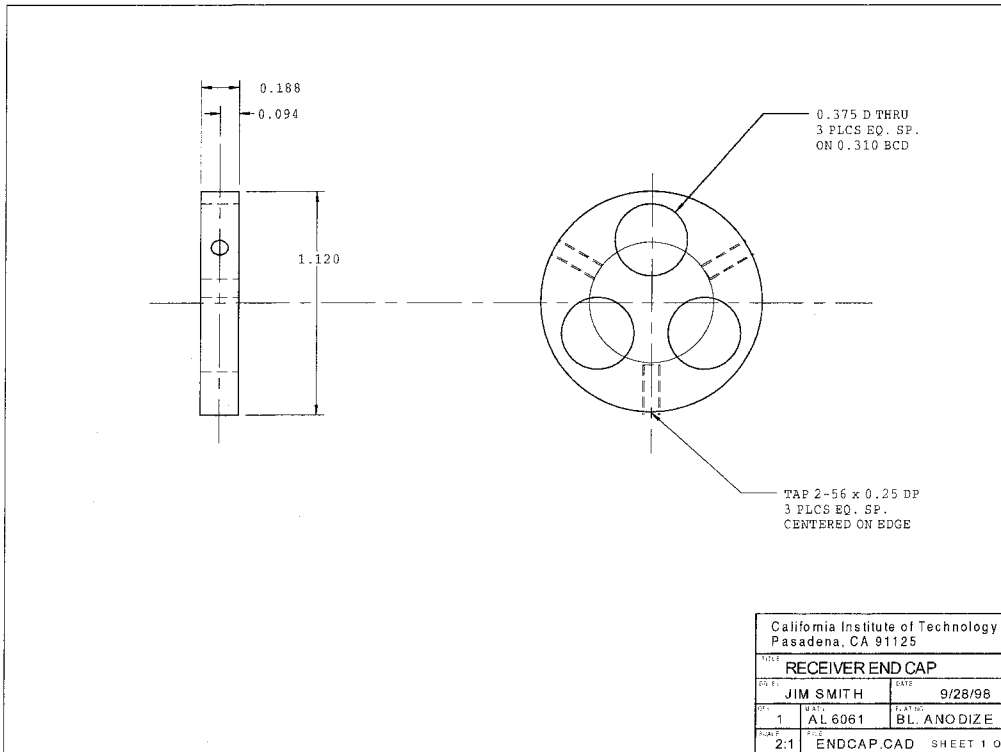
1. Vendor Key: N: Newport Corp.; EGG: EG&G; MG: Melles Griot; E: Ealing; TL: ThorLabs
2. Prices are from 1992 price lists.











Bibliography

- [1] Eugene Hecht and Alfred Zajac. *Optics*. Addison-Wesley series in physics. Addison Wesley, Reading, MA, 1974.
- [2] E.D. Hirleman. History of development of the phase-Doppler particle-sizing velocimeter. *Part. Part. Syst. Character.*, 13(2):59–67, 1996.
- [3] W. D. Bachalo and M. J. Houser. Phase Doppler spray analyzer for simultaneous measurements of drop size and velocity distributions. *Opt. Eng.*, 23:583, 1984.
- [4] K. Bauckhage. The phase-Doppler-difference-method, a new laser-Doppler technique for simultaneous size and velocity-measurements 1. Description of the method. *Part. Part. Syst. Character.*, 5(1):16–22, 1988.
- [5] T. Wriedt, K. A. Bauckhage, and A. Schone. Application of Fourier-analysis to phase-Doppler-signals generated by rough metal particles. *IEEE Trans. Instrum. Meas.*, 38(5):984–990, 1989.
- [6] M. Mitschke, T. Wriedt, and K. Bauckhage. Standard PDA for measuring the size of inhomogeneous droplets. *Meas. Sci. Technol.*, 9(2):197–209, 1998.
- [7] N. Damaschke, G. Gouesbet, G. Grehan, H. Mignon, and C. Tropea. Response of phase Doppler anemometer systems to nonspherical droplets. *Appl. Opt.*, 37(10):1752–1761, 1998.
- [8] T. Wriedt, Z. Jiang, J. Rheims, N. Warncke, and F. Duersterbeck. SCATAP for Windows, 1996.
- [9] G. Goebel, T. Wriedt, and K. Bauckhage. Micron and sub-micron aerosol sizing with a standard phase-Doppler anemometer. *J. Aerosol Sci.*, 29(9):1063–1073, 1998.

- [10] M. Azar and C. A. Ventrice. Size determination of aerosol-particles using the LDA-visibility technique in the backscatter direction. *J. Aerosol Sci.*, 26(6):1009–1017, 1995.
- [11] R. N. Berglund and B. Y. H. Liu. Generation of monodispersed aerosol standards. *Environ. Sci. Technol.*, 7:147–153, 1973.
- [12] National Instruments Corp. Labview, 1998.
- [13] R. D. Rajaona and P. Sulmont. A method of spectral analysis applied to periodic and pseudoperiodic signals. *J. Comput. Phys.*, 61:186–193, 1985.

Appendix B The Design and Operation of a Simple, Low-Cost Drop-on-Demand Generator

B.1 Introduction

The following document describes the design and operation of a piezoelectric Drop-on-Demand (DoD) generator. This device can be used to create a single droplet or a series of droplets of known size, and is compatible with most common laboratory solvents. Droplet sizes that can be obtained with this device are primarily determined by the choice of orifice and the viscosity of the liquid in use, and typically span a range from about 20 μm to as large as 200 μm . Although similar in design to one reported recently[1], this design is distinguished by its low cost, low number of parts, and the ease by which the droplet size can be modified by changing the orifice. Following a brief system overview, a description of the principal components will be given. The first section briefly describes the mechanical design of the DoD generator head, the second will describe the fluid delivery system, and the third the electronics that drive the piezoelectric transducer. In addition to a description of each element, suggestions will be given in these sections where appropriate as to assembly, maintenance, and use. Following the descriptions of these elements, some data on the performance of the DoD will be presented. Rather than being an exhaustive series of tests on this instrument, these data will point out some important issues about the capabilities and limitations of this device, and the relative importance of the pulse properties on the resulting droplets. This document will end with some troubleshooting ideas and other issues that are needed in the normal operation of the generator.

B.2 Operation Principle

An overview of the history of the development of single droplet generators can be found in the literature[2]. The current design can be classified as a "pulsed chamber" system, and is based on the action of mechanically forcing small, controlled amounts of liquid through a small orifice. The principal elements of the mechanical design of the DoD generator head are shown in Figure B.1. In the figure the head is arranged so that droplets are directed upward. In principle, however, the DoD may be operated in any orientation.

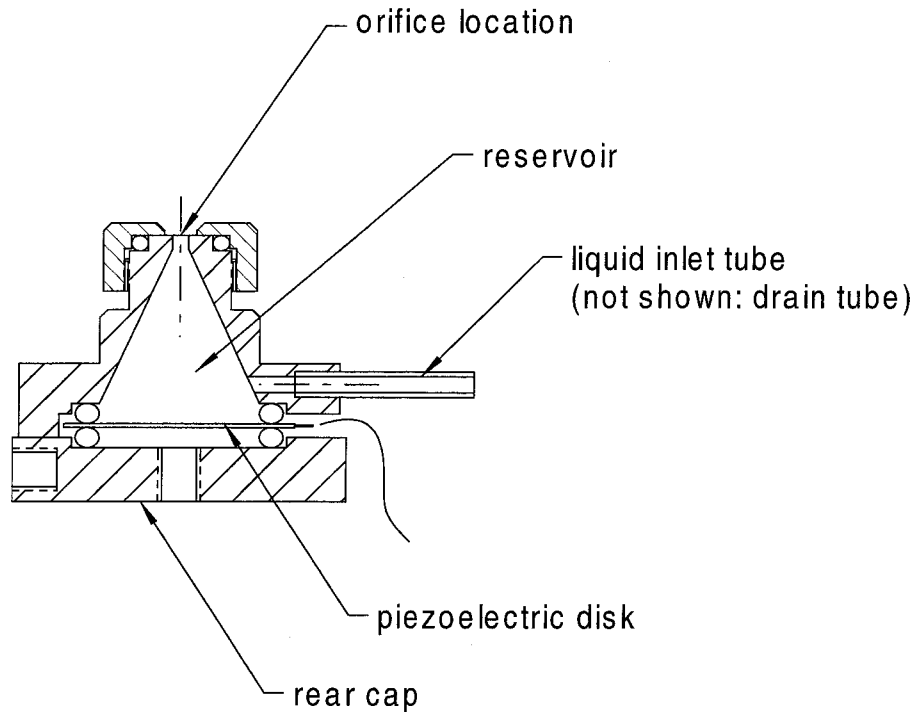


Figure B.1: Overview of DoD generator head showing primary components.

The piezoelectric transducer (PZT) disk is a bimorph design. A square pulse applied to the disk causes it to momentarily bend in such a way that the center of the disk is displaced more than the outside edge. This action causes a pressure wave to propagate through the liquid in the reservoir. Opposite the PZT disk at the outlet of the DoD is a thin stainless steel foil disk with a pinhole (from 20–200 μm in diameter)

drilled in the center. When the pressure wave reaches the pinhole, a small amount of fluid is forced out. This liquid momentarily forms a thin filament that eventually breaks off to form a droplet.

B.3 Instrument Description

A parts list and machine drawings for the complete DoD assembly can be found in Section B.6. The main elements are the DoD generator head, the fluid delivery system, and the PZT driver electronics. A photograph of the DoD head and the fluid delivery system are shown in Figure B.2. A description of each of these elements is presented in this section.

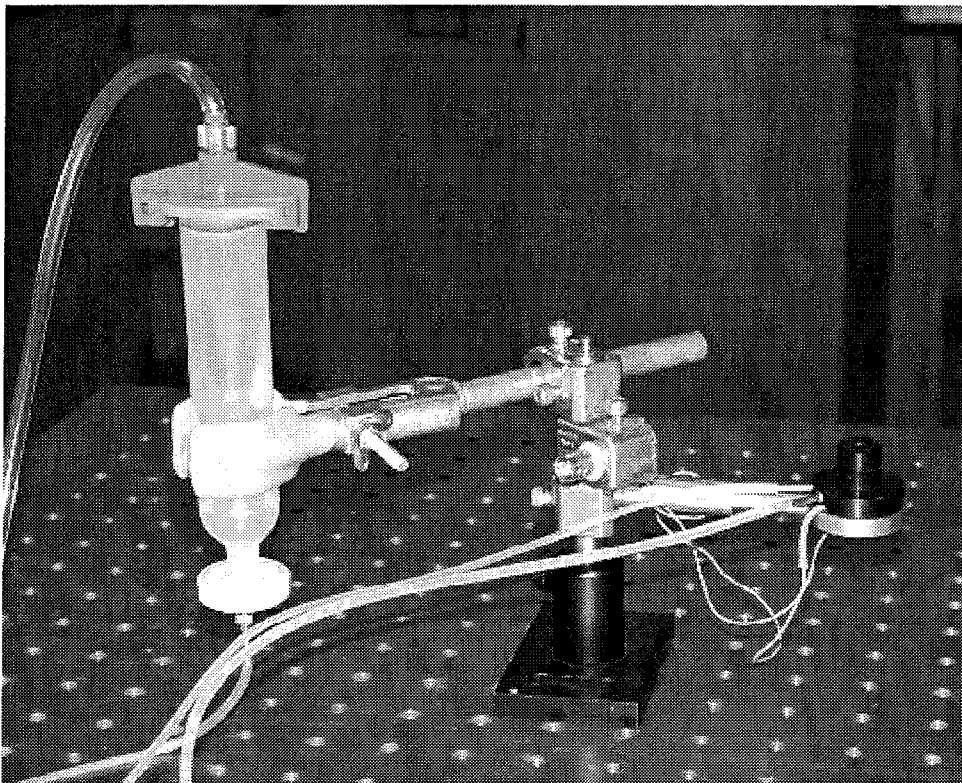


Figure B.2: Photograph of DoD generator head and external reservoir.

B.3.1 Generator Head

The key element of the DoD generator head is an inexpensive bimorph PZT disk manufactured by Motorola Corp. This disk consists of a thin brass center shim sandwiched between two reversed-polarized piezoceramics. It is a "three-wire" device, with one electrical connection required for each of the outer surfaces and a third for the center shim. For the DoD, the two outer surfaces are electrically connected by a small steel spring, which also contacts the brass rear cap as shown in Figure B.3. If a small length of spring cannot be found, it can be cut from a longer spring with a sharp pair of wire cutters. The PZT disk forms one wall of the reservoir, as shown in Figure B.1, and is held in place with two Viton o-rings. The pinhole is located opposite the PZT disk. These pinholes are available off the shelf in a variety of sizes from most optics suppliers. A feature of this design is the ease with which the pinhole can be removed for cleaning or replacement by unthreading the small cap from the reservoir head.

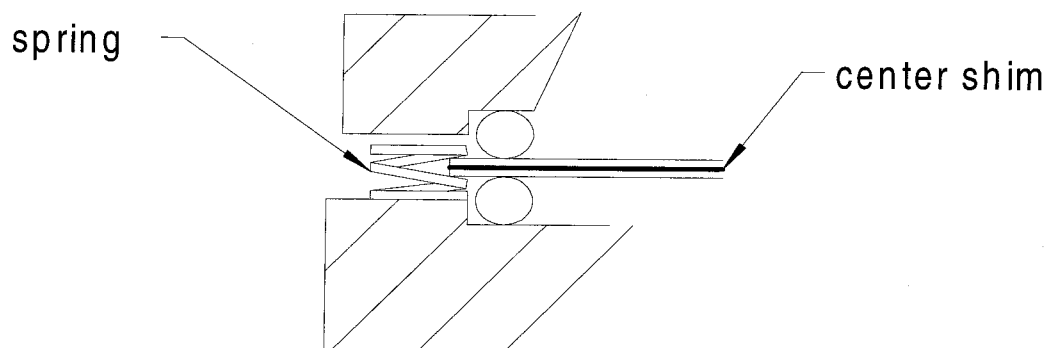


Figure B.3: Detailed view of the spring that electrically connects both outer surfaces of the piezoelectric disk to the generator head.

Occasionally it may become necessary to completely disassemble the DoD head in order to clean the components or to replace the PZT disk. This is done by removing the three bolts on the rear cap. Before disassembling the head, note the position of the small spring on the outside edge of the PZT disk. Also remove the inlet and drain tubes and allow the reservoir in the head to drain. Carefully retain the spring as the

two halves of the head are separated.

The key to re-assembling the head is to insert the spring once the two halves of the head are put together. First check that the o-rings are located in each half of the head, placing a small amount of vacuum grease on the o-rings to tack them in place if they easily fall out. Position the PZT disk (without spring) on the "reservoir" half so that it contacts the o-ring and fits in the recess, with the solder tab of the PZT disk located in the slot cut out for that purpose. Place the rear cap on top of PZT disk so that the o-ring also contacts the surface of the disk. Replace the 3 bolts on the rear cap, making sure to attach the grounding wire to one of the bolts. The final step is to position the spring on the piezo disk, will be describe in the next paragraph.

The spring is inserted onto the edge of the PZT disk with a pair of tweezers. Figure B.3 shows the correct position for the spring. The placement of the spring must be done carefully to avoid contacting the center shim. In addition, the spring must be positioned to lightly contact the inner surface of the back cap when the pieces are together. Avoid compressing the spring too much in the space between the PZT disk and the back cap, as this may apply excessive stress to the edge of the disk and cause the delicate piezoceramic to crack. The spring should also contact the PZT disk on the outside edge so that it does not interfere with the o-rings. Finally, the spring should be placed on a location on the perimeter of the disk close to the solder tab in the slot provided. As stated in the previous paragraph, carefully noting the position of the spring before disassembly will aid in this final step in the assembly.

Once the spring is inserted, assembly is complete. To test the head, connect the signal and ground wires to the PZT driver system and listen for a distinct popping sound. No sound is an indication that the spring may be in contact with the center shim, or that it is not properly contacting the rear cap.

B.3.2 Fluid Delivery System

The fluid delivery system is shown in Figure B.4. It is a gravity-fed system: the liquid level in the external reservoir determines the fluid pressure in the generator

head. Fluid enters the head via the fluid inlet tube, and can be flushed through the head by opening the clamp on the drain tube or by removing the orifice. Increasing the pressure in the headspace of the external reservoir can increase the flow of fluid through the system. An empty syringe can be attached to the headspace tube and compressed to create this increased pressure. Another useful application of the headspace tube and empty syringe is for checking the condition of the orifice during normal operation. Depending on the solution being used, pressuring the headspace of the external reservoir and using a clean orifice should create a jet of fluid that is not deflected to one side as it exits the orifice. A syringe filter is attached to the external reservoir to reduce clogging the orifice. During normal operation the headspace tube is left disconnected.

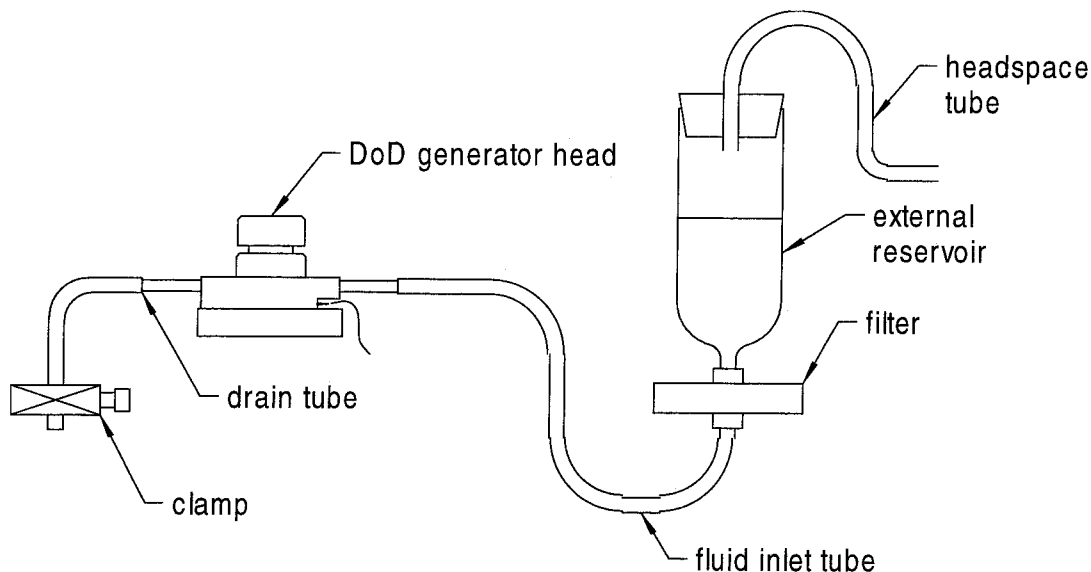


Figure B.4: Schematic of fluid delivery system.

After assembly of the DoD generator head, it is important to flush the system with at least 100 ml of fluid. This serves two purposes: the first is to remove any particles that may remain on the inner surfaces of the PZT disk or the reservoir, and the second is to remove any air bubbles within the reservoir of the DoD head. The presence of air bubbles within the reservoir will interfere with the acoustic wave that

propagates through the fluid when the pulse is applied to the disk and may seriously affect the performance of the system. Lightly tapping the head with the handle of a screwdriver or similar tool while flushing the system with the orifice removed is the best way to remove these bubbles.

As mentioned earlier, the fluid level in the external reservoir determines the pressure of the fluid within the internal reservoir of the DoD, and thus can be crucial to the performance of the system. The importance of this depends upon the fluid that is used to create the droplets and the size of the orifice in the DoD. For example, pure water has a surface tension that is sufficiently large as to make the liquid level in the external reservoir of lesser importance for successfully creating droplets. This is observed to be true even for orifices as large as 100 μm . Pure methanol or acetone, on the other hand, can be quite sensitive to the liquid level in the external reservoir. Flooding may occur if the height of the liquid surface is too large with respect to the orifice, and air will form just beneath the orifice if this level is too low. This is more likely to be a problem for large orifices of 50 μm and greater. Until now, a very simple mounting system for the external reservoir consisting of a laboratory clamp that is mounted on the same post as the DoD head (as shown in Figure B.2) is all that has been needed. Changing the liquid level is done by loosening the clamp and sliding the reservoir to a new location. If one is working with low surface tension fluids such as acetone, methanol, or a mixture of a low surface tension fluid with water, then a more sophisticated mounting and adjustment system may be needed. In this case the system can be improved upon by adding a traversing device to the clamp that holds the reservoir to allow for more precise control of the liquid level.

B.3.3 Electronics: PZT Driver Circuitry

A schematic of the driver circuitry for the PZT disk is shown in Figure B.5. It consists of a pulse generator that is used to create a low-voltage pulse and a high voltage operational amplifier (op amp) that voltage-amplifies the pulse before it is applied to the disk. Separate laboratory power supplies are used for the supply voltages to

the high voltage op amp. The supply voltage for the op amp should not exceed the lesser of the maximum voltage for the amplifier chip or the recommended maximum voltage for the PZT disk. In the current design the limiting element is the PZT disk, which has a maximum pulse voltage of approximately 50 V. Higher voltage of up to 100 V can be applied to the disk but will result in a reduced life span. It is therefore recommended that the supply voltages to the op amp be set to (50 V), and that higher voltages be used with due consideration to the lifetime of the PZT disk.

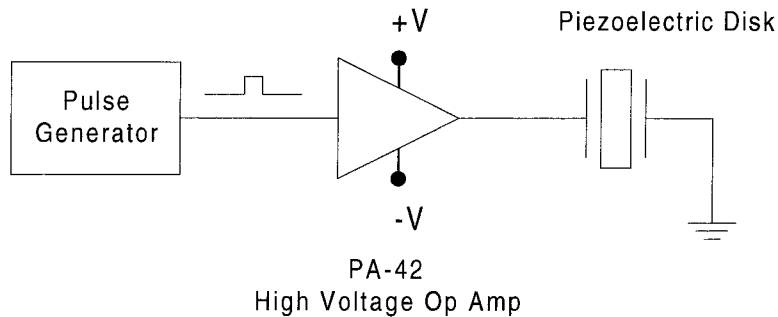


Figure B.5: Schematic of the PZT driver electronics.

If the user would like to create single, isolated droplets with the DoD system, then a pulse generator must be capable of supplying a single, isolated pulse. The polarity of the applied pulse is a function of the orientation of the disk - the correct polarity will push fluid out of the orifice and create a droplet, whereas the opposite polarity momentarily withdraws the liquid surface from the orifice. Sometimes this latter action will still result in a droplet as the trailing edge of the pulse returns the fluid surface back to the orifice. This process is inefficient however, and decrease in the performance of the generator will be noticed when the polarity is incorrect. It is difficult to determine a priori the proper position of the disk within the DoD. Thus it is necessary to be able to switch the polarity of the applied pulse in order to assure the most efficient production of droplets. Most pulse generators have the capability of switching the polarity of the pulse. If this feature is not available then a simple inverter circuit can be inserted between the pulse generator and the high voltage op

amp to achieve the proper polarity.

As the next section will demonstrate, the properties of the pulse can dramatically affect the performance of the DoD. The most important parameters are the pulse amplitude, width, and slew rate. If these parameters are not set properly, then multiple droplets for each applied pulse are usually observed. The user is encouraged to experiment with all of these parameters to find the optimal conditions for creating single droplets with each pulse. The lowest allowable pulse amplitude should be used in order to preserve the life of the PZT disk.

B.4 Performance

The data presented in this section are intended to demonstrate the capabilities of the DoD and its sensitivity to the characteristics of the applied pulse. For these investigations, a 75 μm orifice was used and the solution was pure methanol with approximately 10^{-4} M of NaCl added as electrolyte. The first implementation of this device was as a source of charged droplets, and Figure 6 shows a typical distribution of diameter and velocity for charged droplets in the constant electric field of an ion mobility spectrometer. All data in this section were acquired with a Phase Doppler Anemometer (PDA), a single-particle optical sizing system that can simultaneously obtain size and velocity for each droplet. Since for the charged droplets the velocity is dependent upon parameters such as the electric field strength and droplet density, the main area of interest in Figure 6 is the measured diameter. The data in the figure points out two important issues regarding the diameter of the droplets produced by the DoD. The first is that, as a rule of thumb, the droplet diameter is about 1.5–2 times the diameter of the orifice. This is generally observed for droplet generators of similar design[2]. The second observation that is demonstrated in Figure B.6 and verified by numerous other tests, is that the dispersion in diameter under normal operating conditions is less than 10% of the average value.

The data in Figure B.7 were taken to demonstrate the dependence of the diameter and velocity of droplets directly emitted from the DoD to the magnitude of the applied

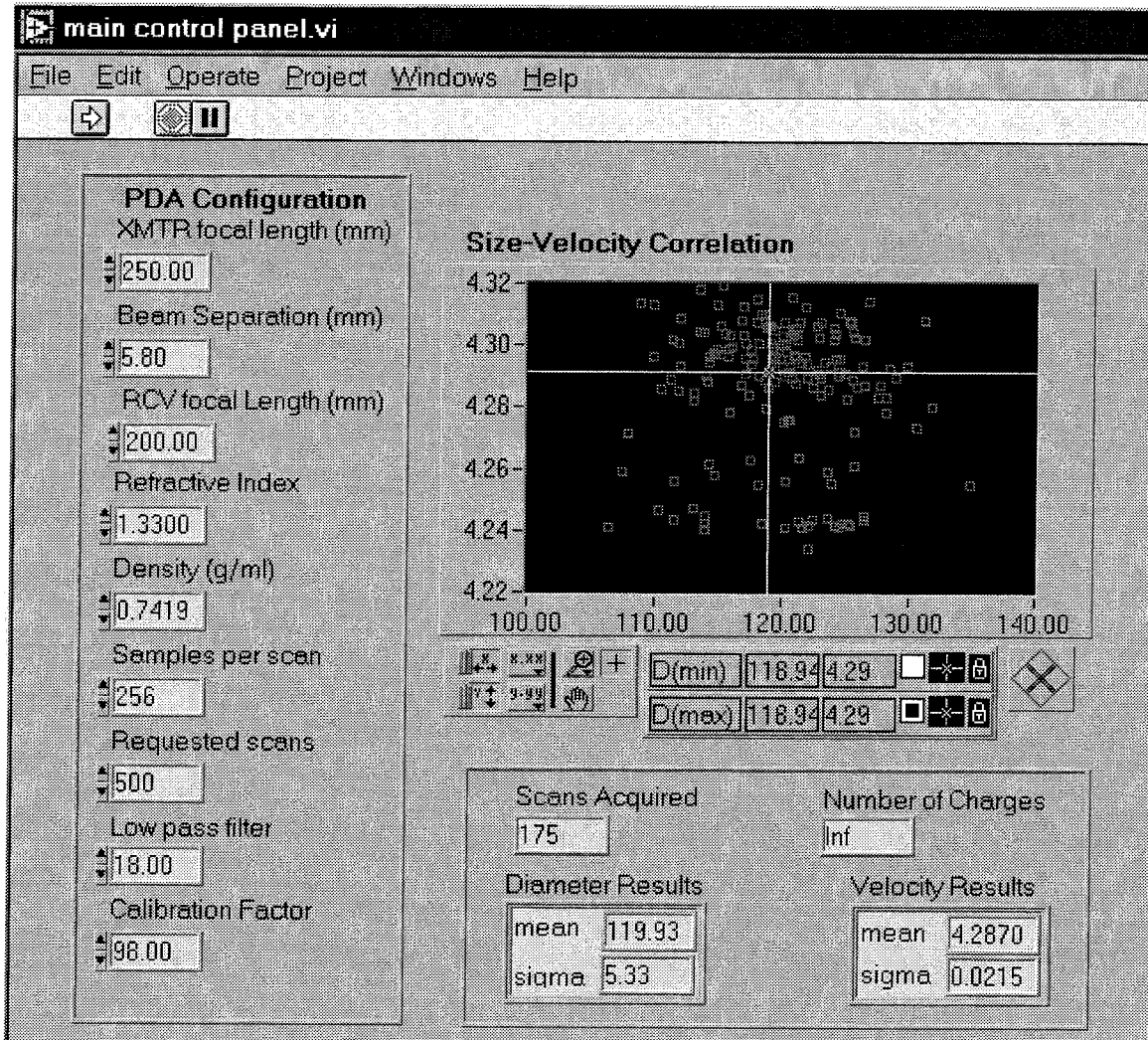


Figure B.6: Typical size (horizontal axis, in μm) and velocity (vertical axis, in cm/s) distribution for charged droplets injected into an ion mobility spectrometer, as measured with a phase Doppler anemometer.

pulse. These measurements were made 4 mm above the orifice of the DoD. The pulse applied to the PZT disk was 204 μs in width at 0 V, rose with a slew rate (due to capacitance of the piezo) of 1 V/ μs , and fell at a rate of 0.6 V/ μs . As the graph demonstrates, the droplet diameter is not well correlated to the pulse height, but does appear to increase slightly with increasing pulse height. In addition, one might expect a better correlation between the velocity and the pulse amplitude, and this does appear to be the case. In general, the velocity of the droplet will increase with increasing pulse amplitude. A more rigorous study of the effect of pulse and fluid properties on the performance of a droplet generator of similar design can be found in the literature[2].

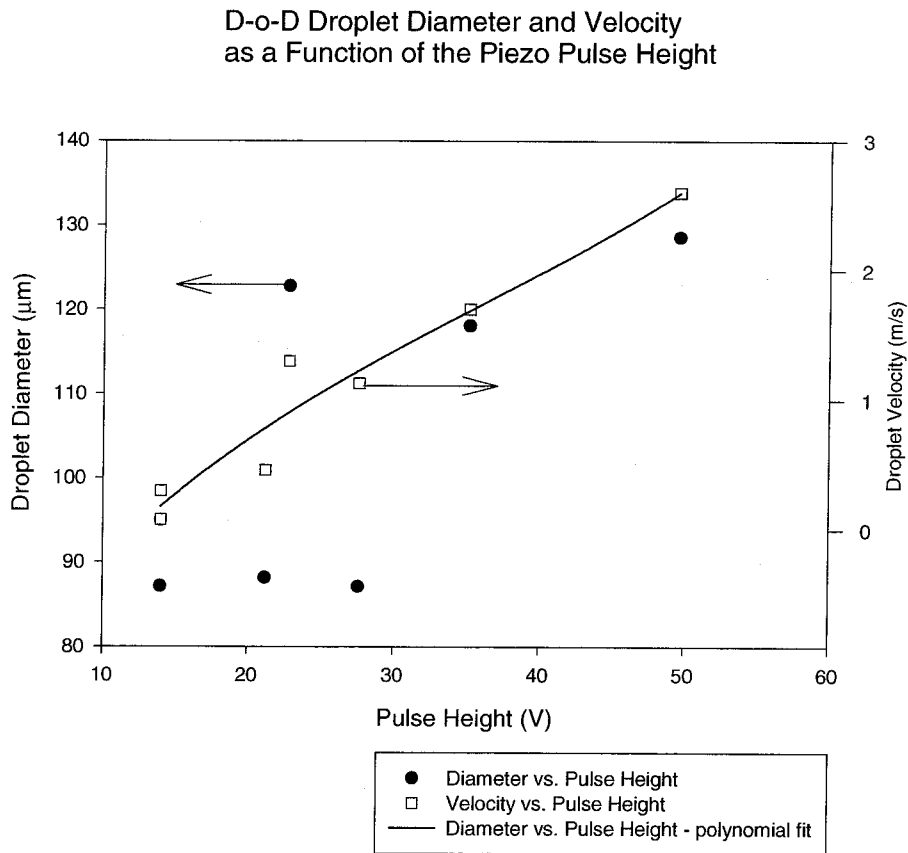


Figure B.7: Droplet diameter and velocity as a function of pulse properties, as measured with a phase Doppler anemometer.

B.5 Operation and Troubleshooting

In the previous sections describing the components of the DoD system, various issues relating to operation and assembly were raised. In this section, a few concluding remarks will be made to supplement these operational issues. By design, the DoD is a simple device, and the user should not lose sight of this fact when encountering difficulties with this system. This section will begin with suggestions on storing the DoD head after use and restarting droplet production after a period of inactivity. The remainder of the section will be devoted to a discussion of the three problems that one might encounter with the system - flooding of the orifice during operation, the unexpected cessation in the production of droplets, and inconsistent droplet production.

To shut down the system before a period of inactivity, such as at the end of the day, flush the DoD head with about 100 ml of solvent. This is especially important to preserve the life of the PZT disk, whose thin conducting surface is easily etched by reactive agents in the reservoir. The user may consider removing the aperture and storing it in a bottle of clean, soapy water. This may not be necessary for overnight storage, and may in fact be detrimental to system performance as removing and handling the aperture increases the likelihood that the reservoir can be contaminated with particles. To restart the DoD with the aperture installed, first pressurize the headspace in the external reservoir to assure that the orifice is clear and there are no air bubbles in the reservoir. Remove any excess liquid on the outer surface of the orifice disk by blowing very lightly with clean compressed air or by swiping with a lint-free tissue. Only light pressure from the air stream or tissue is needed - excessive force may introduce air bubbles just below the orifice and prevent droplet production. Once the orifice is verified to be clean turn on the PZT driver circuitry. It may be necessary to increase the amplitude or width of the pulse to initiate droplet production. Also, it may be useful to operate the pulse generator at about 2-10 Hz in order to receive immediate feedback on the effects of the pulse properties on droplet production. Once a single droplet is observed with each pulse, the user may operate in "drop-

on-demand” mode, whereby a single, isolated pulse can be applied to create a single droplet. The system can also be used to create a continuous stream of droplets by adjusting the repetition rate of the pulse generator.

If the droplet generator is operated so as to direct droplets upward, then flooding of the orifice can be a recurring problem, especially with liquids of low surface tension. It is usually an indication that the fluid level in the external reservoir is too high and must be lowered. If the problem recurs in spite of efforts taken to adjust the liquid level, then it is possible that the orifice is not seated properly in the DoD head. When screwing on the cap that retains the orifice on the head, it is often possible for the thin foil orifice to fall out of the recess in the cap that keeps it in proper position. This problem can be eliminated completely if the user applies a small amount of fluid to the recess in the cap before dropping the foil orifice into the recess. In this way the orifice is tacked into position in much the same way that a contact lens is held to the finger by wetting solution when inserting the lens into the eye. If the orifice is seated properly and flooding continues, then two other options are possible for correcting the flooding. One is to implement a fine adjust for the reservoir height such as the traversing mechanism suggested in the previous section on the fluid delivery system. If smaller droplets can be used, then one other possible remedy for this situation is to change to a smaller orifice.

Most often, a flooding problem is quickly fixed. A more common problem may occur when the droplet generator has worked properly for a period of time and then unexpectedly ceases to produce droplets. There are several possible causes for this, thus making it a difficult one to troubleshoot. The most likely cause of the cessation of droplet production is clogging of the orifice, especially if the orifice is smaller than $50\ \mu\text{m}$. This can be tested by pressurizing the headspace of the external reservoir and checking for a straight stream of liquid exiting the orifice. If the stream is deflected to one direction or does not appear at all, then replacement or cleaning of the orifice is needed. For orifices smaller than $50\ \mu\text{m}$ it may be difficult to create such a jet with liquids such as water. If the condition of the orifice is in question a visual inspection with a microscope is recommended. Another issue to consider is the level of the fluid

in the reservoir. This may be a critical issue for lower surface tension liquids such as methanol or acetone, and can be corrected by simply raising the level of the liquid surface in the external reservoir. Cessation of droplet production may be caused by a damaged PZT disk, a PZT with poor electrical connection to the driver circuitry, or a problem with the driver circuitry itself. If the stoppage is accompanied by a lessening of the audible clicking sound of the PZT disk, then this is more than likely the problem.

One final potential problem with the DoD will be discussed: one where the production of droplets does not completely stop yet does not occur with every pulse. This can be caused by any of the conditions presented in the previous paragraph. In addition, a few other sources are also possible. One is that there are some air bubbles trapped in the reservoir in the DoD head. This can be tested by removing the orifice and pressuring the headspace of the external reservoir while gently tapping the head, as suggested in the section on the fluid delivery system. If air bubbles are observed during this procedure then this is a likely cause of the observed behavior. Changing the characteristics of the applied pulse can also correct this problem, and this can be easily confirmed by adjusting the pulse amplitude, width, and slew rate and noting any changes to the droplet production. Increasing the pulse repetition rate to 2–10 Hz is helpful for viewing the effect of changing the pulse properties on droplet production.

B.6 Parts List and Drawings

Table B.1: Drop-on-demand parts list.

Description	Location on Assembly Diagram	Vendor ¹	Part Number	Qty	Unit Price ²	Extended Price
<u>Off-the-Shelf Parts:</u>						
piezoelectric disk ³	6	RS	40-1383	1	4.99	4.99
o-ring	7			2		
pinhole	2	MG	04 PIP series	1	22.00	22.00
high voltage power operational amplifier		A	PA42	1	44.80	44.80
<u>Machined Parts:</u>						
pinhole ring	1			1		
reservoir	3			1		
stainless steel tube	4			2		
back cap	5			1		

1. Vendor Key: RS: Radio Shack; MG: Melles Griot; A: Apex Microtechnology

2. Prices are from 1998 price lists. No price for machined parts indicates that part was machined by author. Price for piezoelectric disk is per item cost for a minimum order of 500.

3. Piezoelectric disk is extracted from a Radio Shack 2" tweeter. The part number listed above is for the tweeter.

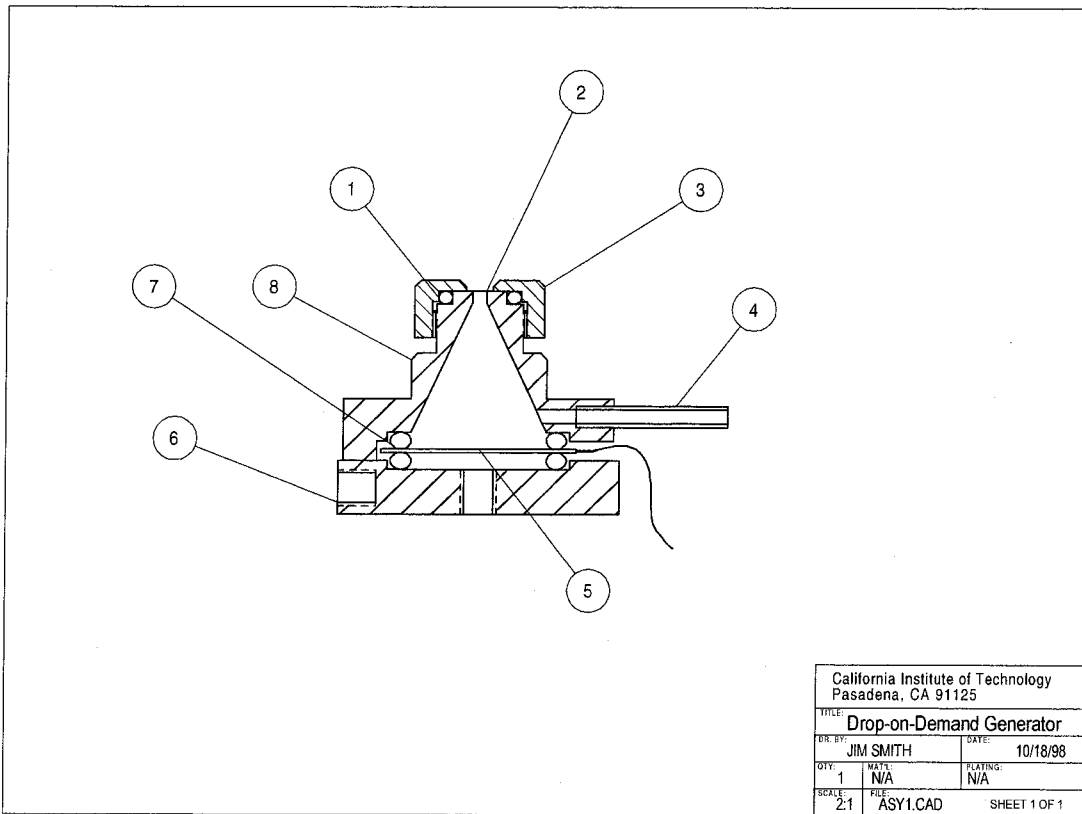
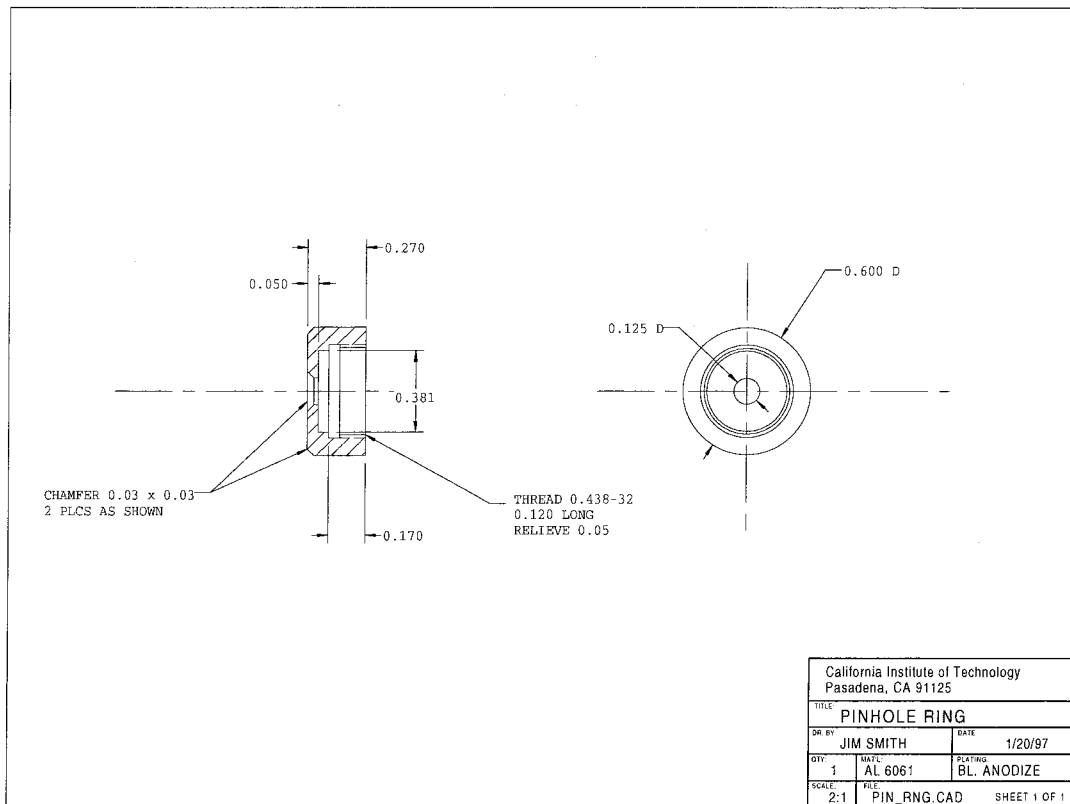
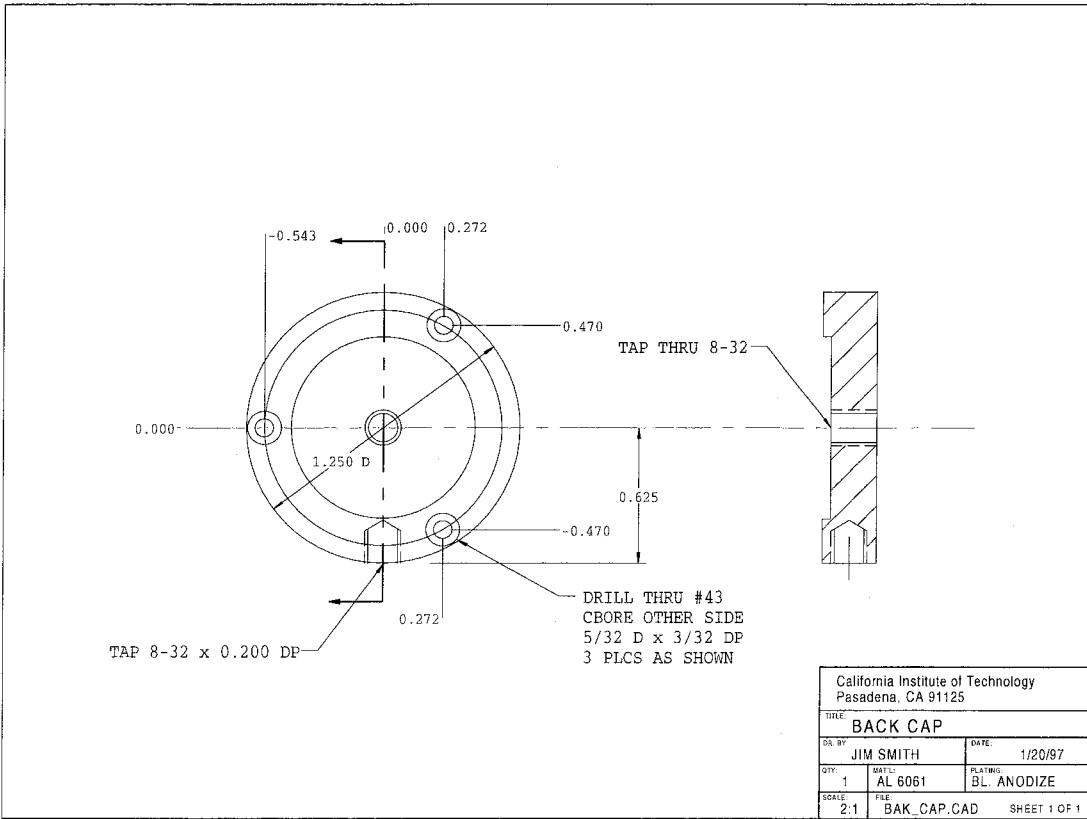
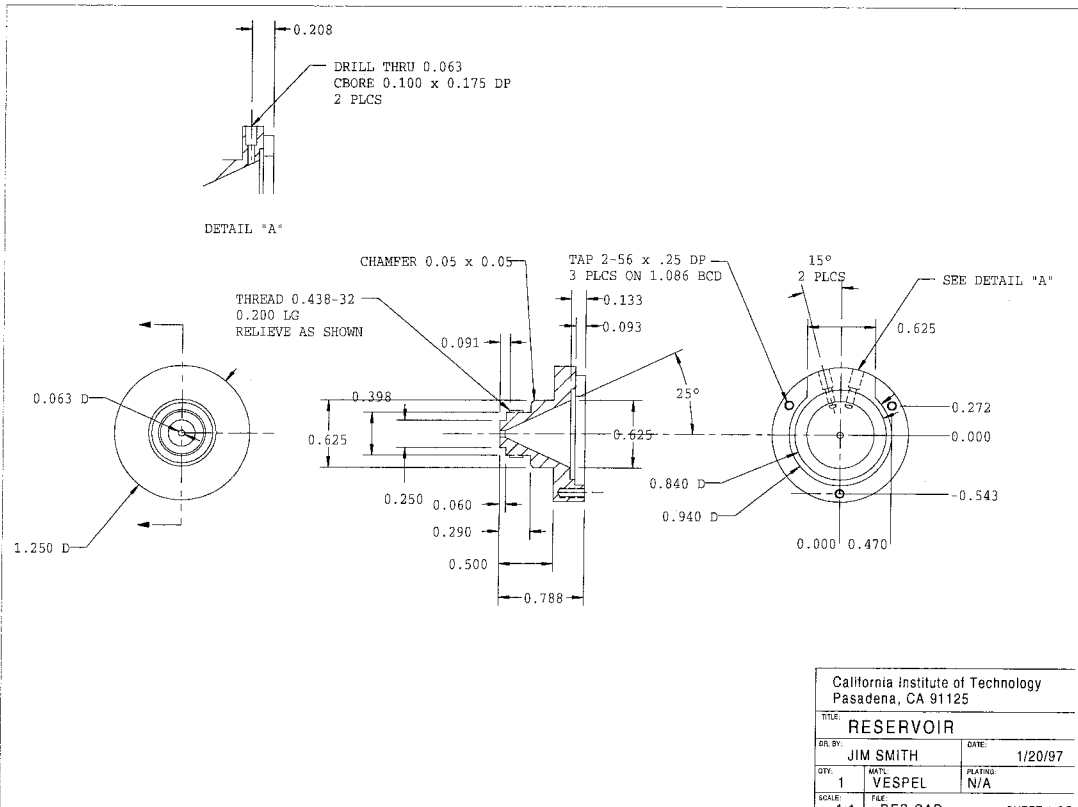


Figure B.8: Assembly diagram for drop-on-demand generator head.





Bibliography

- [1] J.C. Yang, W. Chien, M. King, and W.L. Grosshandler. A simple piezoelectric droplet generator. *Expts. in Fluids*, 23(5):445–447, 1997.
- [2] A.R. Womac, J.R. Willford, B.J. Weber, K.T. Pearce, and D.L. Reichard. Influence of pulse signal spike and liquid characteristics on performance of uniform-droplet generator. *Trans. ASAE*, 35(1):71–79, 1992.

Appendix C An Optical Receiver for Laser Induced Fluorescence Studies

C.1 Introduction

A laser induced fluorescence (LIF) receiver is presented. Among its unique features is its ability to collect light that is scattered within any point in its 0.1–4 mm radius measurement volume with equal efficiency. This allows for quantitative measurements of scattered light intensity when large measurement volumes are needed. Other features include a long minimum working distance (defined as the distance from the front of the collection lens to the object plane) of 64 mm for a 4 mm radius measurement volume. High sensitivity is achieved using photomultiplier detectors combined with off-the-shelf LIF filter cubes. These components are briefly discussed below.

C.2 Instrument Description

A parts list and machine drawings for the complete DoD assembly can be found in Section C.3. The main elements are the receiver head, light guide, and the detector assembly. These are pictured in Figure C.1, and described below.

C.2.1 Receiver Head and Optical Light Guide

The receiver head is a cylindrical cell that contains the collection lens and mounting receptacle for the light guide. The lens is an off-the-shelf three-element assembly (Edmond Scientific Co.) designed for wide field imaging with excellent correction for spatial aberration. By adjusting the distance between the lens and the input ferrule to the light guide, the receiver can be made to image a circular region from 0.1–4 mm in radius to the 2 mm radius input aperture of the light guide (described below).

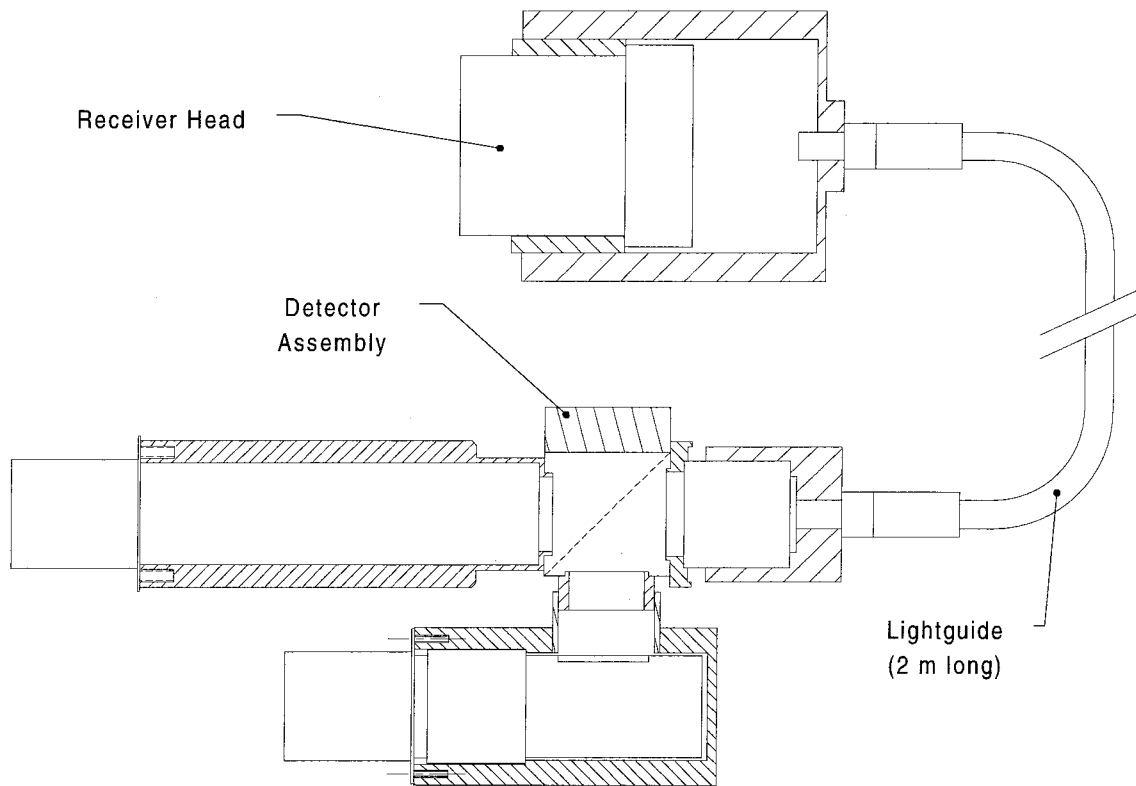


Figure C.1: Overview of LIF receiver system showing primary components.

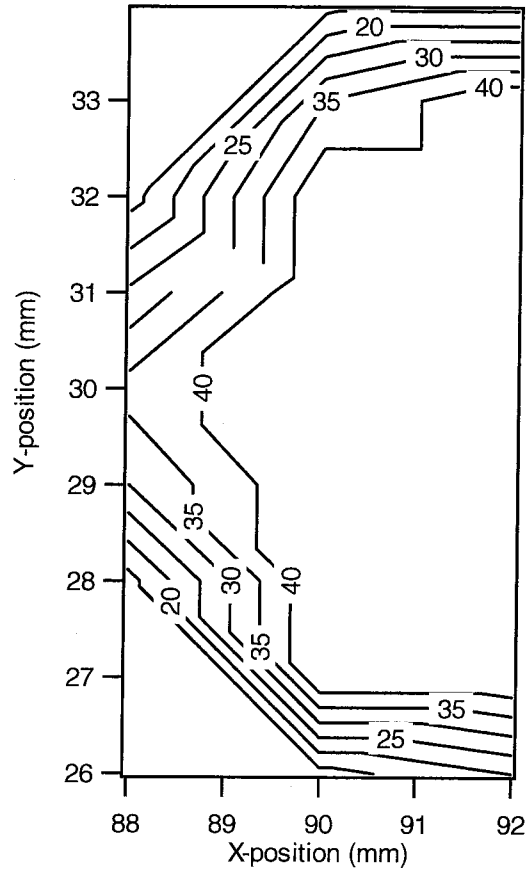


Figure C.2: Optical response in one-half of the measurement volume, showing uniform collection efficiency.

The sensitivity of the system to light scattering within this region is very uniform. This is demonstrated in the contour plot in Figure C.2. The plot is the result of a test in which a stream of droplets was passed through a uniform intensity planar light sheet. The receiver was positioned so that its measurement volume was co-planar to the light sheet. The intensity of the scattered light from the droplets was recorded as a function of the position of the droplets in the light sheet. The plot shows that the receiver response is uniform over a 4 mm radius, then falls off to zero over a 1 mm annulus.

The optical light guide is a liquid light guide (Edmond Scientific Co.) which features a large numerical aperture and a high (80%) transmission efficiency at 500 nm.

Since it does not use optical fibers to transmit light, there are no packing fraction losses and, thus, a uniform collection efficiency over the entire input aperture.

C.2.2 Detector Assembly

The detector assembly features a commercial LIF filter block (Omega Optical), which separates the excitation and emission bands with no detectable cross-talk. This filter cube is currently configured for LIF studies of fluorescein-type fluorophores. Other fluorophores can be accommodated, but this necessitates the replacement of the filter block for one designed for use in the required wavelength ranges. Two photomultiplier tubes are positioned to detect the separated bands, which can be optionally configured in photon counting mode to achieve the maximum sensitivity.

C.3 Parts List and Drawings

Table C.1: LIF receiver parts list.

Description	Location on Assembly Diagram	Vendor ¹	Part Number	Qty
<u>Off-the-Shelf Parts:</u>				
filter block	1	O	SF22	1
2" wide-angle ERFLE eyepiece	2	E	D41,347	1
pmt – straight viewing	10	H		1
pmt – side viewing	11	H		1
pmt preamplifier	13	H	E717-21	2
liquid light guide	14	E	A53,690	1
<u>Machined Parts:</u>				
block mount	3			1
light guide holder	4			1
collection lens holder	5			1
long pmt cover	6			1
spacer 1	7			1
spacer 2	8			1
pmt housing	9			1

1. Vendor Key: N: Omega Optical; E: Edmond Scientific; H: Hamamatsu

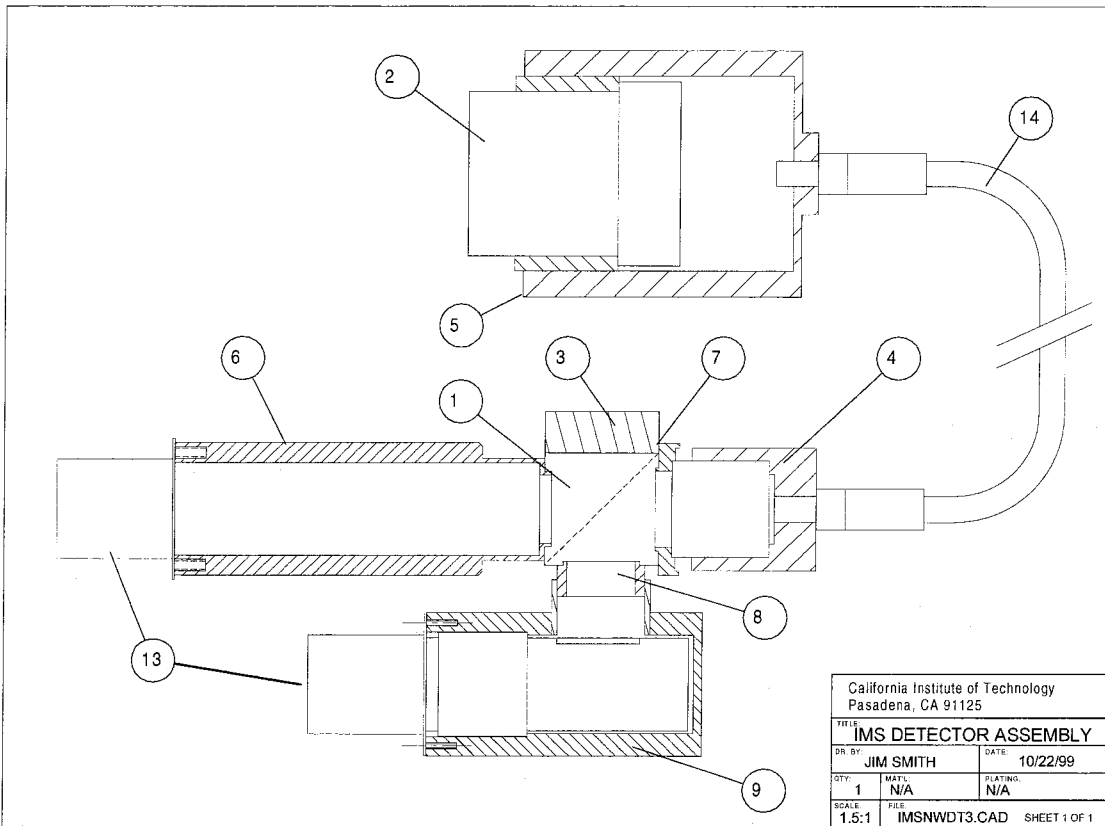
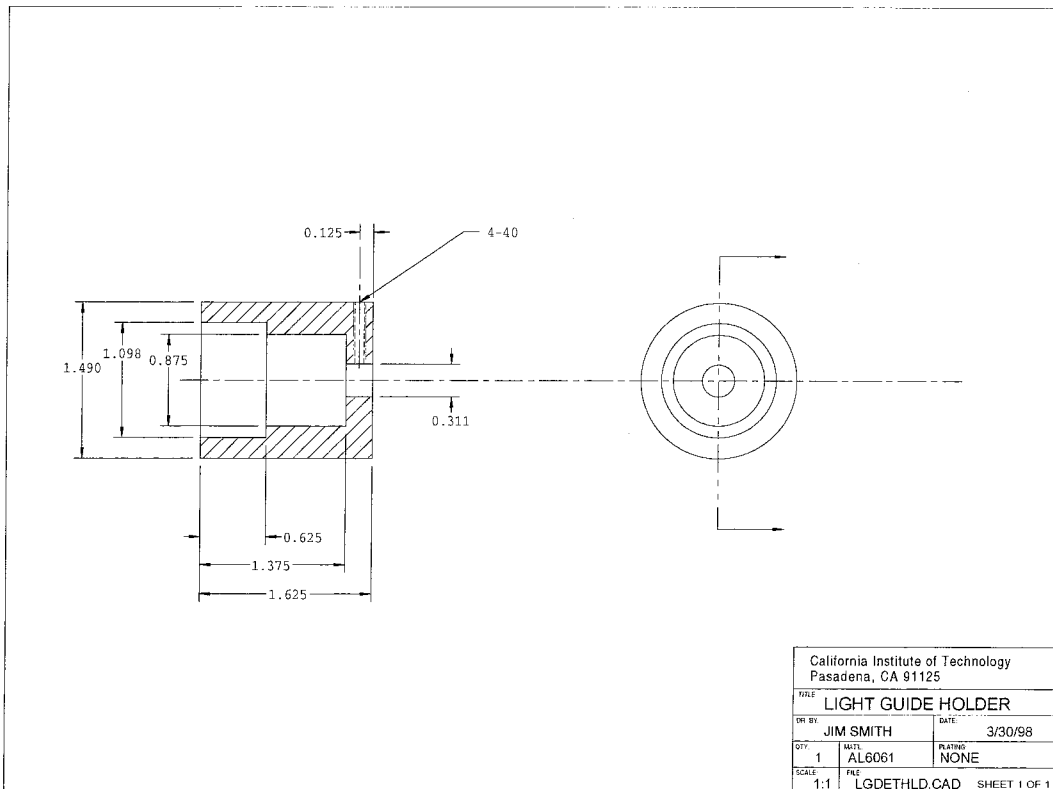
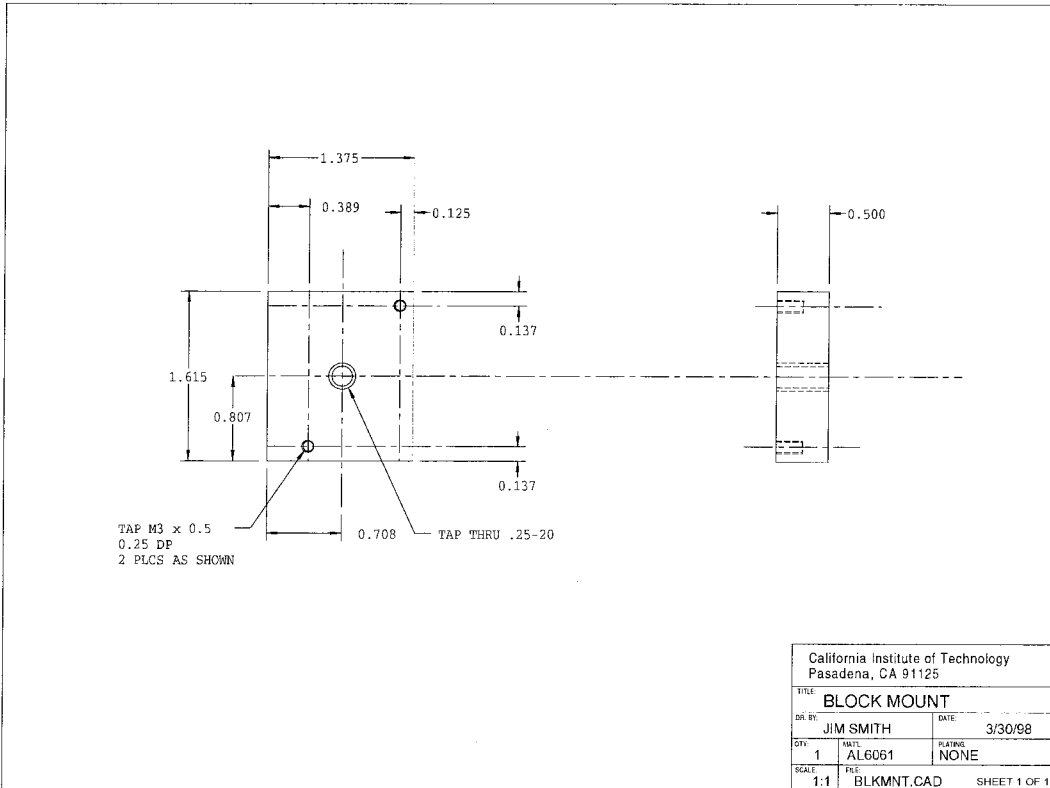
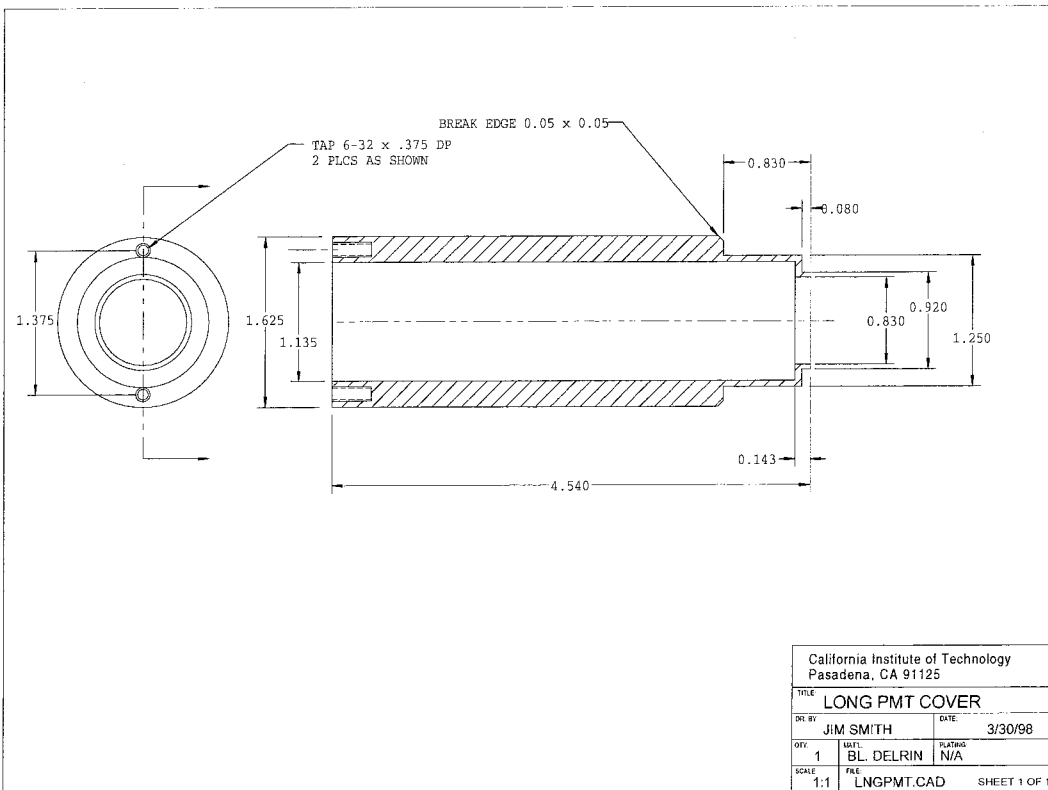
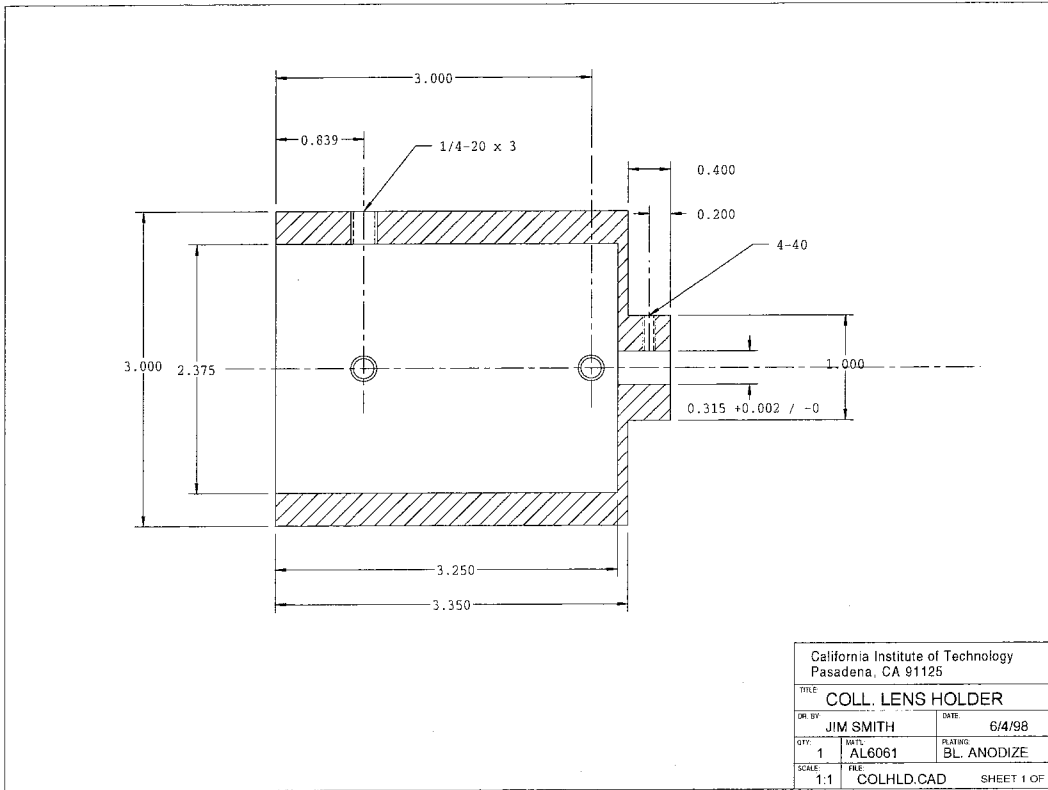
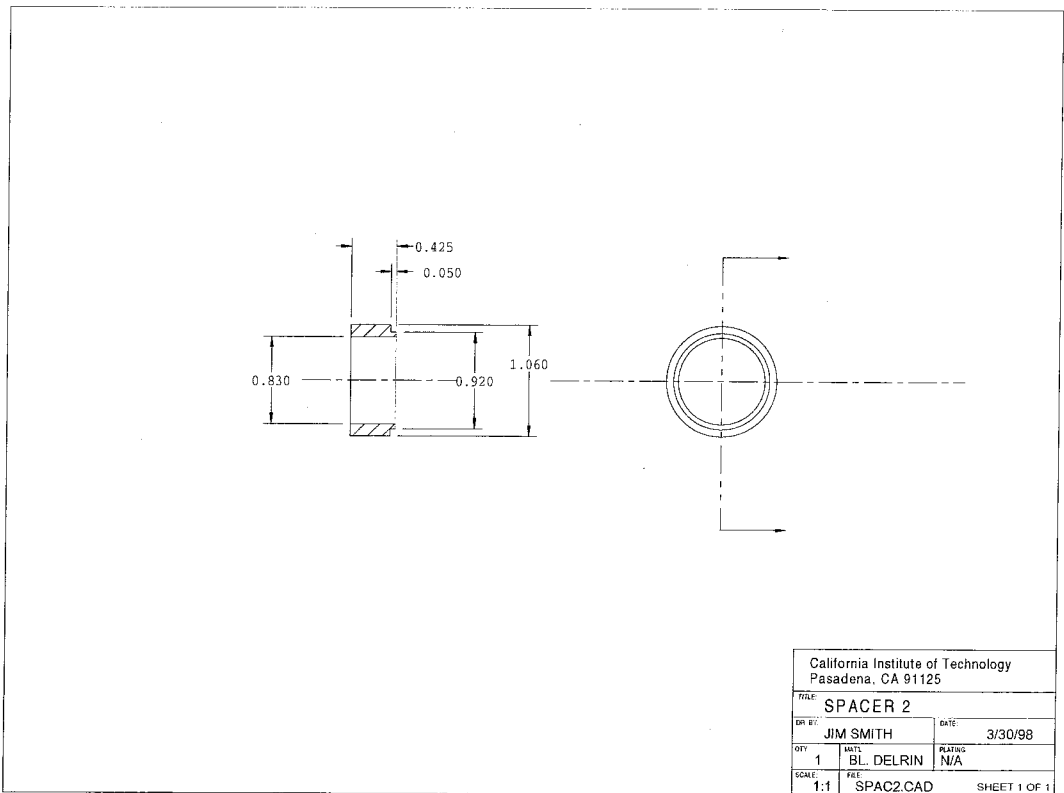
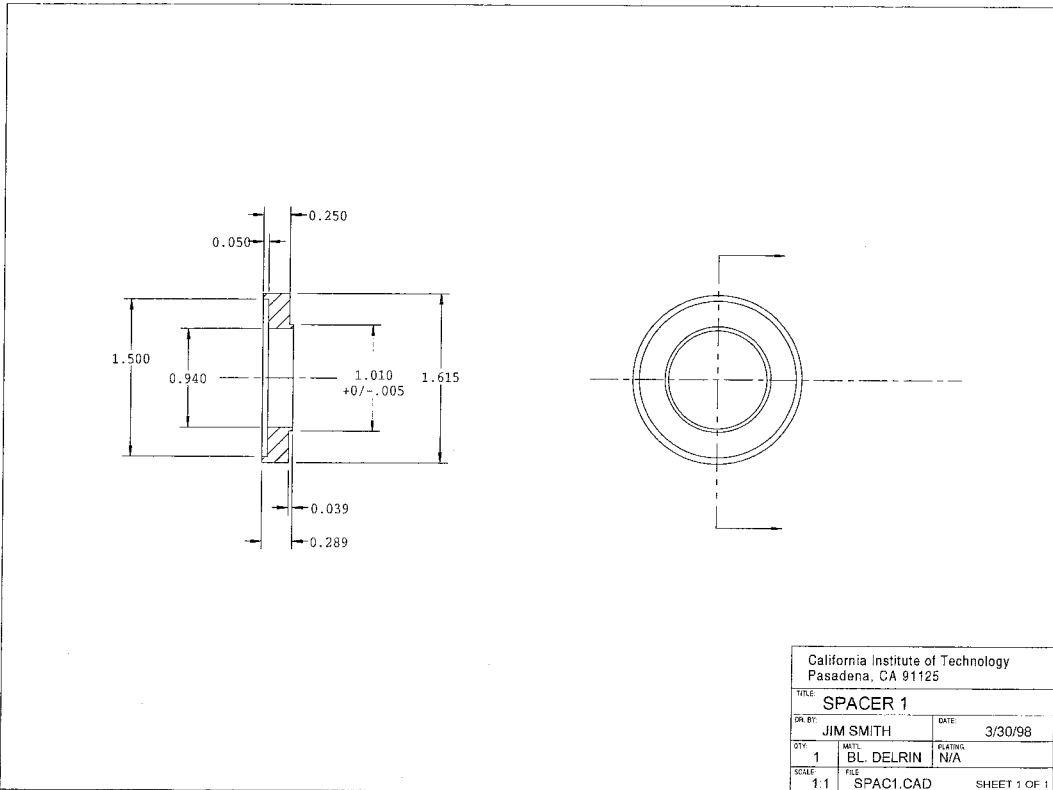
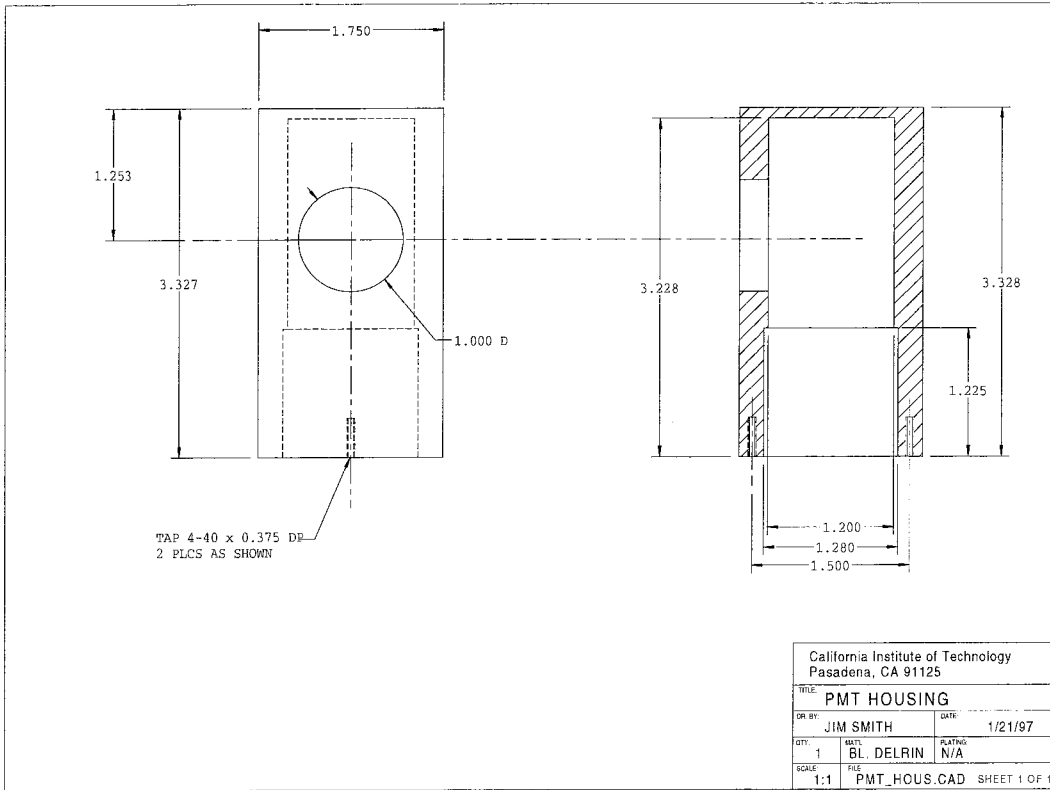


Figure C.3: Assembly diagram for LIF receiver. For parts description see Table C.1.









Appendix D Quantification of the Energetics of Droplet Fissioning with Droplet Ping-Pong Measurements

D.1 Theory

One notable result of observations of droplet disruption using the drift cell field reversal (“ping-pong”) technique is that it is possible to monitor a highly charged droplet through several fission events despite having no radial trapping field. This fact can be used to calculate the radial component of the impulse imparted to a droplet as a result of Rayleigh instability. In the following derivation, the radial force imparted to the droplet during the fission event is represented by the function $F(t)$, as shown in the lower part of Figure D.1. The radial velocity, v , of the droplet as a function of time can be derived from the force balance equation:

$$\frac{dv}{dt} + \frac{v}{\tau} = \frac{F(t)}{m}, \quad (\text{D.1})$$

where

$$\tau = \frac{mC_c}{3\pi\mu D_p} \quad (\text{D.2})$$

is a characteristic relaxation time for the droplet associated with aerodynamic drag (assuming Stokes flow), m and D_p are the mass and diameter of the droplet, respectively, C_c is the slip correction factor, and μ is the gas viscosity. Equation D.1 can be solved to obtain the droplet’s radial velocity for $t \leq \delta t$ by using $e^{t/\tau}$ as an integrating

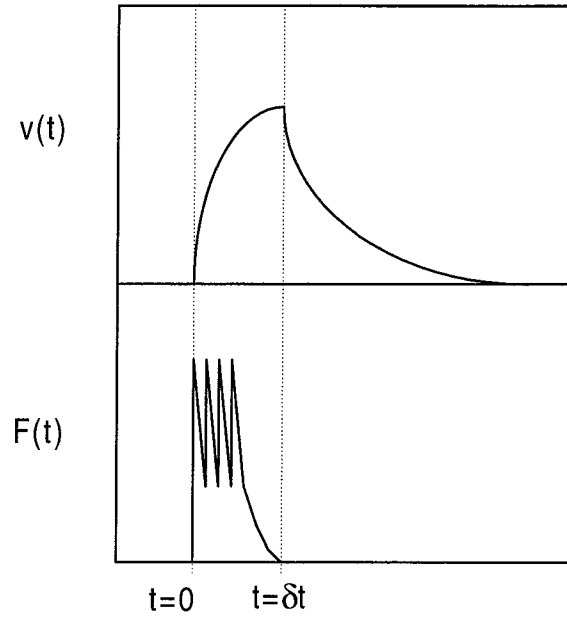


Figure D.1: Model for impulse imparted to parent droplet during Rayleigh instability.

factor and the limiting condition that $v(t = 0) = 0$:

$$v(t \leq \delta t) = e^{-t/\tau} \int_0^t \frac{F(t')}{m} e^{t'/\tau} dt'. \quad (\text{D.3})$$

For times greater than δt , the radial force is, by definition, zero. The radial droplet motion is governed by aerodynamic drag alone:

$$v(t > \delta t) = v(\delta t) e^{-(t-\delta t)/\tau} \quad (\text{D.4})$$

A schematic representation of time dependence of droplet velocity can be seen at the top of Figure D.1. The radial position of the droplet as a function of time, $x(t)$, is found by integrating Equations D.3 and D.4.

If one now considers a simple model of the disruption process whereby the force to the parent droplet is constant over time δt , then the analysis is greatly simplified.

Performing the integration in Equation D.3 results in:

$$v(t \leq \delta t) = \frac{F\tau}{m} (1 - e^{-t/\tau}). \quad (\text{D.5})$$

This is integrated once more to give the radial position of the droplet at $t = \delta t$:

$$x(\delta t) = \frac{F\tau}{m} [\delta t - \tau (1 - e^{-\delta t/\tau})]. \quad (\text{D.6})$$

To get the radial velocity for $t > \delta t$, Equation D.5 is solved for $t = \delta t$, and this result substituted into Equation D.4. The result is:

$$v(t > \delta t) = \frac{F\tau}{m} (1 - e^{-\delta t/\tau}) e^{-(t-\delta t)/\tau} \quad (\text{D.7})$$

This result is integrated to obtain the radial position for $t > \delta t$:

$$x(t > \delta t) = x(\delta t) + \frac{F\tau^2}{m} e^{\delta t/\tau} (1 - e^{-\delta t/\tau}) (e^{-t/\tau} + 1) \quad (\text{D.8})$$

If the observation time is great compared to the characteristic time for relaxation, a safe assumption in the case of the ping-pong experiment, then $t \gg \delta t$ leads to the simplification that $e^{-t/\tau} \cong 0$. Substituting Equation D.6 into Equation D.8 results in additional cancellations, leaving the simple result:

$$x(t > \delta t) = \frac{\tau F \delta t}{m} e^{\delta t/\tau} \quad (\text{D.9})$$

The product $F\delta t$ is the impulse of the disruption on the parent droplet, and $e^{\delta t/\tau}$ a factor that takes into account aerodynamic drag forces that take place during the time that the force is applied (i.e., during the fission process). Investigators who have studied the fission process using the electrodynamic have observed that the process of breakup is instantaneous[1]. If δt is associated with the breakup alone and not longer range electrostatic interactions between the parent droplet and its offspring, then based on the fact that $\delta t \ll \tau$ one can make the further simplification that $e^{\delta t/\tau} \cong 1$.

Further cancellations can be made by substituting the equation for τ (Equation D.2), into Equation D.9. This results in:

$$x(t > \delta t) = \frac{C_c F \delta t}{3\pi\mu D_p} \quad (\text{D.10})$$

With this result and the observation that droplet breakup is repeatedly observed with the phase Doppler anemometer (PDA), an estimate of the maximum radial impulse imparted to the parent droplet during fission can be made. For this calculation, the value of $100 \mu\text{m}$, a typical value for the measurement volume diameter of the PDA, is used for the maximum radial displacement of the droplet. Two observations lead to the conclusion that this represents not just the radial impulse, but the magnitude of the impulse over all three dimensions. First, observations of droplet fissioning are routinely made through as many as 6 discharge events (essentially until the droplet diameter shrinks to zero). Second, the change in the intensity of the phase Doppler signal through a single fission event, which can be used as a marker of the approximate movement of the droplet, is observed to be random. Thus one can conclude that the displacement that results from the fission process has no preferred direction. The result is plotted in Figure D.2.

D.2 Conclusion

A method is presented for quantifying the radial component of the force imparted to the droplet during disruption. If a simple model of droplet breakup is used whereby a constant force is supplied to the parent droplet over a time that is short compared to the aerodynamic relaxation time for the droplet, then the result is a linear dependence between the impulse applied to the droplet and the observed displacement. By applying the observation that droplets in the size range of $1\text{--}50 \mu\text{m}$ are routinely detected with the phase Doppler anemometer through numerous discharge events, then the result of this analysis is that the maximum impulse force must be range from 2×10^{-8} dyne·s (for a $10 \mu\text{m}$ droplet) to 8×10^{-8} dyne·s (for a $50 \mu\text{m}$ droplet).

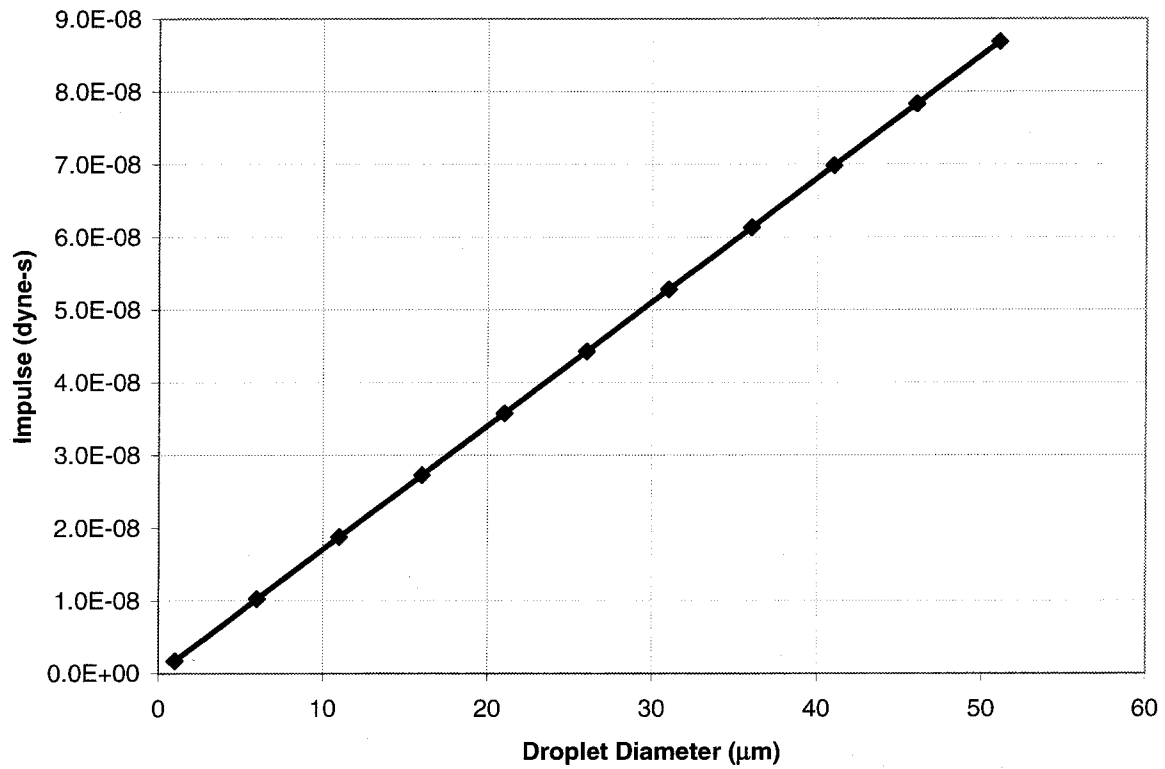


Figure D.2: Maximum impulse imparted to a water droplet as a function of droplet diameter, assuming that displacement lies within the 100 μm PDA measurement volume.

Clearly, additional work can be done to develop a more accurate model of the forces present during droplet breakup. The results of observations of charge and mass loss from a disruption can be used to estimate, for example, the effect of electrostatic interactions on $F(t)$.

Bibliography

- [1] EJ Davis and MA Bridges. The Rayleigh limit of charge revisited: light scattering from exploding droplets. *J. Aerosol Sci.*, 25:1179–1199, 1994.